The Effects of a Sliding Air Bubble on Heat Transfer from an Inclined Surface

Brian Donnelly

Department of Mechanical & Manufacturing Engineering

Parsons Building

Trinity College

Dublin 2

Ireland

January 2011

A thesis submitted to the University of Dublin in partial fulfillment of the requirements for the degree of Ph.D.
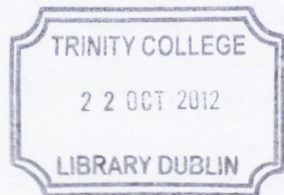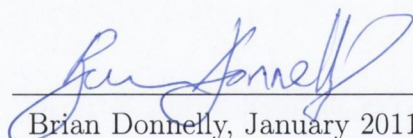
Declaration

I declare that this thesis has not been submitted as an exercise for a degree at this or any other university and it is entirely my own work.

I agree to deposit this thesis in the University's open access institutional repository or allow the library to do so on my behalf, subject to Irish Copyright Legislation and Trinity College Library conditions of use and acknowledgment.

Brian Donnelly, January 2011

Abstract

An investigation into the effect of a single sliding air bubble on heat transfer from a submerged, inclined surface has been performed. It is known that bubbles, both vapour and gas, can increase heat transfer rates from adjacent heated surfaces. However, the mechanisms involved are dynamic and complex and, in some cases, poorly understood. Although numerous studies exist for free rising bubbles, research on their effects on heat transfer are limited. Even fewer studies have been performed in relation to sliding bubbles. A comprehensive review of the available existing literature is presented.

The present study utilises high speed, high resolution, infrared thermography to measure the two dimensional surface heat transfer adjacent to a sliding bubble. The three dimensional bubble position and shape in two planes are simultaneously recorded with two high speed digital cameras. Fluid velocity in a plane parallel to the surface is computed using a high speed particle image velocimetry system. The equipment is mounted to a purpose built tilting water tank to observe the bubble as it slides. Computer code was developed to analyse and combine the data in a virtual three dimensional environment. Accurate, repeatable bubble volumes of 0.05, 0.1, 0.2 and 0.4 *ml* were released onto a surface inclined at 30° to the horizontal.

It was found that bubbles sliding on the heated surface greatly increase heat transfer rates. The effects were observed over large areas and persisted for a long duration. The bubble itself exhibited complex shape and path oscillations and was found to be greatly influenced by surface active contaminants. It is most likely that the wake generated behind the sliding bubble, identified through PIV, is responsible for both the behaviour of the bubble and the heat transfer effects observed. The nature of this wake is proposed to be that of a chain of horseshoe vortices.

Acknowledgments

This work would not have been possible without the help and support of the following people I have had the pleasure and opportunity to work with. First, I would like to thank my family, especially my mother and father without whom I would not be where I am today. They provided never ending support and interest throughout my Ph. D studies.

I would also like to extend my gratitude to my supervisor, Professor Darina B. Murray, for her attention to detail, support and guidance throughout my time at Trinity College. In addition I would like to thank Dr. Tony Robinson and Dr. Tadhg O'Donovan for their advice, enthusiasm and support.

I would like to thank Mr. Gerry Byrne for his positive outlook and much appreciated humour in addition to his technical help. I would like to acknowledge the excellent work being performed in the engineering workshop by Mick Reilly, Alex Kearns, Gabriel Nicholson and J. J. Ryan who helped create the experimental apparatus. I would also like to extend my gratitude to Joan Gillen for all her administrative help.

To all my fellow researchers; Alan McGuinn, Gerard McGranaghan, Rayhaan Farrelly, Seamus O'Shaughnessy and Tom Lupton, it has been a pleasure.

Last but by no means least, I would like to extend a special thank you to Louise and all my friends, without whom I would have lost my mind a long time ago.

Nomenclature

α Thermal diffusivity $[m^2/s]$

α^* Absorbtivity [-]

α_s Surface inclination angle $[degree]$

β Thermal expansion coefficient $[K^{-1}]$

ΔT Temperature difference $[°C]$

δ_{ss} Foil thickness $[m]$

ϵ Heat transfer coefficient enhancement factor [-]

κ Viscosity ratio [-]

λ Wavelength $[m]$

μ Viscosity $[kg/ms]$

ν Kinematic viscosity $[m^2/s]$

ω_z Vorticity [-]

ρ Density $[kg/m^2]$

ρ^* Reflectivity [-]

σ Surface tension $[N/m]$

τ Transmissivity [-]

θ Surface inclination angle [$degree$]

θ_b Bubble inclined angle [$degree$]

θ_c Correction angle [$degree$]

a_n Acceleration in direction n [m/s^2]

A_s Surface area [m^2]

b Bubble base width [m]

Bi Biot number [-]

C_D Drag coefficient [-]

c_p Specific heat capacity [J/KgK]

D Measured diameter [m]

d_e Equivalent diameter [m]

dx Foil element dimension [m]

e Eccentricity [-]

Eo Eötvös number [-]

F Force [N]

f Frequency [Hz]

Fr Froude number [-]

g Gravitational acceleration [m/s^2]

Gr Grashof number [-]

h Heat transfer coefficient [W/m^2K]

h_{fg} Latent heat of vapourisation [J/Kg]

2

I Current [Amp]

Im_n Image number n [$-$]

k Thermal conductivity [W/mK]

L Characteristic length [m]

m Mass [kg]

Mo Morton number [-]

Nu Nusselt number [-]

P Perimeter [m]

P_∞ Pressure [Pa]

Pr Prandtl number [-]

q Heat rate [W]

q'' Heat flux [W/m^2]

R Electrical resistance [Ω]

r Radius of curvature [m]

r_e Equivalent radius [m]

Ra Rayleigh number [-]

s_n Displacement in direction n [m]

$Scale_x$ Scaling factor for x [$-$]

Sr Strouhal number [-]

Sr Strouhal number [-]

t Time [s]

3

T_∞	Bulk fluid temperature [°C]
T_s	Surface temperature [°C]
Ta	Tadaki number [-]
U	Relative velocity [m/s]
U_T	Terminal velocity [m/s]
U_x	Uncertainty in measurement x [%]
V	Bubble volume [ml]
V	Voltage [$volt$]
v	Velocity [m/s]
v_f	Fluid velocity [m/s]
V_w	Wake volume [ml]
We	Weber number [-]
x	x-coordinate [m]
y	y-coordinate [m]
z	z-coordinate [m]

Contents

List of Figures

List of Tables

Dedicated in memory of Stephen Quirke

Chapter 1

Introduction

1.1 Background

It is known that the presence of bubbles in a system can lead to increased heat transfer rates from adjacent heated surfaces. In certain applications, such as shell and tube heat exchangers, vapour bubbles are created at nucleation sites on the liquid-solid boundary during boiling. It has been found that these bubbles increase heat transfer both when they detach from the surface and when they slide along or near adjacent heated surfaces. In other applications such as chemical reactors, gas bubbles may be introduced to the flow to increase both heat and mass transfer. In both situations the bubbles, whether gas or vapour, can come in contact with a downward facing heated surface. Bubbles of this nature are known as sliding bubbles.

Heat transfer between the inclined surface and the fluid depends on the interaction at the surface which is still the focus of much research. Heat transfer has been found to be influenced by bubble volume, surface inclination angle, micro-layer evaporation, wake disturbances and heat transfer into and out of the bubble. The relative contribution of each of these to the overall heat transfer is still a much debated topic. Due to the complexity of such systems, ever more elaborate ways of measurement and analysis are continually being developed. Recent advances in two dimensional temperature measurement have allowed for the first time a more in depth investigation into the sliding bubble phenomenon.

Work presented here has been performed in conjunction with a numerical study carried out by Dr. Yan Delauré and Dr. S. Senthil Kumar in Dublin City University. A detailed description of this work is presented in the Ph.D thesis "Computations of Bubble Dynamics with Heat Transfer".

1.2 Research motivation

The aim of the present study is to investigate the effect of a single sliding air bubble on heat transfer from an inclined, heated and unheated surface. Simultaneous measurement of heat transfer, fluid motion and bubble motion is performed in order to further understand the complex interactions in the fluid and at the surface. This is only made possible through the use of high speed, two-dimensional fluid and temperature measurement devices.

A high frame rate, high resolution, thermal camera measures the rear surface temperature of a thin stainless steel foil that forms the sliding surface. The foil approximates a uniform heat generation boundary condition; although additional analysis is performed to account for lateral conduction within the foil, heat capacitance effects and losses to the surroundings in order to quantify the heat transferred to the fluid. The camera is capable of precise, two dimensional measurement of the test surface which measures $140 \times 60 \ mm^2$. This corresponds to approximately 4 discrete temperature measurements per square millimeter of surface.

This system is linked to a high resolution, high frame rate visual camera system that simultaneously records bubble dynamics. Two cameras mounted perpendicular to each other observe the bubble shape in two planes and bubble position in three dimensions as it slides over the heated surface. Purpose written computer code analyses the images and calculates various parameters such as position, shape, velocity, orientation & eccentricity. Results from this system are coupled with thermal measurements allowing a three dimensional virtual reconstruction of the environment.

Fluid measurement is performed using a high frame rate particle image velocimetry (PIV) system. This allows two dimensional fluid velocity in a plane parallel to the surface to be linked with heat transfer and bubble position. The three state of the

art systems, working together, allow a unique new insight into the sliding bubble phenomenon.

The main objectives of this research are to construct an experimental apparatus capable of measuring the interaction between bubble, fluid and surface. Results from this are analysed and interpreted in order to fill a gap in the literature on sliding bubbles and heat transfer.

1.3   Dimensionless numbers

Due to the broad range of parameters involved in the study of sliding and rising bubbles, results are generally presented in dimensionless form to allow easy comparison across a broad range of fluid and bubble properties. The following sections describe the significance of each of the main dimensionless numbers presented throughout this study.

1.3.1   Reynolds number

The Reynolds number provides a measure of the ratio of inertial to viscous forces. Depending on the flow parameters, either the inertial forces dominate ($Re \gg 1$), the viscous forces dominate ($Re \ll 1$) or there is an approximate balance ($Re \approx 1$). The Reynolds number can be used to determine similarities between different experimental (or numerical) setups such as the onset of turbulence or certain flow regimes eg. an attached wake or regular vortex shedding. It is used in the present study (sometimes in conjunction with the Morton or Eötvös number, discussed below) to predict approximate bubble shapes, terminal velocity and the onset of wake structures. It is presented as

$$Re = \frac{\rho U L}{\mu} = \frac{\rho U_T d_e}{\mu} \tag{1.1}$$

where ρ and μ are the fluid density and viscosity respectively, U is the relative velocity and L is a characteristic length. In the study of rising bubbles, the relative velocity is the terminal rise velocity, U_T, and the characteristic length is usually chosen to be the diameter of a sphere with the same volume as the bubble, the 'equivalent diameter',

d_e[1].

1.3.2 Eötvös number

The Eötvös number[2], sometimes referred to as the Bond number, is a ratio of the gravity or buoyancy forces to the surface tension force,

$$Eo = \frac{\Delta\rho g L^2}{\sigma} = \frac{\Delta\rho g d_e^2}{\sigma} \tag{1.2}$$

When the 'particle' density is negligible[3], this reduces to

$$Eo = \frac{\rho g d_e^2}{\sigma} \tag{1.3}$$

where $\Delta\rho$ is the difference in density between the two phases, g is the gravitational acceleration, L is the characteristic length and σ the surface tension. Once again, the characteristic length for a bubble is generally chosen to be the equivalent diameter, d_e. High Eötvös number flows ($Eo \gg 1$) indicate the system is generally unaffected by surface tension forces. Low Eötvös number flows ($Eo < 1$) indicate surface tension dominates while intermediate values illustrate an approximate balance.

1.3.3 Morton number

The Morton number, sometimes referred to as the M-group or property group, involves only the physical properties of the surrounding medium and the pressure field. It is defined as

$$Mo = \frac{g\mu^4\Delta\rho}{\rho^2\sigma^3} \tag{1.4}$$

where g is gravitational acceleration, μ is the fluid viscosity, $\Delta\rho$ is the difference between the particle and flow density, ρ is the fluid density and σ is the surface tension. For systems with negligible particle density, the Morton number reduces to

$$Mo = \frac{g\mu^4}{\rho\sigma^3} \tag{1.5}$$

---

[1]For larger bubbles (volume usually greater than 3 cm^3), the base width, b, is generally used as the characteristic length resulting in $Re = \rho U_T b/\mu$.

[2]Named after the Hungarian physicist Loránd Eötvös and is pronounced 'Ertversh'.

[3]The particle, in the present study, is the bubble.

Note that the Morton number is independent of bubble size or velocity. Low viscosity fluids generally have a low Morton number, such as water ($Mo = 2.5 \times 10^{-11}$), while high viscosity fluids, such as corn syrup, generally have high Morton number (Mo in the order of 10^8). The Morton number can be used in conjunction with either Re or Eo to predict bubble shapes and terminal velocity.

1.3.4 Weber number

The Weber number is often used in fluid mechanics where there is an interface between fluid flows, such as in this case, an air bubble in water. It is a measure of the relative values of the dynamic pressure ($\propto \rho U^2$) to the surface tension pressure ($\propto \sigma/L$). It can be written as

$$We = \frac{\rho U^2 L}{\sigma} = \frac{\rho U_T^2 d_e}{\sigma} \tag{1.6}$$

where ρ is the fluid density, U is the relative velocity, L is the characteristic length and σ is the surface tension. The bubble terminal velocity, U_T, and equivalent diameter, d_e, are used here. It can be expressed in terms of the Reynolds, Morton and Eötvös numbers as

$$We = Re^2 \sqrt{\frac{Mo}{Eo}} \tag{1.7}$$

The Weber number can, in certain cases, be used to indicate specific bubble motion characteristics, e.g. the onset of bubble path oscillations for spherical cap bubbles in pure liquids occurs at $We_{os} = 3.18$.

1.3.5 Tadaki number

As presented in Fan & Tsuchiya [1], experimental evidence suggests that for $Mo < 2.5 \times 10^{-4}$, the relationship between d_e/b (bubble equivalent diameter/bubble width) and Re is a unique function of Mo; this meant d_e/b could be correlated with a single parameter called the Tadaki number

$$Ta = ReMo^{0.23} \tag{1.8}$$

where, for ellipsoidal bubbles, such as those in the present study,

$$\frac{d_e}{b} = \left(\frac{h}{b}\right)^{\frac{1}{3}} \tag{1.9}$$

where h is the bubble height and b is the bubble breadth measured parallel and perpendicular to the fluid flow respectively. Thus, in certain circumstances, the Tadaki number can be used to predict the bubble aspect ratio when the Reynolds and Morton numbers are known.

1.3.6 Strouhal number

The Strouhal number is a dimensionless number describing oscillating flow mechanisms. It is given as

$$Sr = \frac{fL}{U} = \frac{fd_e}{U_T} \tag{1.10}$$

where f is the frequency of vortex shedding, L is the characteristic length and U is the relative velocity ($L = d_e$ and $U = U_T$ for results presented in this study). The Strouhal number can be used to describe vortex shedding and associated path oscillations behind sliding and rising bubbles.

1.3.7 Froude number

The Froude number is a measure of the ratio of inertial to buoyancy forces, it is generally defined as

$$Fr = \frac{U}{\sqrt{gL}} \tag{1.11}$$

where U is the relative velocity, g is the acceleration due to gravity and L is the characteristic length. It is modified to account for bubbles sliding under an inclined surface, since only a certain fraction of the buoyancy forces acts parallel to the surface,

$$Fr = \frac{U_T}{\sqrt{gd_e \sin\theta}} \tag{1.12}$$

where θ is the surface inclination angle, U_T is the bubble's sliding terminal velocity and d_e is the equivalent diameter. It can be expressed in terms of the bubble volume, V, as

$$Fr = \frac{U_T}{\sqrt{gV^{\frac{1}{3}} \sin\theta}} \tag{1.13}$$

where

$$V = \frac{1}{6}\pi d_e^3 \tag{1.14}$$

1.3.8 Rayleigh number

The Rayleigh number can be used to indicate flow transitions in natural convection heat transfer such as the onset of turbulence. The Rayleigh number is defined as

$$Ra = GrPr \tag{1.15}$$

where Gr and Pr are the Grashof number[4] and Prandtl number respectively. The Grashof number is a measure of the ratio of buoyancy to viscous forces and is defined as

$$Gr = \frac{g\beta \left(T_s - T_\infty\right) L^3}{\nu^2} \tag{1.16}$$

where g is the acceleration due to gravity, β is the volumetric thermal expansion coefficient, T_s is the surface temperature, T_∞ is the bulk fluid temperature, L is the characteristic length and ν is the kinematic viscosity (μ/ρ). The Prandtl number is a measure of the ratio of momentum to thermal diffusivity and is defined as

$$Pr = \frac{c_p\mu}{k} = \frac{\nu}{\alpha} \tag{1.17}$$

where c_p is the specific heat capacity, μ is the viscosity, k is the thermal conductivity, ν is the kinematic viscosity and α is the thermal diffusivity ($= k/\rho c_p$).

1.3.9 Nusselt number

The Nusselt number represents the dimensionless temperature gradient at a heated surface. It is defined as

$$Nu = \frac{hL}{k} \tag{1.18}$$

where h is the heat transfer coefficient, L is the characteristic length and k is the thermal conductivity. The characteristic length for a horizontal heated surface submerged in a fluid is

$$L = \frac{A_s}{P} \tag{1.19}$$

where A_s is the surface area and P is the perimeter. Numerous correlations exist relating the Rayleigh number to the Nusselt number depending on the system setup.

---

[4]The Grashof number in natural convection flow is analogous to the Reynolds number in forced convection flow.

Thus, the Nusselt number and Rayleigh number can be used to estimate the heat transfer coefficient and surface heat transfer rates.

Chapter 2

Literature Review

The shape, motion and behaviour of bubbles is dependent on a large amount of parameters. Numerous studies have been performed on free rising bubbles, such as investigations into effects of fluid contamination, the rise velocity, shape and trajectory characteristics, wake formation and shedding and pressure distribution. There have even been studies into the fluid motion within the bubble. The work on sliding bubbles is less comprehensive but includes studies on effects of geometry, fluid parameters and bubble volume in addition to limited work on their effects on heat transfer. The following literature review considers both free rising and sliding bubbles and includes heat transfer aspects where available.

2.1 The effects of surfactants

Before a discussion on bubble motion can be presented, it is important to consider the effects of contaminants that may be present within the fluid. Surfactants are impurities in the continuous phase[1] that gather on the bubble surface, reducing its mobility and influencing the surface tension. As the bubble rises, the main flow pushes these impurities from the front stagnation point to the rear. The resulting concentration gradient generates a tangential surface tension gradient. This in turn causes a tangential stress, also known as Marangoni stress, to oppose the flow shear stress. The motion of the surface is restricted and the drag coefficient approaches that of a solid

---

[1]The continuous phase is water in the present study.

sphere, (Frumkin & Levich [2], Griffith [3] and Alves et al. [4]). This is known as the stagnant cap hypothesis because the front of the bubble remains uncontaminated and freely mobile, while the rear (the 'stagnant cap') is rendered immobile by surfactants. Even trace amounts of surfactants can slow the rise velocity of bubbles due to their effect on the interface, this in turn has an effect on the bubble wake and drag coefficient. The rise velocity of air bubbles strongly depends on the water purity, especially in the range $d_e = 0.5 - 17$ mm (the range of the present study is $d_e \approx 5.5 - 11$ mm). For example, velocities of 0.36 m/s have been observed (Duineveld [5]) for $1.6 - 1.8$ mm air bubbles in purified water, while this reduces to less than half that in tap water. This can result in difficulties in comparing experimental data, even when great care has been taken to remove surfactants.

Systems which exhibit high surface tension, e.g. water and air, are most susceptible to the effects of impurities so it is better to try and account for, rather than remove them. When accounting for impurities both the nature and amount must be considered. Contaminants with the greatest retarding effect are those that are insoluble in either phase and those with high surface pressures. Further complicating this is the fact that the bubble interface may start off with no surfactants but gather them as it rises.

Alves et al. [4] investigate the effect of bubble contamination on rise velocity and mass transfer. In their experiments the bubble is kept stationary relative to the observer by releasing it to a downward flow, the setup is unique in that it can measure the change in terminal velocity as the bubble gathers surfactants on the interface. This rig consists of a 1.6 m long, 22 mm diameter tube as the test section. The shape, terminal velocity and mass transfer to the bubble were recorded for air bubbles of $1 - 5$ mm diameter in water. The pressure could be manipulated to allow the bubble to either dissolve in the fluid, grow, or remain at constant diameter. Results for the terminal velocity in pure and contaminated systems agreed well with Clift et al. [6]. Figure 2.1 shows the evolution of the bubble velocity with time as surfactants build up at the interface i.e. from a pure to contaminated system.

More recently, Saito et al. [7] present a study of the effects of surfactants on the fluid motion around a 2.89 mm diameter zig-zagging bubble (a bubble whose path
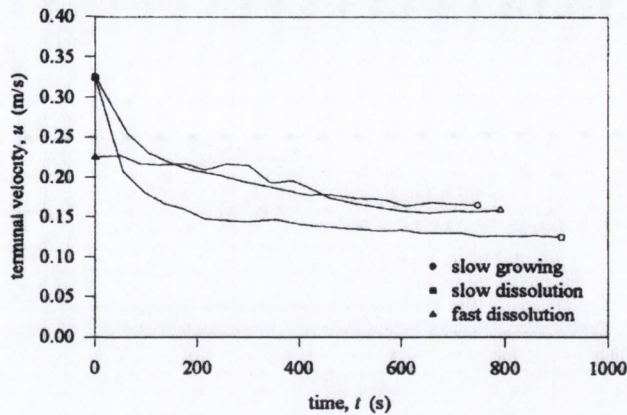
Figure 2.1: Initial and final bubble terminal velocity in distilled, clean distilled and clean millipore water (dark symbols; initial, open symbols; final). The Figure illustrates the reduction in terminal velocity over time as surfactants build on the interface. The rig pressure can be varied to allow the bubble to either dissolve, grow or remain a constant size, Alves et al. [4]

oscillates). They use a recursive cross-correlation PIV technique in order to capture the large dynamic range of velocities in the system. Figure 2.2 illustrates the effect of surfactants on the wake intensity around a rising bubble. The only difference between tests is the inclusion of surfactants of 150 *ppm* (parts per million) and 500 *ppm* (Figure 2.2 (c) and Figure 2.2 (d) respectively) of 1-pentanol in purified water. Vortex shedding was observed at the outside of the trajectory in all cases (i.e. at the maximum lateral displacement) but the intensity in the far wake region differed. Interestingly, the intensity of the 150 *ppm* solution was highest compared to the others. This was attributed to fluctuation of the flow separation point in conjunction with the boundary of slip (contaminated) and non-slip (not contaminated) on the bubble surface, thus magnifying the vortex intensity. At 500 *ppm*, the surface is saturated with contamination and has a no-slip boundary condition over all of its surface, thus this boundary oscillation does not occur.

Completely 'pure' systems rarely exist in engineering, and as such, the effect of surfactants, although important in their own right, has limited practical importance. Surfactant effects become important when comparing results between, for example, two tests performed with the same experimental apparatus on different days or comparing
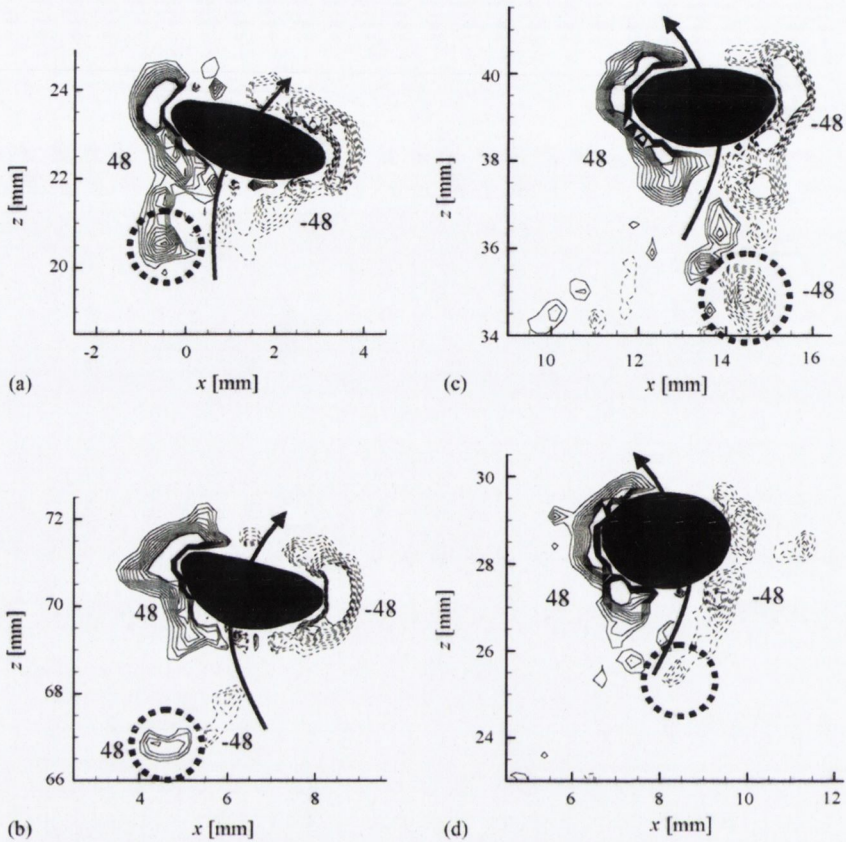
Figure 2.2: Vorticity profile of the surrounding liquid of a bubble: (a) purified water ($t = 0.25\ s$), (b) purified water ($t = 0.73\ s$), (c) 150ppm ($t = 0.15\ s$), (d) 500ppm ($t = 0.12\ s$). The figure illustrates the effect of surfactants on the wake intensity, Saito et al. [7]

results from different experimenters, where observed differences may only be due to the presence of surfactants.

2.2 Free rising bubbles: bubble dynamics

It is important to study the motion of single, free rising bubbles in order to understand how a bubble may influence heat transfer as it slides along an inclined surface. Bubbles, whether sliding or free rising, exhibit similar characteristics in both their motion and wake behaviour. These factors have been strongly linked with increased heat transfer from the surface. Thus, the study of free rising bubbles provides a foundation for the

study of sliding bubbles and their effect on surface heat transfer. The terminal rise velocity, shape characteristics, wake formation and vortex shedding, pressure distribution around a bubble and shape oscillations are discussed in the following sections. As highlighted by Clift et al. [6], bubbles, drops and particles have a great deal in common from a fluid dynamics perspective. Many of the fluid flow phenomena observed for spherical/circular solid particles are also observed for falling drops and rising bubbles, and as such, a great deal of information currently exists in the literature.

2.2.1 Terminal velocity, shape and motion

The dynamic pressure generated by the relative velocity between the bubble and surrounding medium determines the bubble's shape. High pressure at the front stagnation point results in an inward pressure against the bubble front surface. At the sides the flow must accelerate around the bubble interface resulting in decreased pressure. This causes the bubble sides to protrude outwards. Downstream of the bubble, the presence of the wake (which will be discussed in Section 2.3) ensures the pressure is not fully recovered. An elongation in the direction perpendicular to the bubble motion is predicted, due to this pressure acting on the bubble.

While the bubble shape can generally described as ellipsoid, at any one moment in time it can be far from that. The instantaneous bubble shape is the result of superposition of various modes of interface fluctuations taking place at different amplitudes and frequencies. The dominant mode can be periodic, characterised as an elongation and contraction of the bubble width that occurs at twice the bubble path oscillation. For larger bubbles (i.e. spherical cap bubbles), the base can oscillate in conjunction with vortex shedding.

Davies & Taylor [8] present one of the earliest studies of large bubbles rising within a fluid. They analysed the rise velocity of spherical cap air bubbles in water and nitrobenzene. The bubble volume varied from $1.5 - 200\ ml$. Bubbles of this volume take on the shape that is referred to as a spherical cap (bubble shapes will be discussed in more detail in a later section but these can be thought of as an approximate 'dome' shape.). They concluded that the velocity could be calculated by analysing a bubble's

radius of curvature, i.e. that radius of curvature of the spherical surface. They present an equation that describes the terminal velocity, U_T, as

$$U_T = \frac{2}{3}\sqrt{gr} \qquad (2.1)$$

where g is the acceleration due to gravity and r is the radius of curvature. Comparison between theory and experiment showed excellent agreement. In their calculations they assume that the flow over the spherical cap bubble is similar to that of inviscid flow over a sphere, an assumption which was shown to be valid.

Further to this research, Saffman [9] performed a study of free rising air bubbles in filtered water with bubble equivalent diameter in the range of $1 - 8$ mm (tests performed in the present study cover the range $d_e \approx 5.5 - 11$ mm, although these slide on an inclined surface). The shape of the bubbles in these experiments approximated that of an oblate spheroid[2]. He found that bubbles moved in one of three modes, straight, zig-zag or spiral, depending on the diameter. When d_e was smaller than 1.4 mm the bubble rose steadily in a straight line (rectilinear motion). With d_e in the range $1.4 - 2$ mm, the bubble was found to zig-zag, the plane in which it zig-zagged remaining fixed as it rose. Bubbles with d_e in the range of $2 - 4.6$ mm were more complicated, either spiraling or zig-zagging. Above 4.6 mm the spiral or zig-zag motion begins to slowly disappear and is completely gone above 6 mm. For the size range in which both spiraling and zig-zag motion can occur, bubbles would usually zig-zag if they left the injecting tube in one piece[3], but the presence of an obstruction immediately after the injector made the bubble spiral. For two bubbles being released it was found that the second bubble usually followed the mode of motion of the first. The mode of motion was observed to change from zig-zag to spiral but never vice versa. Bubbles were also projected at speed into the test tank but no difference in motion was observed. Additional tests were performed using unfiltered water; no difference was observed except that the onset of zig-zagging occurred at $d_e = 1.6$ mm, rather than 1

---

[2]Oblate refers to the orientation of the spheroid; an oblate shape has its longer axis perpendicular to the oncoming flow, prolate shapes have the longer axis parallel to the flow and would generally be considered streamlined.

[3]It was found that when trying to inject larger volume bubbles, on occasion, the bubble would break into two smaller bubbles upon release.

mm, and spiraling motion did not occur below $d_e = 2.2\ mm$. Overall, the experiments indicate that when a bubble's diameter reaches a value where straight line motion becomes unstable, the bubble will begin to zig-zag. At larger diameter, this motion is itself unstable and spiraling occurs. By assuming inviscid flow near the front of the bubble and that the bubble and its wake approximate a sphere (similar to the analysis performed by Davis & Taylor [8]), theoretical calculations of terminal velocity were made that compared well with the experiments. Modifying the theory to account for the presence of impurities also gave good results for rise velocity predictions. Reference to a possible periodic discharge of vorticity from the wake was made.

In 1978 a comprehensive review of the literature was compiled by Clift et al. [6] in an attempt to highlight the similarities between different fields of engineering concerning bubbly flows. It highlighted the important similarities, and differences, between gas bubbles, liquid drops and solid particles. As a starting point of the analysis the authors assume the creeping flow approximation. A solution to this was derived independently by Hadamard [10] and Rybczynski [11] which, as reported by Clift et al. [6], treated the sphere as a fluid with zero surface active contaminants[4] and thus constant interfacial tension (surface tension). The theory leads to an important conclusion that a bubble will remain spherical until inertial forces become significant. Another corollary is that it is not necessary for surface tension forces to be predominant for a bubble to remain spherical. Surface active contaminants may cause marked changes in internal circulation and drag but the effect on shape was found to be negligible. These findings are only strictly true when the creeping flow approximation is valid i.e. at low Reynolds numbers. The terminal rise velocity of the bubble using the Hadamard-Rybczynski solution is found to be

$$U_T = \frac{2ga^2\Delta\rho}{3\mu}\left(\frac{1+\kappa}{2+3\kappa}\right) \tag{2.2}$$

where κ, the viscosity ratio, is the ratio of the bubble viscosity, μ_b, to the viscosity of the bulk medium, μ, a is the bubble radius and $\Delta\rho$ is the density difference between the bubble and fluid. Stokes's solution for flow past rigid spheres can be obtained from this solution if slightly different boundary conditions are used with $\kappa \to \infty$ (i.e. the

---

[4]Examples include detergent and organic particles that may enter the fluid if exposed to the environment.

bubble viscosity is very low compared to the fluid). This yields the terminal velocity as

$$U_T = \frac{2ga^2\Delta\rho}{9\mu} \tag{2.3}$$

The Hadamard-Rybczynski theory predicts the terminal velocity of a fluid sphere to be 50% higher than that of a rigid sphere. However, other experimental results (Bond and Newton [12]) show that smaller bubbles follow Stokes' law, but as the diameter is increased, there is a sharp rise in terminal velocity to correspond closely with the Hadamard-Rybczynski result. It was deemed that the most reasonable explanation of why there is so much scatter in the experimental results, when compared to the two theoretical predictions, is the effect of surfactants. As contaminants are collected on the surface, they are swept to the rear of the bubble, leaving the front 'clean'. This results in a surface tension gradient along the interface that reduces the circulation within the bubble, effectively making it act as a rigid sphere. The effects of these contaminants are much greater on smaller bubbles which could explain the difference in experimental results described above. Experiments in ultra clean systems result in rise velocities much closer to the Hadamard-Rybczynski result. In reality it is very difficult to remove all impurities from a system so the Hadamard-Rybczynski theory is essentially redundant, although it serves as an important limiting case. Clift et al. [6] give the terminal rise velocity of small bubbles in contaminated systems at low Reynolds number as

$$U_T = U_{T,Stokes}\left(1 + \frac{Z}{2}\right) \tag{2.4}$$

where

$$Z = \left(\frac{2}{2 + 3\kappa}\right)(2(Y-1)) \tag{2.5}$$

where the first term in Z follows from the Hadamard-Rybczynski analysis and the second accounts for surfactant effects. Y is defined as $U_T/U_{T,Stokes}$, the ratio of bubble terminal velocity to the Stokes terminal velocity. Figure 2.3 provides values of Y versus Eötvös number ($Eo = gd_e^2\rho/\sigma$) using Griffith's [3] results.

Ellipsoidal fluid particles are also discussed by Clift et al. [6]. The conditions for a bubble to be ellipsoidal are outlined in Figure 2.6 (see page 39), but in most systems this shape occurs when a bubble is in the range of $d_e = 1 - 15$ mm (intermediate
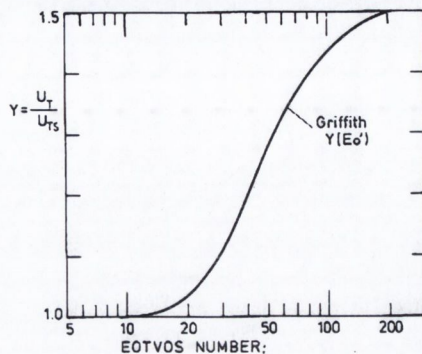
Figure 2.3: Ratio of bubble terminal velocity to Stokes terminal velocity ($Y = U_T/U_{T,Stokes}$) versus Eötvös number for use in Equation 2.5, Griffith [3].

size), excluding systems of high Morton number (i.e. systems with high fluid viscosity). Figure 2.4 shows the terminal velocity of air bubbles in water at 20 °C for both pure and contaminated systems. It is compiled by Clift et al. [6] from experiments conducted by numerous other authors. The variation observed is partly due to experimental scatter but, according to Clift et al. [6], mainly due to the presence of surfactants in the individual systems. The upper and lower curves can be seen to converge for small diameters. This is due to the fact that even the smallest amounts of impurities prevent circulation in bubbles of this size range. The curves also converge at large diameter as the surface tension forces, which are affected by the presence of impurities, cease to be important. The corresponding drag curves appear in Figure 2.5. The upper curve

d_e (mm)	Re	Eo	Path
< 1.3	< 565	> 0.8	Rectilinear
1.3 to 2.0	565 to 880	0.8 to 0.5	Helical
2.0 to 3.6	880 to 1350	0.5 to 0.36	Plane (zig-zag), then helical
3.6 to 4.2	1350 to 1510	0.36 to 0.28	Plane (zig-zag)
4.2 to 17	1510 to 4700	0.28 to 0.23	Rectilinear but with rocking

Table 2.1: The observed motion of intermediate sized air bubbles in water at 28.5 °C, including the corresponding Reynolds and Eötvös numbers, Clift et al. [6].

for terminal velocity in Figure 2.4 is approximated closely by the equation

$$U_T = \left[\left(\frac{2.14\sigma}{\rho d_e} \right) + 0.505 g d_e \right]^{\frac{1}{2}} \tag{2.6}$$
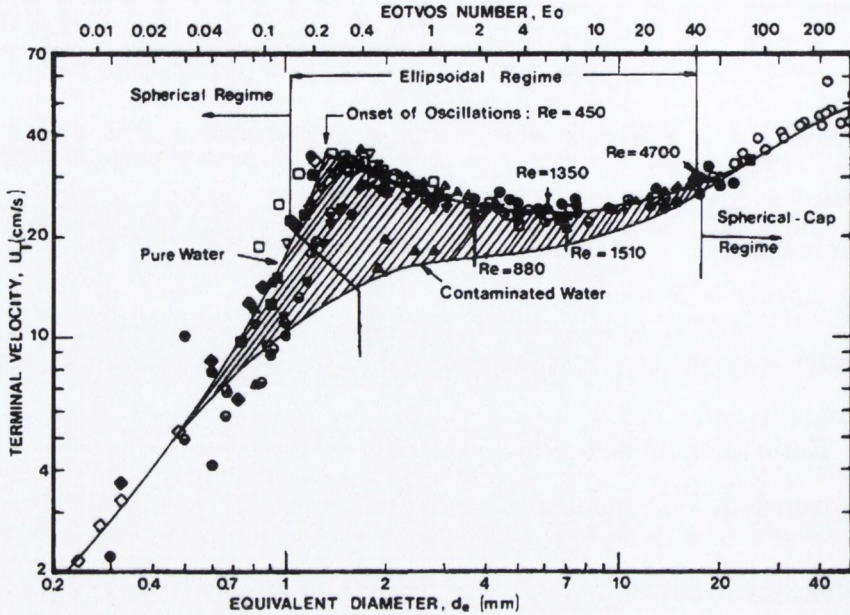
Figure 2.4: Terminal velocity of air bubbles as a function of equivalent diameter, d_e, in water at 20 °C. The upper curve represents pure systems, the lower curve contaminated systems. The figure includes the spherical, ellipsoidal and spherical cap regimes, Clift et al. [6].

where σ is the surface tension, ρ is the density of the surrounding fluid and d_e is the equivalent diameter. This is only valid for $d_e > 1.3\ mm$ and predicts an upper limit to the rise velocity of bubbles in this range. Experimental evidence from Aybers & Tapucu [13] suggests that when surfactants continue to gather on the bubble interface during rise, the bubble may never reach a stable terminal velocity. Results for the observed paths of bubbles from these experiments can be seen in Table 2.1 (from Clift et al. [6]).

Bringing together a huge amount of experimental data, Grace et al. [14] present the correlation

$$J = 0.94H^{0.757} \text{ for } (2 < H \le 59.3) \tag{2.7}$$

$$J = 3.42H^{0.441} \text{ for } (H > 59.3) \tag{2.8}$$

where

$$H = \frac{4}{3}Eo\,Mo^{-0.149}\left(\frac{\mu_f}{\mu_w}\right)^{-0.14} \tag{2.9}$$
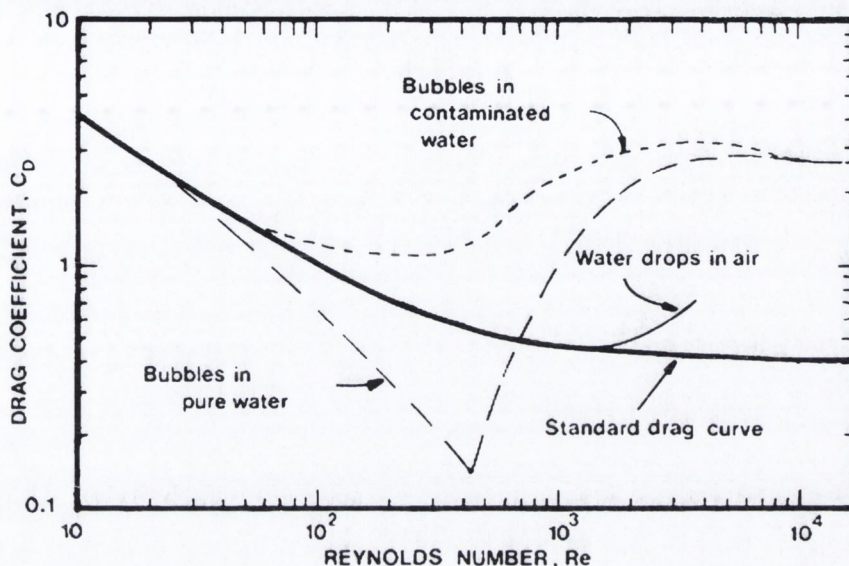
Figure 2.5: Drag coefficient as a function of Reynolds number for bubbles in water. The upper curve represents contaminated systems, the lower curve pure systems. The $C_D - Re$ curve for water drops in air and standard drag curve for rigid spheres are also illustrated, Clift et al. [6].

$$J = ReMo^{0.149} + 0.857 \qquad (2.10)$$

provided $Mo < 10^{-3}$, $Eo < 40$ and $Re > 0.1$ (the continuous phase in the present study is water so the ratio $\mu_f/\mu_w = 1$ while $Mo = 2.55 \times 10^{-11}$, $Eo \approx 3 - 12$ and $Re \approx 1000 - 2400$ which satisfy the constraints). In these equations Mo and Eo refer to the Morton and Eötvös numbers respectively, ρ is the fluid density, μ_f is the fluid viscosity and μ_w is the viscosity of the water in the experiments performed by Johnson & Braida [15] (0.0009 kg/ms). The different equations for J correspond to the transition from non-oscillating to oscillating bubbles. No other paper to date had covered such a broad range of data as compiled by Grace et al. [14], and in addition, others required data to be read off a graph or the use of iterative solutions. The terminal rise velocity can be obtained when certain fluid properties are known. Inputting these values into equation 2.9 gives a value of H. This value is then used to calculate J through equation 2.7 or 2.8. J can then be used, in conjunction with equation 2.10 and the equivalent diameter to calculate the Reynolds number and corresponding terminal

37

velocity, U_T. Clift et al. [6] also consider deformed fluid particles of large size, satisfying the constraints: $Eo > 40$ and $Re > 1.2$. This generally corresponds to bubbles with $d_e > 18\ mm$ and volume greater than $3\ ml$. The shape of bubble that satisfies these criteria is that of the spherical cap. The terminal rise velocity of these bubbles is determined from theory that assumes inviscid flow near the front of a sphere where the bubble forms a cap; surface tension forces are ignored. Experimental results were found to be well predicted by the theory. The terminal velocity for bubbles of this size is found to be

$$U_T = \frac{2}{3}\sqrt{ga\frac{\Delta\rho}{\rho}} \tag{2.11}$$

where a is the radius of curvature of the front of the bubble, $\Delta\rho$ is the density difference and ρ is the density of the fluid. It is similar to the Davies & Taylor [8] result[5] (Equation 2.1) and it is recommended for $Re > 40$. A second result from the same theoretical calculation gives the rise velocity of oblate spherical cap bubbles as

$$U_T = f(e)\sqrt{gb\frac{\Delta\rho}{\rho}} \tag{2.12}$$

where

$$f(e) = \frac{1}{e^3}\left(\sin^{-1}e - e\sqrt{1 - e^2}\right) \tag{2.13}$$

where e is the eccentricity and b is the vertical semi-axis. This equation is recommended for $1.2 < Re < 40$ but requires the eccentricity to be known.

Up until the early 1980's the study of free rising bubbles was mainly limited to calculation of the terminal rise velocity for a specific bubble shape or size. Bhaga & Weber [16] extended this research by investigating the effect of the Morton number and Reynolds number on the terminal velocity and shape of free rising air bubbles in aqueous-sugar solutions. They present a shape regime map reproduced in Figure 2.6. Shapes identified by Bhaga & Weber [16] fell into the following categories; spherical, oblate ellipsoid, oblate ellipsoidal cap, spherical cap with open or closed wake and skirted bubbles with smooth or wavy skirts (skirt thickness is in the order of $100\ \mu m$). Figure 2.7 illustrates how the bubble shape changes from an almost complete oblate spheroid to a smaller segment of an oblate spheroid and then to a spherical cap with

---

[5]The ratio $\Delta\rho/\rho$ approaches one in water, this equation then approximates Equation 2.1.
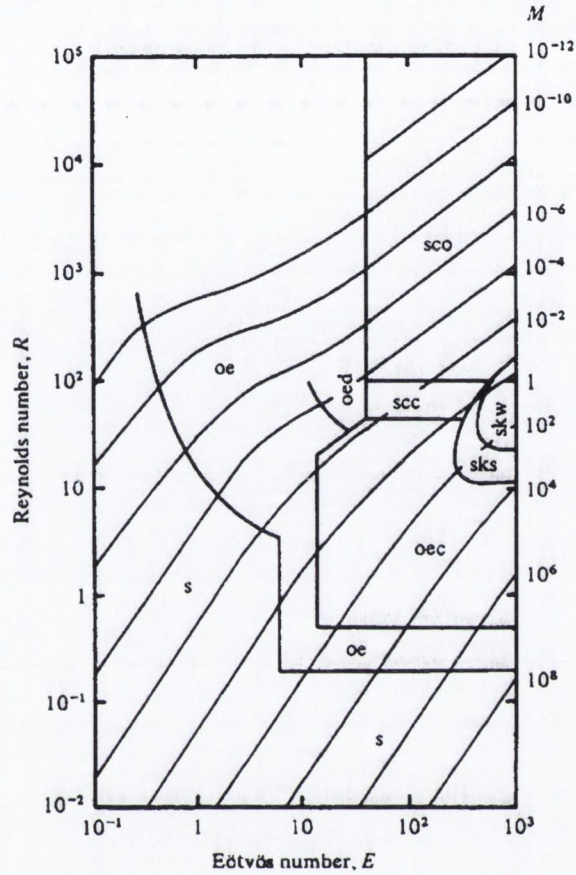
Figure 2.6: Bubble shape regime map; a function of Reynolds, Eötvös & Morton numbers. The shapes corresponding to the labels in this figure are illustrated in Figure 2.7, Bhaga & Weber [16].

changing fluid properties. They found that the shape of a bubble is only a function of the Reynolds number for high Morton number liquids (i.e. $Mo > 4 \times 10^3$), while for low Morton number liquids the shape is a function of both Re and Mo.

Durst et al. [17] used laser-Doppler anemometry (LDA) to measure both the local fluid velocity and the bubble rise velocity for a column of bubbles released at a constant frequency within a cylindrical vessel. Only bubbles that rose in a straight line were selected. An increase in the bubble release frequency led to a slight increase in the rise velocity of the bubbles. Their experiments also took account of the effect of surfactants on bubble motion. Results were compared to their own numerical study and found to be in good agreement. The vessel walls were deemed to have negligible effect on the

39
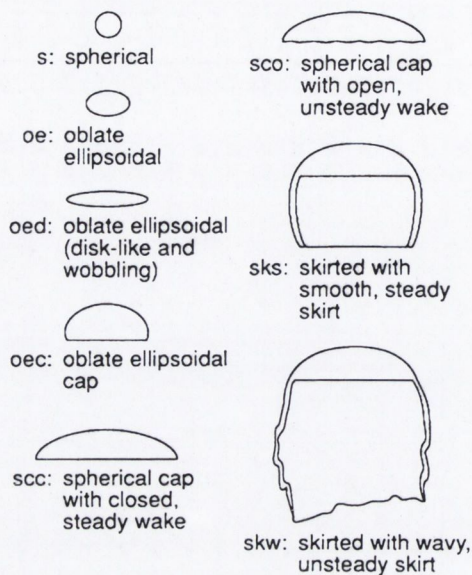
Figure 2.7: Bubble shapes observed in infinite Newtonian fluids. The conditions for these shapes to occur are presented in Figure 2.6, Fan & Tsuchiya [1].

bubble and fluid motion as the geometry satisfied the condition presented by Govier & Aziz [18].

$$\left(\frac{d_e}{D}\right)^{2.25} \ll 1 \tag{2.14}$$

where D is the diameter of the containing cylinder. Bubble rise velocities measured by Durst et al. [17] were found to correspond closely to Stokes' law for creeping flow of rigid spheres.

$$U_T = \frac{g d_e^2 \rho}{18\mu} \tag{2.15}$$

where ρ and μ are the fluid density and viscosity respectively. The effect of surfactants on bubble shape and rise velocity was closely monitored in their experiments. Surfactants were found to enter the test fluid through an opening at the top of the cylindrical vessel. They state that for any kind of particle-liquid system there will be a characteristic bubble velocity versus height distribution which applies to high impurity concentration and characterises the diffusion-controlled stiffening of the bubble due to concentration increase of impurities in the bubble interface; this is independent of fluid surfactant concentration. This effectively leads to a decrease in bubble rise velocity with increasing distance from the nozzle. In addition, the LDA measurements

by Durst et al. [17] revealed no flow separation[6] at the trailing edge of the bubble for $Re = 64$, indicating that the bubble interface is in motion due to the flow field of the air inside the bubble. They conclude that this indicates that the effects of surfactants on their experiments were negligible since the interface was deemed mobile.

Raymond & Rosant [19] present a numerical/experimental comparison of the shape and terminal velocity of rising bubbles in the range $1 < Re < 100$ and $0 < We < 5$. Experiments were performed in water/glycerol mixtures in a tank measuring $300 \times 200 \times 500$ mm^3. Their experiments covered what they considered to be a gap in the literature concerning the bubble aspect ratio in large Morton number systems. They found good agreement between numerical and experimental results even though their model makes the assumption that the fluid is surfactant free. They conclude that the surfactant influence must remain small in their test range. Ruzicka [20] presents a separate study that extends the test parameters to include single and multiple bubbles rising in a line.

Tomiyama et al. [21] performed a numerical and experimental study of the terminal velocity of air bubbles rising in water. They concluded, contrary to previous speculation, that the large scatter in terminal velocity in the literature is due to initial shape deformation rather than surfactant concentration. In fact, bubble motion, shape and velocity are all very sensitive to initial shape deformation. Small initial deformation results in low terminal velocity and high aspect ratio (a more spherical shape) and vice versa. They conclude that the main effect of surfactants is to cause the damping of bubble shape oscillations. Figure 2.8 illustrates aspects of this finding.

Choi et al. [22] used a hybrid PIV technique (PIV incorporating Particle Tracking Velocimetry) to analyse the flow around an air bubble and solid spherical particles rising in water. They found that while the rise velocity increased with diameter for solid particles of constant density, it did not change much with increasing bubble diameter. They found that the resistance due to deformation canceled out the extra buoyancy effect of increased volume. The solid particle velocity increased with density difference and its motion changed from straight to zig-zag, indicating that the mode

---

[6]Above a critical Reynolds number, flow over the bubble begins to separate from the interface, this will be discussed further in relation to the bubble wake.

(a) Small initial shape deformation
(zigzag motion)

(b) Large initial shape deformation
(zigzag then helical motion)
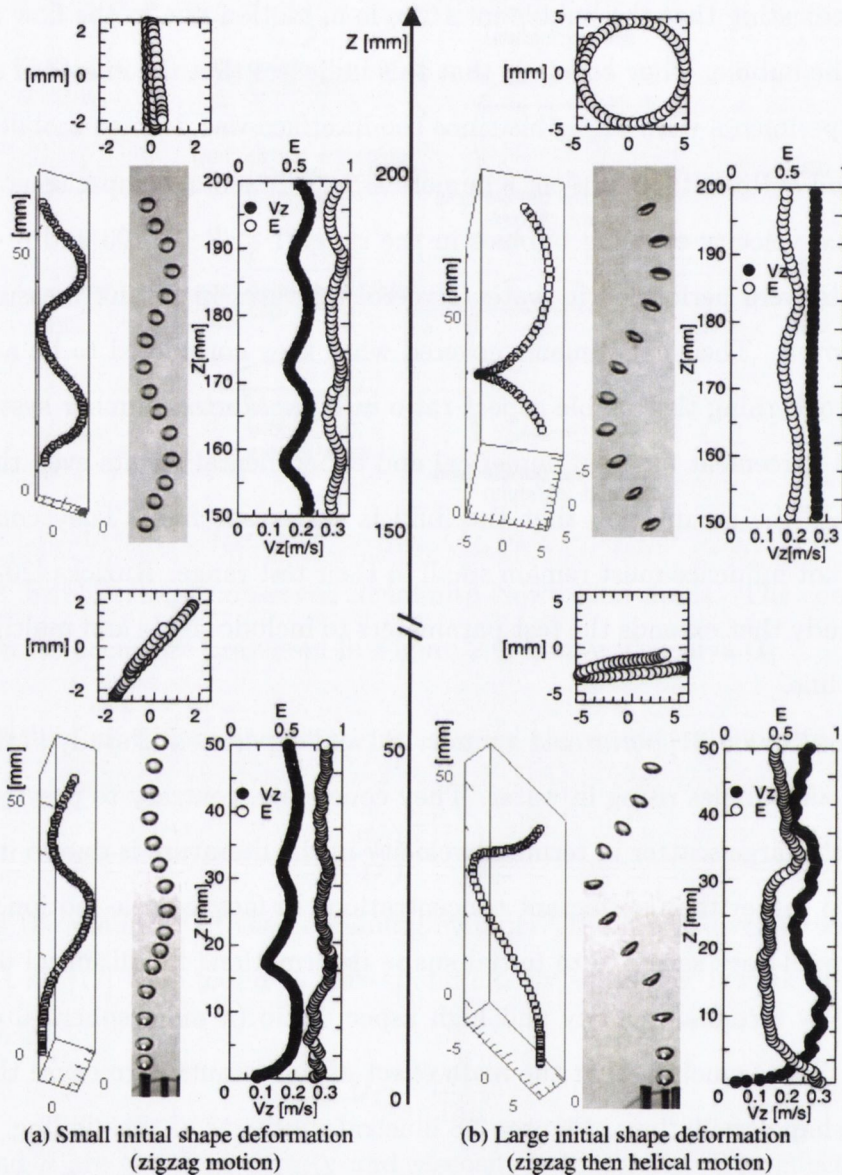
Figure 2.8: Consecutive images, top and birds eye views of trajectory, instantaneous aspect ratio (E) and instantaneous rising velocity (v_z) of a single air bubble ($d_e = 3$ mm) in distilled water: (a) illustrates a small initial shape deformation (zigzag motion) and (b) a large initial shape deformation (zigzag then helical motion). Bottom images show bubble injection and top images steady state behaviour. The distance from injection point, Z, is also supplied. Reproduced from Tomiyama et al. [21].

of motion is dependent on velocity.

Celata et al. [23] investigate the effect of the bubble wake on vapour bubble rise velocity in FC-72 and R-114. This is performed for both single bubbles and a plume of bubbles from nucleation to terminal velocity. They found that although most prediction techniques for terminal velocity have been developed for two component systems[7], some of them still give a good prediction for single component systems. For multiple bubbles in the range $d_e = 0.1 - 0.7$ mm they concluded that the wake effect[8] is completely absent in their experimental observations. They also note that the surface tension force plays a dominant role in the rise velocity of bubbles in the range $0.4 - 0.5$ mm, while the viscous force plays a decisive roll for smaller bubbles. For bubbles larger than 0.2 mm, a correlation by Fan & Tsuchiya [1] (similar in form to equation 2.15) is fairly accurate at predicting terminal velocity. A second study by Celata et al. [24] expanded on this by introducing gas (nitrogen) as well as vapour bubbles into FC-72 and water. They found that the best model to predict the terminal velocity and aspect ratio was that of Tomiyama et al. [21], primarily due to the inclusion of the bubble shape effects in terms of aspect ratio. To conclude, they found no clear difference between gas-liquid and vapour-liquid data for rising bubbles.

The following numerical studies, although outside the scope of the current study, are included for reference. Hua & Lou [25] and Hua et al. [26] developed an improved numerical algorithm for the front tracking method to simulate a rising bubble in 2-D and 3-D respectively while Gupta & Kumar [27] use the Lattice Boltzman Method (LBM) to understand the behaviour of bubble motion and coalescence for both single and two-phase fluids. Similarly, Amaya-Bower & Lee [28] provide a comprehensive study of the dynamics of single rising bubbles also using the Lattice Boltzman Method for $1 \times 10^{-5} < Mo < 3 \times 10^4$ and $1 < Eo < 1 \times 10^3$. All found a good agreement with the results of Bhaga & Weber [16] for each of the eight different bubble shape regimes (see Figure 2.7). The pressure contours for each shape regime are calculated along with the wake characteristics, they were found to depend strongly on the size,

---

[7]Two component systems contain two different fluids, rather than two phases of the same fluid.

[8]When one bubble travels behind a second bubble the wake of the first bubble can affect the motion/velocity of the second.

velocity and deformation of the bubble.

2.3 Free rising bubbles: the wake

Understanding the effects of a sliding bubble on heat transfer requires understanding of the structure and nature of the bubble wake. As a bubble rises, work is done on the fluid by the bubble at a rate equal to the velocity times the buoyancy force. In very viscous fluids, this work is dissipated due to the effects of viscosity. In a less viscous fluid, not all of the work is dissipated by viscosity, some is converted into wake structures which can in turn induce secondary motion (secondary motion refers to oscillations of the bubble path).

For free rising bubbles, when the relative velocity between the bubble and the surrounding fluid is very low (for example, bubbles with $d_e < 1\ mm$ in water, i.e. $Re \ll 1$), the fluid will closely follow the bubble interface. The whole contour of the bubble forms part of a streamline. As the Reynolds number exceeds a certain critical value, the flow over the surface will start to separate (flow separation refers to the detachment of the boundary layer from the bubble surface). The separated streamlines will rejoin some distance behind the bubble, forming a closed region described as the wake. The wake is formally described as the entire region of non-zero vorticity downstream of a object in uniform flow. It is generally divided into two regions; the primary wake and the secondary wake. The primary wake can be open or closed and concerns fluid flow near the rear of the bubble, where vortex formation, growth and shedding occurs (commonly referred to as the recirculation region). The recirculation region sometimes consists of a toroidal shaped vortex, which would appear as two counter rotating vortices in cross section. This exists immediately behind the bubble at a constant relative distance (see Figure 2.9 for an illustration). Although circulatory flow patterns may exist in the primary wake, the boundary between it and the secondary wake may not be clearly defined.

The secondary wake consists of the remainder of the wake and has an open structure. It can contain free shear layers and vortices shed from the primary wake. Structures that have been observed in the secondary wake of a rising bubble are commonly

observed behind solid disks, cylinders and spheres. These include the Kármán vortex street, which consists of an asymmetric double row of vortices (in two dimensional cross section) which can be located a considerable distance downstream of the object. Even when vortices are shed symmetrically they can eventually align into the characteristic structure of the Kármán street. The three dimensional wake is quite difficult to define and a number of configurations have been proposed and experimentally observed such as toroidal vortex rings, helical vortices, bispiral vortices and horseshoe vortex loops.

The motion of small, spherical bubbles is usually rectilinear. As the volume is increased, the shape deforms into an oblate spheroid, wake instabilities set in and result in a spiraling or zig-zagging bubble. A further increase in volume changes the shape from ellipsoidal to spherical cap, the radius of the spiral or the amplitude of the zig-zag gradually reduce and the motion returns to rectilinear but rocking (the bubble travels in a straight line but pivots about a central point). As the size of the spherical cap bubble increases the path returns to rectilinear only. This general description is valid for low Morton number systems (i.e. air bubbles in water), whereas for high Morton number systems the motion is found to be always rectilinear.

Bubbles of intermediate size, such as those in the present study, show two types of secondary motion. The first type, 'rigid body', rock from side to side or follow a zig-zag or spiral trajectory. The second exhibit shape oscillations, i.e. movement of the bubble surface. Both types of motion can be superimposed, making the study and classification of intermediate sized bubbles quite complicated. Secondary motion is most likely related to wake shedding, as the onset of oscillations coincides with the onset of vorticity shedding from the wake. The frequency of wake shedding corresponds closely to the frequency of shape oscillation; when the two frequencies are identical, resonance is expected to occur and this is one proposed explanation of why bubbles break up as they rise.

For the case of larger bubbles, most of the literature simplified the analysis by only considering flow around the front of a bubble with negligible effects of viscosity. In reality, some consideration of the flow near the rear of the bubble must be considered to fully describe the bubble's motion (conversely, an analysis of the bubble shape, velocity and motion can lead to understanding of the wake dynamics). The formation of an

attached wake and subsequent wake shedding appear to be a function of the aspect
ratio (the ratio of the bubble's major and minor axes) and also related to the internal
fluid motion being damped out by the effects of surfactants. For contaminated systems,
the appearance of an attached wake occurs at Reynolds numbers of approximately 20
while wake shedding usually occurs at $Re = 200$. Removal of contaminants can result
in the wake development being delayed up to Reynolds numbers of 800 to 1000; a
reduction in wake volume is also noted.

The following sections present studies focused on the wake behind free rising bub-
bles and although the present study is focused on sliding bubbles, parallels can be
drawn between the two research areas.

2.3.1 Wake structure

In order to further the prevailing understanding of fluid motion in the wake behind
rising bubbles, Fan & Tsuchiya [1] compiled a comprehensive review of the existing
literature. This was done mainly in the context of three or four phase fluidised beds and
bubble columns, but also tackled single bubble rise characteristics. Fan & Tsuchiya
[1] began their review by highlighting the physical significance of the bubble wake. It
was known that bubbles induce fluid mixing; this has been recognised as a key factor
responsible for solids mixing in gas-liquid-solid fluidised beds and gas diffusion in gas-
liquid contacting systems. It is achieved by fluid entrapment in the wake of the bubble
(fluid entrained in the wake moves some distance with the bubble and is then shed).

Figure 2.9 (a) and (b) illustrate the primary wake for large bubbles in a viscous
medium at low Reynolds number ($Re < 110$). The wake is laminar and closed, con-
sisting mostly of a well developed toroidal vortex ring and a stagnation region near the
rear stagnation point which are both invariant in time (the primary wake is indicated
by the shaded region enclosed by dashed lines). Depending on the Reynolds num-
ber and wake stability, this stagnant region may have a negligible volume as reported
by Collins [29], or a non negligible volume in a cusp shape as reported by Batchelor
[30]. At higher Reynolds numbers, for intermediate to large bubbles, the wake flow
is unsteady but has cyclic vortex shedding as indicated in Figure 2.9 (c). Vortices
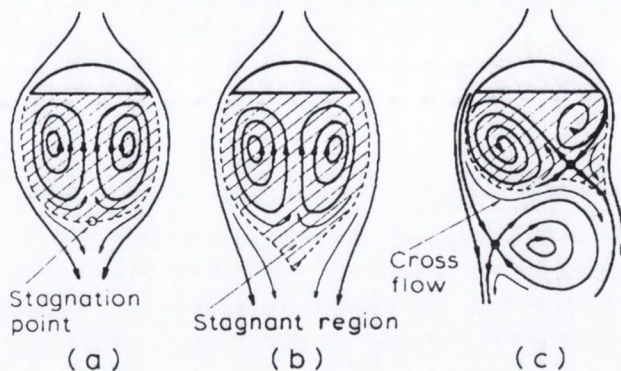
Figure 2.9: Schematic definition of primary wake boundary. (a) Laminar, closed, steady wake with negligible volume, (b) laminar, closed, steady wake with non-negligible volume and cusp shape and (c) Unsteady wake flow with steady, well developed, vortex shedding, Fan & Tsuchiya [1].

generated in the formation region are well developed before leaving the primary wake and are shed in the alternate axisymmetric mode.

Bhaga & Weber [16] found that the shape of the bubble is affected by the structure of a closed toroidal wake located below the bubble. This was observed for all bubbles except those of very high Reynolds number. Skirted bubbles (see Figure 2.7; *sks* and *skw* for illustrations of skirted bubbles) also contained a closed toroidal wake, the presence of the skirt having a negligible effect on the rise velocity, although it did reduce circulation in the wake itself. Figure 2.10 gives a generalised description of the wake behind spherical cap bubbles, although it is worth noting that similar structures appear behind ellipsoidal bubbles and numerous other bluff bodies[9]. This flow model includes irrotational flow of an ideal fluid outside the body and in its wake, inviscid rotational flow inside the closed wake and a thin boundary layer enclosing the bubble and closed wake.

The figure illustrates not only the structure of the wake, but a description of the pressure distribution from front to rear (pressure distribution will be discussed further in Section 2.3.5). The local fluid flow at the upstream stagnation point is brought to

---

[9]A bluff body is one which presents a large portion of its surface area to the oncoming flow i.e. it is not particularly streamlined.
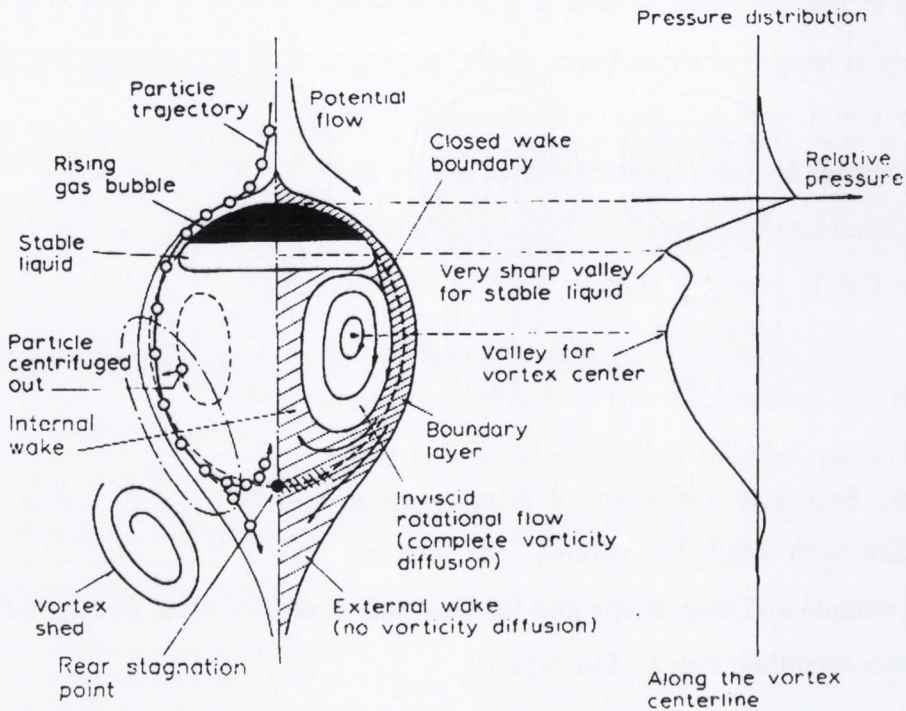
Figure 2.10: Idealised steady state fluid flow field and solid particle trajectories around a single spherical cap bubble. Included is the relative pressure. The figure consists of (1) potential flow of an ideal fluid outside the body and its wake, (2) inviscid, rotational flow inside the closed wake (a toroidal vortex), (3) a thin boundary layer enclosing the bubble and its wake and (4) internal and external wakes along the axis of symmetry, Bhaga & Weber [16].

a halt; this appears as an inwards push on the bubble surface caused by the elevated pressure. The presence of the bubble means the fluid must accelerate to maintain the flow; this results in the pressure at the surface decreasing from a maximum at the front along the sides. This pressure difference increases as the relative velocity between the bubble and fluid increases (i.e. as the Reynolds number increases). Although this explains why a bubble may take an ellipsoidal shape, it does not explain the transition from ellipsoidal to spherical cap shape (Figure 2.7; *oec*, *scc* and *sco*), especially the appearance of a sharp edge along the bubble rim as indicated in Figure 2.10. This occurs because of a toroidal shaped vortex below the bubble base. This vortex pushes the bubble base up along the axis of symmetry and draws it down at the edge of the

base, producing the cap shape. At the edges, the flow separates from the interface and rejoins further downstream. The area enclosed forms the near wake (a region of low pressure) that usually, as in this case, contains a toroidal vortex. Depending on the fluid and bubble parameters, vortices may be ejected periodically from this region that travel downstream into the far wake. Both the shape and path of bubbles depends on the nature of this vortex shedding.

Fan & Tsuchiya [1] present detailed descriptions of the wake structure in relation to vortex formation and shedding. Figure 2.11 shows a photograph and schematic representation of the wake behind an ellipsoidal bubble of $Re = 3550$. Visible immediately behind the bubble is a helical vortex extending downstream as far as two cycles of spiraling. This is followed by a streamlined flow engulfing a vortex ring. After
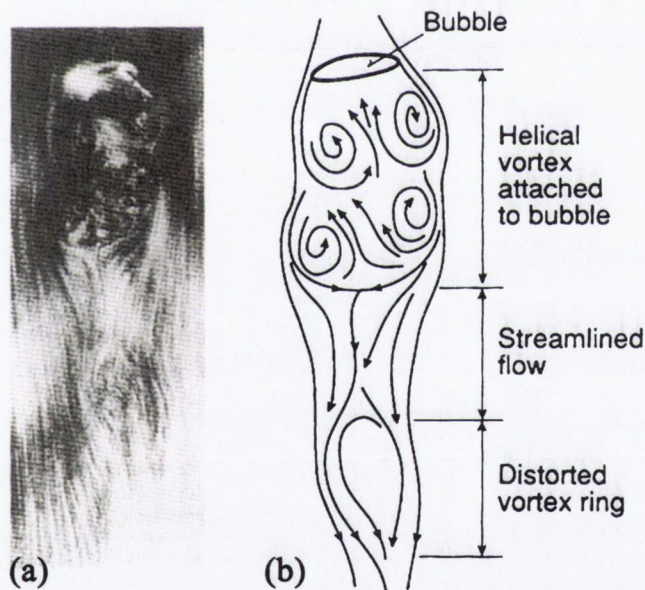
Figure 2.11: (a) Photograph and (b) schematic of an ellipsoidal bubble in water and its wake consisting of disrupted helical vortex and a vortex ring dragged downstream at $Re = 3550$. The lower vortex ring appears distorted due to its considerable velocity relative to the bubble (the camera moved at the same velocity as the bubble), Fan & Tsuchiya [1].

bubble injection, the bubble begins to accelerate. The wake grows in size by accumulating fluid from outside the wake; after some time the symmetry of the wake flow will

be perturbed and eventually some wake material will be discharged. Experimental observations indicate that in the Reynolds number range, $70 < Re < 250$, a growing laminar toroidal vortex shifts to a periodic laminar wake which successively discharged horseshoe shaped wake fragments (see Figure 2.14 on page 54 for an illustration of a horseshoe vortex). In the range $250 < Re < 5000$, a growing turbulent toroidal vortex shifted to a periodic turbulent wake which shed turbulent vortex rings.

Two factors must be taken into account to explain the onset of flow separation from a bubble (or any free surface). First, the flow behind a bubble is towards the base along the central axis (see Figure 2.10), this is due to the fact that the pressure downstream of a rising bubble cannot be completely recovered (apart from at very low Reynolds numbers). Second, the bubble goes through a shape deformation immediately after injection and begins to generate vorticity at a high rate. This high vorticity generation rate reflects a high velocity gradient near the bubble edge, resulting in flow separation. Once separation occurs, a pair of vortical flows must exist behind the bubble. Figure 2.12 illustrates the mechanism behind alternate vortex shedding from a rising bubble. Vorticity generated at the separation points is conveyed along the free shear layer. This layer tends to roll up into a spiral shape and eventually a circular cross sectioned vortex. The vortex is still attached to the bubble and is continuously supplied with vorticity via the shear layer. It continues to grow until it becomes strong enough to draw the opposite shear flow across the wake. This has the effect of cutting off its own supply of vorticity and the vortex sheds from the bubble.

Brücker [31] used Particle Image Velocimetry (PIV) in combination with high speed imagery to investigate the flow in the wake of both single and interacting air bubbles freely rising in water. The experiments focused on ellipsoidal bubbles of diameter 4 to 8 mm. Bubbles of this size were found to exhibit spiraling, zig-zagging and rocking motion during their rise. The test section was 1.2 m high and had a cross section of $100 \times 100 \ mm^2$. Bubbles were held at a constant height relative to the observer. This was achieved by pumping water against the bubble flow direction. A uniform flow with low turbulence was achieved by a contraction passage with a contraction ratio of 5:1, located upstream of the inlet to the test section. Demineralised water seeded with small tracer particles was used as the test liquid. Measurements of the bubble's rise
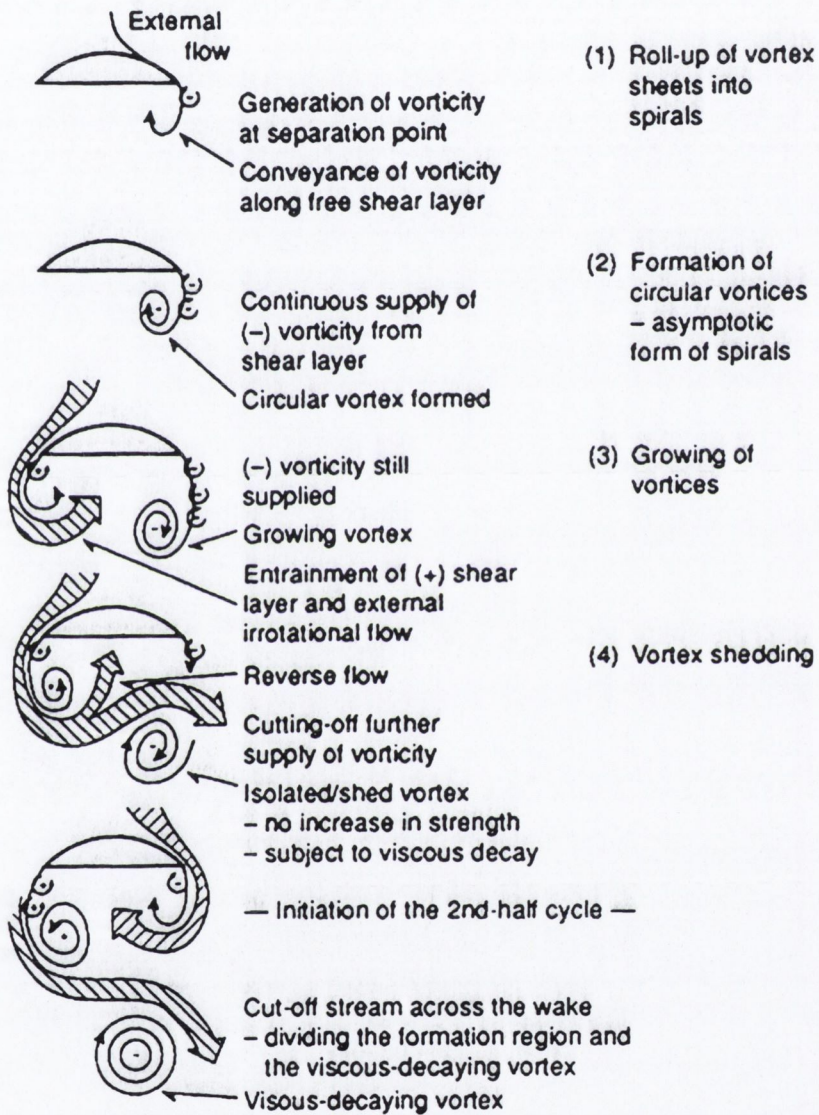
Figure 2.12: Mechanistic description of alternate vortex formation and shedding in two dimensions, Fan & Tsuchiya [1].

velocity and comparison with the literature (Clift et al. [6]) lead to the conclusion that the system behaved like that of an impure/contaminated liquid. Bubbles were released from the bottom of the tank and allowed to rise, the pump was then turned on to hold the bubbles in a stationary vertical position. The Reynolds number in their work was based on the measured diameter D of the spheroid and not the equivalent diameter, d_e, used by most researchers; this was chosen in order to compare the bubble's behaviour to known literature on solid bodies such as spheres or disks. The terminal velocity is calculated as

$$U_T = \sqrt{u^2 + v^2 + w^2} \tag{2.16}$$

where u, v are the lateral speeds of the bubble in the x and y direction (perpendicular to the flow direction) and w is the rise speed. Fluid flow velocity was measured in planes both parallel and perpendicular to the bubble flow direction.

PIV measurements were taken 10 mm downstream of the bubble in a plane perpendicular to the flow. The flow field in this cross section showed the alternate generation of a pair of counter-rotating vortices close to the bubble base as illustrated in Figure 2.13. At the beginning of the cycle (Figure 2.13 (A)), a stagnation point exists in the cross flow at the left hand side of the bubble. The flow field at this point resembles a dipole-like vector field (a sink and source in the cross flow along the y axis). The bubble is positioned near the left hand stagnation point. In Figure 2.13 (B), this critical point has been split up into two foci which indicate the centers of streamwise vortices. This hints that the head of a hairpin vortex has passed the plane and left its legs (which correspond to the pair of streamwise vortices) in the cross section. A schematic of this flow structure is presented in Figure 2.14. The location of the vortex pair in the horizontal plane is clearly shifted toward the left hand side of the bubble in the positive y direction.

A strong cross flow in the positive y direction can be observed; this is a consequence of the induction effect of the vortex pair. Due to the asymmetry of the cross flow around the bubble, a net lift force exists in the negative y direction which explains the lateral drift of the bubble to the right. Figure 2.13 (D) shows that the vortices become progressively weaker and the lateral motion of the bubble begins to decelerate. A new
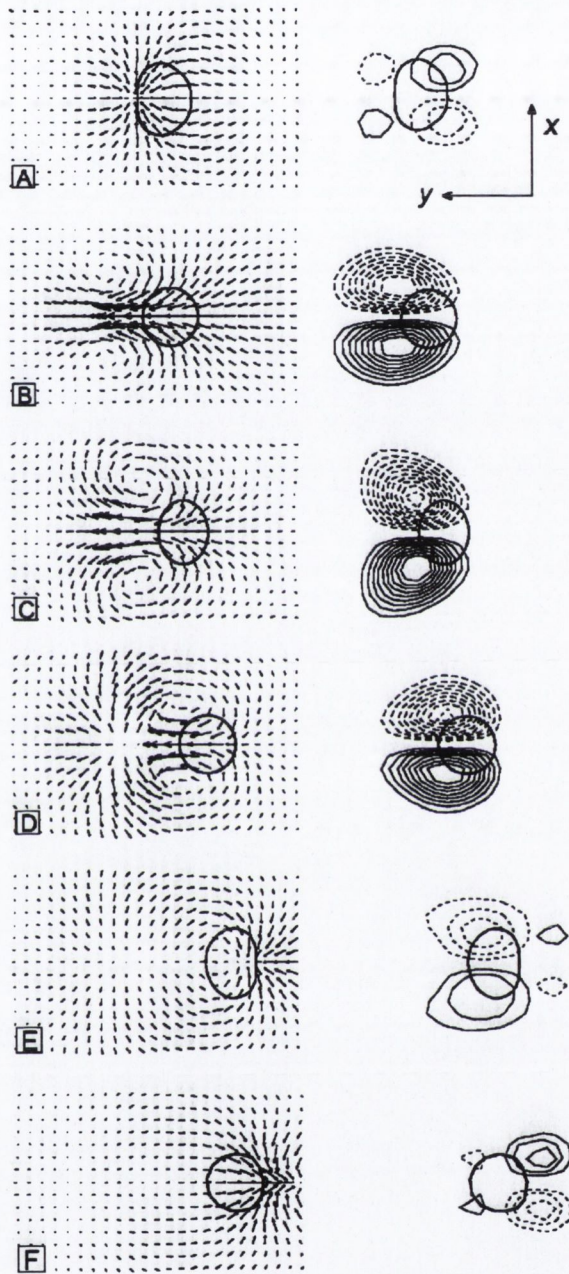
Figure 2.13: Evolution of the velocity field and streamwise vorticity distribution in a horizontal plane 1 cm downstream of a zig-zagging bubble. The zig-zag motion of the bubble in the horizontal plane is along the y axis. Left column: velocity field ($v_{max} = 7$ cm/s); right column: regions of concentrated streamwise vorticity, ω_z (contour lines start from $\pm$ 1/s in steps of 1/s; solid line: positive value, dashed lines: negative value), Brücker [31].
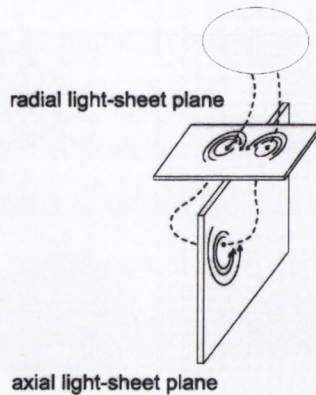
Figure 2.14: Schematic of a hairpin vortex. The bubble is traveling from bottom to top in a zig-zag motion. In this representation, one vortex is generated for each 'zig' and 'zag' of the bubble, Brücker [31].

counter-rotating pair is generated at the right hand side of the bubble (Figure 2.13 (E)) and once again the dipole-like character appears. Figure 2.13 (F) indicates the passing of the next hairpin vortex which is now at the right hand side of the bubble. This vortex increases in strength and replaces the previous one. The bubble reverses its motion and begins to drift to the left. This accounts for the zig-zag of the bubble driven by the alternate generation of a pair of longitudinal vortices of alternate circulation and the associated lift force.

De Vries et al. [32] used a Schlieren optical technique to visualise the wake behind high Reynolds number bubbles and solid spheres in highly purified water. This technique is used because it does not contaminate the water and therefore does not affect the zero tangential stress condition at the bubble interface (i.e. it does not act as a surfactant). Above a certain volume, $d_e > 1.6$ mm, the bubbles exhibited a zig-zag or spiraling behaviour. The same behaviour has been observed for solid spheres but at lower Reynolds numbers ($Re \approx 200$ for spheres compared to $Re \approx 600$ for bubbles). This was attributed to the different boundary conditions at the interface; no-slip and non-deformable for the sphere, zero tangential stress and deformable for bubbles. These conditions affect the vorticity production at the surface and the wake structure (as previously observed by Saito et. al. [7]). The authors question the common belief

that the reason for formation of vortex structures behind bubbles and spheres are the same (previously described by Brücker [31]). The reason for their questioning is that previous experiments added dye or seeding to the flow, thus affecting the interface and resulting bubble behaviour. Their rig consisted of a $150 \times 150 \times 500 \ mm^3$ glass water tank filled with ultra purified water (less than 10 parts per billion organic particles). The Schlieren technique uses density variations to visualise a fluid; these density variations are generated by heating the upper part of the tank. As the bubble rises through the lower, cooler layers, it entrains cold water in its wake and drags it into the heated water above. The temperature gradient was shown to have negligible effects on the bubble motion (De Vries et al. [33]). The authors identified a double-threaded wake consisting of a pair of counter-rotating vortex filaments. This wake occurred whenever the curvature of the path was non-zero along with a lift force of approximately $2.4 \times 10^{-5} \ N$ directed towards the center of the path. At the center of the zig-zag, where the path curvature is zero, the double-thread wake briefly becomes a single-thread and then reverts to double-thread but of opposite sign, the lift force also switches direction. At a distance behind the bubble, the double wake becomes unstable and forms vortex blobs. The authors confirm the results of Lunde & Perkins [34] and Brücker [31] that vortex loops, resembling hairpin vortices (see Figure 2.14), are formed and closed behind the bubble but postulate that this occurs when the bubble is at the zig-zag axis of symmetry as opposed to the maximum distance from the axis. Figure 2.15 illustrates their observations.

In a later study by Sanada et al. [35], photochromatic dye is used to visualise the wake behind a rising bubble. They experimentally found, for the first time, a standing wake in the region behind small ($d_e \approx 2 \ mm$) rising bubbles. They also confirmed the numerical prediction made by Mougin & Magnaudet [36] that the double threaded streamwise vortices behind the bubble change places with each other twice in one period of oscillation. The authors also question the statement by Brücker [31] and Lunde & Perkins [34] that a horseshoe vortex is formed every time the bubble changes direction, they found that more than two vortices are formed in one period. Figure 2.16 illustrates this observation. The authors suggest this multiple vortex formation is probably linked to shape oscillations. This work was extended to include a pair of
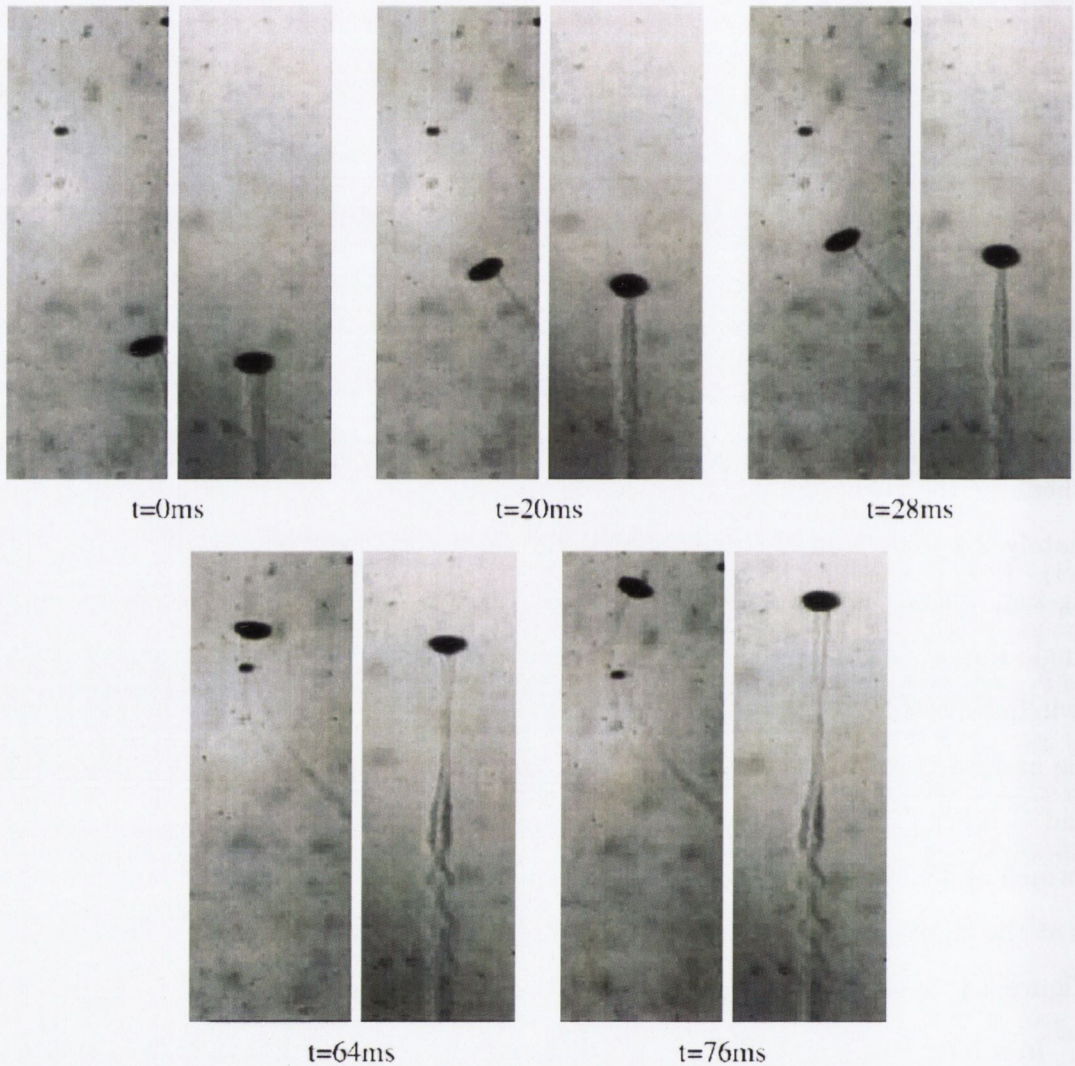
Figure 2.15: Successive images of a zig-zagging bubble at $t = 0$, 20, 28, 64 and 76 ms. The left image is recorded perpendicular to the right image simultaneously. The double threaded wake exists until $t = 20$ ms, the point at which the path curvature is zero. It then forms a single thread and sheds a horseshoe shaped vortex. This wake becomes unstable downstream, De Vries et al. [32].

rising bubbles [37].

Flow visualisation techniques provide a very useful insight to the structure of the wake behind rising bubbles. Bubbles sliding under inclined surfaces are found to exhibit similar motion and shape characteristics to free rising bubbles (i.e. path and shape oscillations), so it is possible that the structure of the wake and its behaviour are similar in both cases.

2.3.2 Detached vortex characteristics

Figure 2.17 shows the trajectories of vortex centers being shed from a bubble rising in stationary water. The results are from experiments performed by Tsuchiya [38] for an 8 *mm* thick two dimensional bubble[10] with a base width, $b = 31$ *mm*. The bubble rises rectilinearly with a rocking motion and some shape dilations. The overlapping bubble circumference represents the maximum and minimum angles of attack over the observation period. As can be seen from Figure 2.17 (a), the shed vortices follow a certain path from the bubble edge to the wake central axis, and then descend downwards (alternate vortex shedding mode). For the simultaneous vortex shedding mode (Figure 2.17 (b)), both vortices descend parallel to each other until the symmetry of the wake flow is disturbed. Simultaneous shedding occurs right after the initial stable growth period and only occasionally during the steady shedding period. Once this occurs, one vortex (vortex 2 or 4) grows in size and strength faster than the other (vortex 1 or 5). This dominant vortex has a great impact on the trajectory of the other; it follows the same type of path as the vortices in the alternate shedding mode, pushing the weaker vortex away from the wake central axis. The ratio of the velocity of shed vortices with respect to the bubble velocity, u_v/U_T is 0.33 for vortices 3, 6 and 7 in Figure 2.17 (a).

Figure 2.18 shows the normalised equivalent circular diameter of the vortex core (d_v/b where d_v is the vortex diameter and b is the bubble width) versus the net time elapsed from the moment of generation of each vortex ($t-t_{v0}$) in stationary water, along with a curve approximation from Tsuchiya [38]. The moment of vortex generation,

---

[10]The bubble is released between two plates separated by a spacing of 8 *mm*.
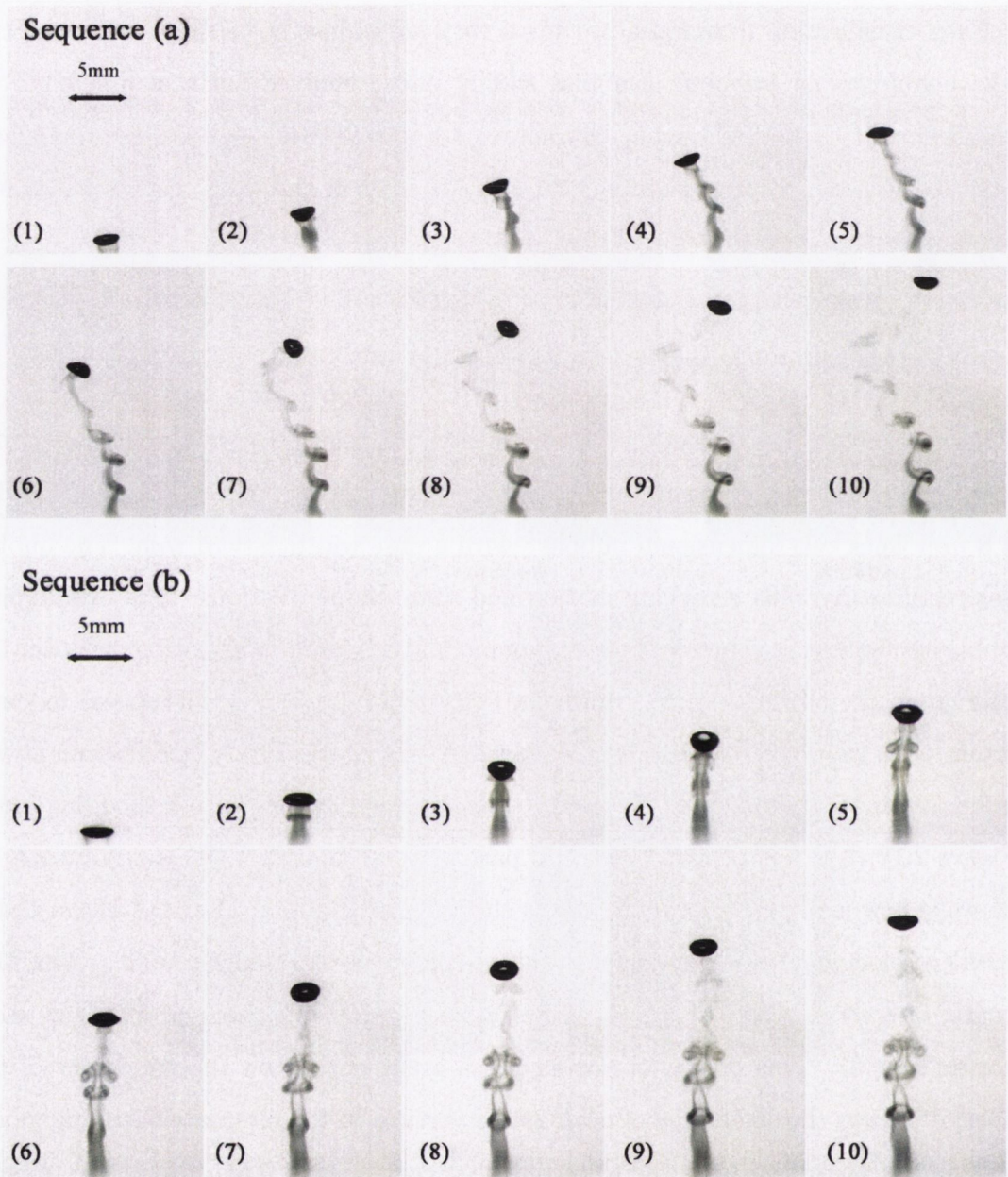
Figure 2.16: Photochromatic dye observation of multiple horseshoe vortex shedding behind a rising bubble, $Re = 330$, $We = 3$. Images in each sequence are separated by 10 ms. Sequence (a) is recorded at $90°$ to the bubble oscillation plane in sequence (b), although they are not from the same test (i.e. they were not recorded simultaneously), Sanada et al. [35].
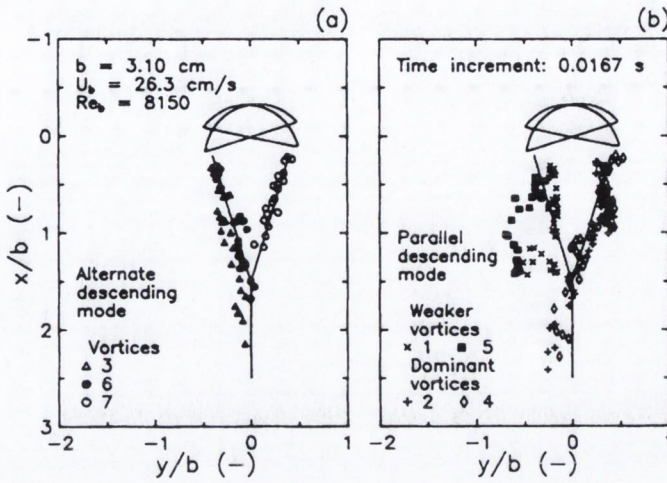
Figure 2.17: Vortex center trajectories after shedding behind a circular cap bubble in stationary water; bubble base width, $b = 31\ mm$, $U_T = 263\ mm/s$ and $Re = 8150$. (a) alternate descending mode, (b) parallel (simultaneous) descending mode. The axes, x and y are normalised with respect to the bubble width, b, Tsuchiya [38].
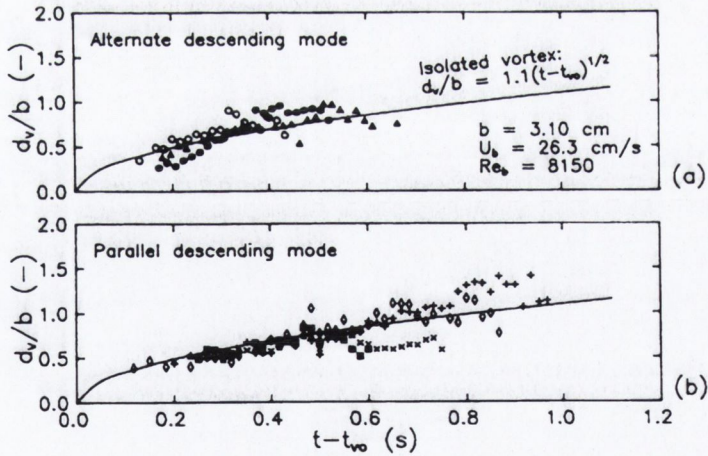
Figure 2.18: Time variation of vortex diameter in stationary water for a bubble with base width, $b = 31\ mm$, $U_T = 263\ mm/s$ and $Re = 8150$. The vortex diameter is normalised with respect to the bubble base width, b. The x axis represents time elapsed from when the vortex was shed in either (a) alternate descending mode or (b) parallel descending mode, Tsuchiya [38].

t_{v0}, is estimated by extrapolating the time at which $x/b = 0$ for each vortex (where x is the distance the vortex has traveled downstream). The vortex core diameter is the area enclosed by the outermost recognisable looped flow about the vortex center and is measured experimentally.

Vortex-vortex interactions induce vortex shape deformation. If the eccentricity is approximately one, no vortex interaction is expected. Figure 2.19 shows the positional variation of vortex eccentricity for both parallel and alternate shedding modes. A value
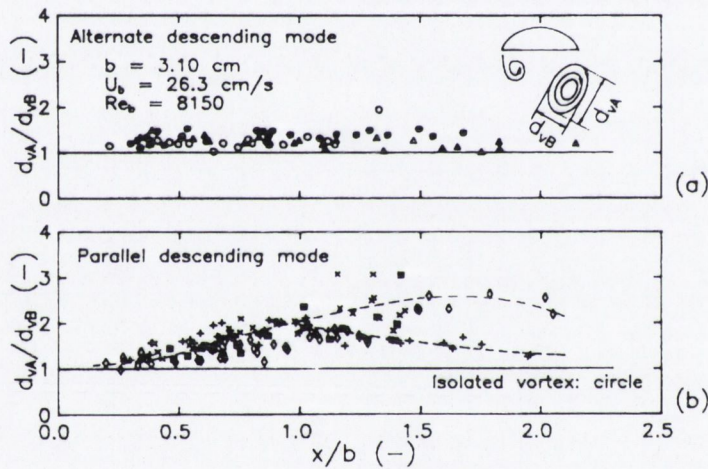
Figure 2.19: Positional variation of vortex eccentricity in stationary water for a bubble with base width, $b = 31\ mm$, $U_T = 263\ mm/s$ and $Re = 8150$. The ratio d_{va}/d_{vb} is illustrated in the figure. The x axis represents the vortex position normalised with the bubble base width, b, for (a) alternate descending mode or (b) parallel descending mode, Tsuchiya [38].

slightly above one indicates weak interaction between vortices, which is the case with the alternate descending mode as indicated in Figure 2.19 (a), compared to the parallel descending mode illustrated in Figure 2.19 (b). High eccentricity (around a value of 3) can lead to vortices being torn into two smaller ones.

2.3.3 Path oscillations

The following stability map (Figure 2.20, from Fan & Tsuchiya [1]) is useful in determining whether a bubble's rise path will oscillate or not in various pure or contaminated systems. As indicated in the figure, the bubble rise path will exhibit oscillation if the Weber number exceeds the stability line (the solid, roughly horizontal line in Figure 2.20) in both pure and impure systems. In contaminated systems, an additional criterion must be met; $Re < 200$ (the vertical dashed line in Figure 2.20). Thus, for pure systems, the bubble rise path will be stable provided the Weber number is less than We_{os} given as

$$We_{os} = 21.5Re_{os}^{-0.32} \tag{2.17}$$

where

$$Re_{os} = 9Mo^{-0.173} \tag{2.18}$$

provided $2 \times 10^{-11} < Mo < 6 \times 10^{-7}$. For impure systems, the rise path is stable provided $We < We_{os}$ and $Re < Re_{os}$ (the dashed, vertical line in Figure 2.20) where

$$Re_{os} = 202 \tag{2.19}$$

However, some experimental data exists, specifically for water, that suggests Re_{os} can be between 200 and 700 depending on its purity.

When the bubble exhibits zig-zag, spiral or rocking motion, it also changes its orientation. This is usually measured as an angle of attack, α, defined as the angle between the bubble's major axis and the undisturbed incident flow. Periodic variations in the angle of attack are closely related to wake shedding; both generally occurring at the same frequency. Figure 2.21 illustrates the variation of the bubble inclined angle ($\theta_b = 90° - \alpha$) as a function of Reynolds number. The figure illustrates that θ_b has an average value of approximately 25°, almost independent of Reynolds number, up to approximately $Re = 4000$. In the range $4000 < Re < 5000$, θ_b abruptly decreases. This marks the transition from ellipsoidal to spherical cap bubbles, the latter rising rectilinearly.

The frequency of path oscillations (f_{os}) is usually represented by a dimensionless group called the Strouhal number ($Sr = f_{os}d_e/U_T$). In contaminated systems, it
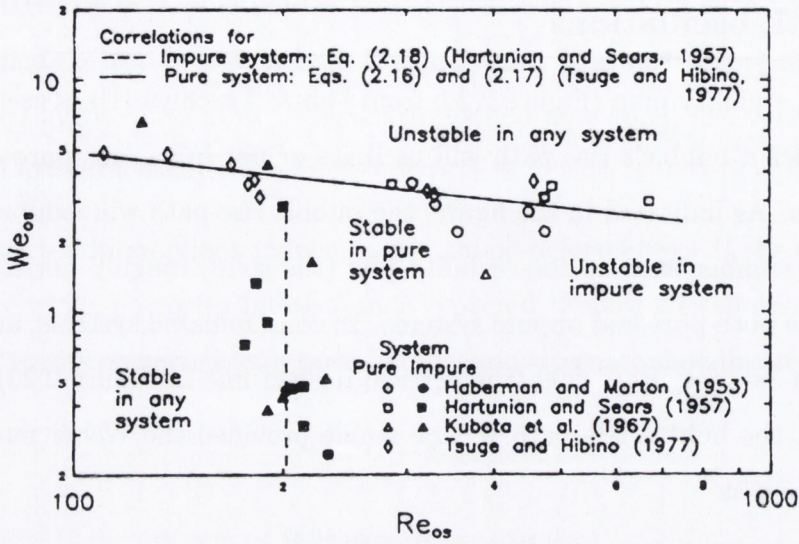
Figure 2.20: Stability map for bubble rise path for air bubbles in liquids, Fan & Tsuchiya [1].

was found experimentally that the frequency decreases monotonically from 7.7 to 4 Hz as the equivalent diameter increases from 2 to 8.5 mm. In purified systems, the frequency remained fairly constant, ranging from $6.2 - 8.3\ Hz$. Dimensional analysis of experimental data identified a unique relationship between the Strouhal number and drag coefficient as expressed in Equation 2.20.

$$Sr = \begin{cases} 0.1 C_D^{0.734} & (C_D \leq 2) \\ 6.13 \times 10^{-3} C_D^{4.71} & (C_D > 2) \end{cases} \tag{2.20}$$

This relationship is independent of whether the system is pure or contaminated but does have drawbacks: C_D must be estimated and the onset of oscillation must be specified (otherwise Sr may be non-zero even in the spherical regime, where the rise path is rectilinear). In this regard it is more convenient to correlate the Strouhal number directly with the Tadaki number number ($Ta = Re\ Mo^{0.23}$) as illustrated in Figure 2.22.

As previously mentioned, the frequency of oscillation of a bubble is strongly linked with the shedding of vortices. A possible explanation of why this may be so becomes apparent by observing oscillating cylinders in cross flow. In experiments by Ongoren & Rockwell [39], cylinders were oscillated transverse to the incident flow at controlled
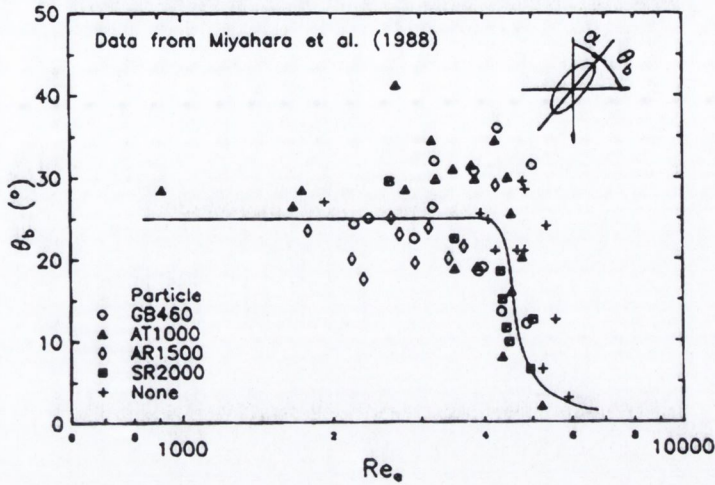
Figure 2.21: Variation in the bubble inclined angle, θ_b, versus Reynolds number. The inclined angle is defined as $\theta_b = 90° - \alpha$, where α is the angle of attack, Fan & Tsuchiya [1].

frequencies and amplitudes resulting in the near wake structure becoming synchronised with the motion of the cylinder. The following two relevant findings were reported; first, the extent of the synchronisation range depends strongly on the oscillation amplitude; the higher the amplitude, the wider the extent of the synchronisation range and second, as the frequency ratio approaches one the scale of the vortex formation decreases substantially and becomes a minimum. The fact that smaller ellipsoidal bubbles have a higher oscillation frequency than larger spherical cap bubbles can be explained based on the first finding. Smaller bubbles can move more freely and hence have larger oscillation amplitudes. Increasing the bubble size leads to a decrease in amplitude therefore synchronisation of the bubble and wake shedding becomes less realisable. It was found that drag coefficient decreases with decreasing primary wake size (see section 2.3.5), therefore the bubble should take the minimum possible wake size. Based on the second finding, this reduction in wake size can be realised most effectively by oscillating the bubble at the frequency equal to the vortex shedding frequency, the bubble will ascend with the least energy loss.

Later studies were performed by Žun & Grošelj [40] on rise velocity, lateral displacement (the amplitude of path oscillations) and oscillation frequency. This was
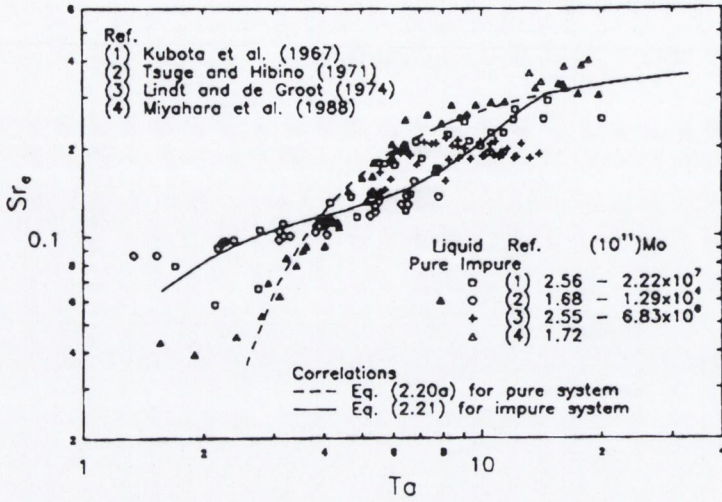
Figure 2.22: Relationship between the Strouhal number and the Tadaki number for rise path oscillations of air bubbles in liquids. The dashed line represents pure systems, the solid line contaminated systems, Fan & Tsuchiya [1].

done in both pure and contaminated water for non-rectilinear bubble motion. Tests were performed in a glass tank $160 \times 160 \times 1450 \ mm^3$, wide enough to avoid wall effects and tall enough to let bubbles reach their terminal velocity. The authors identified two distinct peaks in the amplitude *vs.* equivalent diameter trend for pure systems. The first represents the periodic movement while the second is attributed to bubble rocking. They also noted that an increase in amplitude results in a lower oscillation frequency and vice versa. In contaminated systems, the retardation effects due to interface impurities shift the peaks in amplitude towards higher equivalent diameters.

2.3.4 Shape oscillations

Lunde and Perkins [34] observed the shape oscillations of rising air bubbles in unfiltered tap water. The apparatus was a clear tank $700 \ mm$ long with a $100 \times 100 \ mm^2$ base. No effort was made to purify the apparatus or water so some contaminants were assumed to be present. As reported by Lunde and Perkins [34], Duineveld [5] has shown that there appears to be a limiting surfactant contamination level below which the contaminant does not noticeably affect the bubble motion. The authors believed they

Optical bubble size, d_e (mm)	2.20	3.02	3.52	4.32	5.16
Equivalent major axis, D_E (mm)	3.04	3.90	4.53	5.80	6.95
Ellipticity, ϵ	2.03	2.16	2.13	2.4	2.45
Terminal velocity, U_T (m/s)	0.326	0.299	0.284	0.264	0.245
Reynolds number, Re_d	991	1166	1286	1531	1751
⇓ Frequencies ⇓					
d_E: Mode (2,0), shape (Hz)	-	60.6	49.1	35.3	25.8
A: Mode (2,0), motion (Hz)	90.2	60.7	48.9	33.1	24.9
R Mode (2,2), shape (Hz)	62.7	40.4	33.1	22.3	17.3
Vortex shedding (Hz)	13.1	13.5	13.7	10.7	10.8

Table 2.2: The results experiments by Lunde and Perkins [34] on the frequency of bubble shape and path oscillations.

were operating below this level. They used five different nozzles which produce highly repeatable bubbles. Bubbles were allowed to travel the first 150 mm of the tank before being recorded at a frame rate of up to 500 frames per second; this corresponded to four times faster than the highest shape oscillation frequencies investigated. A mirror arrangement allowed simultaneous viewing of the bubble from two perpendicular sides. Five different bubble sizes were observed, those with equivalent diameter $d_e = 2.4$, 3.02, 3.52, 4.32 and 5.16 mm (bubbles in the present study vary from $d_e \approx 5.5 - 11$ mm). The mean results for five bubble sizes are presented in Table 2.2. The equivalent major axis of the ellipse is defined as

$$D_E = \sqrt{d_{major} d_{minor}} \tag{2.21}$$

where d_{major} and d_{minor} are the major and minor axes as measured from the direct and mirrored image of the bubble, averaged between numerous tests. The ellipticity is defined as

$$\epsilon = \frac{D_E^3}{8r_e^3} \tag{2.22}$$

where r_e is the equivalent spherical radius. In Table 2.2, d_E is the oscillation in the equivalent major axis, A is the oscillation in the acceleration of the bubble and R is the oscillation in the axes ratio. The vortex shedding frequency, or the frequency of lateral motion of the bubble, is also presented. These values were obtained from power spectrum analysis.

Brücker [31] presents results for bubble shape oscillations observed for a 6 *mm* zig-zagging bubble with a mean aspect ratio, E, of 0.66. The bubble rise speed, w, was approximately 200 *mm/s*. The shape oscillation frequency was measured to be 4.2 *Hz* with a maximum lateral velocity of 100 *mm/s*. The Reynolds number was 1320 while the Strouhal number was calculated to be 0.11. Figure 2.23 shows the variation of the position of the bubble centroid in the horizontal plane with time. The
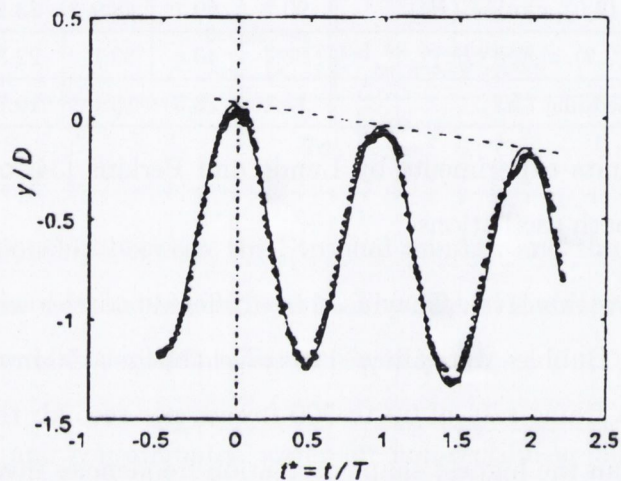
Figure 2.23: Motion of a zig-zagging bubble of diameter $D = 6$ *mm* in the direction perpendicular to gravity over time. The y position is normalised with respect to the bubble diameter and the time is normalised by the time it takes to complete one oscillation, T, Brücker [31].

zig-zag motion is clearly seen as a sinusoidal function of the y coordinate over time with amplitude 1.3D (approximately 10 *mm*). The average position of the bubble is seen to drift in the negative y direction indicated by the dashed line connecting the maxima in Figure 2.23, this implies a net lift force in the horizontal plane. Figure 2.24 shows the evolution of the bubble width, b, over one complete zig-zag (normalised with respect to the mean bubble diameter, D). The time, t^*, is made dimensionless with the duration, T, of one zig-zag. The labels A-F correspond to the labels in Figure 2.13. The deformation in the bubble is caused by an uneven pressure distribution in the equatorial plane at the inversion points, caused by the shedding of vortices at the bubble base. There is a strong correlation between the breadth oscillations and the
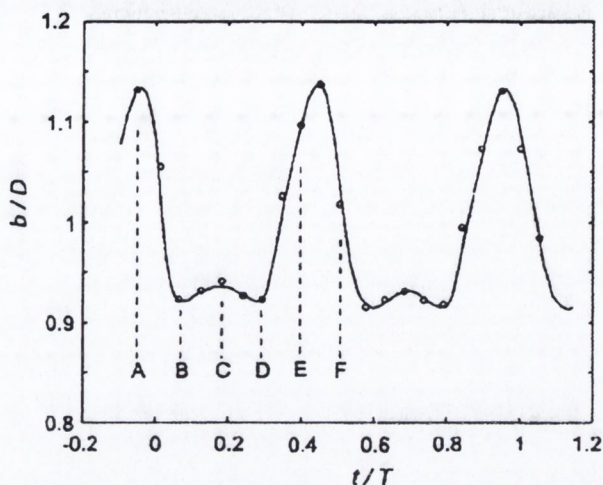
Figure 2.24: Bubble width (b) variation with time. The width is normalised with respect to the mean, major bubble diameter, D. Time is normalised by the time it takes to complete one oscillation, T. The labels (A) to (F) correspond to the fluid velocity measurements illustrated in Figure 2.13, Brücker [31].

motion of the bubble. The phases of large bubble breadth in Figure 2.24 represent a lower aspect ratio, i.e. a more oblate spheroid. The peaks repeat at each point where the bubble reverses its motion. The frequency is therefore twice that of the zig-zag motion. This motion, associated with vortex shedding is referred to as 'VS type' oscillation. A secondary peak is observed in Figure 2.24 at $t^* = 0.2$ and 0.7. Lunde and Perkins [34] also recognised a second peak in the frequency spectrum of the oscillation of bubble aspect ratio. In their results for a bubble of $d_e = 5.8$ mm, this secondary peak appears at a frequency of 35 Hz in comparison to the first peak, corresponding to a vortex shedding frequency of 10.7 Hz (see Table 2.2). Lunde and Perkins [34] suggest that this additional oscillation was associated with capillary waves traveling from the front to back of the bubble. Brücker [31] observed this frequency to be 17.7 Hz. The difference in frequency could be caused by the difference in aspect ratio between the two bubbles in each test. Brücker [31] also suggests an alternate explanation of this secondary oscillation linked to the spacing between the legs of hairpin vortices observed behind the bubble.

Brenn et al. [41] analysed the shape oscillations and path transitions of rising

bubbles in a $40 \times 40 \times 420 \ mm^3$ demineralised water tank. 3.4 mm bubbles were injected into the tank at 5 Hz from seven inlets simultaneously. The shape of the bubble was photographed with a high speed camera and approximated with Legendre polynomials. Bubbles rose rectilinearly for 25 mm and then began to spiral, at the same time the bubble surface began to oscillate. The authors found a strong link between the bubble shape oscillations and path instability.

2.3.5 Wake size and pressure distribution

The volume of the wake in dimensionless form, presented by Bhaga & Weber [16], is calculated to be

$$\frac{V_w}{V} = 0.037 Re^{1.4} \text{ for } (3 < Re < 110) \tag{2.23}$$

where V_w is the wake volume and V is the bubble volume. This compares well with the known literature (Kalra & Uhlerr [42]). It was found that the bubble's wake carried with it a larger amount of fluid than that of rigid spheres due to their deformation from a spherical shape. The liquid velocity within the closed wake was found to be much lower than that of the bubble rise velocity and to a stationary observer the bubble moves a large volume of surrounding fluid upwards with it.

Tsuchiya and Fan [43] measured the dynamic variation in the primary wake size in a two dimensional system. They monitored a bubble rising inside an 8 mm wide channel with a video camera rising at the same speed. This allowed the camera to remain at the center of a coordinate system aligned with the bubble. Figure 2.25 illustrates the dynamic variations in the primary wake area, normalised with respect to the bubble area at each instant, k_{pw}, along with the inclined angle, θ_b, over a two second period from injection. The bubble size in this case is defined as the bubble base width, $b = 30 \ mm$, which is commonly used as the length scale for spherical cap bubbles.

Although the bubble reaches its steady state geometry in less than 0.3 seconds, the wake steadily grows in size for about 0.75 seconds before shedding any wake material (the steady growth period). The inclined angle, θ_b, remained constant at around 90° which indicates the flow is symmetrical about the bubble vertical axis. When

θ_b deviates from this value the wake is considered to have initiated shedding. Once this asymmetry sets in, the periodic vortex shedding and periodic variation in primary wake size follow (steady shedding period). This cycle can be characterised by a saw tooth wave function. The shape and size of the primary wake varies periodically; the maximum in size occurring just prior to vortex shedding and the minimum immediately after.
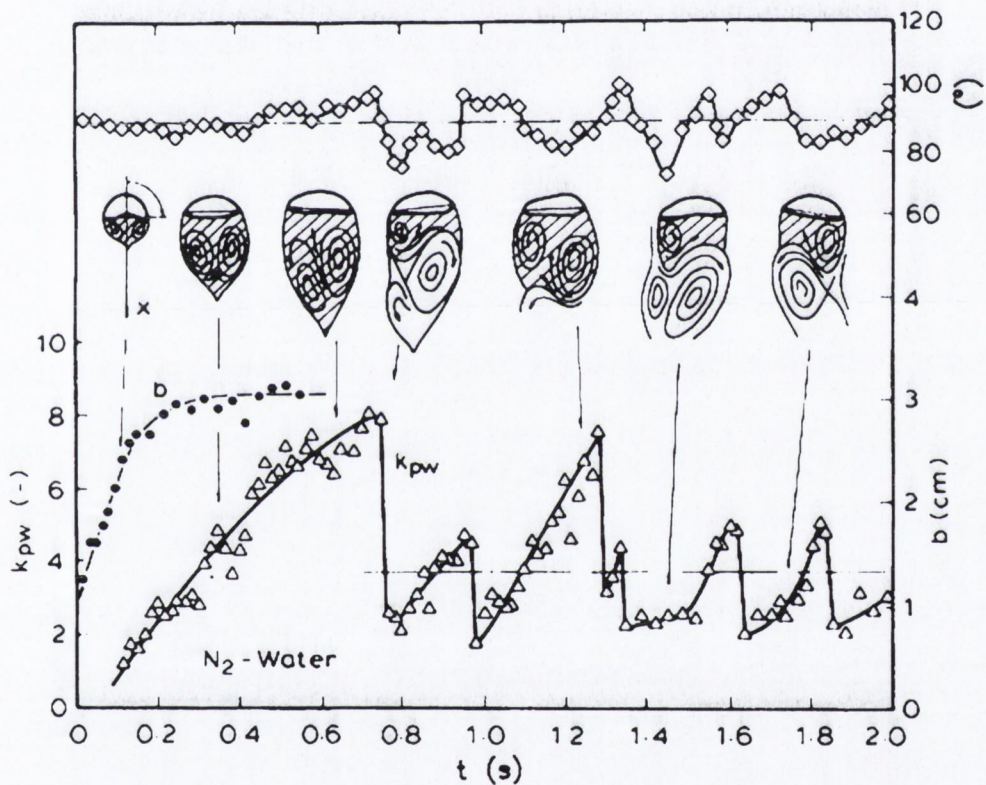
Figure 2.25: Top: variation in angle of attack, α (axes located at upper right hand side). Center: schematic of wake configuration at various points in time. Bottom left: development of base width, b (axes located on lower right hand side). Bottom: dynamic variation in primary wake area normalised with respect to the bubble area, , k_{pw} (axes located on lower left hand side), Tsuchiya [43].

Fan & Tsuchiya [1] also investigate the wake flow and pressure. The changes in the bubble's wake flow imply variations in the pressure distribution behind the bubble. The pressure in the bubble base region is directly involved in the force balance of the

bubble, thus influencing the bubble rise velocity and shape deformation. In addition, the pressure in the primary wake indirectly affects the wake size. Understanding the pressure distribution behind a rising bubble will provide a detailed, localised view on the mechanism of vortex shedding and its related phenomena.

As reported by Fan and Tsuchiya [1], Lazarek and Littman [44] measured the pressure distribution for a circular cap air bubble in stationary water contained in a 12.7 mm thick column. Figure 2.26 shows the isobaric representation of the pressure field around a bubble of $d_e = 51$ mm ($Re = 2.67 \times 10^4$). The pressure in Figure 2.26
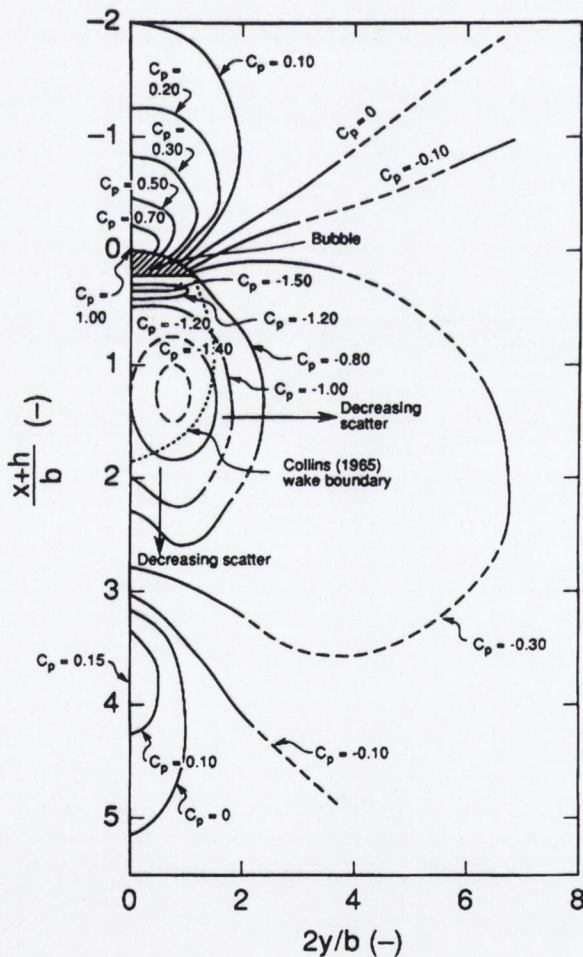
Figure 2.26: Isobaric representation of the pressure field around a circular cap bubble where $C_p = (P_T - P_\infty) / \left(\frac{1}{2}\rho U_T^2\right)$, Fan and Tsuchiya [1].

is represented by the pressure coefficient defined as

$$C_p = \frac{P_T - P_\infty}{\frac{1}{2}\rho U_T^2} \tag{2.24}$$

where P_∞ is the static pressure due to the liquid head above the measurement point, P_T is the measured pressure, ρ is the fluid density and U_T is the terminal velocity. Also shown in Figure 2.26 is the near wake boundary for a circular cap bubble of 6.4 mm thickness observed by Collins [29] at $Re = 2 \times 10^4$. As indicated in Figure 2.26, Lazarek and Littman [44] detected two types of pressure minima in the near wake. The first occurring symmetrically with respect to the bubble centerline at $2y/b = \pm 0.75$, which is very close to the location of Hill's vortex ring center for a three dimensional laminar wake (Hill's vortex is located at 0.707). The second is a sharp minimum pressure layer with a quick, localised recovery immediately beneath the bubble base. The former provides direct evidence that a pair of standing vortices exist in the near wake. The bubble base region is occupied with a liquid layer of turbulent flow as indicated by the stable primary wake and the absence of vortex shedding.

A thorough description of the characteristics of free rising bubbles has been presented with respect to the rise velocity, shape and general wake behaviour. The review is now expanded to include the dynamics of bubbles sliding underneath an inclined surface.

2.4 Sliding bubbles: bubble dynamics

Maxworthy [45] extended existing measurements for free rising bubbles to include bubbles sliding under an inclined plate. This was performed with spherical cap air bubbles in water and the experimental findings were compared to their own numerical results. Plate angles, α_s, of 5° to 90° to the horizontal were tested with bubble volume varying from 5 to 60 ml at intervals of 5 ml (the present study uses bubble volumes of 0.05, 0.1, 0.2 and 0.4 ml sliding under a surface inclined at 30° to horizontal). Plan and side view photographs obtained for different sized bubbles at various angles are shown in Figure 2.27 and 2.28 respectively. Plots of sliding velocity versus bubble volume for a range of angles were produced. The large amount of data recorded were reduced

using the radius of curvature of the leading edge as a length scale, resulting in plots of modified Froude number[11] versus bubble volume. Except at low angles, the Froude number was approximately constant over the range of bubble volumes tested, even though there was an appreciable change in bubble shape. Reducing these data further gives plots of Fr_1 and C_D versus angle, α (see Figure 2.29). A theoretical analysis based on the methods of Davies & Taylor [8] was developed which corresponded well with the results obtained from the experiments.

Tsao & Koch [46] observed $1-1.4\ mm$ sliding air bubbles in water at high Reynolds numbers. The wall inclination angle was varied from $10°-85°$ relative to the horizontal. Bubbles were released one or more diameters from the wall. After a transient period during which the bubble bounced off the wall with variable amplitude, the bubble motion was characterised as either steady sliding motion (observed for inclination angles below $55°$) or a bouncing motion with constant amplitude. The threshold value of $55°$ corresponds to a Weber number of 0.4. The authors note that in order to sustain this steady sliding motion, a hydrodynamic lift force must balance the component of buoyancy forcing the bubble against the wall. The inertial lift force was estimated to be insufficient to balance the buoyancy force pushing the bubble against the wall, thus, the lift was attributed to the viscous lubrication stress generated in the gap between the bubble and the wall.

Sateesh et al. [47] developed a model to simulate the effect of bubbles sliding on a heated surface during nucleate boiling. The model accounted for different mechanisms of heat transfer including micro-layer evaporation, transient conduction, natural convection and the effects of sliding bubbles. The model was validated against experimental results for water, R134a (a common refrigerant) and propane. An earlier study by Van der Geld [48] concentrated on deriving equations of motion for an expanding spherical bubble near a plane wall.

Perron et al. [49] performed an experimental investigation of single bubbles sliding under a slightly inclined surface. The bubble volume was varied from $0.3 - 9\ cm^3$

---

[11]The Froude number, in this case, is modified to account for surface inclination angle and is given as $Fr_1 = \dfrac{U_T}{\left(gV^{\frac{1}{3}}\sin\alpha\right)^{\frac{1}{2}}}$, where the volume, $V = \frac{1}{6}\pi d_e^3$ and α is the inclination angle. Fr_2 is the unmodified Froude number, $Fr_2 = \dfrac{U_T}{(gd_e)^{\frac{1}{2}}}$.
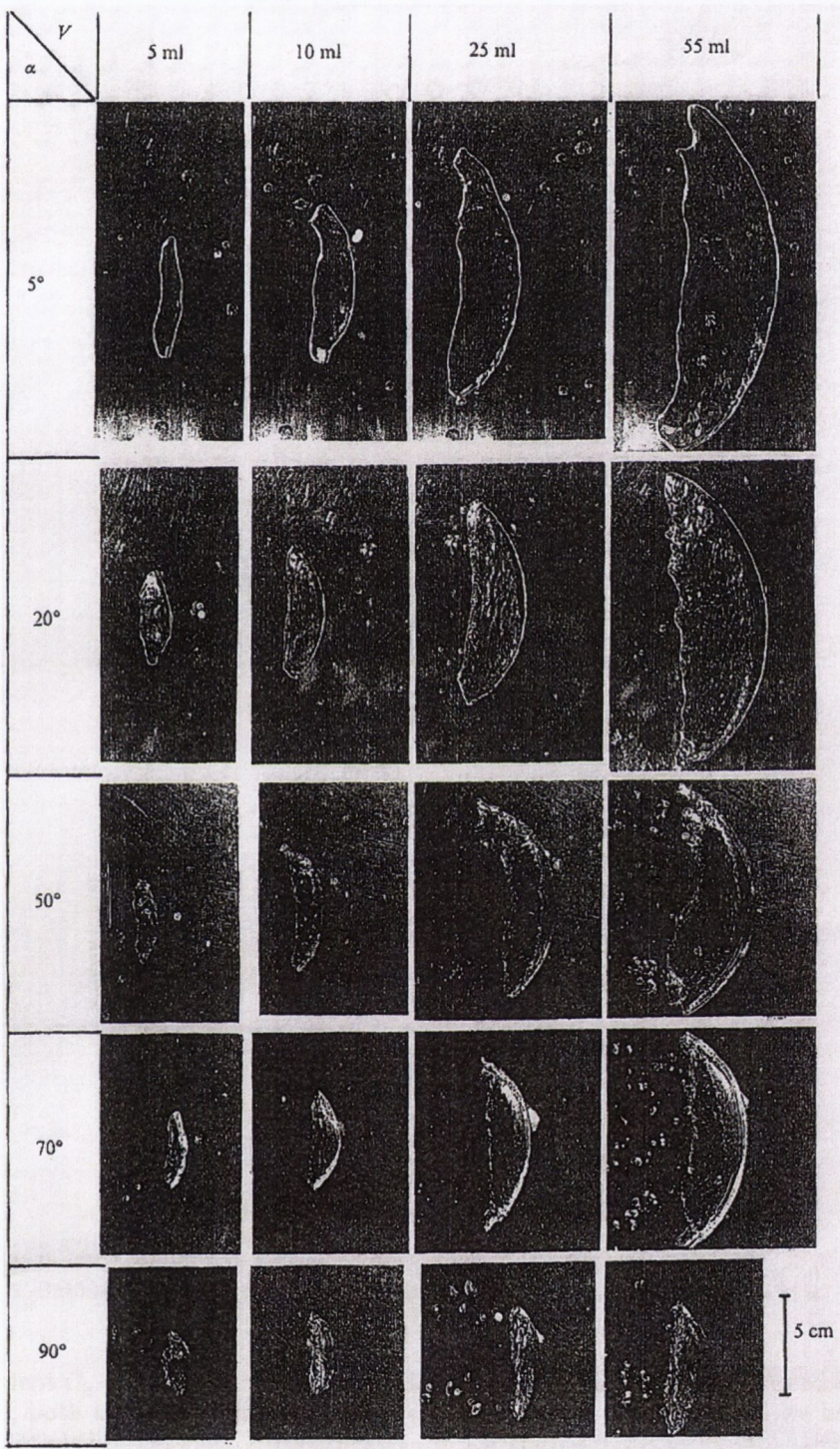
Figure 2.27: Photographs of the shapes of air bubbles in water under an inclined surface (plan view). Rows represent constant inclination angle, columns represent constant volume, Maxworthy [45].
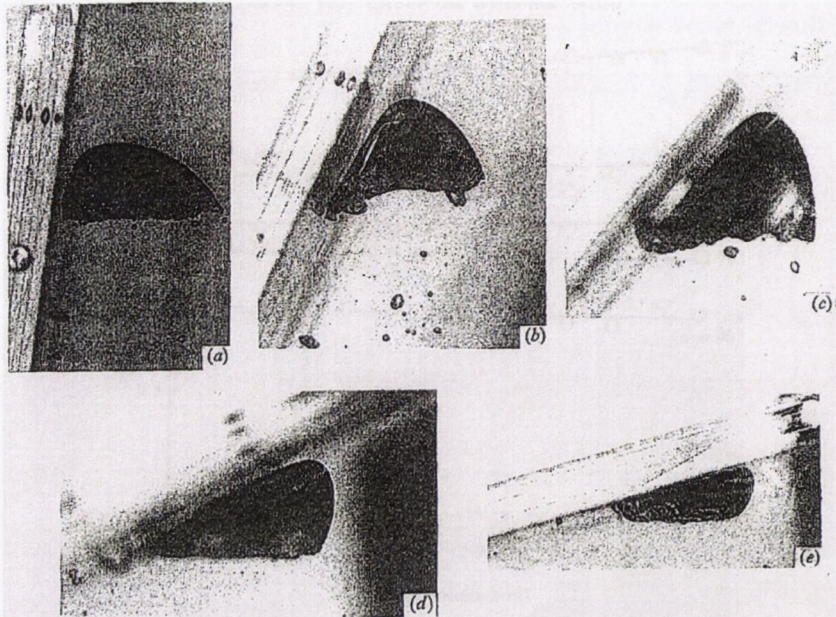
Figure 2.28: Photographs of the shapes of 60 *ml* air bubbles in water under inclined surfaces (side view). Included are surface inclination angles of (a) 82°, (b) 65°, (c) 50°, (d) 25° and (e) 15°, Maxworthy [45].

and the inclination angle varied up to 10°. The effects of inclination angle and bubble volume on the terminal velocity (and terminal Froude number) are studied. The experimental rig consisted of a Plexiglas plate measuring 160 *mm* wide and 900 *mm* long. The angle of the plate could be varied to the horizontal. At 1° inclination, the bubble could not reach the appropriate velocity to maintain the wetting film[12] over the whole length of the plate. For this reason, tests were performed from 2 − 10°. Bubbles were released onto the plate through two mechanisms; behind a removable barrier and through an inverted cup. The bubble terminal velocity was found to be the same; independent of release mechanism. A high speed camera mounted on a traversing rig observed the bubble as it slid along the plate. The camera could move at the same velocity as the bubble in order to keep the bubble central in the view of the camera. Position, instantaneous velocity and aspect ratio were analysed. To

---

[12] As the bubble slides over the surface a small amount of fluid usually exists between the bubble and the surface; this is referred to as the wetting film. In boiling applications this is referred to as the liquid micro-layer.
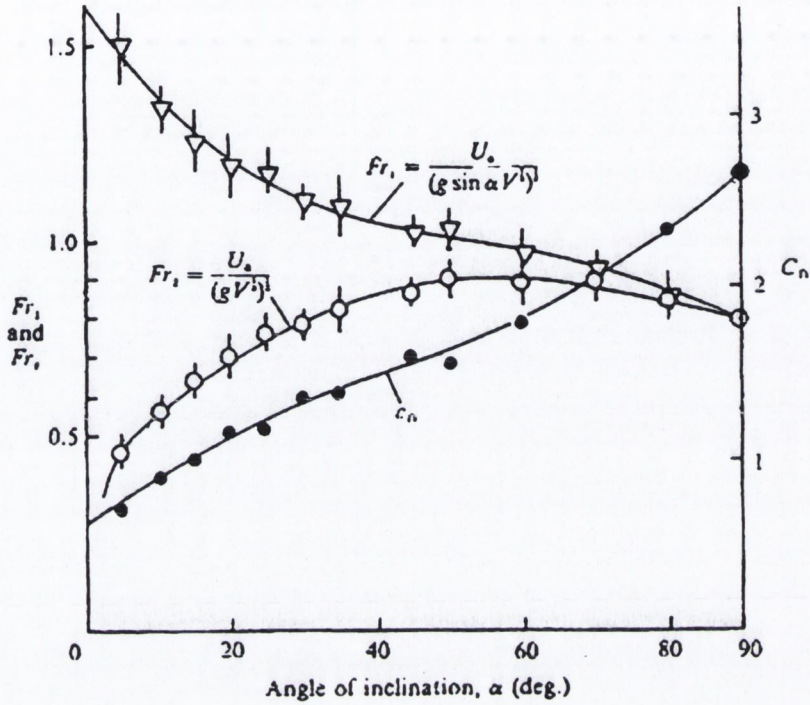
Figure 2.29: Froude number versus surface inclination angle, α. Fr_1 is modified to account for surface inclination angle while Fr_2 is the unmodified Froude number. The drag coefficient is calculated from $C_D = 1.65/Fr_1^2$, Maxworthy [45].

ensure the terminal velocity was reached, the first data point was taken 1.5 s from the onset of the wetting regime. Figure 2.30 shows the shape of a static bubble at various volumes. The radius of the circular contact zone, the height of the bubble and the contact angle are all shown.

For small volumes the bubbles are spherical but become gradually flattened as the volume increases. For a system such as the one in their experiments (air-water-Plexiglas), the static contact angle, θ_c, is about 80°. The contact zone appears as a perfect circle with radius R_c. The height of a bubble, h_b, increases with increasing volume to a maximum, h_{max}. A further increase in volume decreases the height slightly to a limiting value, h_{lim}. The bubble shapes were identified and separated into six sub-regimes identified with increasing volume. The four main sub-regimes are identified in Figure 2.31 as (C) semi-rigid bubble, (D) oval oscillating bubble, (E) deformable
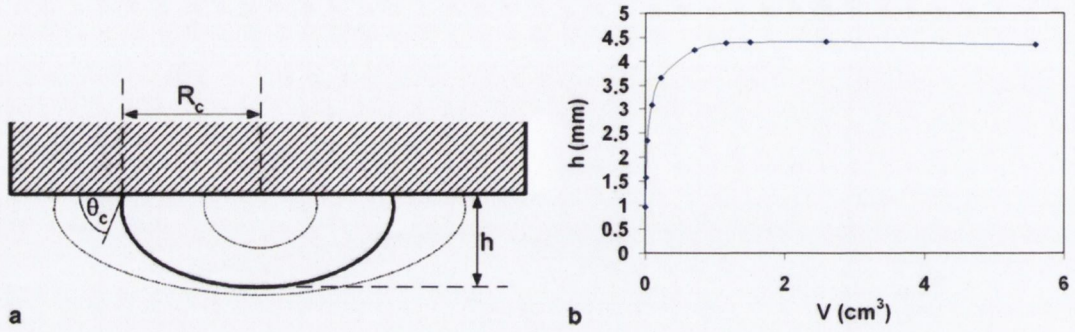
Figure 2.30: (a) General shape of bubbles of different volume under a horizontal surface and (b) the variation in h with volume, V. θ_c is the static contact angle, R_c is the radius of the circle inscribed by the contact region and h is the 'height' of the bubble, Perron et al. [49].
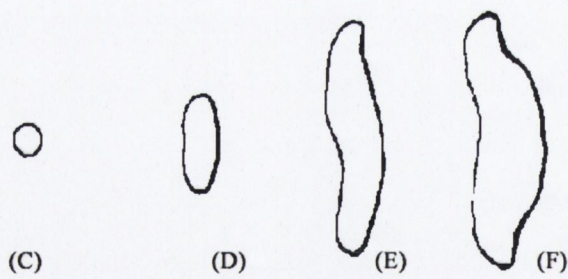
Figure 2.31: Characteristic shapes of bubbles moving under an inclined surface at a given inclination with increasing volume from (C) to (F) (plan view). The bubble is moving from left to right in all images, Perron et al. [49].

bubble and (F) bulged bubble. Bubbles in sub-regime (A) are immobile while bubbles in sub-regime (B) move at a very slow rate and are excluded from the diagram.

The limits between each sub-regime depend on the inclination angle. At high inclination angles (A), (B), (C) and (D) can disappear completely while at low inclination (E) and (F) might not exist. The terminal velocity was found to increase with the inclination angle at a given volume. The increase is most sensitive for both low bubble volumes and low inclination angles. For high bubble volumes the increase is more linear. The bubble's inertia was found to control the terminal velocity of the bulged bubbles (sub-regime (F)) while surface tension and viscous forces play an important role for bubbles at low angles and small bubble volumes. Figure 2.32 shows the variation of the drag coefficient as a function of the inclination angle for two different sub-regimes (deformable (E) and bulged (F)). The value of the Eötvös number $Eo = 39.1$ and 79.93 correspond to the (E) and (F) sub-regimes respectively. The rate of increase of the drag coefficient with inclination angle is larger for the deformable bubble and both exhibit a linear trend.
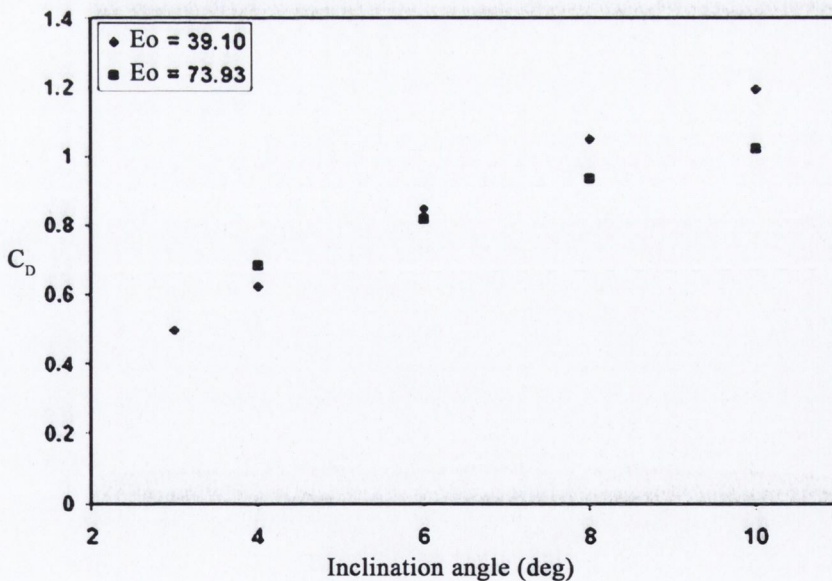
Figure 2.32: Variation in the drag coefficient, C_D, as a function of inclination angle for the 'deformable' ($Eo = 39.1$) and 'bulged bubble' ($Eo = 73.93$) bubble sub-regimes, Perron et al. [49].

Figure 2.33 shows the experimental results in dimensionless form for inclination

angles of $2°$, $3°$, $4°$, $6°$, $8°$ and $10°$. All the curves beyond $3°$ present a sensibly constant Froude number at high Eötvös numbers for the studied range of bubble volumes and inclination angles. This indicates that the ratio of the inertial and gravity forces remain constant even if the volume is increased. The plateau in these results corresponds to the bulged bubble sub-regime (F).
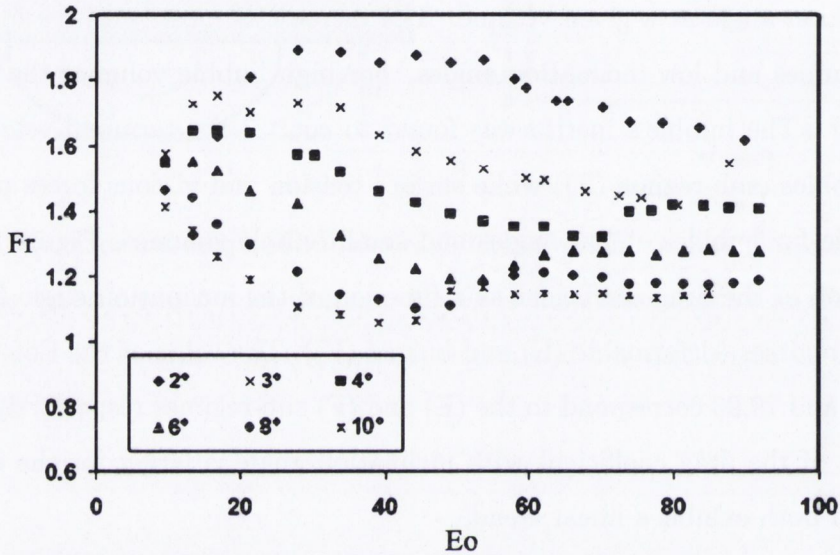
Figure 2.33: Variation in the Froude number, Fr, as a function of the Eötvös number, Eo, for different inclination angles, Perron et al. [49].

A further study was performed by Perron et al. [50] that focused more on the fluid properties. The analysis covered a Morton number range from 2.59×10^{-11} to 25.2, the Eötvös number varied from 10 to 150 and the surface inclination angle varied from $2°$ to $6°$. In order to cover a large Morton number range several fluids such as glycerin, propanediol, isopropanol and water were used. Bubbles moving through low Morton number liquids were found to be much more deformable than those moving through high Morton liquids, the aspect ratios of 5 and 2 respectively confirm this. Figure 2.34 illustrates the bubble shape for various volumes and Morton number at an inclination of $4°$.

Li et al. [51] present a study of FC-87 vapour bubbles sliding under a wall of uniform temperature inclined to angles between $2°$ and $15°$. Similar to Perron et al. [49] [50], the bubble generally grew from a 1 mm sphere to an ellipsoid to a cap shape over the
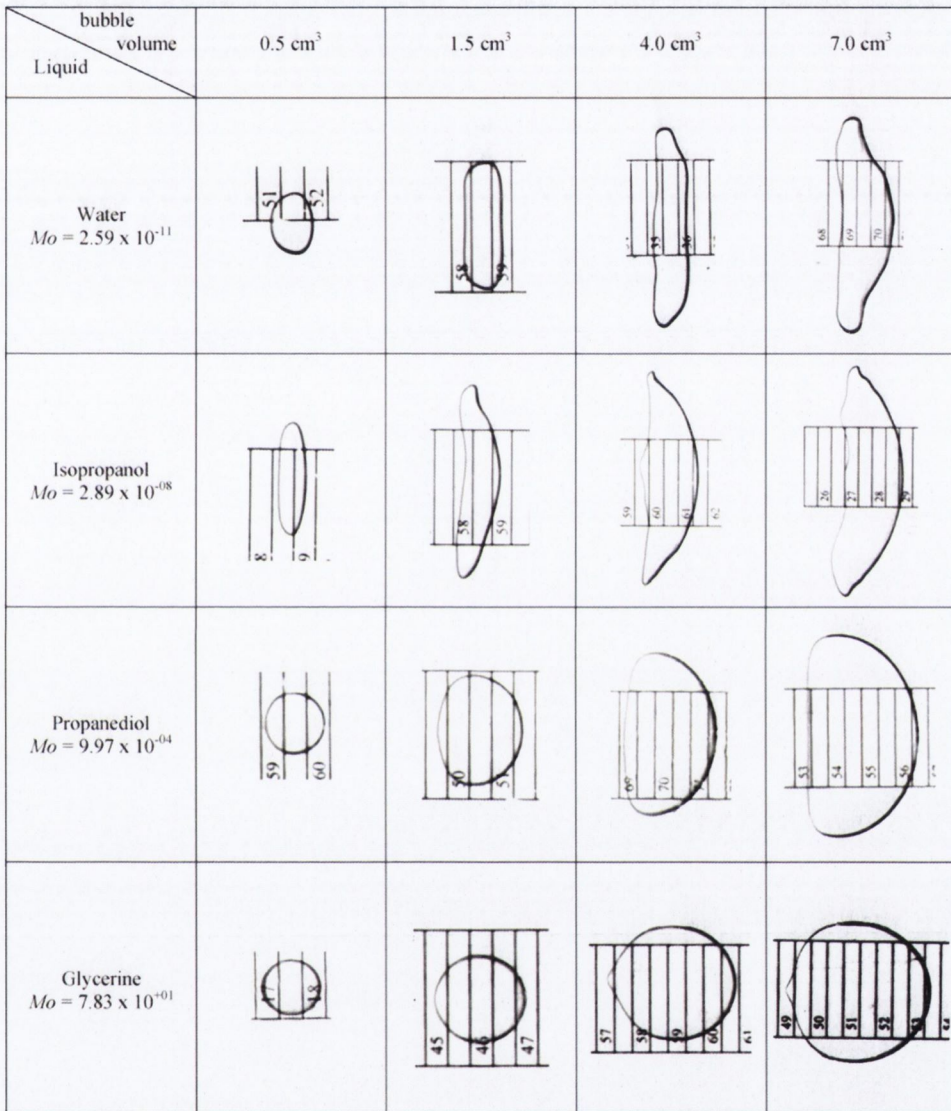
Figure 2.34: The shapes of bubble under inclined surfaces with changing volume and Morton number at a surface inclination angle of 4°. Rows represent constant Morton number while columns represent constant volume. The bubble is traveling from left to right in all images, Perron et al. [50].

length of the plate. Figure 2.35 (a) and (b) show the growing bubble from top and side views respectively for a surface inclination angle of 10°. The results correspond well with the illustration of Perron et al. [49] (see Figure 2.31). Bubble velocities correlated well with bubble dimensions and surface inclination. The observations in this study compared well with the water and air experiments of Maxworthy [45]; the behaviour of bubble velocity and Froude number appeared to be the same for the two studies, the Froude number having strong dependence on angle. From this, the authors deduce that the growing vapour bubble behaves like a bubble of constant volume at each stage of growth. The ratio of bubble width to length is found to be an excellent shape transition indicator, the transition occurring at a Reynolds number of 1500 for inclination angles of 10° and 15°. At lower angles (5°) a more gradual transition occurs, while at 2° no abrupt change occurs at all. The authors suggest that the Weber number, along with the Reynolds number, is an important determinant of bubble development. A later study by Zaruba et al. [52] presents theoretical and experimental results for bubbles rising and sliding along vertical unheated walls.
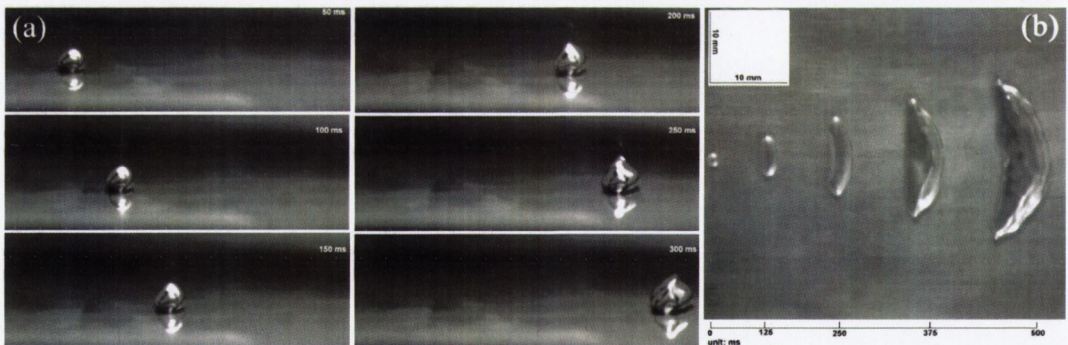
Figure 2.35: Vapour bubble shape variations with volume at an inclination angle of 10°: (a) side view and (b) plan view. The bulk fluid is FC-87 held at a temperature of 25 °C (5 °C subcooling), Li et al. [51].

Podvin et al. [53] compare their model prediction with experiments for small bubbles, $1 - 2$ mm in diameter, interacting with an inclined wall. The rig consists of a Plexiglas tank $300 \times 300 \times 30$ mm^3 filled with distilled water. Air bubbles were injected into the tank using pressurised air and a syringe with a solenoid valve. The Reynolds number varied from 40 to 560 while the Weber number ranged from 0.02 to 1.8. The

flat surface could be rotated between 5 and 90 degrees. A high speed camera was used to record the bubble under illumination by a halogen lamp at 300 *fps* over an area of $40 \times 30 \ mm^2$. The bubbles were allowed to reach their terminal velocity before impacting the surface. Their numerical model used lubrication theory to describe the fluid flow between the bubble and the wall. Lubrication theory assumes the pressure and velocity are uniform across the thin liquid film between the bubble and the surface; this limits the validity of the model. For the experimental results, bubbles in the range of $d_e = 1.2 - 1.8 \ mm$ exhibited three different behaviors mainly dependent on inclination angle. At low angles (10°), the bubble bounced two or three times and then stopped moving. Between 10° and $55 - 60°$ the bubble slid at constant speed along the wall although sometimes exhibited 'transient bouncing' where the bubble rebounded with decreasing amplitude. At angles above 60° the bubble experienced steady bouncing with constant amplitude. The numerical model predicted the rebound amplitude well for wall inclination angles below $55 - 60°$. However, the model cannot reproduce the slight variations in tangential velocity caused by the rebound due to the lubrication assumption.

Once a thorough understanding of the dynamics of free rising and sliding bubbles is obtained along with an understanding of the fluid flow around such bubbles, it is then possible to investigate how this affects heat transfer from a heated surface. The next stage of this review is expanded to include the effect of sliding bubbles on heat transfer from an inclined submerged surface.

2.5 Bubbles and heat transfer

The majority of research on sliding bubbles and heat transfer presented in the literature is for vapour bubbles sliding on a heated surface. Heat transfer enhancement due to sliding vapour bubbles is a complex mechanism found to be a combination of the effects of bubble nucleation, detachment and sliding. This can be broken down further into heat transfer through the liquid micro-layer (a thin layer of fluid between the bubble and the surface), bulk fluid agitation and mixing in the wake. The relative contribution of each of these elements is still a much debated topic as the following

literature review will reveal. The following section considers heat transfer both at the location of the bubble and in its wake along with an investigation into the liquid micro-layer between the bubble and surface. Although the present study is concerned with sliding air bubbles, the literature serves as a good reference point for possible heat transfer mechanisms, particularly in the wake. Where available, publications on the effect of sliding gas bubbles on heat transfer will be included.

2.5.1 Bubble induced heat transfer

An early study by Cornwell [54] investigated the influence of bubbly flow on boiling from a tube in a bundle. The aim of the study was to identify the individual contribution of each of the three terms in the right hand side of Equation 2.25 to the overall heat transfer coefficient, h.

$$h = h_{fc} + h_{sb} + h_{nb} \qquad (2.25)$$

where h_{fc} is the contribution due to liquid convection at the local fluid velocity and h_{sb} is the contribution from bubbles existing in the approaching free stream. In a tube bundle these bubbles originate from upstream tubes and slide along the downstream tubes. This term itself is determined partly by turbulence caused by sliding bubbles and partly by evaporation of a thin layer under the bubble . h_{nb} is the contribution from bubbles which nucleate and grow on the test surface.

The rig consisted of thirty four 19 mm diameter tubes mounted in two in line columns within a Perspex boiling cell. The working fluid was R113 (a common refrigerant) at 1 atm and a constant mass flux. The test-tube, which could be heated, was made from copper and was fitted with six radially positioned thermocouples; it was mounted in row three of the tube bundle. All the tubes in the bundle except the test-tube were heated to give a constant mean bundle heat flux. A small amount of heat, insufficient to cause nucleation, was passed to the test-tube which separated out the nucleation component of Equation 2.25, h_{nb}. Separate tests under single phase liquid conditions allowed measurement of the forced convection heat transfer coefficient; this value was adjusted to the local liquid velocity to give the convective component, h_{fc}. This allowed calculation of the contribution due to the sliding bubbles alone.

Boiling in R113 resulted in numerous small bubbles being generated. It was clear that a heat transfer mechanism, which was neither liquid convection (at the local velocity) nor nucleation, was responsible for a large part of the heat transfer from the tube. It was postulated that this mechanism was due to bubbles within the flow that slide around the tube. Furthermore, nucleation was found to only occur on the upstream tubes. When a sufficient amount of bubbles are being generated, the combined effects of liquid convection and sliding bubbles on downstream tubes are sufficient to maintain the heat flux without bubble nucleation. This work was later extended to include air bubbles(Houston & Cornwell [55]) under similar conditions. This extension revealed that bubbly-flow turbulence is a prominent mechanism in the heat transfer, condensation does not add significantly to the heat transfer but evaporation is a major factor (although it is not significantly more than the bubbly-flow turbulence).

Kenning & Yan [56] investigated sliding vapour bubbles under plane and curved surfaces. Bubbles were generated by boiling at the surface using an electrically heated metal shim. They used the Liquid Crystal Thermography technique in conjunction with a video camera to measure the temperature on the heated surfaces and to track the moving bubble. A single camera was used along with a mirror arrangement to record both parameters simultaneously. Two dimensional dynamic temperature and wall heat flux plots of the surface are presented. The wall heat flux q_w'', is calculated using the following equation, which assumes a thin heated surface

$$q_w'' = q_0'' - \alpha_w \rho_w \frac{\partial T}{\partial t} + k_w \left(\frac{\partial^2 T}{\partial x^2} + \frac{\partial^2 T}{\partial y^2} \right) \qquad (2.26)$$

where q_0'' is the input electrical heat flux, α_w, ρ_w and k_w are the thermal diffusivity, density and thermal conductivity of the wall respectively. Due to heat input from the heated surface the vapour bubble grew with time and the instantaneous bubble volume, V_{bubble}, is obtained from

$$V_{bubble} = \frac{\pi d_b b_b h_b}{6} \qquad (2.27)$$

where d_b, b_b and h_b are the bubble depth, breadth and height respectively and are obtained from the video footage. The authors related the rate of heat flow into the bubble to its volume increase and found that the heat flux from the wall is not sufficient

to explain the bubble growth. They conclude that in order to explain this growth, heat
flow to the bubble must also come from the superheated liquid around the bubble. No
hot spot in the temperature contours beneath the bubble was evident so it was assumed
that a continuous layer of liquid existed between the wall and bubble (referred to as
the liquid micro-layer) i.e. 'dry out' did not occur[13]. The thickness of this layer, δ, is
calculated to be in the range of 100 to 200 μm using Equation 2.28 (this assumes a
linear temperature distribution within the micro-layer).

$$q_w'' - q_v'' = \frac{1}{2}\rho c_{p,f}\delta\frac{\partial T_w}{\partial t} \tag{2.28}$$

where ρ is the fluid density, $c_{p,f}$ is the fluid's specific heat capacity and q_v'', the total
heat flux to the bubble, is given by

$$q_v'' = \frac{1}{A}\rho_v h_{fg}\frac{\partial V}{\partial t} \tag{2.29}$$

where A is the projected area of the bubble, ρ_v is the vapour density, V is the volume
and h_{fg} is the latent heat of vaporisation. The value obtained by Kenning & Yan [56]
corresponded closely to values obtained from a numerical study by Kaneyasu et al.
[57]. The main focus of this study was to validate the liquid crystal technique which
was successfully achieved.

In a more in depth study, Cornwell & Grant [58] investigated heat transfer to
vapour bubbles in water and Flutec (a commercial refrigerant) under a horizontal
tube. The three main contributions to heat transfer are identified as nucleation, micro-
layer evaporation and liquid disturbance. It has been identified that most of the heat
transfer in industrial applications such as shell and tube heat exchangers is attributed
to bubbles that slide around the tube rather than those that nucleate on the surface.
Cornwell & Grant [58] again utilise the liquid crystal technique in this study, the aim
of which is to identify whether or not a micro-layer exists beneath the bubble and
to examine the influence of mechanisms due to liquid disturbance and evaporation
on local heat transfer. The experimental rig simulated a horizontal tube by using
a 25 μm thick, curved, stainless steel shim 50 mm in diameter (for measurement of

---

[13]Dry-out occurs when the thin liquid layer beneath the bubble evaporates, the vapour within the
bubble presents a thermal barrier, raising the surface temperature.

the local heat transfer coefficients rather than mean values). The shim is electrically heated using a low voltage d.c. power supply. The shim can be replaced by a solid half cylinder of the same dimensions heated by electrical heaters. This is used for obtaining mean values. The shim is positioned on the upper surface of a Perspex sided cell which contains the working fluid (water or Flutec PP1). A mirror positioned outside the cell allows both the inner and outer surfaces of the shim to be recorded using a single high speed camera. Vapour bubbles are produced by a small heater under the shim or by nucleation on the surface.

During boiling, half of the heat transfer was found to be due to the bubble induced turbulence rather than evaporation for a heat flux of 100 kW/m^2. The sizes of the bubbles present were dependent on the fluid used. In water, large slow moving bubbles were observed compared to small, faster moving bubbles in Flutec. A temperature increase was observed below the water vapour bubble and dry-out was attributed as a possible explanation. For Flutec vapour bubbles, the faster moving bubbles made it difficult to ascertain whether the increase in heat transfer was due to destruction of the thermal boundary layer or to micro-layer evaporation. Due to the micro-layer thickness (calculated to be 200 μm), it was decided that surface cooling was due to boundary layer disturbance alone as evaporation would require micro-layer thicknesses ten times lower than that observed. In the case of water, bubbles were found to pass close to the heated surface and receive heat from the outer reaches of the boundary layer. They could also penetrate the boundary layer, 'stick' to the surface and cause dry-out. The bubble would remain there until growth and buoyancy eventually drew it away. In the case of Flutec, this phenomenon did not occur, possibly due to the size and velocity of the bubbles.

To conclude, the study demonstrated that there are no unique answers to questions regarding the existence or otherwise of a micro-layer beneath the bubble. Neither the bubble sweeping mechanism nor the micro-layer evaporation mechanism is dominant under all conditions and both must be included in any analysis of local heat transfer.

A similar study was performed by Yan et al. [59] on sliding and sticking vapour bubbles under inclined plane and curved surfaces. For the sliding bubble experiments, the rig consisted of a flat 75 μm thick stainless steel plate measuring 40×35 mm^2.

It was heated using ripple-free d.c. current and could be held at an angle between 15 and 45° from horizontal. The lower surface was immersed in degassed water at atmospheric pressure and the water pool was held at a temperature 96 to 100 °C. In order to eliminate the effects of nucleating bubbles, steam was generated by external heaters and injected into the pool through either a single injector or an array of injectors close to the lower end of the inclined plate. The liquid crystal technique was once again used in conjunction with a high speed camera and mirror arrangement to record both bubble motion and heat transfer.

One series of tests used bubbles of size $2 - 10 \; mm$ with a relatively low superheat of 3 - 5 °C, depending on the inclination angle (the heat flux was restricted to 5 kW/m^2 to avoid nucleation on the surface). The plate angle is set to 15° and the bubble moves with a velocity of 140 mm/s. For large bubbles, it was found that despite the bulk temperature of 96 °C (plate temperature of 105 °C) the bubble grew as it moved. It left behind a cooled trail approximately the width of the bubble. Just behind the bubble's leading edge there was a rapid decrease in wall temperature and the heat flux increased towards the middle of the bubble to four or five times the undisturbed value. The heat fluxes under the bubble are consistent with conduction causing evaporation of a micro-layer about 50 μm thick at its center, reducing to 25 μm at the rear. Temperatures below saturation have been observed just before the rear edge of the bubble, suggesting that the three-dimensional flow behind the bubble must pull subcooled bulk liquid into this region. In the wake of the bubble, the heat transfer coefficient is observed to be three to five times the undisturbed value, covering an area approximately the width of the bubble. This cooling persists long after the bubble has passed. At low angles (15°), bubbles occasionally stuck to the surface and then moved along it slowly. It would appear that the dry-out region under the bubble moves with it but impedes its motion.

For steam bubbles at increased plate angles of 30 and 45°, moving at 190 and 220 mm/s respectively, there was a progressive reduction in cooling under the bubble but improved cooling in the wake. The wake cooling persisted behind the bubble, affecting an area 50% wider than the bubble. This was found to be consistent with a finding by Kenning & Kao [60] that a gas bubble sliding up a vertical plate could

improve heat transfer over an area more than 40 times its own projected area. For small bubbles it was found that there was very little cooling underneath but increased cooling in their wakes. Yan et al. [59] concluded that most of the cooling occurs in the wake of the bubble, affecting large areas of the wall. The relative contributions of each mechanism are influenced by the wall thickness, its properties and the heat input which all affect the wall temperature. Increased heat transfer under the bubble reduced the temperature so much that there was little temperature difference to drive the heat transfer in the wake even if the heat transfer coefficient was high. This effect would be reduced on a thick, highly-conductive wall. The analysis of curved surfaces in Yan et al. [59] was similar to that of Cornwell and Grant [58].

Thorncroft and Klausner [61] (also Thorncroft et al. [62]) present an investigation of the influence of sliding air and vapour bubbles on forced convection heat transfer. Their two main objectives were to demonstrate the importance of the energy transport mechanism associated with sliding bubbles in forced convection boiling and to distinguish the importance of bulk turbulent enhancement in the presence of sliding air bubbles. The rig consisted of a vertical transparent Lexan channel measuring 12.7 × 12.7 *mm* with an electrically heated foil forming one of the sides. The working fluid was FC-87, a refrigerant manufactured by the 3M Corporation. A gear pump drove the working fluid through the flow loop, where it was preheated by four heaters. The fluid was routed through a series of valves to create the upflow or downflow in the transparent section. Visual measurements of the bubbles were made using a high speed camera. The wall temperature was measured using 6 thermocouples. An injection system, located at the entrance to the test section, allowed air bubbles to be injected at the heater surface; the air was preheated to the bulk liquid temperature. The growth rates of bubbles were experimentally measured and found to be represented well by a power law curve fit (see Equation 2.30).

It was found that a smaller number of active nucleation sites were required to achieve the same heat transfer in upflow as would be achieved in downflow under the same hydrodynamic conditions. In other words, active nucleation sites in upflow resulted in greater heat transfer from the surface than those in downflow. Sliding bubbles were observed to remain close to the heated surface during upflow. This

indicated that there exists a significant heat transfer mechanism related specifically to sliding bubbles. As noted in previous investigations of boiling in tube bundles by Cornwell [54], Thorncroft and Klausner [61] observed that the nucleation sites were mainly confined to the upstream end of the heated plate. This was due to the fact that sliding bubbles deplete energy from the heating surface, reducing the potential for nucleation downstream. Heat transfer due to sliding bubbles was found to account for 52% of the total heat transfer, the contribution to heat transfer due to bubble growth was negligible.

In an attempt to distinguish the contribution of heat transfer due to turbulent convection to heat transfer due to latent heat transport, air bubbles were injected along the heated surface. Air bubbles were nominally 1 *mm* in diameter and were injected at various air flow rates that mimicked nucleation from a single nucleation site. An increase in the heat transfer coefficient was observed for all injection flow rates, an effect which diminished with increasing flow rate. The maximum increase observed was a factor of two. In conclusion, the bulk turbulent and nucleate boiling heat transfer mechanisms are in fact inter-dependent. The bubble dynamics in forced convection boiling are strongly influenced by the bulk flow behaviour, and the bulk flow turbulent heat transfer appears to be strongly influenced by the bubble dynamics.

Atmane & Murray [63] studied the effect of liquid motion induced by air and vapour bubbles on heat transfer from a cylinder. They used a heated copper cylinder as the test surface along with a hot film sensor to measure the fluctuating heat flux. It was found that during nucleate boiling, heat transfer was highest on the upper part of the cylinder. This enhancement was due to bubbles nucleating on the lower parts of the cylinder and sliding around. By injecting bubbles from below, heat transfer was enhanced on the lower parts of the cylinder. Heat transfer enhancement was found to be mainly due to liquid agitation by the bubble wake.

2.5.2 Wake effects

An experimental study of the flow pattern and heat transfer associated with a vapour bubble sliding on a downward facing heated surface is presented by Qiu & Dhir [64].

They attempted to improve the understanding of the dynamics of sliding bubbles and the associated heat transfer. They used a polished silicon wafer, 185 *mm* long × 50 *mm* wide, as the test surface to ensure no nucleation on the surface. Kapton foil heaters provided the heat to the surface and miniature thermocouples measured the surface temperature; the wall superheat could be maintained nearly uniform in the sliding direction by separately heating the elements. The working fluid was PF-5060. Holographic interferometry was used to measure the fluid temperature in a plane parallel to the bubble flow direction and perpendicular to the heater surface. Bubbles were generated by an artificial cavity machined into the heater surface. The work by Qiu and Dhir [64] covered the shape and trajectory of sliding bubbles, the bubble growth rate, flow patterns associated with sliding bubbles and the heat transfer underneath and in the wake of a sliding bubble.

At plate inclination angles less than 60° with respect to the horizontal, it was found that the bubbles change shape from a sphere at nucleation to an elongated spheroid or crescent at the downstream end of the plate. The lower the inclination angle, the larger the bubble dimension was in a direction perpendicular to the flow. Larger wall superheat lead to larger bubbles. The extreme case of this was at low plate angle (5 and 15°) and high superheat, where the bubble covered the width of the test plate (49 *mm*), at the downstream end of the heater. A wedge like liquid gap was observed underneath the bubbles for plate angles between 15 and 60° that penetrated into the bubble base. The wedge angle decreased with increasing bubble size. No liquid wedge existed for plate angles of 5°, where the bubbles were generally flat in shape. In magnified images the liquid wedge is seen to penetrate almost to the downstream side of the bubble where the thickness varied from 0.16 *mm* to 64 *μm* from front to back. This value corresponded well to the value obtained by Kenning et al. [65]. The apparent wedge angle is measured to be 14° compared to the actual wedge angle beneath the bubble of $\approx$ 1°. This is illustrated in Figure 2.36.

The change in thickness of the liquid layer indicated an increasing temperature gradient along its length; this indicated an increase in the heat transfer coefficient underneath the bubble from the upstream side to the downstream side. 'Fresh', hot liquid was observed to continuously enter the liquid layer as it slides, this contradicted
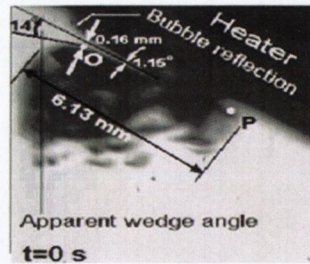
Figure 2.36: Photograph of sliding vapour bubble including the shape and liquid film layer at a surface inclination angle of 32°. The bubble is traveling from right to left. Illustrated are the apparent wedge angle (14°) and wedge angle (1.15°). $\Delta T_{sub} = 1.3\,°C$, $T_w - T_s = 3\,°C$, Qiu & Dhir [64].

previous work by Kenning et al. [65] where they assumed the flow diverted around the base.

For all angles of inclination below 60°, the terminal velocity increased with plate angle for a constant bubble size and shape. For plate angles greater than 60°, only spherical bubbles were observed, which slightly grew over the plate length. These bubbles slid along the lower part of the plate but, after a few centimeters, began to lift off, rise almost vertically and hit the surface again. This is illustrated in Figure 2.37. The occurrence of lift-off means that the forces pushing the bubble towards the wall such as gravity and the expansion force cannot overcome the shear lift force lifting the bubble away. A recoil force results from the evaporation of the thin film on the wall while the shear lift force can be created by vorticity due to the relative velocity between the liquid and the bubble.

By obtaining the shape of the bubble in two dimensions from the high speed cameras, the bubble volume was evaluated as a function of time. The equivalent radius, r_e, as a function of time for three inclination angles is presented in Figure 2.38. It was found that the bubble growth can be described by an expression (similar to that presented by Thorncroft and Klausner [61]) in the form

$$r_e = r_0 + Bt^n \tag{2.30}$$

where r_0 is the initial bubble radius, B is the growth constant and n is the exponent
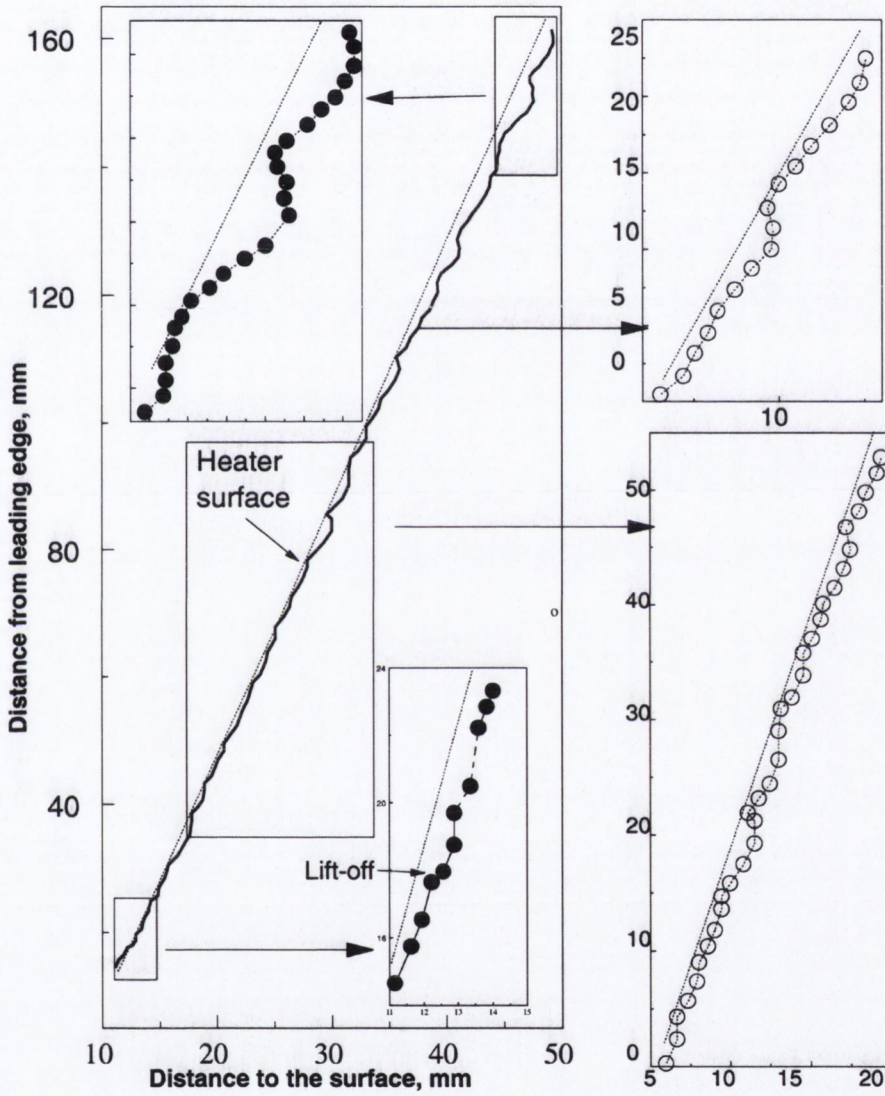
Figure 2.37: Trajectory of sliding bubble for a plate inclination angle of 75° to the horizontal. The working fluid was PF-5060, $\Delta T_{sub} = 1.5\,°C$, $T_w - T_s = 2.6\,°C$, Qiu & Dhir [64].
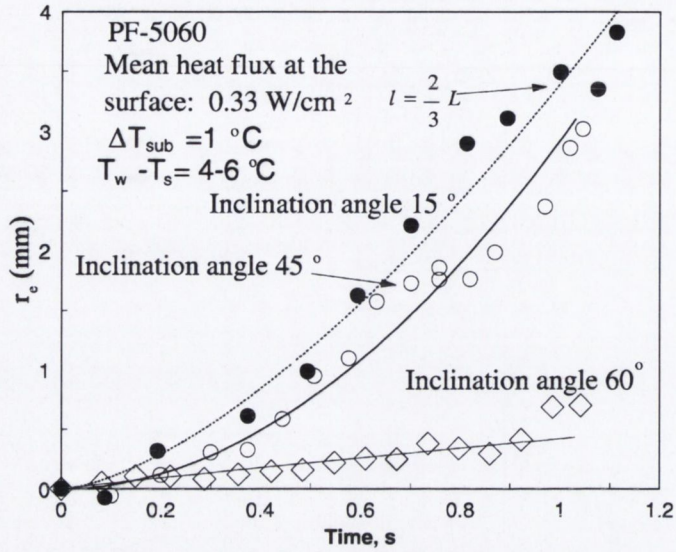
Figure 2.38: The Influence of inclination angle on sliding bubble growth rate. Presented are three inclination angles of 15°, 45° and 60°, Qiu & Dhir [64].

on time.

The flow patterns behind a sliding bubble were also reported for inclination angles close to horizontal and close to vertical ($\alpha = 15°$ and 75° respectively, 11.5 mm from the nucleation point). Bubbles were generally large at this measurement point. Figure 2.39 shows the fringe pattern for the temperature profile around the bubble sliding on a heated surface at $\alpha = 15°$ with a Rayleigh number[14] of 1.26×10^9. At $t = 0.45$ seconds, the bubble has just entered the view of the camera. A natural convection boundary layer can be seen to exist in front of the bubble. The boundary layer is forced away from the heater surface and around the bubble. At $t = 0.474$ s, a laminar region exists both close to the heater surface and further away. A region behind the bubble is seen to be slowly rotating when the video footage is observed. With the expansion of the thermal boundary layer, the temperature gradient just upstream of the bubble is found to fall below that for the undisturbed state. Reduction in the temperature gradient leads to a reduction in heat transfer from the wall. At the rear of the bubble the increased mixing causes thinning of the steep temperature gradient region. This in turn corresponds to a higher rate of heat transfer near the wall.

---

[14]The Rayleigh number $Ra = g\beta\Delta T x^3/\nu\alpha$.
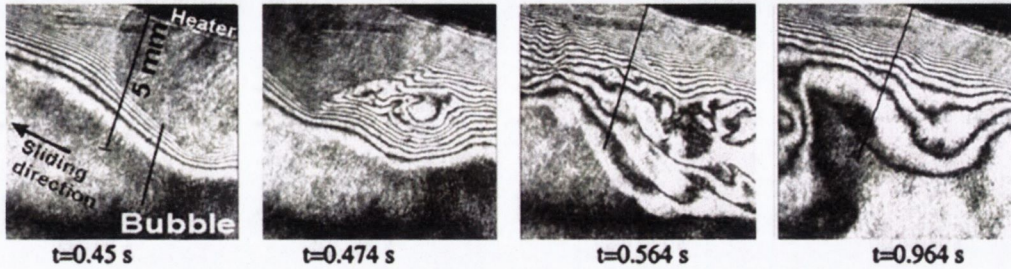
Figure 2.39: Far field fringe pattern around and behind a sliding bubble in a liquid with small superheat, the temperature difference between two consecutive fringes is 0.0255 °C. The bubble is sliding from left to right and the surface is inclined to 15° ($\Delta T_{sub} = 0.5$ °C, $T_w - T_s = 1$ °C, $Ra = 1.26 \times 10^9$), Qiu & Dhir [64].

Increasing the wall superheat, while keeping the subcooling constant, resulted in a larger bubble but similar flow pattern around the bubble. However, when the liquid subcooling was increased, the flow pattern in the wake was found to be different. Figure 2.40 illustrates this. As seen at $t = 0.118$ s, large longitudinal vortices were formed at a certain axial distance downstream of the bubble; these vortices rotate in the anti-clockwise direction. The vortices detached from the thermal boundary layer and moved outwards to the bulk where they dissipated. This indicated extra heat removal besides the enhanced convection due to the wavy structure of the thermal boundary layer near the surface. Other smaller vortices in series were also formed between the bulk liquid and boundary layer as indicated in Figure 2.40, at $t = 0.164$ s. Some of these developed into large vortices while the others dissipated without leaving the thermal boundary layer. PIV flow measurements revealed that, in the frontal portion of the bubble, liquid is pushed outwards away from the bubble. In the rear of the bubble, liquid is pulled inwards and a vortical structure is seen to exist behind the bubble. This is consistent with observations obtained from the fringe patterns. It is clear that the vortical structure can enhance heat transfer from the wall by bringing in cooler liquid from the bulk to the thermal boundary layer.

Increasing the plate angle to $\alpha = 75°$ leads to chaotic, wavy, development of the thermal boundary layer. Vortices were observed to roll over the boundary layer. Bubbles at this angle are generally smaller in size and don't grow significantly as
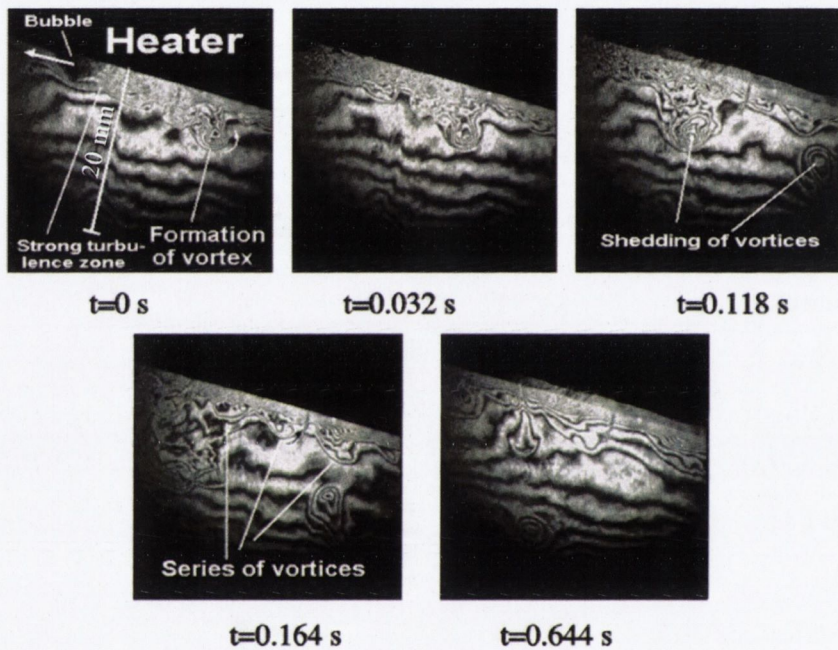
Figure 2.40: Far field fringe pattern around and behind a sliding bubble in subcooled liquid at small superheat, the temperature difference between two consecutive fringes is $0.0255\,^{\circ}$C. The bubble is sliding from left to right and the surface is inclined to 15° ($\Delta T_{sub} = 2.7\,^{\circ}$C, $T_w - T_s = 0.4\,^{\circ}$C, $Ra = 2.4 \times 10^9$), Qiu & Dhir [64].

they traverse the heated surface. For such a small bubble, and a release frequency of less than 2 *Hz*, the bubble had little effect over that of natural convection. The heat transferred to the bubble through the liquid micro-layer was found to contribute about 17 % of the heat required for the bubbles to grow.

Bayazit et al. [66] used Liquid Crystal Thermography to investigate the relative contributions of micro-layer evaporation and wake mixing to the overall heat transfer. The experimental setup consisted of an electrically heated 51 μm thick stainless steel foil measuring 21×16.8 cm^2. The top surface of the foil is coated in liquid crystals while the lower surface is exposed to the working fluid, FC-87. The test surface can be rotated relative to the horizontal. FC-87 vapour is generated separate to the main rig and injected at the lower end of the foil. Two synchronised cameras record the images of the upper and lower surfaces of the foil and the results combined. Tests were performed at a plate inclination angle of 12° to the horizontal. The bubble velocity ranged up to 200 mm/s with the bubble volume up to 2 *ml*.

Their measurements of the velocity and volume of vapour bubbles agreed well with those of Maxworthy [45] for adiabatic gas bubbles. Bubbles were found to grow rapidly, obtain a cap-shaped geometry and create a triangular thermal wake with sharp lateral edges as indicated in Figure 2.41. Thin, apparently turbulent, shear layers were observed shedding from the lateral extremes of the caps. These shear layers may be a train of relatively stationary (with respect to the heated surface) small-scale vortices shed from the extremes of the bubble.

Delauré et al. [67] performed a simultaneous PIV and heat transfer study of a bubble interacting with natural convection from a copper block at various angles. A single air bubble in water was used. A high temporal response heat flux sensor was used to measure heat transfer enhancement from a copper block. Two heat transfer mechanisms were identified in their testing. First, the heat transfer coefficient was found to respond closely to changes in flow velocity. The wake of the bubble, interacting with the thermal boundary layer, resulted in reduced or increased heat transfer at the surface. Second, fluctuations in the fluid temperature due to the bubble's motion were linked to large fluctuations in heat transfer as the bubble drew in cooler liquid from the bulk. The effect on heat transfer was found to be much larger when the two
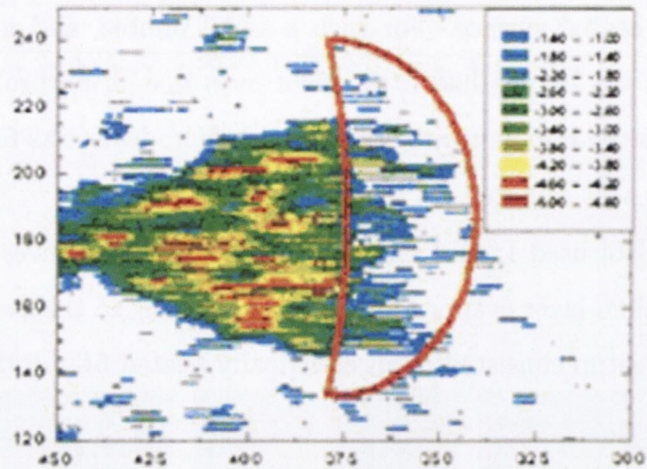
Figure 2.41: Contour plot of the change in wall temperature caused by the passage of a vapour bubble. Red indicates a drop of approximately 4 °C and blue represents a drop of approximately 1 °C, Bayazit et al. [66].

mechanisms combined. Maximum enhancement was achieved when the heated block was inclined to 45°.

2.5.3 Heat transfer to and from the bubble

Further to the work previously performed by Qiu & Dhir [64], Manickam & Dhir [68] used the same experimental rig to further investigate sliding bubbles. This research was confined to a plate inclination angle of 15° to the horizontal. In an attempt to calculate the local heat flux into the bubble, they analysed the fringe pattern around the sliding vapour bubble. They assumed no temperature gradient within the bubble and that the interface is at the saturation temperature. Radial lines were drawn out from the middle of the bubble base, for various angular coordinates θ_q, measured from the upstream side of the bubble, as indicated in Figure 2.42 (a). Figure 2.42 (b) illustrates the heat transfer into the bubble[15] at three different times ((A) $t = 0$ ms, (B) $t = 4$ ms and (C) $t = 8$ ms) along with the time averaged value.

---

[15]Note the the heat flux into the bubble is negative, hence, heat is actually moving out of the bubble, i.e. it is condensing over the measurement surface.
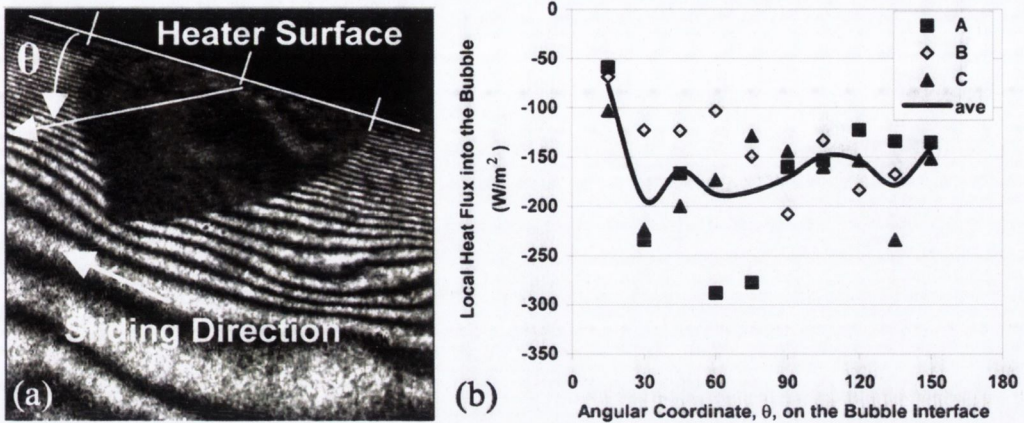
Figure 2.42: (a)Description of coordinate system & (b) variation of heat flux around the bubble interface for three different times, (A) $t = 0\ ms$, (B) $t = 4\ ms$ and (C) $t = 8\ ms$. The solid line represents the time averaged value ($\Delta T_{sub} = 2.7\,^{\circ}C$, $T_w - T_s = 0.4\,^{\circ}C$), Manickam & Dhir [68].

Measurements were only made for θ_q from 15 to 150° as the fringe density became too large near the walls. From Figure 2.42 (b), it was observed that the heat flux into the bubble was low in the frontal area close to the wall, this increased to a maximum at $\theta_q = 30°$. Heat flux for $\theta_q > 30°$ reduced and reached an average value. The data showed much scatter which was attributed to the change in bubble shape between the time intervals. In the frontal region, it was concluded that condensation heat flux was much lower due to the higher local liquid temperature. As θ_q increases, more of the bubble comes in contact with the colder bulk liquid, and the heat flux out of the bubble increases. This occurs up to $\theta_q = 60 - 80°$ where the flow begins to detach and the heat flux begins to decrease again. In the wake region, the heat flux out of the bubble is markedly lower. The heat transfer close to the wall ($0 \leq \theta_q < 15°$, $150 < \theta_q \leq 180°$) was also estimated. It was found that heat transfer through the liquid micro-layer decreases with increased subcooling. They conclude that an increasingly higher portion of energy from the liquid layer went, via condensation at the interface, into heating up the bulk liquid.

Expanding on the experimental work of both Qiu & Dhir [64] and Manickam & Dhir [68], Li et al. [69] composed a numerical study of a single bubble sliding on a downward

facing heated surface. The numerical predictions of the bubble shape agreed well with that obtained through experiment. The bubble changed shape from a sphere at the initial position to an ellipsoid and finally to a cap-shaped bubble at the downstream end of the inclined surface. The flow pattern around the bubble also compared well with the previous experimental data. Heat transfer to the bubble through the micro-layer was found to be the dominant mechanism of bubble growth. This was attributed to the small contact angle and contact area between the bubble and surface.

2.5.4 The Micro-layer thickness

Addlesee & Cornwell [70] developed a theoretical model to predict the film thickness above a sliding vapour bubble and compared it to their own experimental results. The experimental setup consisted of a sloping perspex tube 100 mm diameter and 1 m long. The film thickness was measured using a non-intrusive fiber optic technique described by Yu & Tso [71] where a sensor is mounted flush with the tube surface. A rounded tube was used as this helped guide the bubbles past the sensor. The film thickness was measured for bubble sizes from 0.1 ml to 2.5 ml ($d_e \approx 20 \ mm$ for the 0.1 ml bubble) for angles between 8° and 23°. Figure 2.43 shows the results obtained from this technique. The signal from the sensor rapidly rose and reached a steady value as the bubble moved over it. This was maintained for approximately 1 ms and then fell away with some fluctuations as the bubble tail passed by. The numerical predictions were in good agreement at low inclination angles but underestimated the thickness at higher angles (approximately above 20°).

Li et al. [72] also investigated the thickness of the micro-layer. They used a uniform wall temperature aluminium plate as the test surface. This was heated with two thermofoil heaters. A fiber optic/laser based probe was mounted in a small hole in the aluminium plate to measure the micro-layer thickness. The details of its operation are discussed in detail in Li et al. [72]. Single 1 mm diameter vapour bubbles were injected through a syringe-needle system located near the bottom of the test surface. A high speed camera recorded the bubble motion in two dimensions using a mirror arrangement.
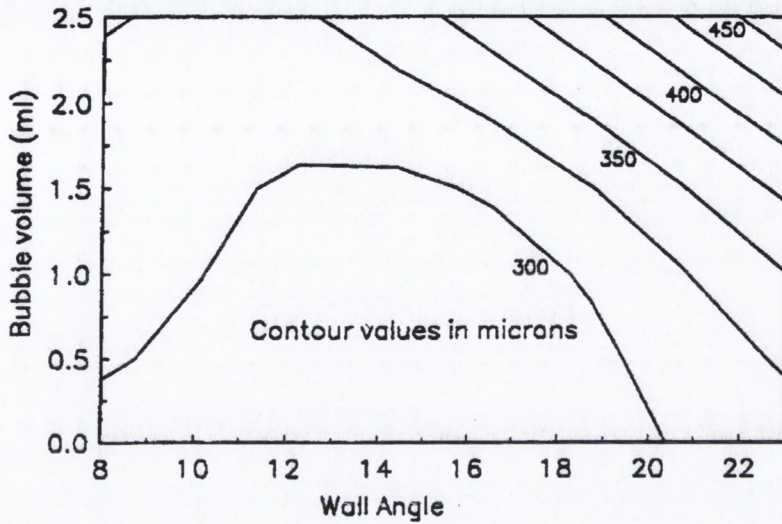
Figure 2.43: Variation in the micro-film thickness as a function of the bubble volume and wall inclination angle to horizontal, Addlesee & Cornwell [70].

Tests were performed at plate inclination angles of $\alpha = 2°$, $5°$, $10°$ and $15°$ to the horizontal. Bubbles were initially spherical but transitioned through an ellipsoidal shape to a final cap shape before they reached the end of the test plate. The film thickness could only be measured if the bubble interface remained flat. Waves which appeared on the surface at higher inclination angles introduced substantial error to the measurement method. Figure 2.44 (a) shows micro-layer thickness versus the time required for the bubble to traverse the probe location for an inclination angle of $2°$. Five test runs are shown, each with increasing bubble size, created by increasing the wall temperature. Increasing the bubble size resulted in wave generation on the interface as observed by a fluctuating signal in run 5 in Figure 2.44 (a).

The spike in the right hand side of each signal is an artifact of the measurement technique. It is caused by the slope of the interface reflecting the light towards the receiving optical fiber at the end of the bubble. The opposite occurs at the leading edge of the bubble, creating a downward spike but the effect is less noticeable. The plateau in the center of the signal is a measure of the micro-layer thickness, the small scatter is attributed to the aforementioned surface waves. The average micro-layer thickness for corresponding plate inclination angle is presented in Table 2.3. The micro-layer thickness was found to be independent of the bubble dimensions, the Reynolds
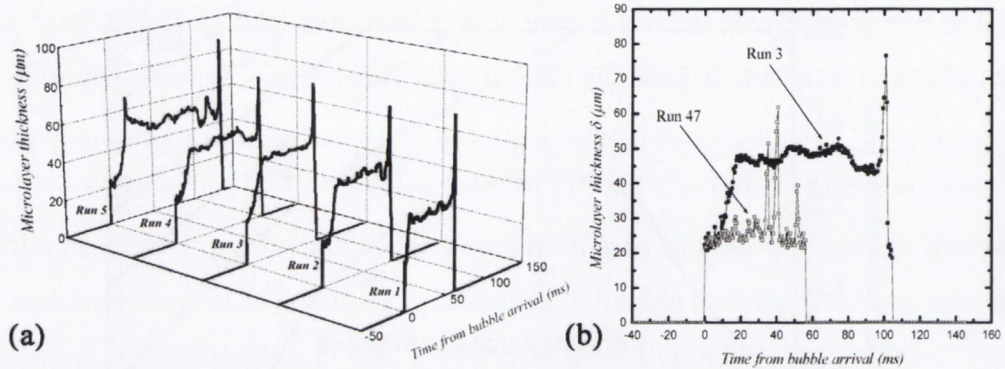
Figure 2.44: (a) Variation in the measured micro-layer thickness with time for five tests with increasing bubble size at 2° plate inclination angle and (b) the effect of surface inclination angle (Run 3 is at 2° and Run 47 is at 15°), Li et al. [72].

Inclination angle, α (deg)	Micro-layer thickness, δ (μm)
2	48.1
5	35.2
10	29.1
15	25.4

Table 2.3: Micro-layer thickness for four inclination angles, Li et al. [72].

number and the Weber number. It did, however, show strong dependence on the plate inclination angle α (see Figure 2.44 (b) for the effect of inclination angle), and the Froude number due to the direct relationship between the Froude number and α as illustrated in Figure 2.45. Li et al. [72] stated that the appearance of waves on the bubble boundary could be caused by a shear driven instability on the micro-layer itself. They identified a threshold value

$$\frac{\mu U_T d_{eq}}{\sigma \delta} \approx 0.4 \tag{2.31}$$

below which no spikes occur in the signal and therefore no surface waves are present.

2.6 Summary

A comprehensive review of the literature has been presented for both free rising and sliding gas and vapour bubbles. Numerous studies have been performed on bubbles
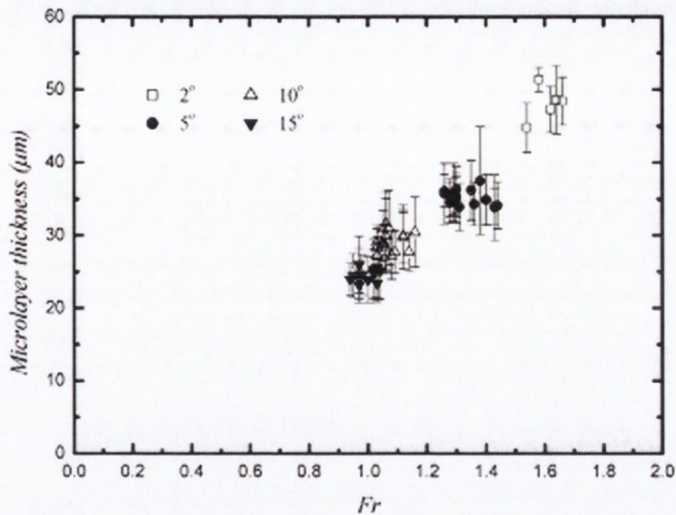
Figure 2.45: The dependence of the micro-layer thickness on Froude number for surface inclination angles of $\alpha = 2°$, $5°$, $10°$ and $15°$, Li et al. [72].

rising in an unbound medium in order to investigate the size, shape, velocity and wake behaviour. We have seen that these parameters are dependent on both the system properties and the bubble volume. The review was then extended to bubbles sliding on unheated, inclined planes. Once again the bubble's behaviour (shape, motion and wake dynamics) were not only dependent on volume and system properties but also on the inclination angle. The shape, size and terminal velocity of gas bubbles sliding under an unheated inclined surface revealed various bubble shapes and the presence of a wetting film between the bubble and the surface on which it slides. The film thickness was influenced by the bubble volume and inclination angle.

A thorough review of the wake behind rising bubbles has been performed. Two distinct wake regions were identified; the near and far wake. The fluid flow around a bubble and the associated wake, both near and far, were highly dependent on the volume and shape of the bubble and on the system properties. Numerous studies of fluid flow around a rising bubble built up a clear picture of how rising bubbles interact with the surrounding fluid. In turn, the effect of the fluid flow on bubble motion was analysed.

Once a thorough understanding of rising and sliding gas bubbles was obtained, the review was extended to include vapour bubbles. These bubbles were either generated

on tubes in a tube bundle or under an inclined heated surface in numerous different fluids. Bubbles were found to increase heat transfer from an adjacent heated surface by impacting and sliding on, or, nucleating from the heated surface. The contribution to the enhanced heat transfer came from three mechanisms; nucleation, fluid mixing (due to the bubble's motion) and heat transfer to the bubble. Heat transfer to the bubble was found to be either through evaporation of the thin liquid layer (the micro-layer) or heat transfer through the surrounding superheated liquid. Numerous studies were performed to elucidate the relative contribution from each mechanism and the thickness of the liquid micro-layer beneath the bubble. Bubble growth rates, shapes and the wake were analysed. The wake behind a sliding bubble was found to enhance heat transfer over an area many times the size of the bubble projected area. The effects were found to last for a long duration.

Although this is an area of increasing interest there is still much work to be done. There have been a number of studies on heat transfer to sliding vapour bubbles and the enhancement in its wake but still little information exists for sliding gas bubbles on inclined heated surfaces. The use of air rather than vapour bubbles and the focus on plate temperatures insufficient to cause boiling have yet to be thoroughly investigated. The aim of the present study is to simultaneously investigate the motion, shape and velocity of sliding air bubbles along with the associated heat transfer. The fluid flow around, and in the wake of these sliding bubbles will be investigated and linked to the heat transfer from the surface. This will further the current understanding of bubble enhanced heat transfer from inclined heated surfaces with the scope to improve heat transfer from such surfaces.

The main gap in the literature concerns the far field/long duration recordings of sliding bubbles; how they move, affect the surrounding fluid and ultimately the heat transfer. How does the presence of the thermal boundary layer affect bubble dynamics? Why do sliding bubbles move the way they do and why do we observe patterns in heat transfer? How do these patterns evolve and how long do their effects last? The purpose of this thesis and acompanying experimental study is to answer these questions through measurement, analysis, observation and interpretation.

Chapter 3

Experimental apparatus

The key goals of the experimental design were:

1. To provide a smooth, solid surface that could be held at accurate and repeatable inclination angles.

2. To be able to heat the surface in a controlled manner.

3. To generate single air bubbles of known, repeatable volume, that could be released onto the surface when required.

4. To record the three dimensional dynamic motion, shape and other physical properties of the air bubble as it slid along the surface.

5. To record the two dimensional heat transfer from the surface synchronised with the recordings of the moving bubble.

6. To measure the fluid velocity, synchronised to surface heat transfer, in a plane in close proximity to the heated surface.

The following is a detailed description of the equipment used to achieve these goals and how they are arranged in the experimental setup. Included is the calibration process, the estimated uncertainty in measurement and experimental procedure.

3.1 Experimental apparatus

The experimental apparatus, or 'rig', is capable of operating in one of two modes. It can either simultaneously record bubble motion and surface heat transfer, referred to as the 'Bubble motion setup', or it can measure the fluid velocity and surface heat transfer[1], referred to as the 'PIV setup'. The experimental apparatus consists of numerous individual elements that operate together during testing such as

- the tilting test tank

- the heated foil and support structure

- the bubble injector

- the visual cameras and lighting

- the infrared camera

- the Particle Image Velocimetry (PIV) system and

- the trigger system

The following sections provide a detailed description of each of these elements.

3.1.1 The tilting test tank

The tilting test tank is the main structural element of the rig. It is used to mount lighting equipment, the test surface, cameras and the PIV laser arm. It can also be tilted relative to the horizontal from 5° to 45°, in increments of 5°. Since all the measurement equipment is mounted to the tank, rotating the tank also rotates the equipment. This means the cameras and lighting etc. are always in the same position relative to the test surface. This part of the rig is comprised of two main parts; the water filled tank and the support stand. This is illustrated in Figure 3.1. The tank itself is an open top cube measuring $420 \times 420 \times 420 \ mm^3$. It is assembled from 6

---

[1]In this setup some properties of the sliding bubble can be obtained directly from the PIV camera images.
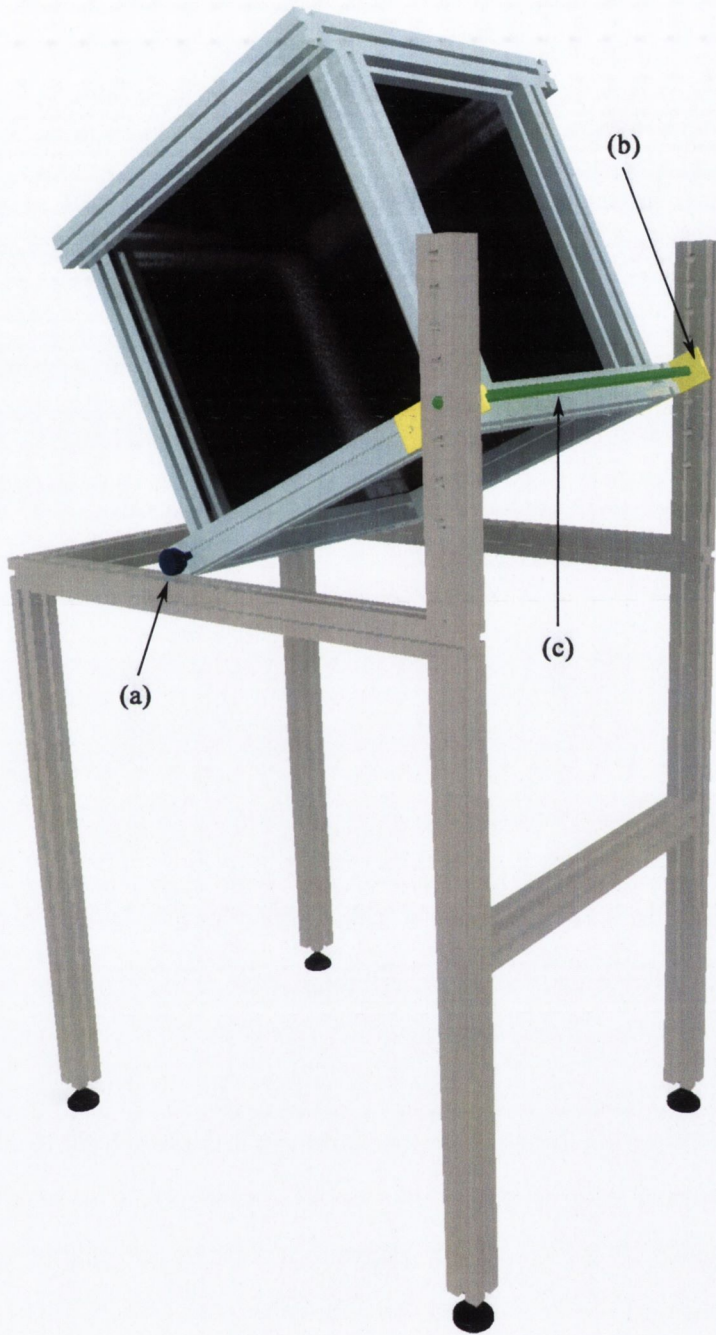
Figure 3.1: Illustration of tilting test tank and support stand. This setup allows the tank and test surface to be rotated to inclination angles of $5-45°$. Indicated are (a) the pivot wheels, (b) the fixing plate and (c) the securing rod.

mm thick plate glass bonded together with silicone adhesive. The tank is supported by $45 \times 45 \ mm^2$ cross section Rexroth aluminium structural members. Two stainless steel wheels are mounted on one end of the tank and two aluminium plates attached to the other. The wheels allow the tank to move freely when being rotated and the two aluminium plates are used to secure it. This is achieved by inserting a rod through the plates and two corresponding Rexroth mounts on the support stand. The heights of the holes in the supports correspond to the inclination angles mentioned above. The tank and surrounding structure sits and rolls on the support stand which is also made from Rexroth. The support stand has adjustable legs that ensure it is accurately leveled before testing commences.

3.1.2 Bubble injection

The bubble injector is a simple design that incorporates an infusion pump, silicone tubing, a 0.5 *mm* diameter needle and syringe, a small aluminium inverted cup, a connecting arm and two control cables. This design was chosen as it allows the user to release a bubble of desired volume upon demand. It also ensures that only one bubble is released at a time. The infusion pump supplies air to the inverted cup via the needle and the user pulls the control cable, this rotates the inverted cup to release the bubble onto the surface. Figure 3.2 illustrates its structure.

It was discovered that using a syringe and needle on their own resulted in difficulty in controlling the release time and bubble volume. Only bubbles of a certain volume could be released from a needle of specific diameter. At large bubble volumes (0.2 and 0.4 *ml*), the buoyancy force of the bubble would outweigh the surface tension between bubble and needle and resulted in a maximum volume obtainable by this method. With the inverted cup design, smaller bubbles are injected into the cup and allowed time to coalesce, then released when required. A small diameter needle is used in order to dispense tiny bubbles (diameter $< 1mm$) which allowed better control of the total bubble volume.

The infusion pump is a medical grade device manufactured by *kdScientific* (KDS 200 CZ) for delivering precise quantities of gas/fluids from a syringe. The operator is

(a) Injector, viewed from above.　　(b) Injector, viewed from below.
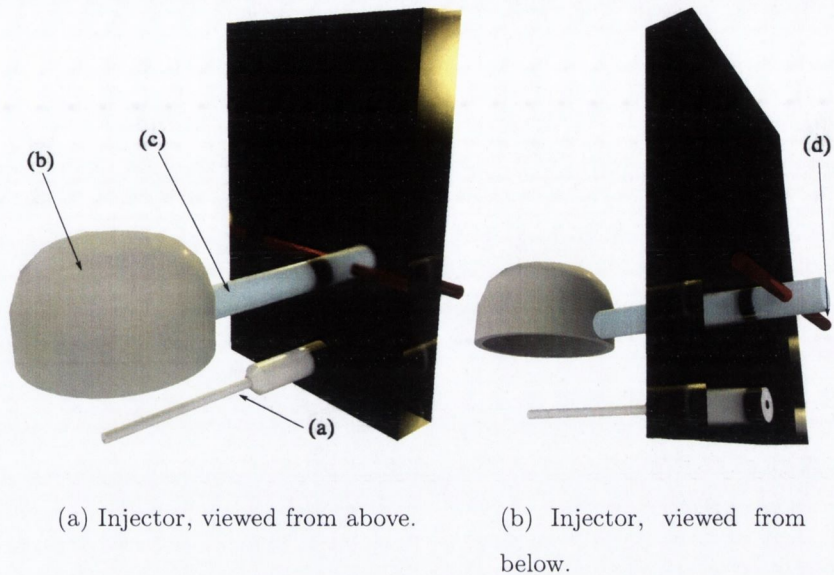
Figure 3.2: Illustration of the bubble injection and release mechanism showing (a) the injector needle, (b) the small aluminium inverted cup, (c) the connecting arm and (d) two control cables (red).

required to provide the machine with the make, model and size of the syringe being used (0.5 *ml* Gastight model 1750). Stored data on the device automatically calculates the volume. A stepper motor rotates a threaded bar which moves a ram to compress the plunger of the syringe, dispensing a volume input by the user. Approximately 1.2 *m* of silicone tubing connects the syringe to the needle positioned below the inverted cup. The cup is mounted on the connecting arm directly above the needle and is rotated to release the bubble by pulling on one of the two cables. The second cable is used to return it to the inverted position. The bubble is released approximately 40 *mm* in the z direction (the axis perpendicular to the surface) from the test surface. From this point it travels approximately 80 *mm* in the y direction (parallel to the surface) before it contacts the heated section and a further 60 *mm* before it enters the measurement area. This is done to negate the effects of the bubble impacting on the surface, allowing the bubble to reach a nominal steady state velocity.

3.1.3 The heated foil

Figure 3.3 shows the heated surface assembly. The surface consists of a 25 μm thick, 130×170 mm^2 AISI 321 stainless steel foil manufactured by Goodfellow. This is bonded along its long side to two copper bars measuring $10 \times 20 \times 170$ mm^3 using silver based electrically conductive glue (Loctite 3888 silver infused epoxy). The glue is applied along the 20×170 mm^2 copper surface using a paint brush. The foil is pressed onto the bars and excess glue and trapped air is removed using a rubber roller. The glue is allowed 48 hours to cure after which it is connected to the power supply and tested to ensure an even current, and hence, an even temperature distribution. Each copper bar has two connections on each end which supply power via 6 mm thick copper cables, from a Lambda d.c. power supply. The power supply is capable of providing 8 volts and 100 amps in either constant voltage or constant current modes. Constant current ensured steady heating of the foil (this forms the uniform wall flux generation boundary condition, assuming no change in local resistance, and therefore current, with temperature). The bars and foil are bolted to two brass bars which are in turn bolted to the foil support structure, made from Peek 1000 plastic. One of the bars forms part of the foil tensioning device. It consists of four screws that pass through springs, then through the brass and into the copper. Tightening the screws compresses the springs which provide foil tension. This is required to take up and slack in the foil as it heats and cools. Peek 1000 was chosen for its structural rigidity and ability to withstand high temperatures (operating temperatures can be in excess of 200 °C). A thermocouple is mounted directly between the copper bar and plastic sheet to monitor the temperature within the test surface structure to avoid any possible overheating.

On the reverse side of the foil is a window made from infrared transparent sapphire glass. This sits on a ledge immediately behind the foil at a distance of 3 mm. This setup is used to trap a small quantity of air behind the foil that heats up when the foil is heated. When it approaches the temperature of the foil it acts like an infrared transparent insulating barrier, ensuring the majority of the heat generated goes into the water. A thermocouple is inserted into the air gap through a 1.5 mm hole drilled in the surrounding structure to measure the temperature. This measured temperature

is used in conjunction with the foil temperature to estimate heat loss through the back of the foil.

A stainless steel sheet measuring $1.5 \times 250 \ mm^3$ is secured to the foil side of the structure. This forms part of the test surface and also stops water entering the rear of the foil. It is sealed around its perimeter with a $3 \ mm$ diameter o-ring that fits into a $2.3 \ mm$ deep groove in the Peek plastic. A sponge rubber strip with a cross section measuring $2 \times 10 \ mm^2$ is bonded to the stainless steel sheet around its inner perimeter. When the sheet is attached to the support structure this forms a seal around the heated foil. The stainless steel sheet is attached to the support structure using 35 M3 taper headed screws. These are countersunk into the stainless steel sheet to avoid obscuring the view of the bubble. Even still, the camera mounted on the side of the tank has to be mounted slightly lower than the surface in order to see the bubble. This was found to have little effect on the measurement of the bubble shape at low angles but required a slight correction in the measured z position of the bubble.

The full assembly is shown in Figure 3.4. The sides of the support structure are made from $6 \ mm$ thick Perspex sheets that are sprayed on their insides with high emissivity paint. This is done to reduce reflections from the surfaces into the infrared camera. They are bonded together using glue which instantly sets when exposed to strong ultra-violet light. A sheet measuring $490 \times 490 \ mm^2$ is bonded to the top of the sides in order to mount the whole structure to the tilting tank. A hole cut in the top allows the infrared camera to view the heated foil. Rexroth bars, $30 \times 30 \ mm^2$ in cross section, provide rigidity to the Perspex and allow it to be firmly bolted to the tilting tank.

3.1.4 High speed video imaging

Two NAC Hi-Dcam II high speed digital video cameras and pci boards are used to record the bubble motion. They are controlled by a dedicated computer using the *Link-sys* camera software. The two cameras, master and slave, are synchronised by a signal cable from the master camera to the slave camera pci board. The two will start
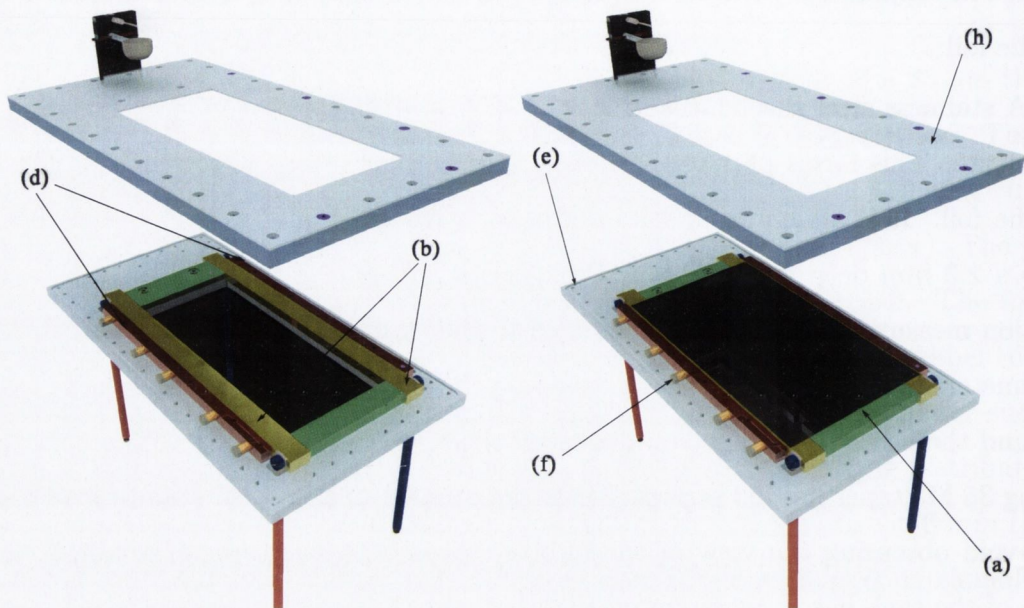
(a) Exploded view; foil omitted, inverted orientation.

(b) Exploded view; including foil, inverted orientation.
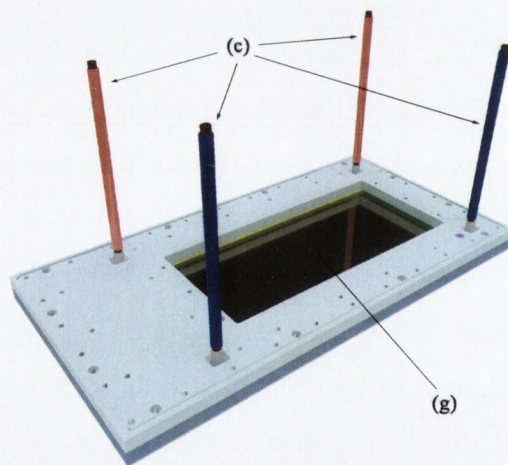
(c) Assembled view of rear surface; correct orientation.

Figure 3.3: Heated surface assembly. This forms the sliding surface for the bubble. Highlighted are (a) the steel foil (the heated surface), (b) copper bars, (c) power supply cables, (d) brass bars, (e) foil support structure, (f) tensioning device, (g) sapphire window and (h) stainless steel sheet.
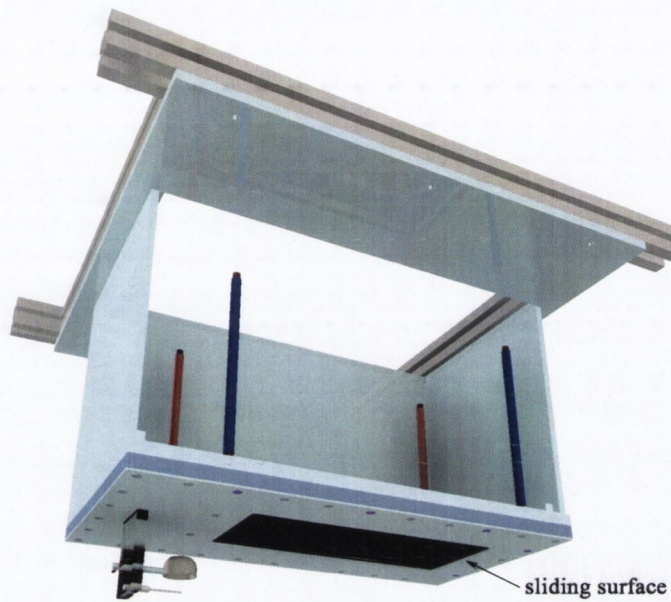
(a) Test section assembly, viewed from below (side panel omitted).
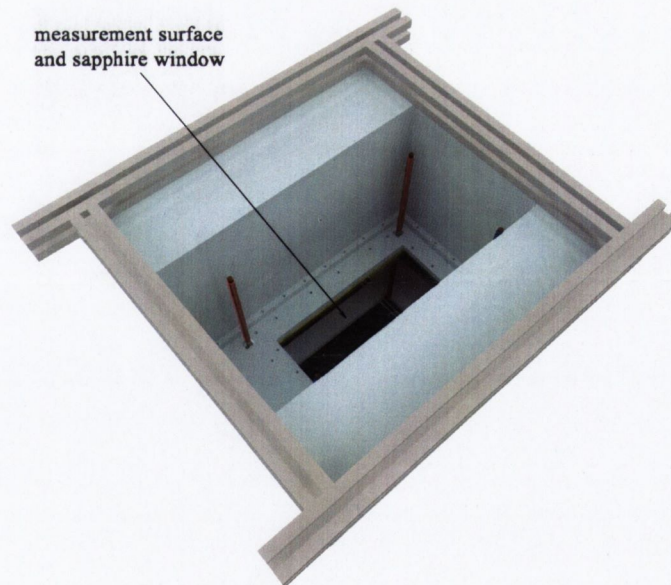
(b) Test section assembly, viewed from above.

Figure 3.4: Illustration of full test section assembly. (a) illustrates the surface on which the bubble slides (b) shows the view of the rear of the foil from which heat transfer is measured. The assembly attaches to the top of the tilting tank shown in Figure 3.1.

recording with a trigger input to the master camera pci board. They are capable of frame rates up to a maximum of 20000 *fps*, dependent on the resolution (maximum of 1280×1024 *pixels*). Although higher frame rates are possible, they require lower resolution due to a limiting data transfer rate. For these experiments, the cameras recorded at 250 *fps* with an exposure time of 0.002 *s*. Short exposure times are required to ensure a sharp image of the bubble is recorded. Longer exposure times would result in the bubble being blurred in the image, this is commonly referred to as motion blur. The chosen exposure time is a compromise between reducing motion blur and the limits of lighting intensity. The shorter the exposure, the higher the intensity must be e.g. if you half the exposure time, you need to double the lighting intensity. The chosen frame rate was found to be suitable to record the bubble in sufficient temporal detail.

The cameras are each mounted on Manfrotto traversing platforms to allow fine adjustment of their position. These platforms are mounted to stainless steel support structures that allow three dimensional positioning within a certain region. The support structures are mounted directly to the tilting tank as illustrated in Figure 3.5.

The cameras are fitted with two identical Nikon *Nikkor* 50 *mm* f/1.4 af-d lenses. These lenses were chosen as they have extremely low image distortion. This means that straight, parallel lines recorded remain straight and parallel in the image. Some lenses suffer from pincushion or barrel distortion, or a complex combination of the two which results in straight lines becoming curved or even wavy (discussed further in Chapter 4). The lens aperture controls the amount of light allowed to reach the sensor. A larger apertures allow more light to reach the sensor but smaller apertures ensures greater depth of field[2]. The lens aperture is set to f/5.6 because the bubble, when it zig-zags, moves closer and further away from the slave camera as it slides along the

---

[2]Depth of field refers to the range that will be in focus for one particular focus setting. Focus is measured from the lens to the subject and the depth of field is plus and minus a percentage of this. A large depth of field means objects closer or further away from the subject will be in focus, while a small depth of field ensures only the subject (or part thereof) will be in focus, everything closer or further will be out of focus.
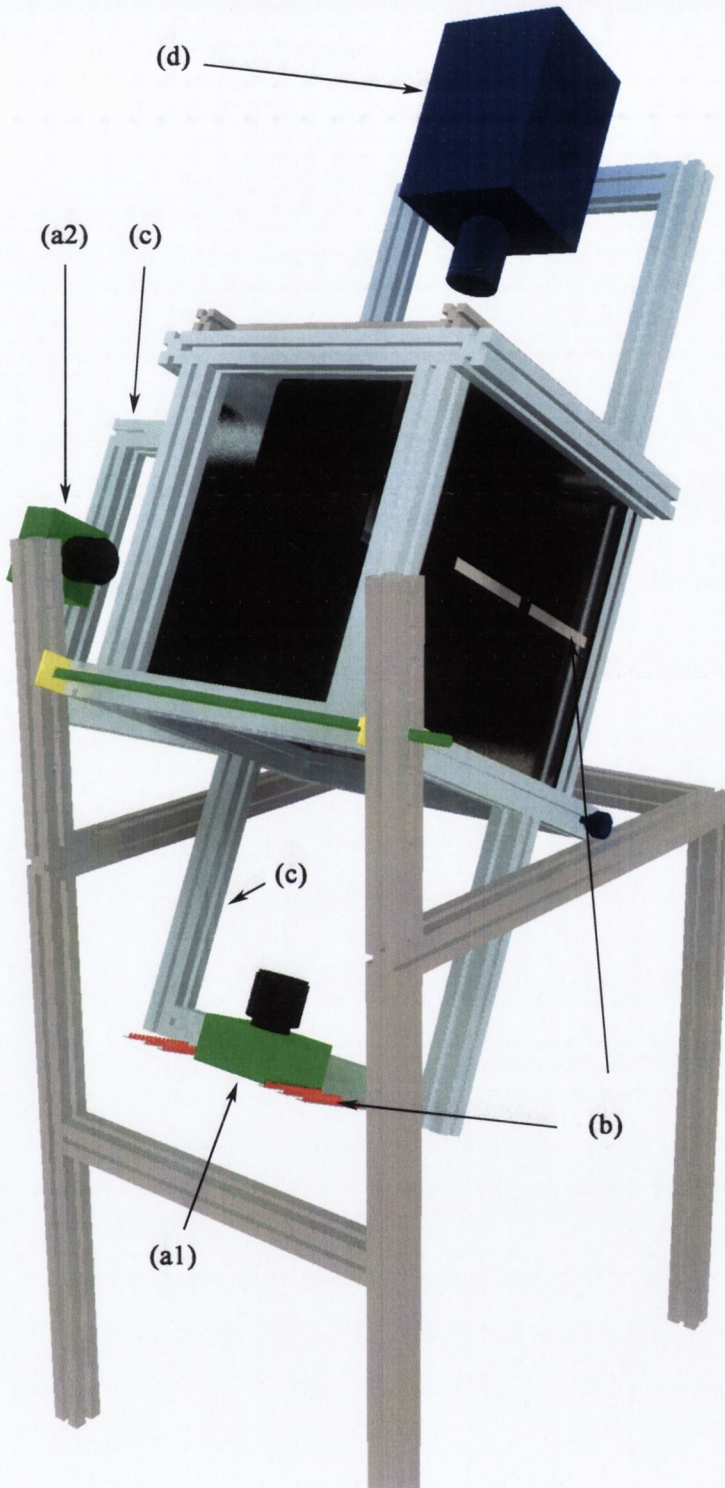
Figure 3.5: Illustration of the visual cameras and lighting system. (a1) master and (a2) slave visual cameras, (b) High intensity lighting, (c) positioning system (×2) and (d) Infrared camera.

plate. Additionally a lens is at its sharpest somewhere in the middle of the range of apertures (f/5.6 to f/8). A suitable compromise between depth of field and lighting was achieved and the bubble is observed to remain sharp and in focus over the test surface.

Illumination of the test area is provided by 8, 15 bulb light emitting diode (LED) strips. Two are positioned pointing through the tank at the slave camera, the other six are positioned around the master camera pointing directly at the heated surface. All the lights are powered by an 18 volt power supply set to 14.8 volts. This is the maximum allowable voltage before damage occurs to the lighting. LED bulbs were chosen for their high light intensity at low temperature. Ordinary incandescent bulbs would flood the test area with infrared radiation, affecting the foil temperature. This would be difficult to account for. In addition to the camera, all the lighting is fixed to the tilting rig. This means the camera and lighting setup does not need to be adjusted when changing inclination angle. This was incorporated into the rig for additional flexibility although only one inclination angle was tested in the present study.

Ideally the image of the bubble should have a dark outline, this is required by the computer code to aid in identifying the bubble. Various adjustments need to be made to the intensity and angle of lighting in order to achieve this. The addition of a sheet of tracing paper between lighting and bubble created a more diffuse light source, greatly enhancing the outline of the bubble.

3.1.5 Infrared thermography

A FLIR SC6000 high resolution, high frame rate infrared camera was used in these experiments. It is used in conjunction with a high speed data recorder (HSDR) and camera controller computer. FLIR's SC6000 camera controller and RDac frame grabber software were both used to acquire the data. The camera has a 640 × 512 pixel focal plane array (FPA) sensor which is vacuum sealed in a cooler assembly. A stirling motor cools the sensor to approximately 78 K to reduce the effects of noise on the image. If the assembly is not cooled the sensor would be flooded with infrared radiation from its own surroundings. The FPA is sensitive in the 3-5μm range of infrared light.

Data are transferred to the HSDR via a 50 *Gb/s* ethernet connection while control is achieved through a USB connection. The frame rate can be controlled by the software or from an external pulse generator, as in this study.

The camera is set to record an image that is 296×512 pixels in size. It is offset, in order to use the central region of the sensor, by 196 pixels in the x direction[3]. This size was adequate enough to cover the entire heated foil surface and results in 151552 discrete temperature measurements per frame. The frame rate is set to 250 *fps* to match that of the visual cameras. The camera has a 14-bit sensor meaning that each pixel can detect between 1 and 16384 discrete levels, or counts. An integration (exposure) time of 0.95 *ms* was chosen so that the highest temperature recorded (no more than $40\,°C$) corresponded to a count value of approximately 15000. A longer integration time results in more light reaching the sensor per frame, which can result in saturation while a shorter integration time increases the signal to noise ratio. This setup ensures the optimum signal to noise ratio.

For every recording, the camera saves seven files, each with the file extension `.sfmov`, `.pod`, `.scg`, `.sbp`, `.sco`, `.cal` and `.inc`. The `.sfmov` file contains the raw infrared measurement data, in counts, from the camera. The `.pod` file contains data on the exact time of each frame obtained from the clock in the HSDR computer. The `.scg`, `.sco` and `.sbp` are the gain, offset and bad pixel files respectively. These, along with the `.cal` and `.inc` are related to sensor calibration and are explained in Section 3.2. After each recording, all the files are loaded into FLIR's ExaminIR software. The raw data in the `.sfmov` file is converted to temperature and exported as a `.csv` (comma separated value) text file containing an array of temperature values ready for import into Matlab.

The camera is mounted onto a frame made from $45 \times 45 \ mm^2$ Rexroth aluminium members. The frame is mounted directly to the tilting tank to ensure image consistency at all inclination angles. The camera is offset in the x-direction by 60 *mm* and positioned at an angle relative to the y-axis. This is done to prevent the camera

---

[3]If the chosen resolution is lower than the maximum the user can decide what region of the sensor to use. In this case the central region was used as lenses generally project the sharpest image towards the center of the sensor.
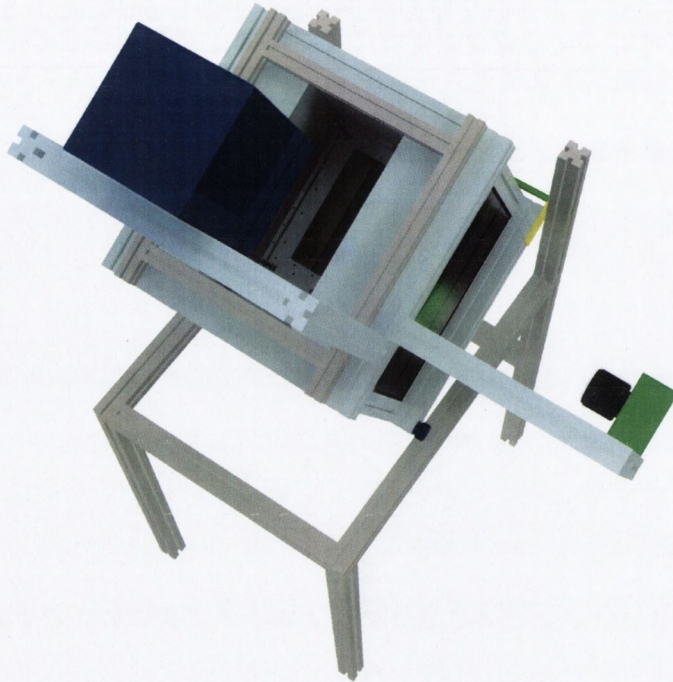
Figure 3.6: Illustration of the infrared camera mounting arrangement as viewed from above. This shows the infrared camera's view of the surface.

observing its own sensor in the sapphire window, which is at such a low temperature it appears in the image (although a small reflection can still be seen on one side of the image, see Figure 5.1 in Chapter 5). This is not in the path of the bubble and as such does not interfere with the measurement area. This section of the rig is illustrated in Figure 3.6.

3.1.6 Particle image velocimetry (PIV)

The PIV system comprises a laser system, high speed video camera and data acquisition and processing software. The fluid must also contain minute particles referred to as seeding or tracer particles in order for the flow to be illuminated by the laser in a chosen plane. The manufacturer, LaVision, supplies all components and the data processing software, DaVis. The configuration is set up as in Figure 3.7. The principle of PIV is based on being able to track minute particles that are assumed to follow the flow. The displacement of these particles per camera frame gives their, and hence the fluid's, velocity. This can be done over a relatively large area providing single

plane, two dimensional fluid velocity. Some systems extend this basic principle to single plane, three component fluid velocity by using two cameras at an angle to each other and the laser sheet.

The laser system includes a Quantronix Darwin Duo high repetition Nd:YLF laser (neodymium: yttrium lithium fluoride, $\lambda = 527\ nm$, 0.1-0.3 J/s at 1000 Hz). This consists of two individual Darwin lasers and a beam combination system fitted in one laser body, allowing high frequency pulses with minute time separation ($\Delta t \approx 6\mu s$, with each pulse lasting in the region of a few nano seconds). An optical arm guides the laser from the laser head to the experimental apparatus. It consists of metal tubing fitted with optics to guide the beam to the arm head where a cylindrical mirror converts the beam to a thin light sheet. The light sheet is then aligned in a plane parallel to the foil surface which forms the measurement plane. It is focused to achieve the thinest possible sheet at the area corresponding to the measurement plane, this thickness is in the order of approximately 1.5 mm.

Seeding is critical to accurate PIV. There are two requirements of seeding particles: (a) they should faithfully follow the flow and (b) they should scatter the incoming laser light. Polyamid particles with a nominal diameter of $50\mu m$ were used in the current study (Dantec dynamics 9080A5011). The seeding is specifically designed for flows in water as they are approximately neutrally buoyant, this ensures that they will not float to the surface or sink to the bottom of the tank, gathering on the glass, obstructing the camera's view of the surface. In order to remove inevitable variation in the seeding particle density, a large amount of seeding were mixed with approximately 250 ml of water an allowed to settle for 24 hours. Over this time the seeding that did not closely match the water density either sank or floated. The fluid and seeding from the central region is removed with a syringe and put into a second container where they were allowed to settle once more for 24 hours. This process is repeated three times in total. The remaining seeding particles are then mixed with the bulk fluid until distributed evenly.

A high speed CMOS camera (Photron HighSpeedStar 6, 1024×1024 *pixels*, 12-bits per pixel) is used to record the illuminated seeding particles within the light sheet. For the present study, recording rates of 125 Hz were used to capture both
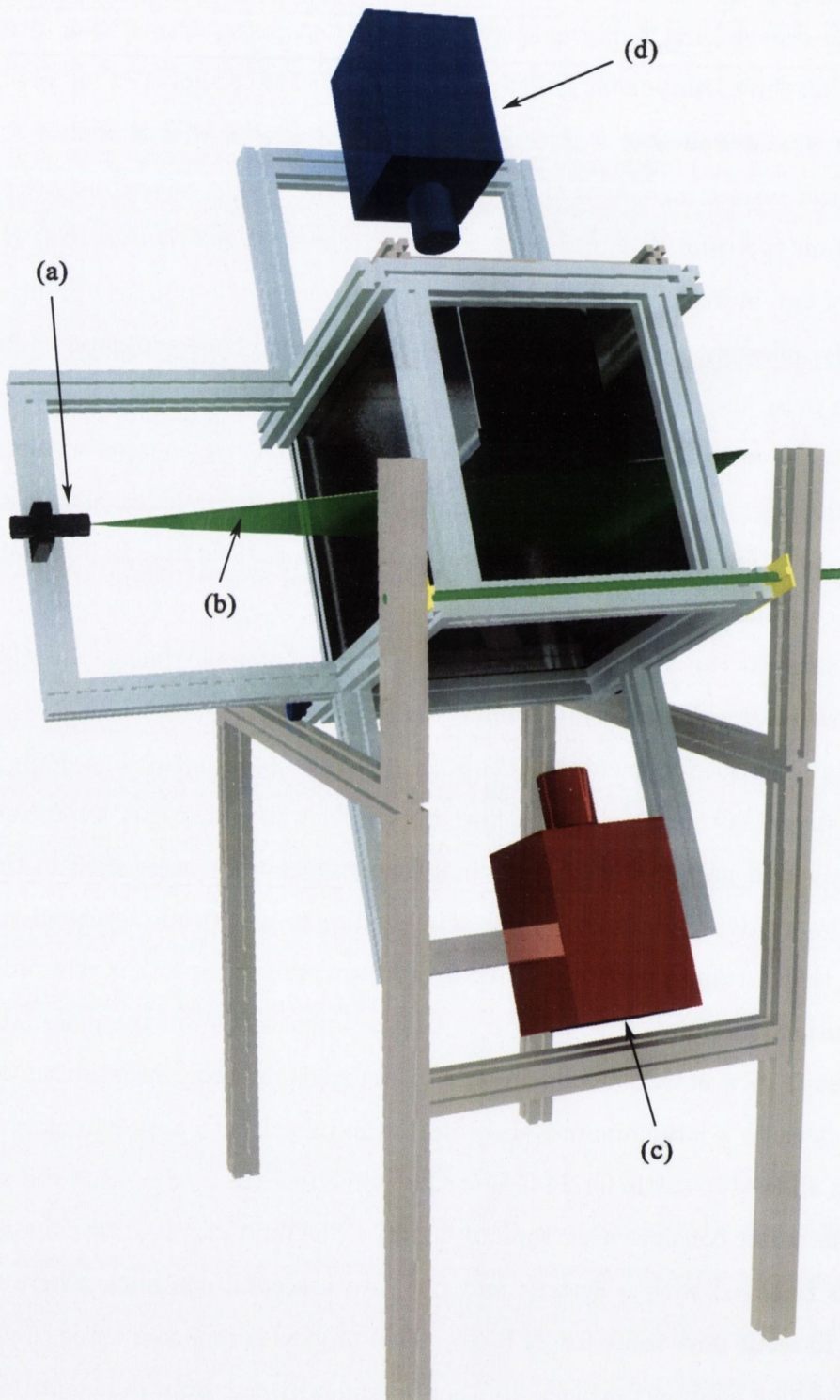
Figure 3.7: Illustration of PIV system as used during testing. Highlighted are (a) the laser head, (b) the illumination plane, (c) the PIV high speed camera and (d) the infrared camera.

the high velocity fluid motion during bubble passage and the lower velocity motion in the far wake (i.e. up to 15 seconds after bubble passage). The chosen frame rate is a compromise between high temporal resolution and long duration recording. The system is set up to record one laser pulse per frame although the results are processed differently depending on whether the near or far wake is to be analysed. This is due to the large velocity differences observed between the two conditions. This is discussed in detail in Chapter 4, Analysis.

3.1.7 Triggering

The trigger ensures that all the relevant systems commence recording at the same time. A frequency generator is used to trigger recording for both experimental setups, i.e. the Bubble motion setup and PIV setup.

The frequency generator is set to output 250 *Hz*. The signal is output from the generator through a BNC connector and coaxial cable. It passes through a simple switch and is then connected to the 'sync. in' connector on the back of the infrared camera. The camera controller software sets the camera to external trigger so it records one frame on every rising edge of the trigger signal. Another BNC connector on the back of the infrared camera ('int. active') outputs a signal whenever the camera sensor is active (i.e. whenever the camera is recording a frame), this will be 250 *Hz* in this case. A coaxial cable connects this BNC to the trigger input on the master visual camera PCI board. The visual cameras begin recording on the rising edge of the signal. Connecting the switch triggers the two systems to record simultaneously.

For the PIV setup, the signal from the thermal camera is connected to the trigger input cable on the PIV input board. Once again, connecting the switch initiates synchronised recording.

3.2 Calibration & uncertainty

The infrared camera requires both calibration and what is referred to as a non uniformity correction (NUC). Calibration allows conversion from counts to temperature

and the NUC ensures that each pixel of the FPA behaves identically.

The NUC requires a highly uniform temperature source in order to be effective. If this procedure is not performed, placing a uniform temperature source in front of the camera will result in a non-uniform temperature recording. The source needs to be heated above the maximum temperature that will be observed by the camera and then cooled to its lower limit. The high temperature source is placed directly in front of the lens and an image is taken, the same is done with the low temperature source. The FLIR 'Rdac' software then calculates a gain, bad pixel, and offset correction for the sensor (`.scg`, `.sbp` and `.sco`). When the correction is applied, each pixel should now read the same value when a uniform temperature source is placed in front of the camera. After the NUC is performed, the camera must be calibrated.

Calibration is performed in situ to ensure the effects of foil emissivity and transmission through the sapphire window are accounted for. The camera is set to the exact same settings as during testing and the water bath is heated to 55 °C. The water is constantly being circulated using a pump to ensure uniform water temperature. A certified RTD (resistance temperature detector) master thermocouple probe is used as a temperature reference (see Appendix A for calibration cert.). The foil surface is assumed to be at the same temperature as the adjacent water. This is believed to be a valid assumption due to the thickness of the foil and the insulating effects of the air gap behind it. The camera is set to average over ten frames in order to smooth out small time dependent fluctuations. Once the system has reached steady state the count value of an interrogation window is recorded. The interrogation window is selected over the parts of the foil that contain no camera reflections, as previously mentioned. The water bath is cooled by 5 °C, allowed time to reach steady state, and a second count value is recorded. This is repeated down to a value of 10 °C (achieved by adding ice to the water bath). The software then saves this data as a `.cal` and `.inc` file ready to be applied to the test data. The calibration is applied to the results to convert from counts to temperature. The calibration curve for the infrared camera is shown in Figures 3.8 with the corresponding cubic curve fit described by equation 3.1. Included in the figure are the 95% confidence limits. At 35 °C, the uncertainty in the regression curve is 281 counts. This corresponds to 0.035% of the total counts recorded
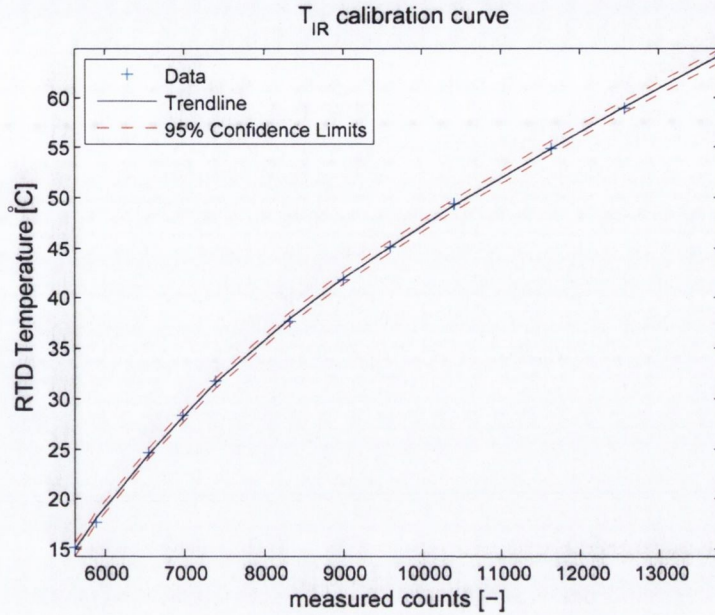
Figure 3.8: Calibration curve for infrared camera, including 95% confidence limits and cubic curve fit.

at this temperature.

$$y = 5.46 \times 10^{-11}x^3 - 1.95 \times 10^{-6}x^2 + 0.03x - 88.55 \qquad (3.1)$$

The two K-type thermocouples, used to measure the bulk water temperature and insulating air temperatures respectively are calibrated in a smaller constant temperature water bath against the same RTD master thermocouple. Measurements are taken every 5 °C from 20 to 55 °C. The calibration curve, regresssion fit and 95% confidence limits for the air and bulk water thermocouples are shown in Figure 3.9 and 3.10 respectively. The uncertainty in the regression curve (with 95% confidence limit) for T_{bulk} at 35 °C is 0.097 °C. The uncertainty in the regression curve (with 95% confidence limits) for T_{air} at 35 °C is 0.074 °C. Equation 3.2 and 3.3 show the equations for a linear curve fit to each calibration data set. These are for T_{air} and T_{bulk} respectively.

$$y = 0.997x + 0.45 \qquad (3.2)$$

$$y = 0.99x + 0.56 \qquad (3.3)$$
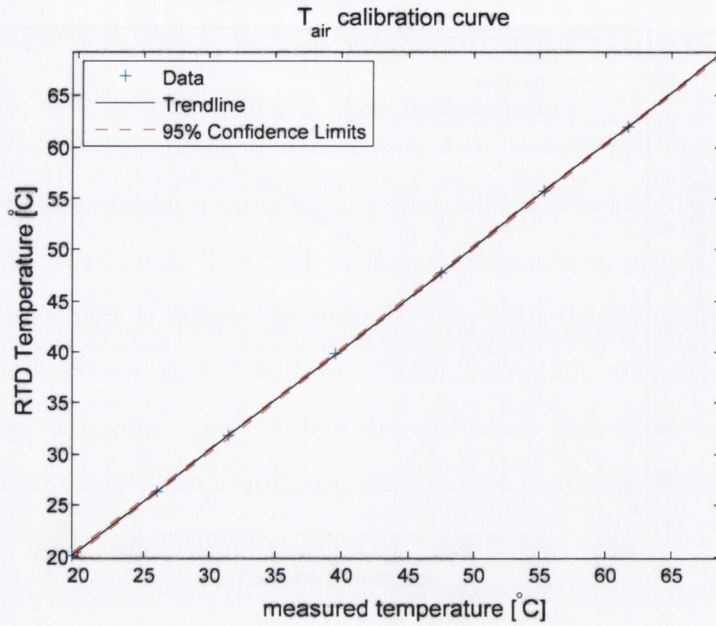
Figure 3.9: Calibration curve for air thermocouple, including 95% confidence limits and linear curve fit.
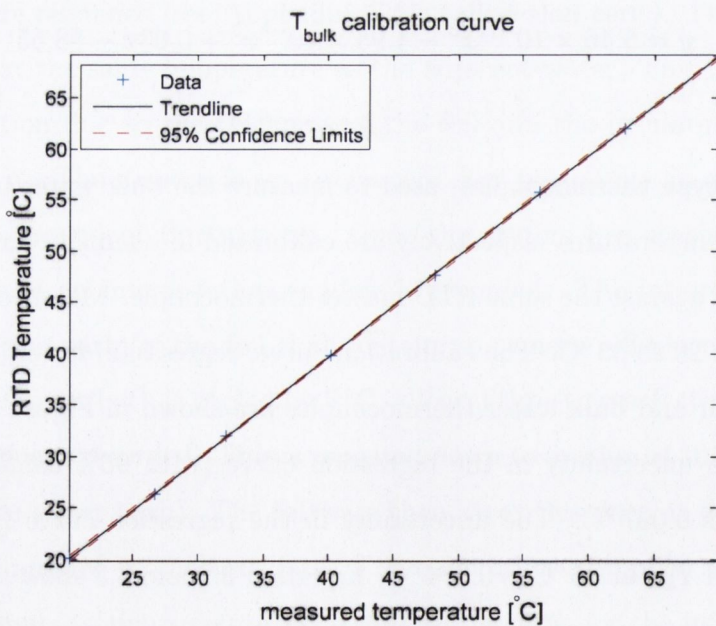
Figure 3.10: Calibration curve for bulk water thermocouple, including 95% confidence limits and linear curve fit.

The uncertainty in predicting the bubble shape from digital images is approximately 1 *pixel*. This corresponds to the error in the boundary detection code. After applying the calculated scaling factor, this equates to ± 0.226 *mm*. The uncertainty in the triggering system is at maximum one camera frame or $1/framerate$. This corresponds to the maximum delay in the visual cameras detecting the trigger input. At 250 frames per second this is calculated to be 0.004 *s*.

Processing PIV images is a statistical technique, therefore numerous approximations are used to eliminate bad vectors. Vector filtering is carried out after each pass of the correlation algorithms, eliminating vectors that are not within $2 \times r.m.s.$ of neighbouring vectors. The laser sheet thickness is approximately 1 *mm*, providing measurements that are a small, but significant, percentage of the bubble diameter, thus the velocity is averaged across the sheet thickness. Background noise is subtracted from each image prior to analysis to provide a clean image. The PIV system has difficulty detecting velocity vectors when there are large differences in velocity throughout the flow. For this reason, depending on whether the bubble was present in the image or whether the bubble had passed, different time separations between correlation frames were used (corresponding to 0.008 *s* and 0.04 *s*). The main function of the PIV measurement technique in the present study is to identify coherent fluid structures in the wake of the sliding bubble. With this in mind, the technique is considered sufficiently accurate.

Table 3.1 presents a summary of each measurement device and it's associated uncertainty. The individual errors propagate through data reduction equations (e.g. calculation of the heat transfer coefficient) contributing to an overall uncertainty in the presented values. The following describes the error propagation through the main parameters and their overall uncertainty.

The uncertainty in bubble position contributes to the uncertainty in velocity. The overall uncertainty is calculated from that described by Coleman & Steele [73] as

$$\left(\frac{U_v}{v}\right)^2 = \left(\frac{U_s}{s}\right)^2 + \left(\frac{U_t}{t}\right)^2 \tag{3.4}$$

Measurement	Symbol	Uncertainty	Device
Infrared camera	T_s	±0.04%	FLIR SC6000
Bulk fluid temperature	T_∞	±0.2%	T-type
Air gap temperature	T_{air}	±0.2%	T-type
Foil thickness	δ	±5%	Mutitoyo calipers
Displacement	s	±0.005%	Visual camera
Current	I	±0.1%	Lambda power supply
Width	W	±0.0001%	Mutitoyo calipers
Length	I	±0.0001%	Mutitoyo calipers
Time	t	±0.1%	Assumed

Table 3.1: Uncertainties in measured variables.

$$\left(\frac{U_v}{v}\right)^2 = (0.005)^2 + (0.1)^2 \tag{3.5}$$

$$\frac{U_v}{v} = 0.011 \tag{3.6}$$

The uncertainty in the heat transfer coefficient, h, involves the contribution from from each measurement device used to calculate h in the following equation

$$h = \frac{q}{A\left(T_s - T_\infty\right)} \tag{3.7}$$

where the heat generated is equal to $I^2 R$, the resistance is $\rho l / A_{cs}$ and the area is $L \times W$, resulting in

$$h = \frac{I^2 \rho}{L^2 \delta \left(T_s - T_\infty\right)} \tag{3.8}$$

the overall uncertainty thus is calculated as (see Coleman & Steele [73])

$$\left(\frac{U_h}{h}\right)^2 = (2)^2 \left(\frac{U_I}{I}\right)^2 + (2)^2 \left(\frac{U_L}{L}\right)^2 + \left(\frac{U_\delta}{\delta}\right)^2 + \left(\frac{U_{T_s}}{T_s - T_\infty}\right)^2 + \left(\frac{U_{T_\infty}}{T_s - T_\infty}\right)^2 \tag{3.9}$$

Substituting in the values of the individual errors results in

$$\left(\frac{U_h}{h}\right)^2 = (2)^2 (0.001)^2 + (2)^2 (0.0001)^2 + (0.05)^2 + \left(\frac{0.04}{40-20}\right)^2 + \left(\frac{0.2}{40-20}\right)^2 \tag{3.10}$$

$$\left(\frac{U_h}{h}\right)^2 = 4 \times 10^{-6} + 4 \times 10^{-8} + 2.5 \times 10^{-3} + 4 \times 10^{-6} + 1 \times 10^{-4} \tag{3.11}$$

$$\left(\frac{U_h}{h}\right)^2 = 2.6 \times 10^{-3} \tag{3.12}$$

resulting in an overall uncertainty of

$$\frac{U_h}{h} = 5.1\% \tag{3.13}$$

at a temperature difference of $20\,°C$.

The uncertainty in the temperature difference is caculated as

$$U_{\Delta T} = 2b_{\Delta T} \tag{3.14}$$

where $b_{\Delta T}$, the systematic error in ΔT, is calculated as

$$b_{\Delta T}^2 = \left(\frac{\partial \Delta T}{\partial T_s}\right)^2 (b_{T_s^2})^2 + \left(\frac{\partial \Delta T}{\partial T_\infty}\right)^2 (b_{T_\infty^2})^2 + (2)\left(\frac{\partial \Delta T}{\partial T_s}\right)\left(\frac{\partial \Delta T}{\partial T_\infty}\right) b_{T_s} b_{T_\infty} \tag{3.15}$$

given $b_{T_s T_\infty}$ is

$$b_{T_s T_\infty} = (0.05)(0.05) \tag{3.16}$$

Subbing in values for the individual errors results in

$$b_{\Delta T}^2 = (-1)^2 (0.17)^2 + (1)^2 (0.17)^2 + (2)(-1)(1)(0.0025) \tag{3.17}$$

$$b_{\Delta T}^2 = 0.052 \tag{3.18}$$

or

$$b_{\Delta T} = 0.22\,°C \tag{3.19}$$

therefore $U_{\Delta T} = 0.44\,°C$.

The error in the Reynolds number is a result of the detection limit of the image analysis software. Neglecting the errors in the fluid properties, μ & ρ, the error in the Reynolds number is calculated as

$$\left(\frac{U_{Re}}{Re}\right)^2 = (0.011)^2 + (0.005)^2 \tag{3.20}$$

$$\left(\frac{U_{Re}}{Re}\right) = 1.2\% \tag{3.21}$$

Table 3.2 presents the uncertainties in the main test paramaters.

Parameter	DRE	Uncertainty
Velocity	$v = x/t$	1.1%
Heat transfer coefficient	$h = q/A\Delta T$	5.1% @ $\Delta T = 12\,^\circ\mathrm{C}$ and 11.3% @ $\Delta T = 2\,^\circ\mathrm{C}$
Temperature difference	$\Delta T = T_s - T_\infty$	$\pm 0.22\,^\circ\mathrm{C}$
Reynolds number	$Re = \rho U d/\mu$	1.2%

Table 3.2: Uncertainties in calculated parameters.

3.3 Experimental procedure

The experimental procedure is basically the same for both the Bubble motion and PIV setup. The tilting tank is first set to the desired angle, $30\,^\circ$ to the horizontal. The tank is filled with tap water, no attempt is made to remove any contaminants that may be present on the micro scale (i.e. surfactants).

An electrical heating element is then immersed in the water and turned on. It was found that untreated water would eventually coat all submerged surfaces in a fine layer of tiny bubbles (approximately 1 mm in diameter). These both obscured the view of the test section and affected heat transfer from the surface. The bubbles are the result of dissolved gas in the water being released over time. When the water reaches approximately $70\,^\circ\mathrm{C}$ the heater is powered off and the bubbles are removed from the surfaces. The water is allowed to cool and the process is repeated until the presence of the bubbles at an acceptable level. This would usually require approximately four cycles of heating and cooling. This can be achieved much quicker by boiling the water but this was not possible to do in the current setup as the high temperatures may damage the apparatus, thus the water temperature was not allowed to exceed $70\,^\circ\mathrm{C}$. The presence of the heating element itself, when powered on, was found to remove a large amount of dissolved gas. After the process is complete the water is allowed to cool to room temperature.

The rig is then either set up in its Bubble motion or PIV configuration. For heated tests, the current to the foil is set to 70 $amps$ and the temperature allowed to reach steady state. Ten minutes was allowed for this to occur after which the desired bubble volume is dispensed into the inverted cup. The trigger switch is connected commencing simultaneous recording and the bubble is released, both the air and bulk

fluid temperature are noted. After the test is complete, the foil power is removed to reduce excessive bulk water heating while preparations are being made for the next test. When ready, it is powered on and another ten minutes is allowed to pass before the next test commences. The procedure is the same for non-heated tests without any foil heating.

The next chapter describes how the raw data are processed into a presentable form. Images from the visual cameras have to be processed to identify the bubble and its associated dynamics. Thermal images are processed to remove image distortion and a discrete energy balance performed to quantify the surface heat flux and heat transfer coefficient on the fluid side of the foil. The velocity magnitude and vorticity are calculated from PIV vector maps. Once processed, both bubble motion and fluid velocity results are then temporally and spatially aligned with heat transfer data.

Chapter 4

Analysis

A significant amount of post processing is required in order to properly present the acquired data. Photographic images recorded using the visual cameras are analysed to identify the bubble from the background. Once the bubble is identified, various characteristics of the bubble are calculated including shape, position and velocity. This is done for the images from both cameras and the results are then scaled and combined to reveal the shape in two planes and the position in three dimensions. Successive images are analysed in this way to reveal the time varying bubble characteristics. The temperature calibrated data from the infrared camera is processed to remove distortion caused by the lens. The data are then processed to account for conduction losses to the air, radiation from both sides of the foil, lateral conduction effects within the foil and thermal storage effects due to its specific heat capacity. The results from the thermal and visual cameras are temporally and spatially combined providing accurate visualisation of the position and shape of the bubble relative to heat transfer effects on the foil.

For fluid flow measurement, the images from the PIV camera are post processed in LaVision's purpose built software, DaVis. These are exported as vector maps of the instantaneous velocity field in a plane parallel to the foil. The vector maps are imported into Matlab, converted to velocity magnitude and vorticity for presentation, then combined with thermal maps in a process similar to the visual cameras. The result of this reveals how fluid dynamics affect surface heat transfer. The precise

details of how this is achieved are described below.

4.1 Visual image processing

Sequences of images from the master and slave visual cameras are exported in the form of rgb[1] bitmaps (file extension *.bmp*) from the high speed camera computer. This format was chosen because the images are uncompressed, thus maintaining all the detail of the original image. They are imported into Matlab individually where they are processed by code purpose written by the author. Some basic information is required prior to processing:

- The user must input the first and last file number, Im_1 and Im_n, in the sequence. Both these images must contain a full image of the bubble. These are used to calculate the scaling factors, $Scale_S$ and $Scale_M$.

- The code requires a reference background image, Im_b, the bubble must not be present in this image. This is used to identify the bubble in each test image, Im_1 to Im_n.

- The frame rate, f, and image storage directories must be input. These are used to calculate the time separation between images, required for velocity and acceleration calculations and to locate the files for processing.

- Information regarding the test parameters must be input such as plate inclination angle, date, bubble volume, test number, test type etc. for easy retrieval of data.

After inputting the data, the code is run on a sequence of images with minimal input from the user. Images are first rotated to conform with the chosen x, y and z axes. The code then identifies the bubble in each image and calculates various characteristics. Figure 4.1 illustrates the axes convention chosen for the current study.

---

[1] rgb refers to the way the colour image is stored; each pixel contains a value of red, green and blue and their relative contribution makes up the colour image.
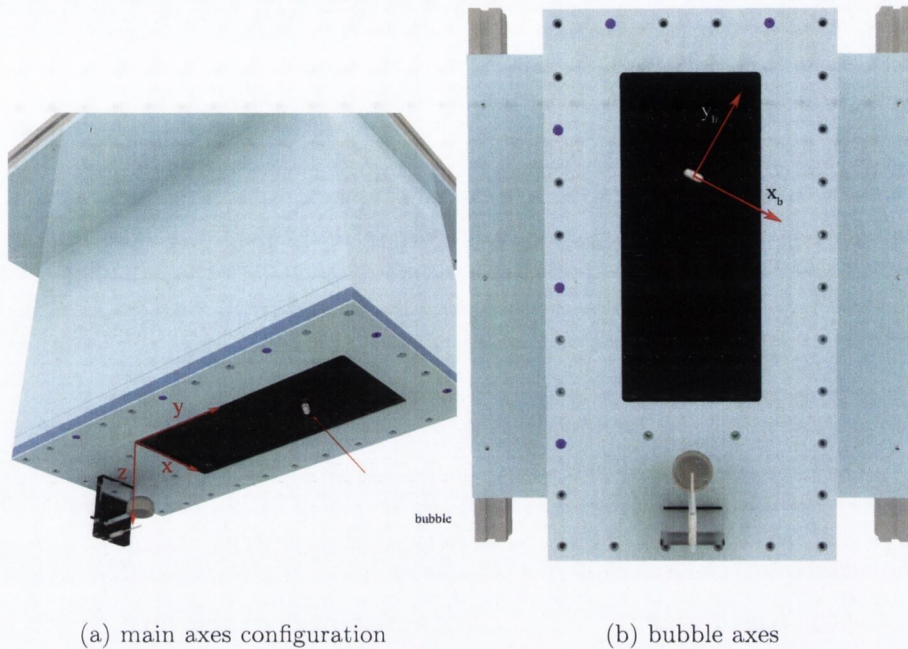
(a) main axes configuration   (b) bubble axes

Figure 4.1: Chosen axes convention for the current study. Included are the x, y and z axes and the bubble axes x_b and y_b (z_b is towards the viewer).

4.1.1 Orientation

The first step in the process is to align the images to coincide with the chosen x, y and z-axes. The master camera images are processed first. The user is asked to input two points on the master camera image that coincide with the chosen y-axis (chosen in this case to be pointing in the direction of decreasing depth in the plane parallel to the surface), these points should be as far apart as possible in order to reduce the relative error. There are visual markers in each image that aids in doing this. The code then works out the angle between the chosen y-axis and the current y-axis, denoted the master camera correction angle, $\theta_{c,M}$ (the slave camera is discussed later). Every image that is loaded from the master camera is rotated by $\theta_{c,M}$ before being worked on by the rest of the code. This means that when the code identifies the bubble in an image it will already be in the correct orientation relative to the y-axis. The x-axis is then located at 90° to this.

Once the master camera images have been processed to identify the bubble (as described in the next section), the slave camera correction angle, $\theta_{c,S}$, is calculated in

the same manner as described above. The images are then rotated to coincide with the chosen, mutually perpendicular, y and z-axes. This work is performed in a purpose written program called `Visual Image Analyser` in Matlab.

4.1.2 Locating the bubble

Both an image containing the bubble, Im_{bubble}, and a background image, Im_b, are loaded into the `Visual Image Analyser` program and rotated. The images are imported at their original resolution of 1280×1024 *pixels*. Processing hundreds of images at this size is computationally intensive (therefore time consuming) so the user is asked to input a bounding box around the bubble approximately three times its width and height with the bubble at its center. The coordinates of this box, along with the full image, are then passed to the `Locater` function which is used to locate the bubble. Before any analysis is performed the full images are reduced to the size dictated by bounding box coordinates.

The `Locater` function works by comparing Im_{bubble} with its corresponding area in Im_b. Mathematically this is achieved by dividing the numerical values of the background image with that of the bubble image, resulting in the quotient, Q, where

$$Q = \frac{Im_b}{Im_{bubble}} \tag{4.1}$$

All elements common to the two images will have the same numerical value and hence the quotient will be one, while anything that differs between the images will have a quotient less than or greater than one. The process is illustrated in Figure 4.2 for the master camera images.

Due to small fluctuations in the sensitivity of the cameras (i.e. noise), common elements will generally have a value within the range slightly above and below one. For this reason, a sensitivity value, $s = 0.15$, is assigned. The quotient image is then converted into a binary image, B, using the conversion value range. All elements within the conversion value range are assigned zero, while all other values are assigned a value of one (visually, for the chosen convention, this corresponds to a white bubble
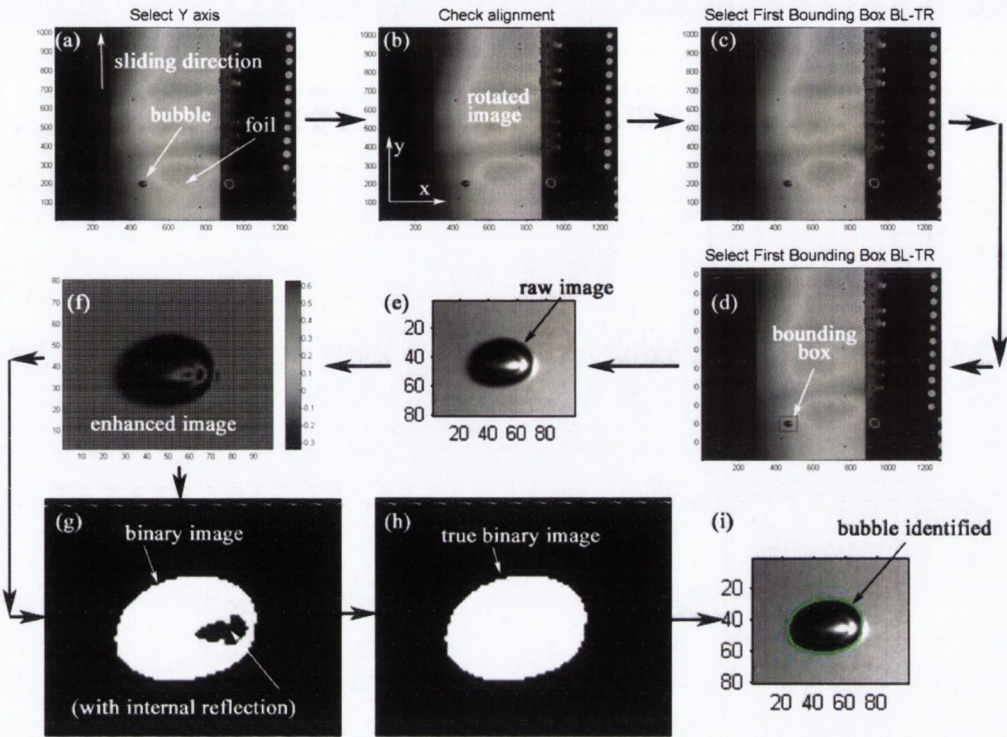
Figure 4.2: Workflow of computer program that identifies the bubble in the master camera images.

on a black background).

$$B = \begin{cases} 1 & \text{for } 1 - s \leq Q \leq 1 + s \\ 0 & \text{for } 1 + s < Q < 1 - s \end{cases} \tag{4.2}$$

The binary image format allows the properties of the bubble to be easily calculated by calling inbuilt Matlab functions `regionprops` and `bwboundaries`. `Bwboundaries` identifies a region within a binary image which, in this case, is the bubble. The function of `regionprops` is to calculate various properties of each region as dictated by the user. At this point in time only the area is required. Next, the binary image is checked to ensure the correct area is detected as the bubble. On occasion, slight differences in the intensity between Im_{bubble} and Im_b can result in falsely detected bubbles. Reducing the size of the image to the small bounding box not only reduces processing time, but reduces the chance of false detection. Even still, false detection occurs, so a part of the `Locater` function detects and removes 'bubbles' that are smaller than the largest detected area. This method works well since the false areas are in the order of a few

pixels compared to hundreds of pixels for the actual bubble. All regions with an area below the maximum detected area are set to black, leaving only the bubble as a solid, white shape.

If the camera image being worked on is from the slave camera the code performs an additional task at this point. It was found that the slave camera image contained a reflection of the bubble due to the highly reflective steel foil (i.e. the surface on which it slides). Since the code only looks for differences between the bubble image and the background image, this reflection is falsely identified as part of the bubble. The boundary between the reflection and the real bubble must be identified in order to remove it. The slave image is oriented so the bubble moves from bottom to top with the reflection on the left hand side of the actual bubble, as shown in Figure 4.3. The code measures the vertical distance (the length of the bubble in the y direction), Δy, moving from right to left across the bubble. If there were no reflection, Δy would go from zero to maximum and back to zero again. With the reflection, Δy goes from zero to maximum, back to a minimum and then increases towards a maximum again. The code identifies where the minimum occurs and sets everything left of this to zero, thus removing the reflection. This is only effective for the smaller bubble volumes tested due to their shape and size. The elongated shape and the slight inclination of the slave camera makes the result invalid for larger volume bubbles.

Now that the bounding box contains only one region, i.e. the bubble projection in that plane, parameters such as the centroid, eccentricity, orientation and boundary are identified (once again using `regionprops`). All of these, except orientation, are returned in the units *pixels* and must be converted into their respective units. The position and shape variables, centroid and boundary, are computed relative to the bounding box's upper left corner. The coordinates of that point relative to the upper left corner of the original image are then added to boundary and centroid in order to obtain their correct positions in the original, full image. The `Locater` function is now finished processing one image and the variables are returned to `Visual Image Analyser` for saving.

Since the bubble position changes from frame to frame, the bounding box must also move. The relative distance between the centroid of the first bubble and the
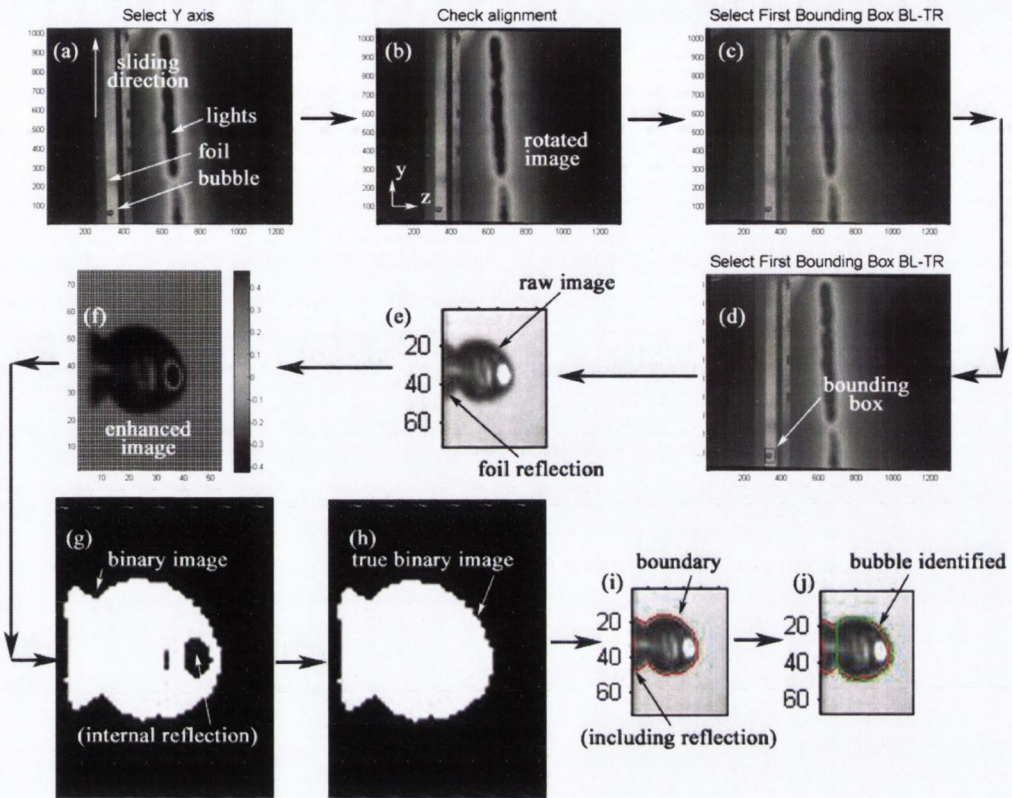
Figure 4.3: Workflow of computer program that identifies the bubble in the slave camera images. Included is the the removal of the bubble reflection from the foil surface.

upper and left sides of the bounding box are calculated for frame number one. These distances are maintained by incrementally moving the bounding box the same distance the bubble centroid moves between frames.

One iteration of the `Locater` and the `Visual Image Analyser` code is complete. The new coordinates of the bounding box along with the next bubble image in the sequence are passed to the `Locater` function and the loop iterates. The bubble properties are calculated for all frames of the camera and saved for later analysis and interpretation.

4.2 Thermal image processing

Infrared radiation lies just outside red end of visible light in the electromagnetic spectrum. The boundaries are not precisely defined but lie in the region of $1~mm$ to $100~\mu m$ between visible light and microwave radiation.

All objects above absolute zero ($0~K$) emit infrared radiation, the intensity increasing with temperature. In conjunction with this, the wavelength at which most of the radiative power is emitted reduces with temperature. This is illustrated when, for example, heated metals glow red, orange and then white as the body begins to emit some radiation in the visible spectrum. Infrared radiation incident on a surface is broken up into that which is reflected, absorbed and transmitted or

$$\alpha^* + \rho^* + \tau = 1 \tag{4.3}$$

where α^*, ρ^* and τ are the material's absorptivity, reflectivity and transmissivity respectively. The surface is classified as gray and diffuse when

$$\alpha^* = \epsilon \tag{4.4}$$

where ϵ, the emissivity, is the ratio of the emissive power of a body, E, to that of a black body, E_b at the same temperature,

$$\epsilon = \frac{E}{E_b} \tag{4.5}$$

and given that the steel foil does not transmit infrared radiation, equation 4.3 can now be restated as

$$\epsilon + \rho^* = 1 \tag{4.6}$$

This is the reason for painting the foil surface, the higher emissivity results in lower reflectivity. The Stefan-Boltzman law relates temperature and emissivity to the emissive power from a body (E) through the Stefan-Boltzman constant

$$E = \epsilon \sigma T^4 \tag{4.7}$$

If we can measure E, then the surface temperature of that body can be evaluated. This is effectively what the infrared camera measures, or more specifically, the portion

of that radiation that lies within the 3-5 μm range of the camera's sensor. Through calibration the relationship between the incident radiation and temperature can be evaluated. By calibrating in situ, the effects of spectral sensitivity, emissivity and transmission through the sapphire window are eliminated as a direct relationship between the infrared radiation reaching the sensor and temperature are established.

Data from the infrared camera are exported via ExaminIR software, calibration applied, in .csv format[2]. One frame of the thermal camera corresponds to one .csv file. This file is imported into Matlab as a two-dimensional temperature array of the back surface of the foil and surrounding area. An energy balance must be performed in order to obtain the heat convected to the fluid from the front side of the foil and hence the heat transfer coefficient. Before this can be performed, distortion of the image caused by lens aberrations must be corrected. Once this is done, the heat transfer map is aligned, both temporally and spatially, with the corresponding bubble image. Various foil properties are input into Matlab along with the calibration curves for the bulk water thermocouple, T_{bulk} and air gap thermocouple, T_{air}.

4.2.1 Removing image distortion

The 50 mm f/3.5 lens supplied with the FLIR camera applies what is known as barrel distortion to the image. Barrel distortion perturbs an image radially outward from its center. The distortion has a stronger effect further from the center resulting in convex sides. Examples of image distortion are shown in Figure 4.4. The effects of this are measured and corrected in Matlab. The parameters for correction are obtained by recording an image of a grid placed at the same distance from the lens as the foil surface. This results in a distorted image of the grid being recorded. The correction value is the one that results in the grid returning to its true shape. As previously mentioned, the distortion acts from the center of the full sensor area of 640 × 512 pixels outwards. So, when using a smaller sensor area (to achieve higher frame rates), such as in this case (320 × 196 pixels), the data must be positioned correctly within a

---

[2].csv denotes a comma separated variable file. It is basically a matrix of temperature values, each entry in the matrix corresponding to one pixel of the camera.
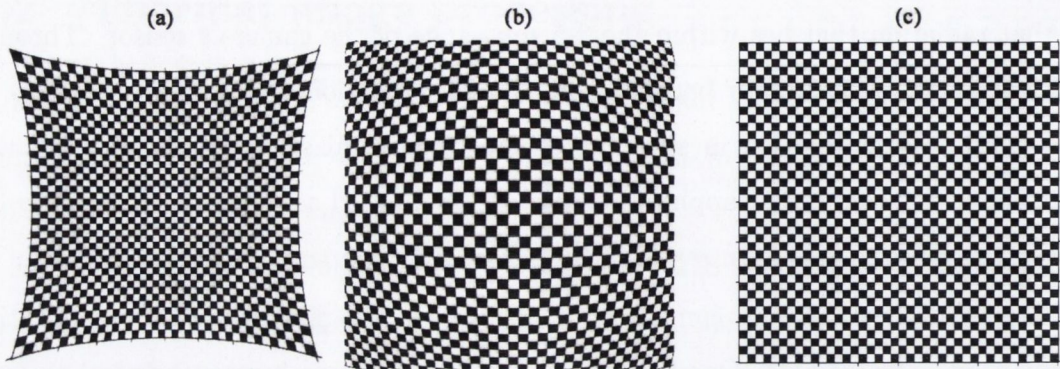
Figure 4.4: An example of (a) pin cushion and (b) barrel distortion on a (c) square grid. Applying the same amount of barrel distortion to an image suffering from pincushion distortion (or vice versa) would result in (c), the square grid.

buffer zone to ensure the correction is applied properly. The code builds up the image until it measures 640×512 pixels and positions the temperature data in the correct x-offset and y-offset positions, in this case 192 pixels in the x direction relative to the top right hand corner.

The lens distortion correction is based on the principle that application of pin cushion distortion cancels the effects of an image suffering from barrel distortion. Mathematically, barrel and pin cushion distortion are opposites. The coordinates of each pixel are converted from Cartesian (x, y) to polar (r, θ) using Matlab's `cart2pol` command. Each position coordinate is then modified by a cubic equation, although other equations can be used depending on the type of distortion. Only the r value is manipulated, where r is the distance from the origin and θ is the angle from the positive x-axis. A new value s is defined as

$$s = r + ar^3 \tag{4.8}$$

where a is a negative number that controls the amount of distortion to be applied (a positive value here would apply further barrel distortion). New coordinates for the thermal image are created by converting the new polar coordinates (s, θ) back to Cartesian using the `pol2cart` function in Matlab. The original image is then spatially transformed by re-sampling it to the new Cartesian coordinates using the `tformarray` Matlab function. Each thermal image in the sequence is manipulated in this way and

saved for further processing.

4.2.2 Foil energy balance

The method of temperature measurement utilised here (i.e. measuring the temperature on the opposite side of the foil to the phenomenon being observed) assumes no temperature difference across the thickness of the foil ($dT/dz = 0$). This assumption can be validated using the Biot number, provided

$$Bi = \frac{h\delta_{ss}}{k_{ss}} \ll 0.01 \tag{4.9}$$

where h is the heat transfer coefficient, δ_{ss} is the foil thickness and k_{ss} is the thermal conductivity of stainless steel. For the current setup ($h_{max} \approx 1200 \ W/m^2K$, $\delta_{ss} = 25 \times 10^-6 \ m$ and $k_{ss} = 16.3 \ W/m^2K$) the maximum Biot number observed is $Bi \approx 0.002$, well within the specified limit. The time constant of the system ($\lambda = c\rho\delta/h$) is calculated as $0.0042 \ s$. This indicates that thermal effects should be dectectable between the bubble and foil through the current setup, if they were present.

In order to calculate the heat convected to the fluid from the front side of the foil, an energy balance is required. In the energy balance, both uniform heat generation and constant temperature through the thickness (see above) of each element is assumed. When a spatial temperature gradient exists over the foil in the x and y directions, dT/dx and dT/dy, thermal energy conducts from areas of high temperature to low temperature at a rate dependent on the temperature gradient, foil thickness and thermal conductivity. Similarly, if the foil temperature changes with time, dT/dt, there is a change in the thermal energy stored within the foil dependent on the mass, specific heat capacity and temperature change. To a lesser extent, radiation from the front and back of the foil transport energy away from the surface, while incident radiation adds to the foil energy, heat exchange between the back of the foil and the air is also accounted for.

In order to calculate the heat convected to the water from the foil, q_{conv}, the energy balance is performed on an element of size $dx \times dx$, corresponding to the size of each pixel, and thickness δ_{ss}, corresponding to the foil thickness. As depicted in Figure 4.5, the energy generated within the foil by joule heating is divided among the individual
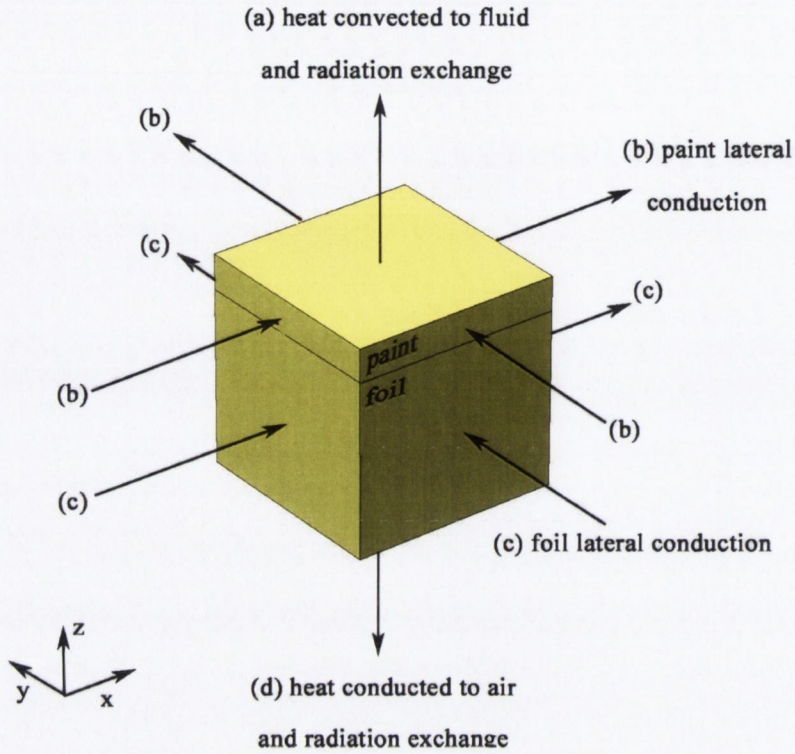
Figure 4.5: Illustration of heat flow through an element of foil of dimensions $dx \times dx_{ss}$ with a paint layer of thickness δ_p. Heat is generated though resistive heating and is transported by convection, conduction and radiation.

heat flows.

$$q_{gen.} = q_{conv.} + q_{lc} + q_{cap.} + q_{cd} + q_{r,f} + q_{r,b} \tag{4.10}$$

where q_{gen} is the heat generated, $q_{conv.}$ is the heat convected to the fluid, q_{lc} is heat transferred through lateral conduction to adjacent foil elements, $q_{cap.}$ is the change in stored energy based on capacitance, q_{cd} is heat 'conducted'[3] to the air and $q_{r,f}$ and $q_{r,b}$ are the radiative heat exchange on front (fluid side) and back (air side) surfaces respectively. Rearranging for the heat convected to the fluid we find

$$q_{conv.} = q_{gen.} - q_{lc} - q_{cap.} - q_{cd} - q_{r,f} - q_{r,a} \tag{4.11}$$

where the individual components, in Watts, are calculated as follows.

$$q_{gen} = I_{el}^2 R_{el} \tag{4.12}$$

---

[3]The air is assumed stagnant and heat transfer by one dimensional conduction across the 3 mm air gap is assumed.

where I_{el} is the current through one foil element of resistance R_{el}. The lateral conduction term is given as

$$q_{lc} = -k_{ss}\delta_{ss}\nabla^2 T \times 4\delta_{ss}dx \qquad (4.13)$$

where k_{ss} and δ_{ss} are the stainless steel thermal conductivity and thickness and $\nabla^2 T$ is the Laplacian of the temperature (the negative sign indicates the heat transfer is in the direction of decreasing temperature), this is transferred through an area of $4\delta_{ss}dx$, i.e. the four sides of the foil element. The heat storage term is given as

$$q_{storage} = m_{el}c_{p,ss}\frac{dT}{dt} \qquad (4.14)$$

where m_{el} and $c_{p,ss}$ are the mass and specific heat capacity of an element and dT/dt is the temperature change with time. The heat transfer due to conduction to the air is given as

$$q_{cd} = -k_{air}\frac{dT}{dz} \times dx^2 \qquad (4.15)$$

where k_{air} is the thermal conductivity of air and dT/dz is the temperature gradient across the air gap, this is transferred through the back of the foil, an area of dx^2. The radiation exchange from the front of the foil can be quantified as

$$q_{r,f} = \epsilon_f\sigma\left(T_s^4 - T_{wall}^4\right) \times dx^2 \qquad (4.16)$$

where ϵ_f is the front surface emissivity, σ is the Stefan-Boltzman constant, T_s is the surface temperature and T_{wall} is the water tank wall temperature, assumed to be the same as the bulk water temperature, T_{bulk}, this is transferred through an area dx^2. Similarly, the radiation exchange from the back of the foil is expressed as

$$q_{r,b} = \epsilon_b\sigma\left(T_s^4 - T_{sapphire}^4\right) \times dx^2 \qquad (4.17)$$

where ϵ_b is the back surface emissivity, $T_{sapphire}$ is the sapphire window temperature, assumed to be the same as the air temperature, T_{air}. This is transferred through an area of size dx^2. All the available energy is generated by resistive heating, the value of which can be derived using Ohm's law, $V = IR$. The equation is rearranged as a function of just the current, I, and the resistance, R, resulting in

$$q_{gen} = I^2 R \qquad (4.18)$$

141

By another derivation of Ohm's law, the total resistance of the foil can be calculated as

$$R_{foil} = \rho_{ss} \frac{l}{A_{cs}} \tag{4.19}$$

where ρ_{ss} is the electrical resistivity of stainless steel, l is the length parallel to the current flow and A_{cs} is the cross-sectional area ($\delta_{ss} \times w$). From this, the total power generated by the foil can be calculated. The power generated by one element of size $dx \times dx \times \delta_{ss}$ is calculated by dividing the total surface area of the foil into elements of size $dx \times dx$. The power generated is then divided evenly amongst each element. This is the equivalent of equation 4.12, where I_{el} is the current through one element and R_{el} is the resistance of one element.

The lateral conduction term (Equation 4.13) in two spatial coordinates can be expressed as

$$q''_{lc} = -k_{ss}\delta_{ss} \left(\frac{d^2T}{dx^2} + \frac{d^2T}{dy^2} \right) \tag{4.20}$$

where $\frac{d^2T}{dx^2}$ and $\frac{d^2T}{dy^2}$ are the discretised, second spatial derivatives, of the temperature in the x and y directions respectively, k_{ss} is the thermal conductivity of stainless steel and δ_{ss} is the foil thickness. The net heat flux by lateral conduction to a foil element at position i, j is

$$q''_{lc,ij} = -k\delta_{ss} \left(\frac{T_{i+1,j} + T_{i-1,j} + T_{i,j+1} + T_{i,j-1} + 4T_{ij}}{dx^2} \right) \tag{4.21}$$

provided $dy = dx$, therefore the net heat transfer through the four sides of an element is

$$q_{lc,ij} = -k\delta_{ss} \left(\frac{T_{i+1,j} + T_{i-1,j} + T_{i,j+1} + T_{i,j-1} + 4T_{ij}}{dx^2} \right) \times 4\delta_{ss}dx \tag{4.22}$$

The derivatives are easily computed in the Matlab environment using the gradient function, grad. The raw temperature map and lateral conduction heat transfer are illustrated in Figure 4.6.

It was found that small, spatial fluctuations in the temperature map result in greater and greater fluctuations in the derivatives. Noise in the original temperature map is amplified upon taking the derivative. Filtering was used to try remove these effects but was found to also reduce the magnitude of the peaks. Various approaches were taken including filtering the first and second derivative as well as the temperature
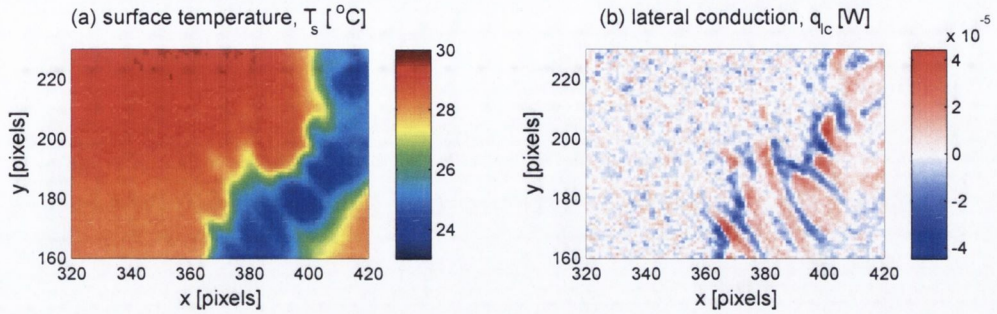
Figure 4.6: (a) Foil temperature and (b) calculated lateral conduction term for a section of the foil surface. Positive values indicate heat transfer into a foil element.

map. In the end it was decided to just use the unfiltered result as the noise was at a level deemed acceptable.

The change in internally stored energy can be calculated by measuring the change in temperature with time of a foil element. The magnitude of this is dependent on the temperature change, the specific heat capacity and the mass of the material. By measuring the time varying temperature with the infrared camera it is possible to calculate the change in internal energy using Equation 4.14. The Matlab code loads two successive thermal images, T_{t-1} and T_t. The discrete change in temperature with time of each element is computed as

$$\frac{dT}{dt} = \frac{T_t - T_{t-1}}{\Delta t} \tag{4.23}$$

where Δt is the time difference between two successive images, i.e. the inverse of the frame rate, $1/f$. This is multiplied by the mass of one element, m_{el}, and the specific heat capacity, $c_{p,ss}$, of stainless steel. For a single element of size $dx \times dx \times \delta_{ss}$ and density, ρ_{ss} the change in stored energy is calculated as

$$q_{storage} = \rho_{ss} c_p dx^2 \delta_{ss} \frac{T_t - T_{t-1}}{\Delta t} \tag{4.24}$$

A sample result is shown in Figure 4.7. Once again, filtering can be applied to this result in order to remove noise but the side effects were found to also reduce the magnitude of the peaks. The noise was deemed to be at an acceptable level and so the filter was not implemented.
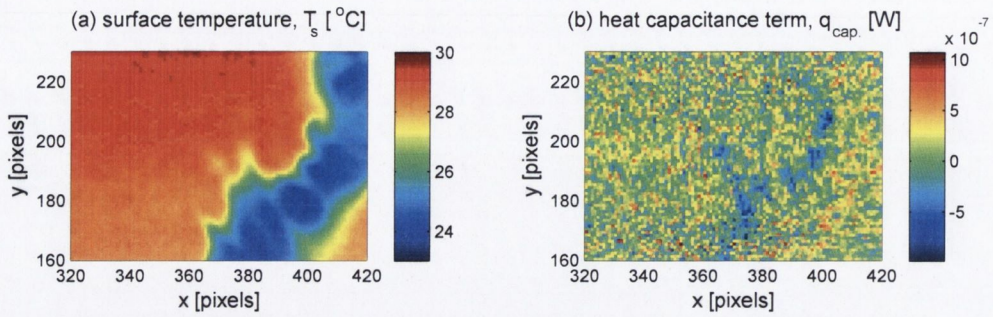
Figure 4.7: (a) Foil temperature and (b) heat capacitance term for a section of the foil surface. Positive values indicate heat transfer into a foil element.
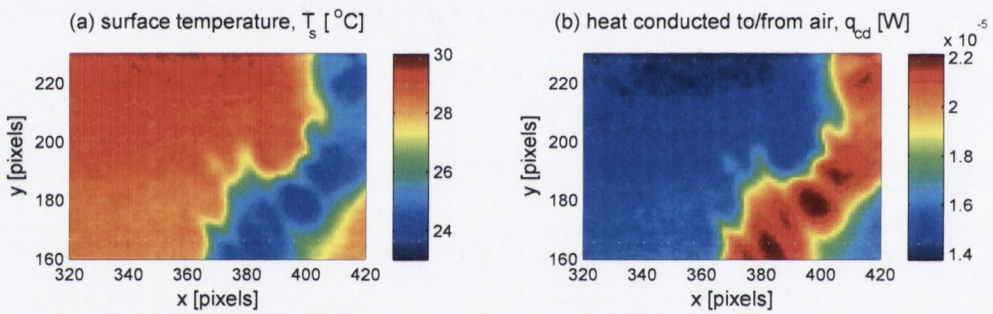
Figure 4.8: (a) Foil temperature and (b) calculated conduction to the air gap for a section of the foil surface. Positive values indicate heat transfer into a foil element.

The rig is designed in such a way as to minimise heat transfer through the back of the foil. This is achieved by trapping a small amount of air behind the foil using an infrared transmissive material, e.g. sapphire. Before testing, the air is allowed to heat to a temperature close to that of the foil. The resulting small temperature gradient and low thermal conductivity of air creates a thermal barrier. This is still accounted for using Equation 4.15.

Interestingly, it was found that when the bubble slides across the foil the temperature reduced below that of the air temperature, approaching that of the bulk water temperature. This reverses the temperature gradient and as such the air actually transfers heat *to* the foil, although at a low rate. Figure 4.8 shows the temperature map, temperature difference and heat conducted to or from the air.
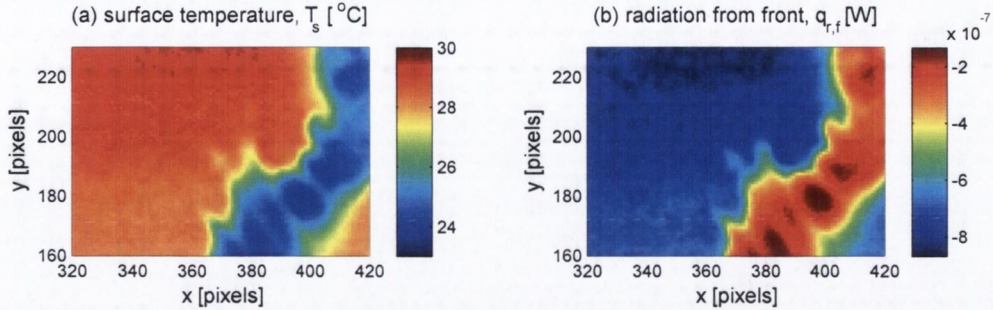
Figure 4.9: (a) Foil temperature and (b) calculated radiative exchange from the front of the foil for a section of the foil surface. Positive values indicate heat transfer into a foil element.

Equations 4.16 and 4.17 approximate the net radiative heat transfer to and from the foil's front and back surfaces respectively. Due to the relatively low temperatures of the foil and surroundings, the radiative heat transfer is extremely small. The radiative exchange on the front of the foil is assumed to be between the foil surface and the glass sides of the tank. The glass sides are assumed to be at the same temperature of the bulk water. On the back of the foil, the radiation exchange is between the foil surface and the sapphire[4], which itself is assumed to be at the same temperature as the air gap between them. Figures 4.9 and 4.10 show the net radiative heat transfer from the front and rear of the foil surface respectively.

Each frame from the infrared camera is loaded into Matlab where the individual correction terms (Equations 4.12 to 4.17) and the heat convected to the fluid (Equation 4.11) are calculated. The heat transfer coefficient between the foil and fluid is then calculated as

$$h = \frac{q''_{conv}}{\Delta T} \qquad (4.25)$$

where

$$q''_{conv} = \frac{q_{conv}}{dx^2} \qquad (4.26)$$

and ΔT is the temperature difference between a foil element and the bulk water

---

[4]The infrared 'transmissive' glass actually only transmits infrared radiation within a narrow band that matches the measurement range of the sensor. Transmitted infrared radiation is neglected.
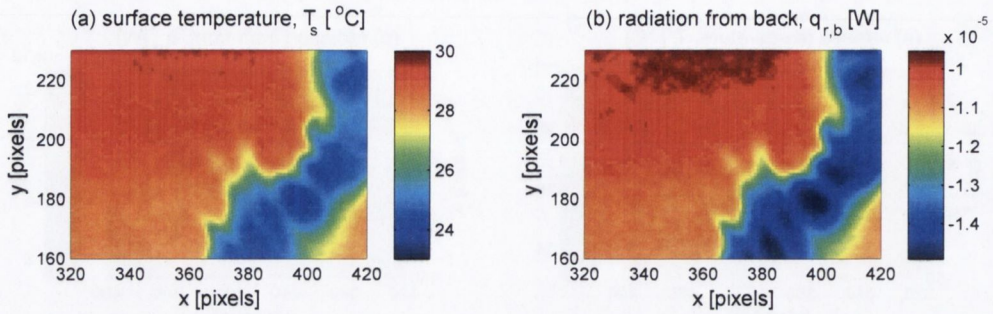
Figure 4.10: (a) Foil temperature and (b) calculated radiative exchange from the back of the foil for a section of the foil surface. Positive values indicate heat transfer into a foil element.

temperature, T_{bulk}. Results are also presented of the ratio of heat transfer coefficients between natural convection and bubble passage

$$\epsilon = \frac{h}{h_0} \tag{4.27}$$

where h is the heat transfer coefficient during bubble passage and h_0 is the heat transfer coefficient for natural convection alone, i.e. before bubble passage.

The foil is coated on one side with matte black paint in order to increase its emissivity, reducing unwanted reflections. It is applied using a spray can and its thickness measured with a micrometer after drying. Numerous attempts were made at achieving a uniform thickness over the surface of the foil and once this was achieved the foil was adhered to two copper bus bars described in Chapter 3 Section 3.1.3. Several measurements with a micrometer (Mitutoyo No. 29334070 IP 65) indicated the paint thickness to be, on average[5], 15 μm. This is calculated by measuring the foil thickness before painting and calculating the difference after painting. The paint is assumed to be at the same temperature as the foil. This adds another two terms to the energy balance to account for the small lateral conduction within the paint layer itself and its heat capacitance,

$$q''_{lc} = -k_p \delta_p \left(\frac{d^2 T}{dx^2} + \frac{d^2 T}{dy^2} \right) \tag{4.28}$$

---

[5]Based on the mean of 12 measurements of the surface thickness.

and

$$q_{storage} = m_{paint}c_{p,paint}\frac{dT}{dt} \tag{4.29}$$

where k_p and δ_p are the thermal conductivity and thickness of the paint layer, m_{paint} is the paint's mass and $c_{p,paint}$ is its specific heat capacity. This can be combined with the foil lateral conduction term for ease of calculation

$$q_{lc}'' = (-k_{ss}\delta_{ss} + -k_p\delta_p)\left(\frac{d^2T}{dx^2} + \frac{d^2T}{dy^2}\right) \tag{4.30}$$

All these terms are individually saved which allows future reference to the relative contribution of each term to the overall heat flow. Figure 4.11 shows the relative contribution of each term relative to the heat generated in Equation 4.10 during bubble passage.

As can be seen in Figure 4.11, the result is a non-uniform convective wall flux with small regions showing values $\pm15\%$ of the average.

4.3 PIV processing

Velocity vectors are processed using LaVision's purpose developed DaVis software. The data are output as velocity vectors and imported into Matlab for further processing and presentation. The basic principle involves a pair of images separated by time Δt, Within this space of time the flow, and thus the seeding particles, are assumed to move a small distance. Images are divided into interrogation areas where mathematical correlation analysis is performed on a cluster of seeding particles within the same area of the two frames. This results in signal peak identifying the common particle displacement, $\overline{\Delta x}$. The velocity vector is computed as

$$\overline{U} = \frac{\overline{\Delta x}}{\Delta t} \tag{4.31}$$

PIV raw data are processed differently depending on the fluid velocity, and thus seeding particle displacement, being observed. In the immediate wake of the bubble, high fluid velocity requires short image separation times (Δt) while further downstream (after bubble passage) requires longer Δt. All recordings are performed at 125 *Hz*, although depending on what is being observed either each individual frame of each
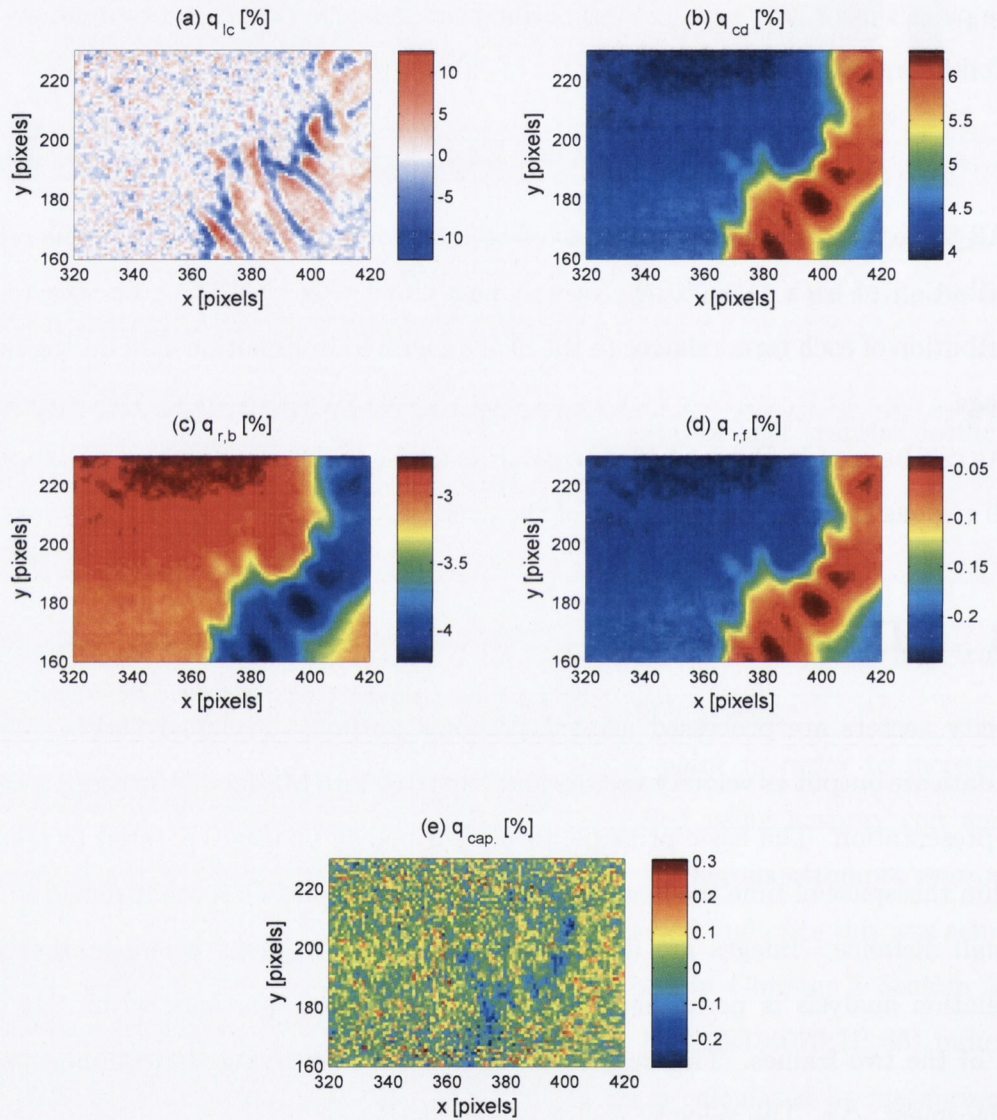
Figure 4.11: The relative contribution from (a) lateral conduction, (b) conduction to air, (c) radiation from the back and (d) front surfaces and (e), heat capacitance. Values are presented as percentage of heat generated.

fifth frame is used in the cross correlation. In addition, a smaller interrogation window is used for the high velocity calculations (64×64 down to 8×8 compared to 64×64 to 12×12 for lower velocity observations, using a multi pass cross correlation with 50% overlap). This is done to achieve the correct pixel displacement relative to the interrogation area (recommended as one quarter of the window size).

4.4 Spatio-temporal alignment

Combining both the thermal and visual processed results is essential to visualise how the bubble affects heat transfer from the foil. This task is performed in a purpose written Matlab program called `Combine & calibrate`. Both the master and slave visual results have to be spatially and temporally aligned with each other, calibrated, and then combined with the correct thermal image.

The foil has four points marked on its surface. The points are made by indenting the foil with a small sharp object so the point can be observed from both sides of the foil. Both the master camera and the thermal camera can view these points during recording and it is they that are used to align and calibrate the data. First, the master bubble motion data is loaded into the `Combine & calibrate` program. A visual calibration image from the master camera is loaded and rotated by angle $\theta_{c,M}$ to its correct orientation. A thermal calibration image, corrected for lens distortion is also loaded. The user is asked to input the coordinates of two points, of known distance apart, on the master camera calibration image. This is used to calculate the master image scaling factor. The distance in pixels between the points is calculated as

$$d_{pix,M} = \sqrt{\left(\Delta pix_{x,M}\right)^2 + \left(\Delta pix_{y,M}\right)^2} \qquad (4.32)$$

and, using the known distance between the two points, the scaling factor for the master camera can be calculated as

$$\text{Scale}_M = \frac{d_{mm,M}}{d_{pix,M}} \qquad (4.33)$$

After the slave images have been processed to identify the bubble, the slave scaling factor, Scale_S, is calculated. This is not input by the user but is calculated by

comparing the distance traveled by the bubble in the master images, $\Delta P_{mm,M}$, with that of the slave images, $\Delta P_{pix,S}$ (using the first bubble image, Im_1, and last bubble image, Im_n, for each camera). Since the two cameras are temporally-synchronised, the distance traveled in mm by the bubble in each image is the same. This is used to calculate the slave camera scaling factor.

$$\text{Scale}_S = \frac{d_{mm,M}}{d_{pix,S}} \tag{4.34}$$

where

$$d_{pix,S} = \sqrt{(\Delta pix_{x,S})^2 + (\Delta pix_{y,S})^2} \tag{4.35}$$

The slave camera data is loaded and placed in a matrix beside the master camera data.

The user is asked to input the coordinates of the four alignment points on both the master visual image and thermal image. These are the base points and input points respectively. The code uses these markers to manipulate the thermal image to correspond with the visual image. Since the thermal camera is aligned at a slight angle to the foil (to reduce reflections being seen by the camera), the foil surface appears skewed. The code also corrects for this.

The base and input points are used to generate a spatial transform structure which is used to manipulate the thermal image to align with the visual image. A projective transformation is applied to the thermal image in which straight lines in the original image remain straight but parallel lines converge towards a vanishing point. The transformation also performs rotation and translation operations. The function `cp2tform` is supplied both sets of control points and instructed to create a projective transform named `tform`. The function `imtransform` is then supplied with the thermal image, the `tform` data and the dimensions of the visual image. It returns the mapped thermal image re-sampled to the dimensions of the visual image. Both the master visual image and the thermal image are now successfully aligned in space.

As previously mentioned, the thermal image not only contains the temperature of the foil but the surrounding structural material too. This additional information is not required so the thermal image is trimmed to only include an area of foil that is affected by the bubble. For this, the mean x-position of the sliding bubble is used.

The center of the thermal image is zeroed on the mean x-position of the bubble plus of minus a desired distance. This distance is chosen by observation of the wake effects of the bubble on the thermal image. The y zero-position is chosen to be 60 mm from the start of the foil. This value is chosen to avoid observing effects of the bubble impacting on the foil surface as it travels from the structural surface to the test surface.

The z-coordinates of the slave bubble centroid is used to position the x and y master bubble centroid and boundaries. This means that the master bubble outline and position is correct in three dimensions. The z-coordinate is measured from the point of contact, instead of a reference point, to the centroid. This corrects for the fact that the slave camera has to be mounted slightly below the foil at an angle in order to see past the stainless steel sheet. In a similar manner, the x position of the master bubble centroid is used to correctly position the y and z slave bubble centroid and boundary, thus correctly aligning the slave bubble image in three dimensions. The individual scaling factors, $Scale_M$ and $Scale_S$, are applied to the centroid, boundary and other data to convert from *pixels* to *mm*. The x and y axis information, base & input points and calibrated & combined bubble data are now saved for plotting.

All the data are now aligned spatially but still need to be aligned correctly in time. The experimental apparatus is set up in such a way that a visual image Im_n should correspond to a thermal image, T_n. This is not the case. It was observed that the thermal camera images could go out of sync with the visual camera by one frame. This was discovered by observing the *.pod* file of the thermal recording. The *.pod* file stores information on the exact timing of each individual image. It was noticed that, on occasion, one single frame of the camera was not recorded. This resulted in the time difference between the two images T_1 and T_2 being double that of the rest of the images, i.e. $2 \times 1/f$. Now, all subsequent frames of the thermal recording lag by one frame, i.e. Im_n aligns with T_{n-1}. The *.pod* file of each recording is examined for this problem prior to plotting so it can be accounted for. Inspection of the *.pod* file shows this problem only occurs within the first two frames of recording.

A three dimensional approximation of the 0.05 ml bubble can be obtained by interpolating data from the master and slave cameras. It can only be done for small bubble volumes due to their symmetry, larger bubbles would possibly require a third

camera viewing the x-z plane, or re-positioning the slave camera closer to the surface. The master camera describes the x-y shape projections of larger volume bubbles quite well but the slave camera can see the front and the rear as they change orientation. This makes it difficult to reconstruct the three dimensional bubble shape by the current method as will become apparent.

For smaller bubbles, the method makes an assumption about the bubble shape. It is assumed that the master camera bubble boundary is representative of the whole bubble shape. This means that the shape (although not size) described by the master camera boundary is the same at all distances from the surface (in the z direction). The code uses the slave camera boundary to scale the master boundary. First, the bubble slave camera boundary is re-sampled at discrete z intervals, this is done by linear interpolation between the points lying higher and lower than the chosen plane in the z direction. In the current study, 20 'slices' of the slave camera bubble boundary are taken at equal intervals. The distance between the front and rear of the bubble is calculated at each interval and the master camera bubble boundary scaled to fit between the two. When in position, this results in a 'cloud' of points representing the predicted three dimensional shape. This is then fitted with a surface that traces the convex hull of the bubble i.e. the smallest surface that contains all points.

Although the same assumption can be made about bubbles of larger volumes, the slave camera cannot get an accurate description of the $y_b - z_b$ bubble boundary projection (see Figure 4.1), required to scale the master camera boundary. This is partly due to the fact that the bubble orientation changes, meaning the slave camera can see some of the bubble front, or rear, as it slides. At one point in each bubble oscillation the slave camera is perpendicular to the bubble's $y_b - z_b$ plane. This could be used in conjunction with the assumption that the $y_b - z_b$ projection does not change throughout one bubble oscillation but another problem prevents three dimensional reconstruction. The slave camera has to be positioned in the positive z direction in order to see the full bubble outline, this is due to the required sealing described in Chapter 3 Section 3.1.3. This means that a secondary bubble image is visible through reflection from the foil surface. This makes it difficult to remove by the method described previously. Since an accurate description of the bubble $y_b - z_b$ projection

152

is impossible by this method, photographic images of the bubble will be presented instead. These still provide good insight into the bubble three dimensional shape.

Chapter 5

Results

Results are presented for a surface inclination angle of 30° to the horizontal. Tests were performed using two different measurement setups: the PIV setup and the Bubble motion setup as previously detailed in Chapter 3. For the Bubble motion setup, five individual tests were performed at each bubble volume of 0.05, 0.1, 0.2 and 0.4 ml. Similarly, three tests were performed at each volume for the PIV setup. Tests were performed on both a heated and non-heated surface resulting in a total of 64 individual tests.

Results for the Bubble motion setup were found to fall into one of two categories; steady state or transitional. The categories were judged on the oscillatory nature of the bubble's path and velocity. Steady state tests were found to exhibit a near constant oscillatory path, while transitional tests exhibited variation. Interestingly, results for the PIV setup were found to behave differently to the Bubble motion setup. Bubbles in these tests did not exhibit large path oscillations but large shape oscillations were noted.

After a brief introduction on the natural convection boundary layer, results of bubble dynamics are presented. Section 5.2 relates specifically to the observations of the bubble itself, its shape and its motion. Steady state tests are discussed in detail followed by the differences observed for transitional tests. Results in this section are from the Bubble motion setup.

Section 5.3 relates to fluid motion. Due to the differences observed between the

Bubble motion setup and the PIV setup, some aspects of bubble dynamics specific to the PIV setup are included here. Following this, a detailed analysis of fluid motion is presented. Where possible this will be linked to bubble dynamics.

After gaining an understanding of both fluid and bubble dynamics, the effects on heat transfer are introduced in Section 5.4 and 5.5. Due to the differences observed between the PIV and Bubble motion setups heat transfer observations are presented specific to each setup. The final section tries to reconcile results observed for the two setups based on similarities observed in relation to heat transfer. Chapter 6 takes the discussion further based on experimental observations and work by previous authors.

Note: It was noticed that tests on the non-heated surface generally had a high frequency fluctuation to both the x and y velocity components (this is calculated based on the x and y centroid position, which also showed the scatter but to a less obvious extent). This may be due to the slightly different behaviour of the surface under cooled and heated conditions. When the surface is heated and cooled, the metal foil expands and contracts. Although there is a tensioning system in place to counteract this effect (see Chapter 3), it does not seem to be able to achieve the same tension between heated and non-heated conditions and thus the foil may move slightly more freely in the z-direction for the non-heated case. If the center of the surface deflects in the z-direction, the bubble position will be affected in the x and y directions too (a slope on the foil causes the bubble to move). Although the fluctuations are small, calculating the derivative of the x and y displacements results in large fluctuations in velocity, even larger still in acceleration. Small vibrations generated in the surrounding lab environment may be the reason for this high frequency scatter and it is not currently attributed to any bubble related phenomena. In order to confirm this, additional tests were carried out using a bubble sliding on an unheated solid perspex surface and no high frequency fluctuations were noted.

5.1 Natural convection

Before the bubble is released onto the surface, heat is transferred to the fluid through natural convection. Heated fluid near the surface is less dense than the surrounding

fluid and therefore more buoyant. The fluid naturally flows upwards but is restricted by the inclined surface. The fluid is deflected by the surface and flows in the positive y direction, i.e. from the bottom to top of Figure 5.1 (a). Fluid traveling within the boundary layer continues to receive heat from the surface, resulting in its density being lowered further. This results in a velocity gradient in the y direction reaching a maximum at the top of Figure 5.1 (a). The velocity varies from 4 to 12 mm/s over the test section, measured in a plane 3 mm from the surface. The low velocity region indicated along the left hand side of the figure is due to edge effects, where unheated support material (not visible in the figure) results in lower fluid velocity. This region is not critical to experiments as the bubble remains close to $s_x = 0$.
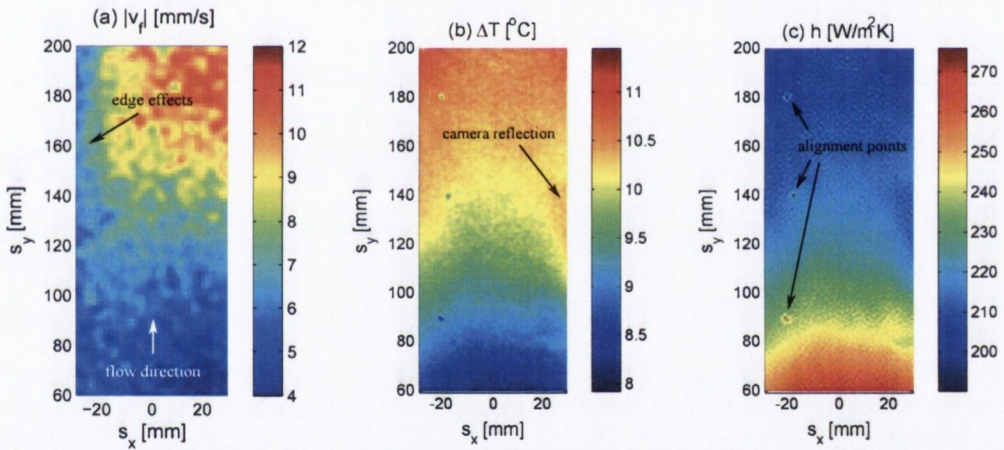
Figure 5.1: (a) Fluid velocity magnitude, $|v_f|$, (b) surface to bulk water temperature difference, $\Delta T = T_s - T_\infty$ ($T_\infty = 26.5\,°C$) and (c) heat transfer coefficient, h, for an inclined, heated surface rotated at 30° to horizontal.

Due to the natural convection velocity gradient, there exists a temperature gradient in the y direction, and due to the uniform wall flux boundary condition, a gradient in the heat transfer coefficient[1]. The bulk water temperature, T_∞, is 26.5 °C in this specific test indicating that the surface temperature, T_s, varies from approximately 34.5 to 38.5 °C from bottom to top of Figure 5.1 (b). The heat transfer coefficient varies

---

[1]The uniform wall flux boundary condition is an approximation, in reality there is a variation of about 15 % in this in small regions during bubble passage, see Chapter 4 for details.

from approximately $270\ W/m^2 K$ at the bottom to $200\ W/m^2 K$ at the top (Figure 5.1 (c)). The region highlighted to the mid right of Figure 5.1 (b) is a result of infrared camera observing a reflection of itself. This region is not critical to observations of heat transfer. The three points indicated on the left hand side of Figure 5.1 (c) (also visible in Figure 5.1 (b)) are used for alignment of the thermal image, bubble images and PIV results. They will be ignored in all subsequent figures.

Fujii & Imura [74] presented a correlation predicting the average Nusselt number for a downwards facing heated surface at arbitrary inclination angle as

$$Nu = 0.56 \left(Gr Pr \cos \theta \right)^{\frac{1}{2}} \tag{5.1}$$

where θ is the inclination angle measured from the vertical, Gr and Pr are the Grashof and Prandtl numbers respectively (the product of these is the Rayleigh number, $Ra = Gr Pr$). The correlation was found to provide excellent agreement with their experimental results for inclination angles between $0°$ (vertical) and $89°$ (almost horizontal) provided $10^5 < Gr Pr \cos \theta < 10^{11}$. In their analysis the characteristic length was chosen to be the length of the plate, L. T_w was chosen as the temperature at the mid point of the wall, i.e. at $L/2$. The value of β was evaluated as the average of that at T_∞ and $(T_w + T_\infty)/2$. The values of thermal conductivity, kinematic viscosity and Prandtl number were evaluated at $T_e = T_w - 0.25 \left(T_w - T_\infty \right)$. The correlation predicts the average heat transfer coefficient for the parameters used in the present study to be $h \approx 290\ W/m^2 K$ which corresponds relatively closely to the measured value, which, in the test section varies from $h \approx 200 - 270\ W/m^2 K$.

Fussey & Warneford [75] calculated the critical Rayleigh number for onset of turbulence for an inclined downward facing heated surface to be

$$Ra_c = 6.31 \times 10^{12} \exp \left(-0.0705\theta \right) \tag{5.2}$$

where θ is the inclination angle measured from vertical. For the present study, the critical Rayleigh number is calculated to be $Ra_c = 43 \times 10^{13}$. The actual Rayleigh number is found to be much lower than this at $Ra \approx 3 \times 10^9$, therefore a laminar boundary layer is assumed for all tests.

5.2   Bubble dynamics

The bubble is less dense than the surrounding medium and therefore more buoyant. A force exists equal to the weight of water displaced that acts vertically upwards through the bubble's center of mass. In an open medium this force would cause the bubble to accelerate vertically until a nominal terminal velocity is reached where the buoyancy force is balanced by the drag force generated by the surrounding fluid motion. Depending on the fluid properties of the system, i.e. Reynolds number, Eötvös number and Morton number, the bubble may travel in a straight line, zig-zig or spiral and thus may have constant or fluctuating x, y and z velocities. The fluctuating velocities relate to fluctuating forces exerted by the fluid on the bubble. The fluid properties, and therefore the forces on the bubble, also dictate the bubble shape.

In the case of the present study the bubble is released onto the underside of a submerged, inclined surface. The buoyancy force is now met with a reaction force from the surface. The y and z components of the buoyancy force (resolved parallel and perpendicular to the surface) reveals that there is a net force parallel to the surface in the direction of decreasing depth. The magnitude of this force component is dependent on both the bubble volume and inclination angle. For this type of setup, the bubble will once again accelerate to a nominal terminal velocity in the y-direction, once the buoyancy force is matched by the drag force acting in the opposite direction. Depending on the fluid structures developed in the wake the bubble may travel in a straight line, oscillate or even lift away from the surface (lift off from the surface was not observed in any of the tests). This indicates that the drag force can have components in the x, y and z directions. When the bubble is sliding on a heated surface, it is these factors that influence the bubble motion and heat transfer from the surface.

In the present study, high speed video recordings allowed a detailed analysis of various aspects of bubble dynamics such as shape, path, eccentricity & orientation, oscillation frequency, velocity, acceleration and ultimately the forces acting on the bubble. The following sections describe these results in detail for each bubble volume on both the heated and non-heated surface. These results are for steady state tests of

which there were 25.

5.2.1 Bubble position and shape

Figures 5.2 to 5.5 show the position and shape of the bubble boundary in the x-y plane with increasing volume for both (a) the heated and (b) the non-heated surface. They are created by superimposing the boundary of the bubble at time intervals of 0.016 s and 0.024 s (every fourth camera frame for the heated tests, every sixth frame for the non-heated tests), for the heated and non-heated tests respectively, over a test area of 140 mm. They show both path and shape fluctuations with time. Included is a photographic representation of the bubble in the y-z plane created by superimposing the bubble image at time intervals of 0.032 s and 0.048 s for the heated and non-heated tests respectively. Each black outline of the bubble in the x-y plane has a corresponding y-z photographic image. As can be seen in Figures 5.2 to 5.5, the bubble position oscillates to some extent in the x direction in all tests. There does not appear to be much difference between the bubble shape and path for the heated and non-heated tests except, marginally, in the case of the 0.2 and 0.4 ml bubble.

For the 0.05 ml bubble (Figure 5.2), the boundary is close to that of an ellipse, slightly elongated in the direction perpendicular to its motion. Its shape remains roughly constant over the test section but changes its orientation[2] as it moves, an effect that will be discussed in Section 5.2.2. The bubble slides along the plate with a slight sinusoidal oscillation, not deviating much from the mean x position (designated $s_x = 0$). There does not seem to be any noticeable difference in motion or shape between the heated and non-heated surface conditions for bubbles of this volume.

When the volume is increased to 0.1 ml (Figure 5.3) the bubble size in the x-y plane increases noticeably while the oscillatory nature persists. The bubble shape is that of an ellipse, elongated in the direction perpendicular to its motion. Once again the bubble shape remains apparently constant over the observed area. Similar to the 0.05 ml bubble there is no perceivable difference in bubble motion between heated and

---

[2]The orientation refers to the angle the major axis of the ellipse makes with the x axis. As the bubble moves, this angle oscillates between a maximum and minimum.
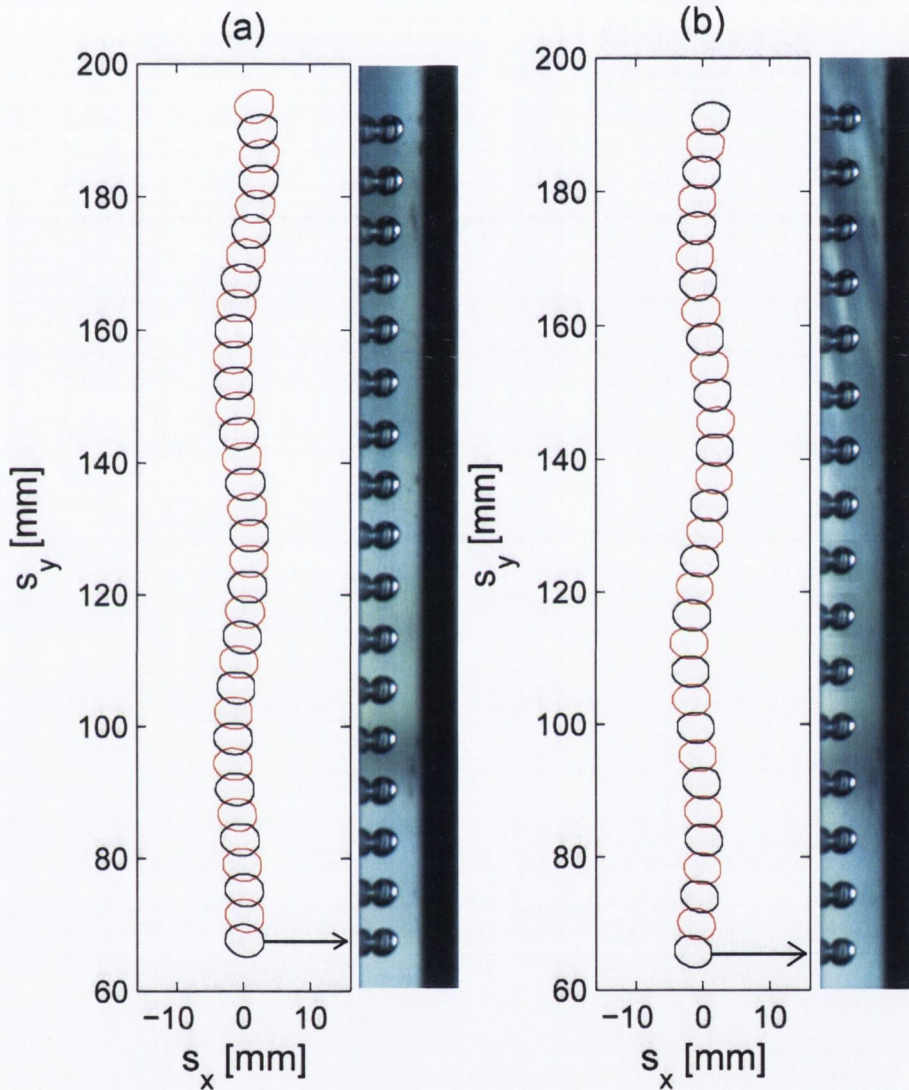
Figure 5.2: Bubble boundary in the x-y plane at time intervals of 0.016 s and 0.024 s for the 0.05 ml bubble sliding on the (a) heated and (b) non-heated surface respectively. The bubble is traveling from bottom to top of the image with $x = 0$ as the mean x position. Included is a photographic representation every second outline of the bubble in the y-z plane corresponding to the black x-y outline.
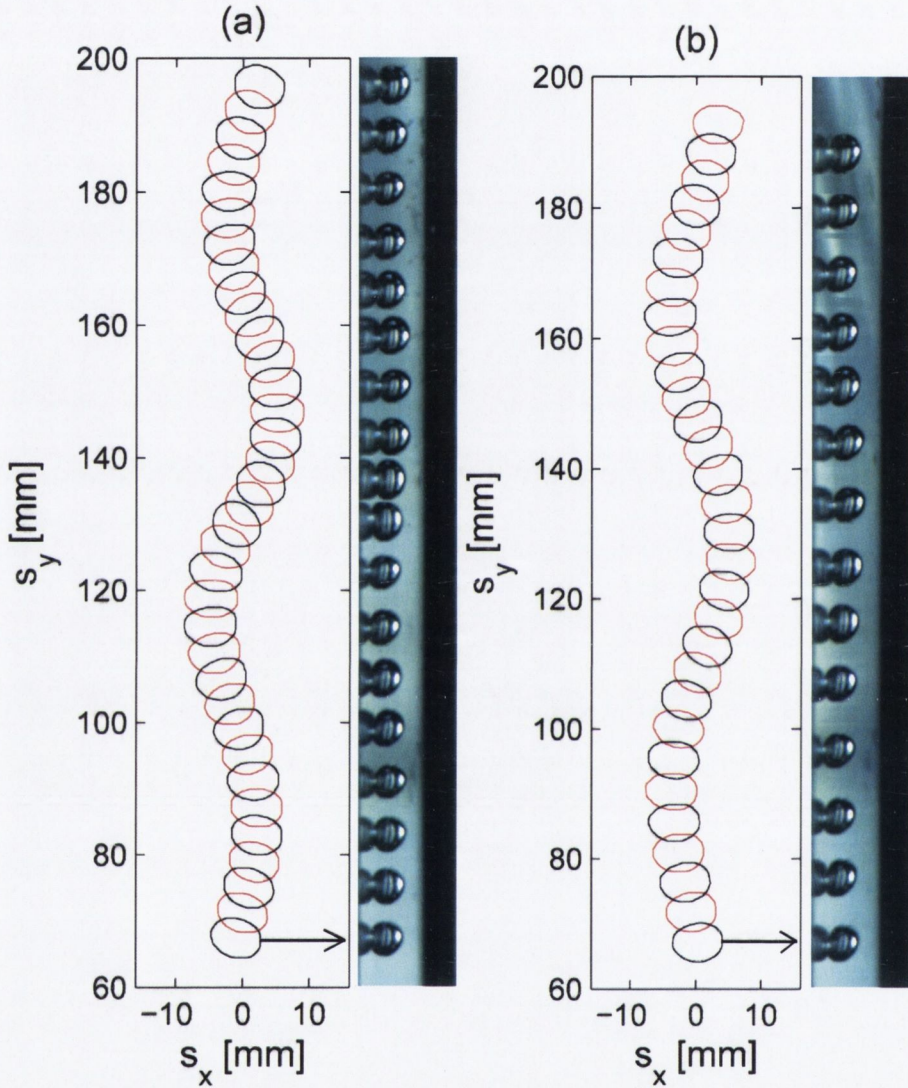
Figure 5.3: Bubble boundary in the x-y plane at time intervals of 0.016 s and 0.024 s for the 0.1 ml bubble sliding on the (a) heated and (b) non-heated surface respectively. The bubble is traveling from bottom to top of the image with $x = 0$ as the mean x position. Included is a photographic representation every second outline of the bubble in the y-z plane corresponding to the black x-y outline.
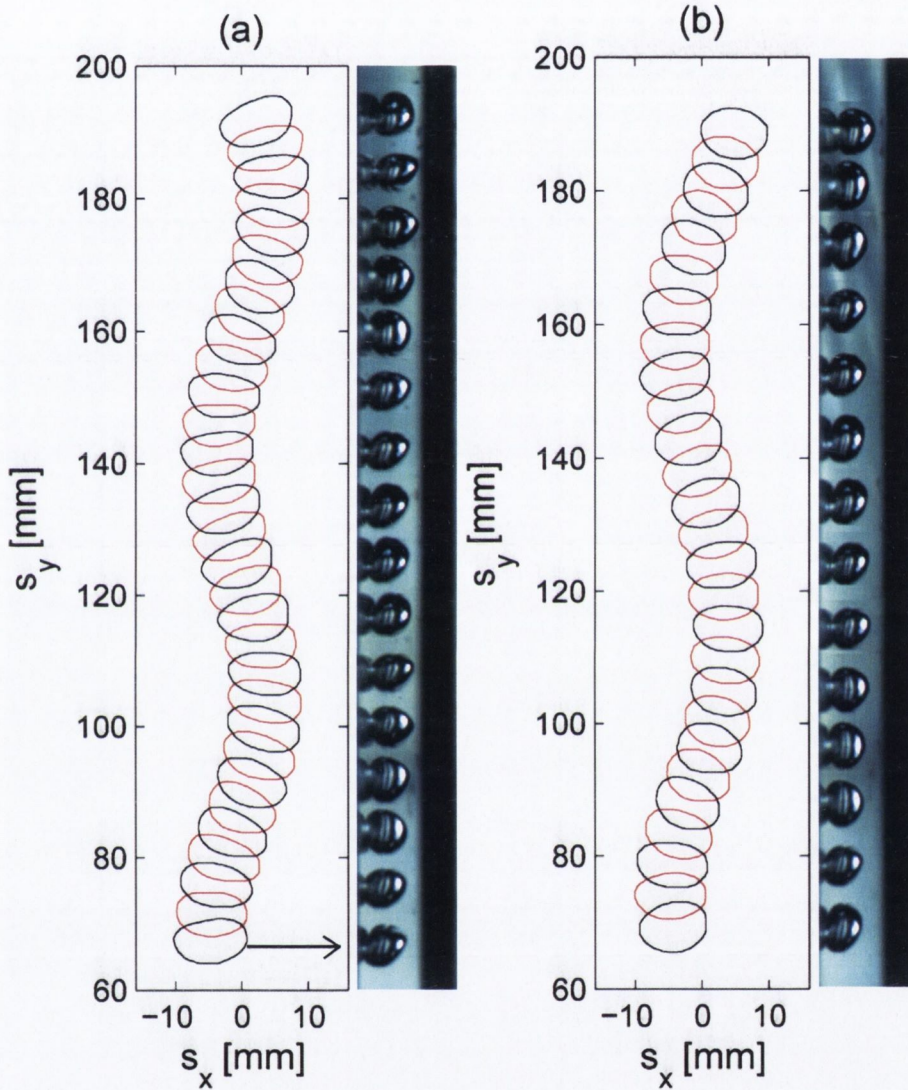
Figure 5.4: Bubble boundary in the x-y plane at time intervals of 0.016 s and 0.024 s for the 0.2 ml bubble sliding on the (a) heated and (b) non-heated surface respectively. The bubble is traveling from bottom to top of the image with $x = 0$ as the mean x position. Included is a photographic representation every second outline of the bubble in the y-z plane corresponding to the black x-y outline.
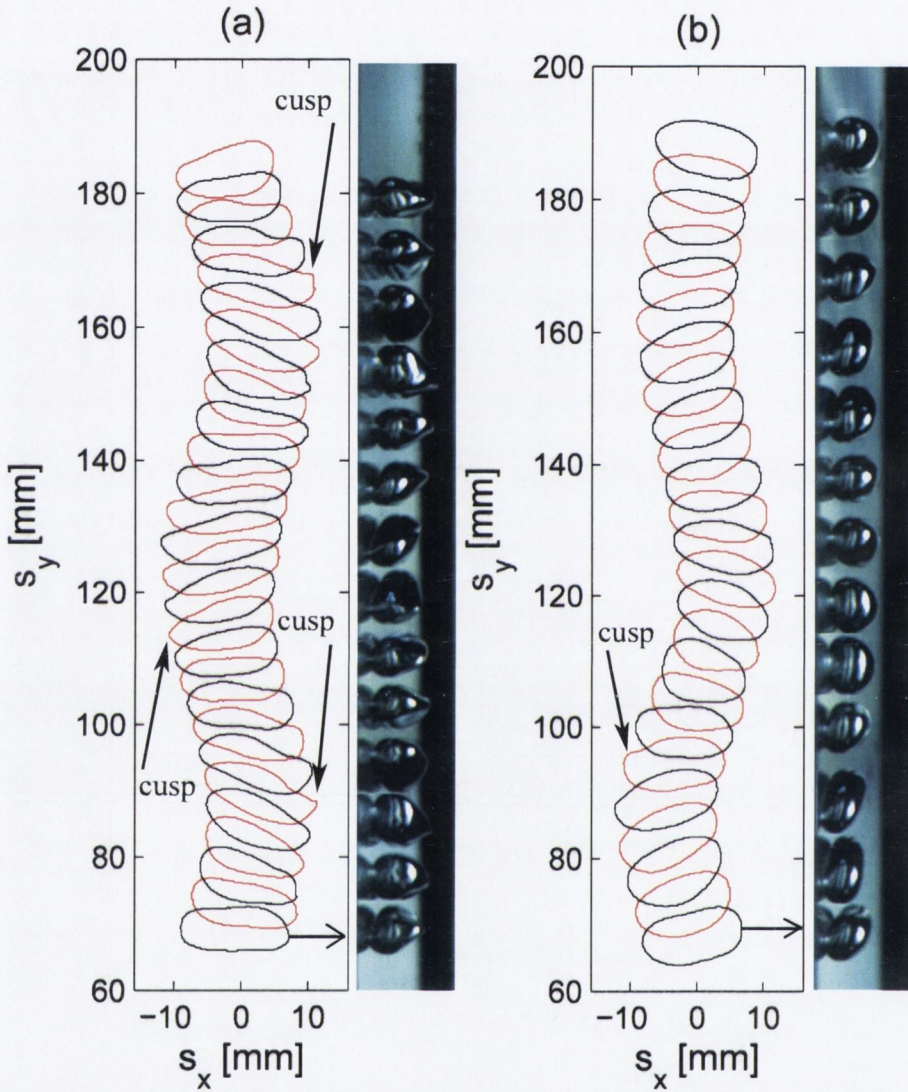
Figure 5.5: Bubble boundary in the x-y plane at time intervals of $0.016\ s$ and $0.024\ s$ for the $0.4\ ml$ bubble sliding on the (a) heated and (b) non-heated surface respectively. The bubble is traveling from bottom to top of the image with $x = 0$ as the mean x position. Included is a photographic representation every second outline of the bubble in the y-z plane corresponding to the black x-y outline.

non-heated tests.

Only when the bubble volume is increased to 0.2 *ml* (Figure 5.4) do differences between surface conditions begin to have a perceivable effect on bubble shape. As expected, in both cases, the bubble shape is much larger than the previous tests and still exhibits its oscillatory motion. Curiously, tests on the heated surface show the bubble to be slightly more elongated for some of its journey. It then returns to a shape that is close to that of the non-heated tests, oscillating between the two states as it moves. The bubble appears to not only have an oscillatory path but also shape oscillations. The bubble sliding on the heated surface, overall, has a more eccentric shape[3] when compared to the non-heated tests, an effect that will be discussed in Section 5.2.2.

These observations are amplified as the volume is increased to 0.4 *ml* (Figure 5.5). In the heated tests, the bubble size in the direction parallel to its motion, i.e. its minor ellipse axis, is not noticeably greater than that of the 0.2 *ml* bubble. It is, however, much wider. The surface deformation over time is much more noticeable now and the bubble appears to develop a sharp cusp on its edge near the maximum x displacement. In conjunction with this, the boundary appears to advance irregularly. When the cusp appears on, for example, the right hand side of the bubble, the left hand side is larger and positioned further up the test section. The cusp then disappears and the right hand side advances, overtakes the left hand side and itself becomes larger. The distribution of the bubble's mass seems linked to the orientation of the bubble. The non-heated tests exhibit a similar trend but not nearly to the same degree. There is evidence of a cusp developing but it is not as obvious and the bubble shape is not elongated to the same extent. A major difference between the heated and non-heated tests is the existence of a thermal boundary layer close to the surface that contains heated, low density, moving fluid (see Section 5.1). Bubbles of larger volume may protrude out of this layer into the adjacent, more dense, cooler fluid region. This results in both a density and velocity difference over the height of the bubble (z-direction). In addition, the temperature variation over the bubble interface will result in a surface

---

[3]The eccentricity is defined as the ratio of the distance between the two ellipse foci and the major axis length, its value has a range of 0 (a circle) to 1 (a line segment).

tension variation. The observed differences in shape between heated and non-heated tests may be due to the surface tension variations.

5.2.2 Eccentricity and orientation

Figure 5.6 illustrates both the fluctuating and mean eccentricity for the tests shown in Figures 5.2 to 5.5. The bubble outline is first fitted with an ellipse that closely approximates its shape. The ellipse has both major (longer) and minor (shorter) axes, the former of which is used to calculate the eccentricity and orientation. The eccentricity is defined as the ratio of the distance between the two foci and the major axis length. It can be thought of as a measure of the elongation of the ellipse. A value of 1 refers to a line segment and 0 is a perfect circle. Calculation of this is discussed in Chapter 4, Analysis.

The 0.05 ml bubble's eccentricity is relatively constant over the observed time period. It is of similar mean value for both the heated and non-heated tests. This indicates that shape fluctuations throughout its journey are small and the effects of heating on eccentricity is minimal for bubbles of this volume. The relatively low eccentricity of the 0.05 ml bubble can make it difficult for the computer program to identify the correct orientation, this may be the reason for the high frequency fluctuations observed for the 0.05 ml bubble. The fluctuations are stronger for tests on the non-heated surface which indicates that the previously mentioned slackening of the surface may also have an effect.

When the volume is increased to 0.1 ml there is both an increase in the mean eccentricity and the extent to which the bubble fluctuates. The 0.1 ml bubble is more elongated than the 0.05 ml bubble, its shape changing throughout its journey. The mean eccentricity is similar for both heated and non-heated tests but the heated test shows larger shape fluctuations.

Increasing the volume to 0.2 ml, the difference between the two surface conditions begins to have a more pronounced effect. The mean eccentricity for the heated tests is higher than that of non-heated tests. This indicates an elongation in the direction perpendicular to its motion, as previously observed in Figure 5.4. This trend continues

Figure 5.6: The time varying eccentricity of a bubble sliding on (a) the heated and (b) the non-heated surface for bubble volumes of 0.05 (red), 0.1 (blue), 0.2 (black) and 0.4 (magenta) *ml*. A value of 0 indicates circular, 1 is a line segment. The dashed lines represent the mean eccentricity over the observed time period.

for bubble volumes of 0.4 *ml*. Once again, this could be due to the presence of the thermal boundary layer in heated tests, mostly affecting bubbles with sufficient volume to protrude out into the cooler fluid.

For all heated tests above 0.05 *ml* the eccentricity-time trend indicates the bubble remains elongated for the majority of the time (an effect more noticeable at higher volumes). It only returns to a less elongated shape for short amounts of time. This is characterised by the relatively smooth peaks but sharp troughs. The non-heated tests also show this trend but to a lesser extent (smoother peaks and troughs). Something within the wake appears to be exerting a force on the bubble that stretches it along its major axis, then releases it for a short amount of time before repeating the cycle.

Figure 5.7 shows the orientation of the ellipse that approximates the bubble. The angle is measured between the major ellipse axis and the positive x-axis. The figure illustrates the time varying direction of the bubble as it traverses the plate.

Interestingly, for all but the 0.05 *ml* bubble, the angle, rate of change of angle and the maximum angle observed are quite similar between the heated and non-heated tests. There is also little effect of increasing volume on these parameters. The orientation angle oscillates from zero to a maximum of approximately 20°, back down to its minimum of −20° and then returns to zero in approximately 0.4 seconds. This corresponds to the bubble aligning its major elliptical axis perpendicular to the direction it travels. The non-heated tests show a similar trend. The 0.05 *ml* bubble does show an oscillating trend but the data are noisy. Once again, this is possibly due to the relatively circular shape of the bubble making it difficult to fit with an ellipse, as previously mentioned.

5.2.3   Path oscillation frequency

Figure 5.8 illustrates the bubble's path oscillation frequency as a function of volume. It is based on the fluctuations in x displacement with time. The figure shows both the value for each individual test and the mean at each volume for heated and non-heated surface conditions. Transitional tests were omitted from calculation of the mean and will be discussed in Section 5.2.6.
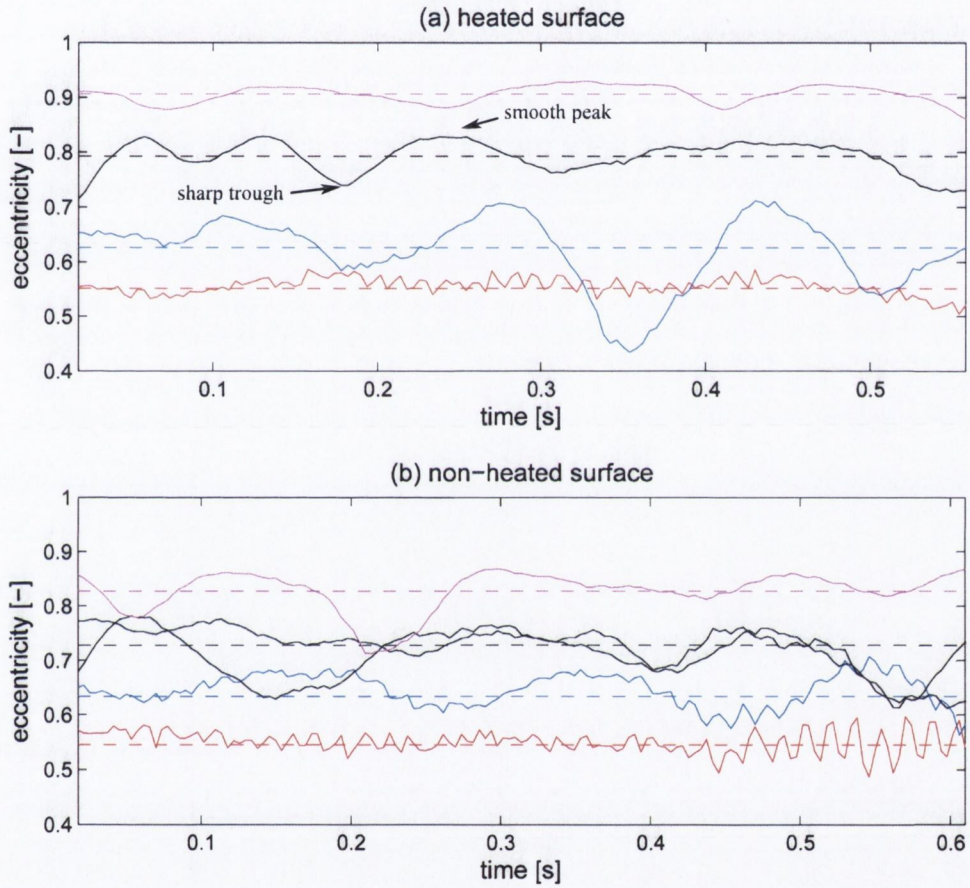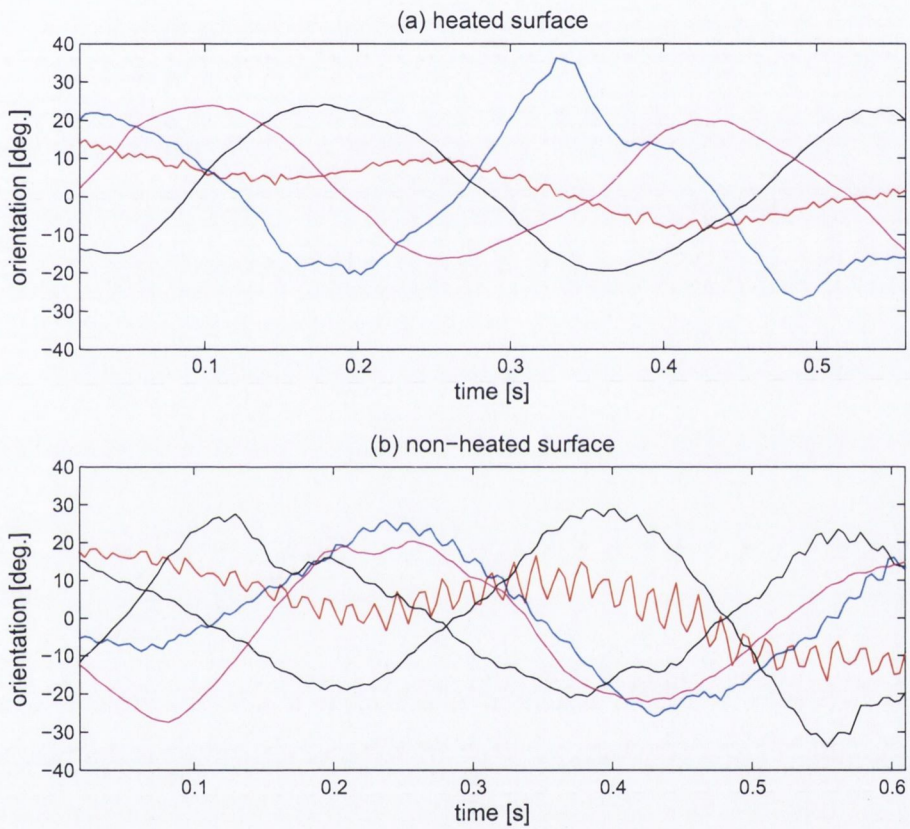
Figure 5.7: The time varying orientation of a bubble sliding on (a) the heated and (b) the non-heated surface for bubble volumes of 0.05 (red), 0.1 (blue), 0.2 (black) and 0.4 (magenta) *ml*. The angle is measured in degrees between the major ellipse axis and the *x* axis.
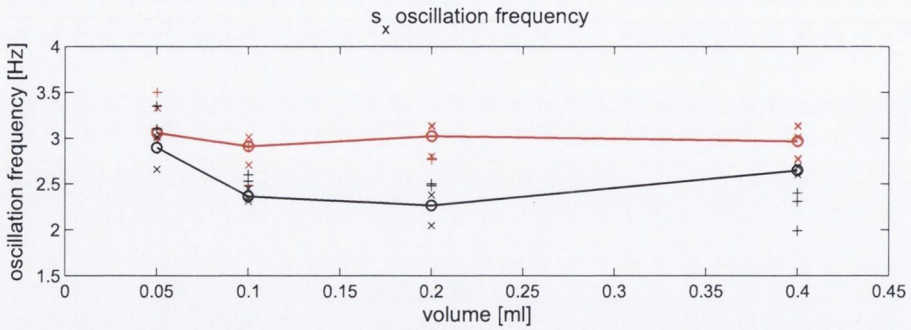
Figure 5.8: Bubble x displacement oscillation frequency variation with volume for both a heated (red) and non-heated (black) surface. Superimposed are the individual values ($\times$) and mean ($\circ$) at each volume. Calculation of the mean excludes transitional tests, although their values are calculated and presented for the portion of the surface where they did oscillate ($+$).

As the figure indicates, the path oscillation frequency appears to be roughly constant at 3 Hz for all bubble volumes on the heated surface. On the non-heated surface, the 0.05 ml bubble has a value close to that of heated tests which reduces to approximately 2.3 Hz for the 0.1 and 0.2 ml bubbles. There is a slight increase again for the 0.4 ml bubble to approximately 2.6 Hz. All bubbles traveling on the heated surface oscillate at a higher rate than those on the non-heated surface. The density difference in the thermal boundary layer generates fluid motion along the surface in the positive y-direction (see Section 5.1). Bubbles sliding along the heated surface within this layer are expected to travel faster than those on the non-heated surface and therefore would have a higher oscillation frequency (relative to a stationary observer). Bubble oscillation indicates a periodic nature to the wake behind the bubble. As it slides along the surface, there appears to be a dominant force within the wake alternately moving the bubble in the positive, then negative x-direction. The frequency of oscillation appears to have a weak dependence on volume, although the oscillation amplitude increases with volume as can be seen in Figures 5.2 to 5.5. The next section considers the bubble velocity and its relevance to bubble position, shape and oscillation.

5.2.4 Velocity

The velocity magnitude is calculated as $|v| = \sqrt{v_x^2 + v_y^2}$ (v_z is negligible), where v_x and v_y are the velocity in the x and y directions respectively. Figure 5.9 shows the time varying velocity magnitude of a single test at each volume. The mean for that specific test is also included.
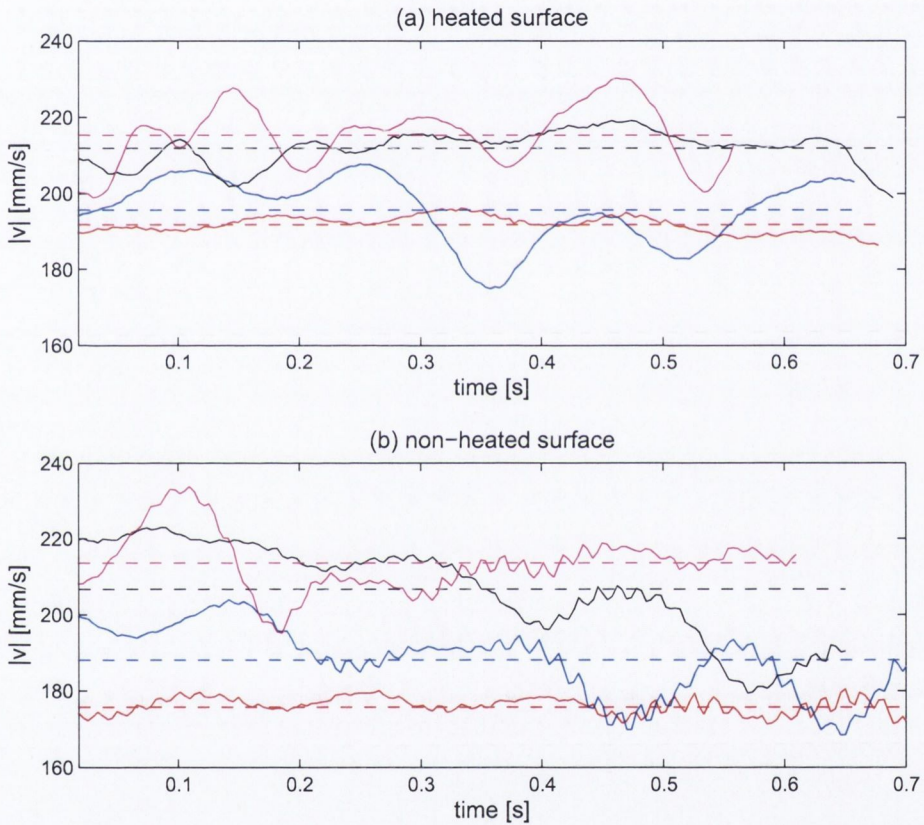
Figure 5.9: Bubble velocity magnitude, $|v|$, vs. time for a single test at each bubble volume of 0.05 ml (red), 0.10 ml (black), 0.20 ml (blue) and 0.40 ml (magenta) for both (a) heated and (b) non-heated surface conditions. Dashed lines indicate the mean value for that test.

As the figure shows, the bubble mean velocity increases with increasing volume in all cases. The velocity of each bubble fluctuates about its own individual mean as it traverses the test section, although not very consistently. These fluctuations are generally observed to increase in magnitude with increasing volume. Not all tests exhibited

this general behaviour, some bubbles travel at a relatively constant velocity over some of the length of the test section before fluctuations occur, this will be discussed in Section 5.2.6 (transitional tests). The non-heated tests exhibit the erroneous high frequency fluctuations highlighted at the start of this chapter but the general trends are still present.

Figure 5.10 condenses the velocity results from all tests into both the mean velocity for each individual test and the overall mean velocity of all steady state tests at each volume. The overall mean is calculated excluding transitional tests but they are included in the figure for reference. It can be seen from Figure 5.10 that heating
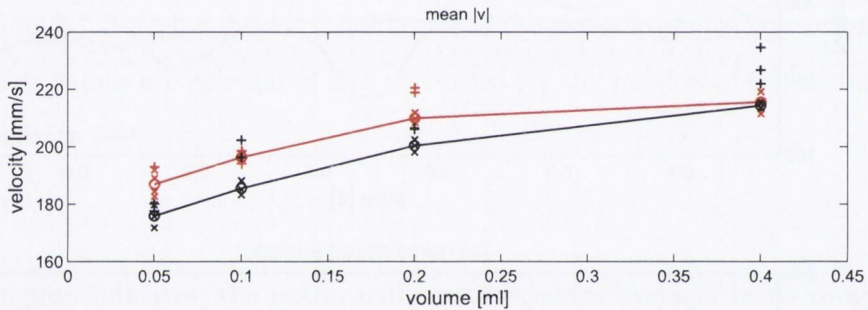
Figure 5.10: Mean bubble velocity magnitude, $|v|$, for each individual test ($\times$) including the mean of all tests at each volume ($\circ$), for both the heated (red) and non-heated (black) surface. Calculation of the mean excludes transitional tests ($+$).

of the surface results in a higher mean bubble velocity, although the 0.4 ml bubble has a similar value on both the heated and non-heated surface. Both curves show a diminishing effect of volume on the mean velocity but the diminishing effect is stronger on the heated surface. The difference in velocity between heated and non-heated conditions is approximately 12 mm/s for the 0.05, 0.1 and 0.2 ml bubble. This is in the region of the velocity of the thermal boundary layer as discussed in Section 5.1 (4-12 mm/s in a parallel plane 3 mm from the surface). As the bubble moves within the thermal boundary layer, it has a higher velocity relative to the surface. Strangely, this effect is not observed for the 0.4 ml bubble, perhaps partly due to the large volume interacting with the slower moving fluid outside the boundary layer. In all steady state

tests, the slowest bubbles sliding on the heated surface still travel faster, on average, than the fastest bubbles on the non-heated surface.

Figure 5.11 shows the oscillation frequency of the bubble's x and y velocities with increasing volume. Included is the ratio of oscillation ($R = f_{v,y}/f_{v,x}$). Figure 5.11 (a) shows, as expected, a strong link between x position oscillations (Figure 5.8) and x velocity oscillations, it is presented here for easy comparison to y velocity fluctuations. Figure 5.11 (b) shows the y velocity oscillation frequency as a function of volume. At low volumes the mean oscillation frequency is very similar for both heated and non-heated surfaces, above this, the frequency reduces for both the 0.1 and 0.2 ml bubbles and then increases again for 0.4 ml. Apart from the 0.05 ml tests, the oscillation frequency is always higher on the heated surface. Calculation of the ratio of oscillations, Figure 5.11 (c), reveals that the bubble y velocity oscillates twice for every x velocity oscillation. The ratio is slightly higher than 2 for the 0.05 ml bubble, although this is probably attributed to experimental scatter and not any natural phenomenon. This would indicate either an over estimation of the 0.05 ml y velocity oscillation or under estimation of the x velocity oscillation. It is most likely that for every x velocity fluctuation the y velocity fluctuates twice. This, again, suggests a periodic nature to the bubble wake.

Figure 5.12 to 5.15 show the bubble's position and shape coloured by v_x, v_y and $|v|$ for the 0.05, 0.1, 0.2 and 0.4 ml bubbles respectively, for the heated surface only. Bubbles sliding on the non-heated surface showed similar trends but with lower magnitudes. A velocity-time graph for v_x and v_y is supplied as a reference.

Figure 5.12 (a) shows a strong link between the x velocity and the bubble's position on its period of oscillation. As the bubble zig-zags, v_x increases from zero at its furthest negative x displacement to a maximum at $s_x = 0$, the mean x displacement. It then reduces to zero once again at the largest positive x displacement. The maximum x velocity is reached each time the bubble crosses the $s_x = 0$ position. Figure 5.12 (b) illustrates the relationship between v_y and bubble shape and position. It can be seen that the y velocity fluctuates at a higher rate than the x velocity, as previously indicated by Figure 5.11, at a ratio of approximately 2 to 1. The y velocity is at a local minimum at $s_x = 0$ throughout the test section accelerating to a maximum at each
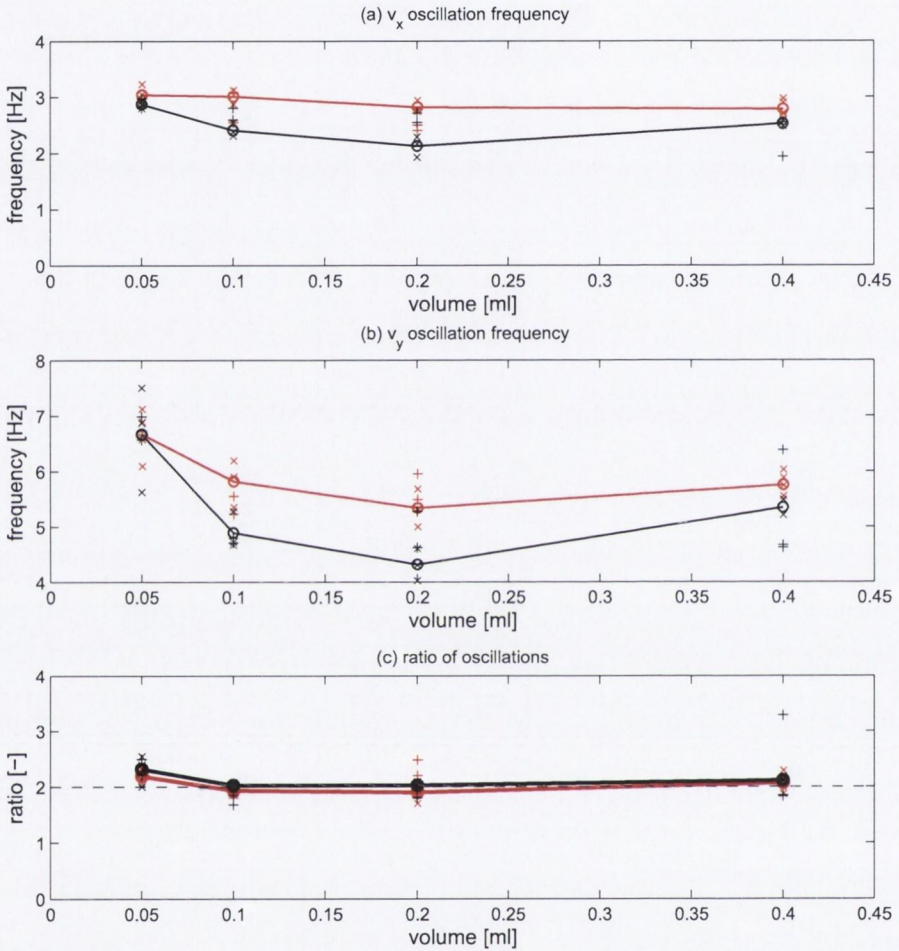
Figure 5.11: (a) v_x oscillation frequency ($f_{v,x}$), (b) v_y oscillation frequency ($f_{v,y}$) and (c) the frequency ratio ($R = f_{v,y}/f_{v,x}$) as a function of volume for both heated (red) and non-heated (black) surfaces. Superimposed are the individual values ($\times$) and mean ($\circ$) at each volume. Calculation of the mean excludes transitional tests, although their values are presented for the portion of the surface where they did oscillate ($+$).
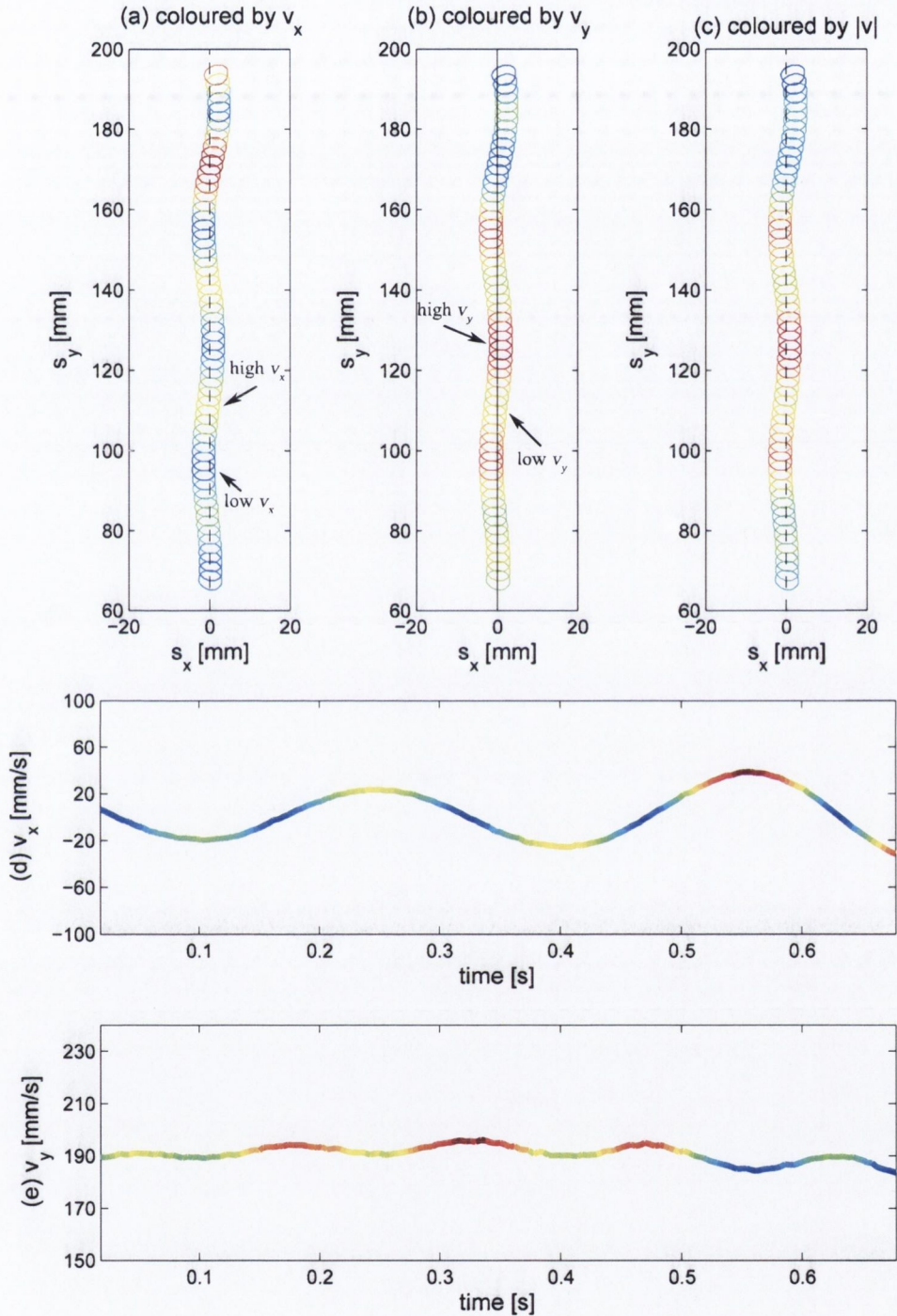
Figure 5.12: Bubble shape, velocity and position for the steady state 0.05 ml bubble sliding on the heated surface. The colour of the boundary represent (a) v_x, (b) v_y and (c) $|v|$ at that instant. The velocity variation in (d) the x direction and (e) the y direction with time are supplied as a reference.
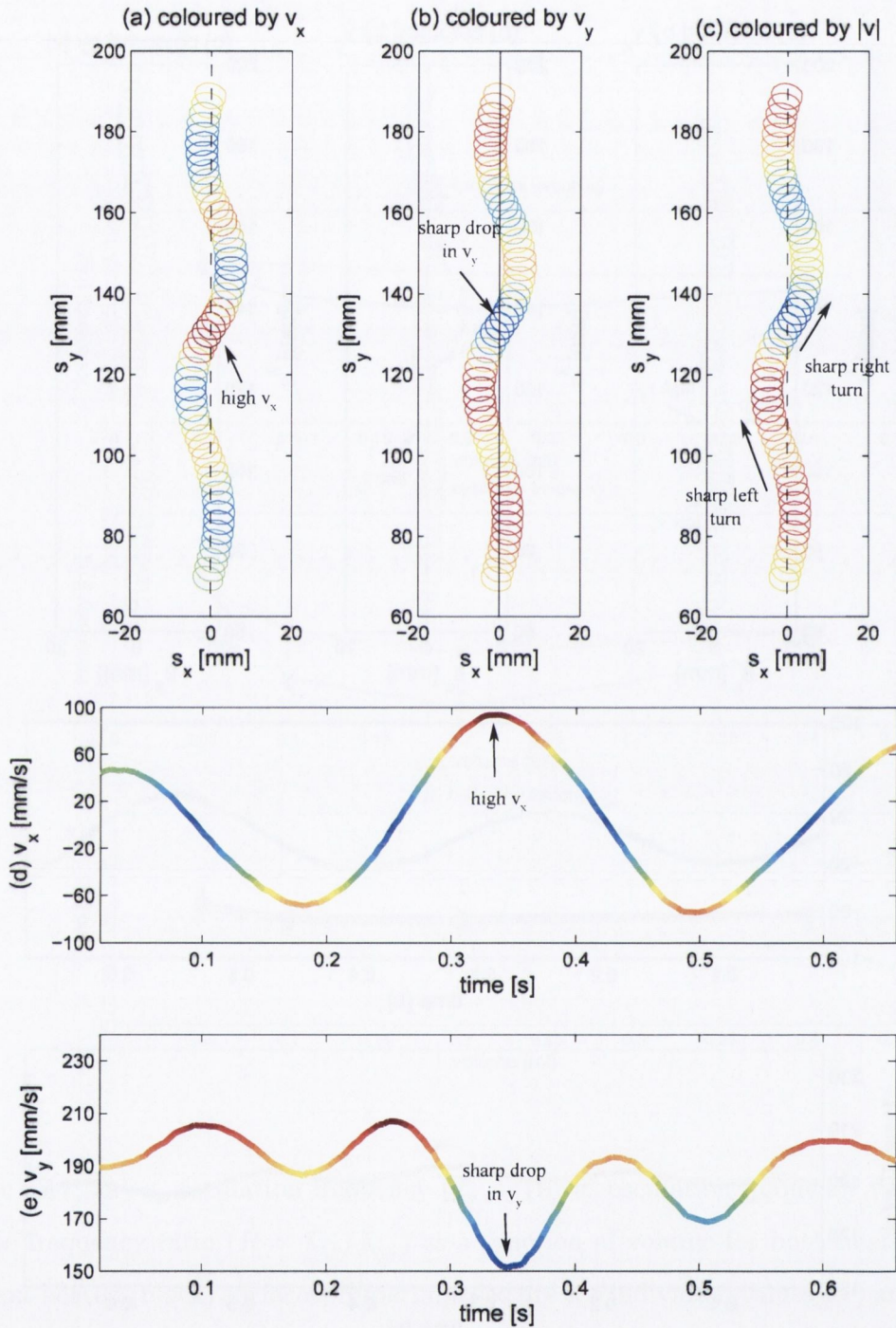
Figure 5.13: Bubble shape, velocity and position for the steady state 0.1 ml bubble sliding on the heated surface. The colour of the boundary represent (a) v_x, (b) v_y and (c) $|v|$ at that instant. The velocity variation in (d) the x direction and (e) the y direction with time are supplied as a reference.
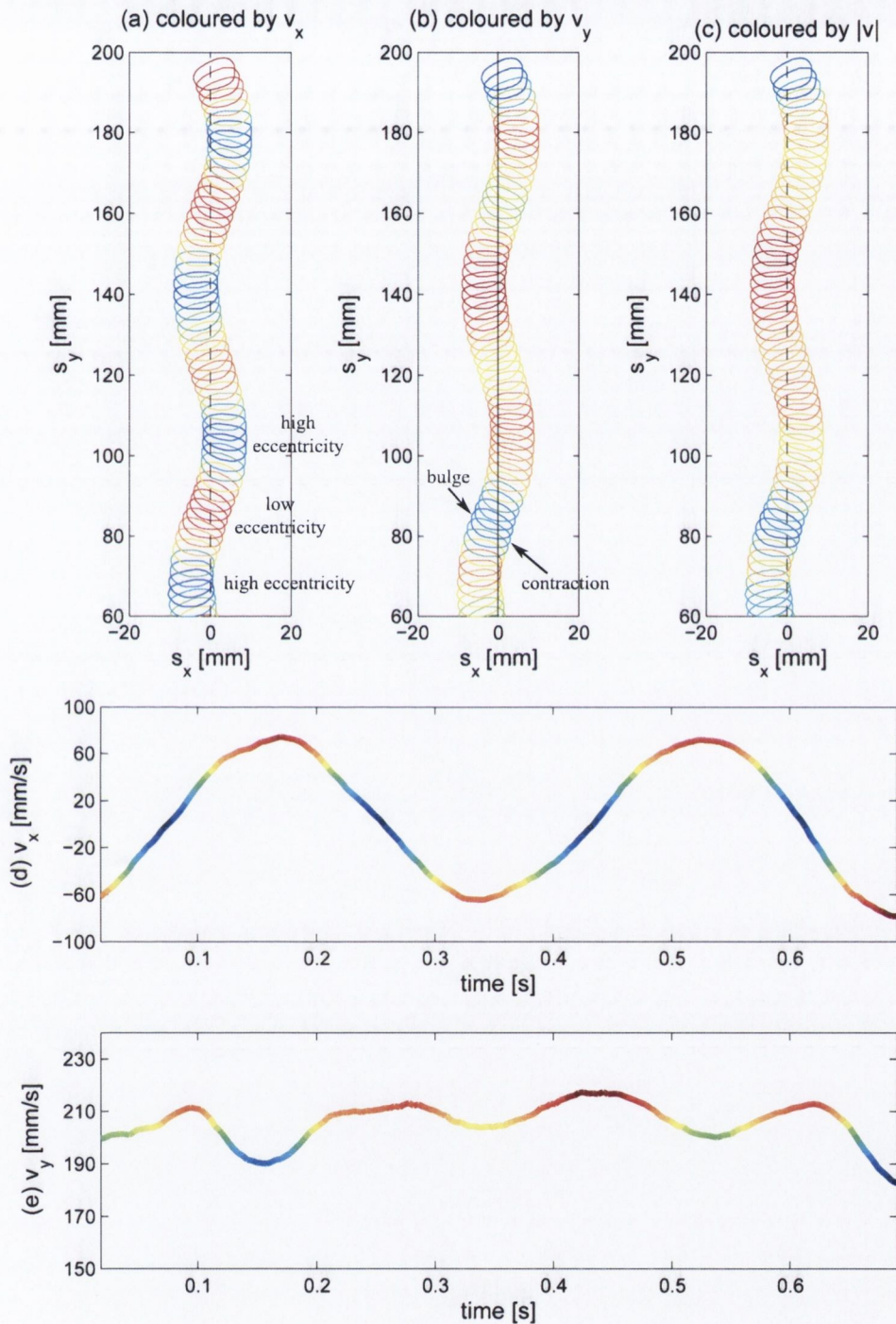
Figure 5.14: Bubble shape, velocity and position for the steady state 0.2 *ml* bubble sliding on the heated surface. The colour of the boundary represent (a) v_x, (b) v_y and (c) $|v|$ at that instant. The velocity variation in (d) the x direction and (e) the y direction with time are supplied as a reference.
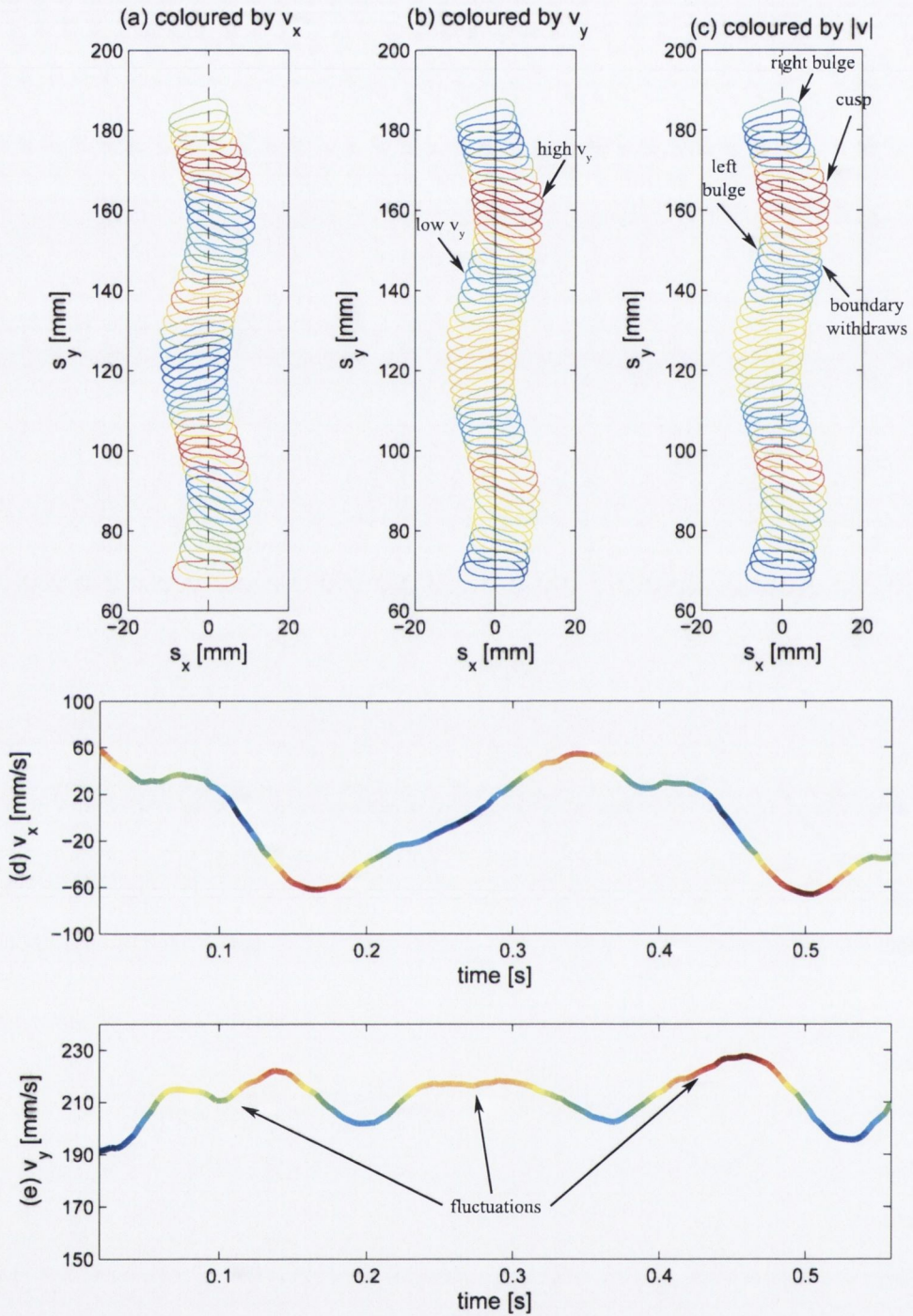
Figure 5.15: Bubble shape, velocity and position for the steady state 0.4 ml bubble sliding on the heated surface. The colour of the boundary represent (a) v_x, (b) v_y and (c) $|v|$ at that instant. The velocity variation in (d) the x direction and (e) the y direction with time are supplied as a reference.

maximum in s_x. Figure 5.12 (c) shows bubble position and shape coloured by velocity magnitude, $|v|$. It can be seen, for most of the test surface, that each time v_x is at a maximum, $|v|$ is at a minimum, this corresponds to the position $s_x = 0$. Similarly, when v_x is minimum, the velocity magnitude is either at, or just about to reach, a local maximum ($|v| = max$). Similar to v_y, each time v_x completes one oscillation, $|v|$ completes two.

Figure 5.13 shows the 0.1 ml bubble. The trends are very similar except for a sharp drop in v_y observed from $t \approx 0.27 - 0.35$ s (i.e. at $s_y = 130$ mm). At this region are the highest x velocity and lowest y velocity observed for the test. Over the same time span, the bubble performs a sharp change in direction in comparison to its previous motion. After this, the y velocity oscillates up towards its previous values. It is most likely that this is the result of a large change in the force exerted on the bubble by the wake. As the bubble approaches $s_y = 85$ mm it is traveling at a high $|v|$, the bubble suddenly veers left and loses momentum. The balance of forces in the wake must be now dominant in the negative x direction and the bubble moves that way. It once again reaches a maximum $|v|$ at $s_y = 115$ mm but this time it suddenly veers right. As this occurs, $|v|$ dramatically reduces. Something within the wake is causing the bubble to decelerate and turn sharply. This will be returned to in relation to observed heat transfer aspects in Section 5.5.

Figure 5.14 shows the effect of increasing the volume to 0.2 ml. In general, the bubble behaves similar to the 0.05 and 0.1 ml tests but there are some additional aspects highlighted here. Shape changes, as discussed in Section 5.2.2, are becoming more obvious and there appears to be a link between the bubble shape and its position and velocity. On each period of path oscillation, e.g. from $s_y = 70-140$ mm, the bubble shape twice changes from high eccentricity (elongated) at its maximum x displacement to low eccentricity (more circular) at $x = 0$, returning high for the next maximum x displacement. When the bubble is moving right the left side of the bubble appears bulged and the right is more contracted. This is reversed when the bubble is traveling left. Wake structures must be affecting both the bubble trajectory and the shape. These effects only become noticeable with the larger, more deformable bubbles.

When the volume is increased to 0.4 ml, the observations made for the 0.2 ml

bubble become more apparent. Figure 5.15 illustrates this. The shape changes are now more dramatic with the cusp developing on alternating sides of the bubble as previously discussed in Section 5.2.1. Once again, there is a local minimum in v_y at each $s_x = 0$, increasing as the bubble travels around the curve to a maximum just before the bubble reaches $s_x = 0$ again. This is most apparent from $s_y = 130\ mm$ onwards. While the bubble is traveling right, the left hand side develops a bulge while at the same time the right hand side becomes contracted, v_y reduces to a local minimum. Soon after this, while v_y is increasing, the right hand side of the bubble withdraws sharply into the bubble. As v_y approaches its maximum, on the apex of the curve, a cusp develops and moves around towards the front right of the bubble. As v_y reduces to a local minimum, it is now the right hand side of the bubble that is bulged. In addition to this periodic shape fluctuation, both the x and y velocity show an additional, small fluctuation in their magnitudes (e.g. at $t = 0.1, 0.27, 0.42$ etc.). This always occurs when the bubble is exhibiting large shape fluctuations, a sudden change in x velocity and coupled with a change in y velocity. It may be due to bubble related phenomena or could be the result of the centroid moving as the bubble shape changes in the $x - y$ plane. This would result in an apparent velocity fluctuation. Wake structures appear to be growing in strength as the volume increases as they now appear to be able to greatly affect the shape of the bubble.

5.2.5 Force and acceleration

In order to obtain a better understanding of the nature of the bubble's wake, the forces on the bubble were estimated based on its acceleration. Figures 5.16 to 5.19 show the position, net forces and acceleration for the individual tests presented in Figures 5.12 to 5.15 respectively. The acceleration is calculated as the second derivative of position with respect to time, and as a result, noise in the original signal becomes amplified upon differentiation. The high frequency fluctuations observed in these figures are attributed to this noise.

Only results for the 0.1 ml bubble on the heated surface (Figure 5.17) are discussed in detail here. Figure 5.16, 5.18 and 5.19 all illustrate similar trends but differing

Figure 5.16: From top to bottom; (a) bubble x displacement, s_x, (b) net force in the x direction, ΣF_x, (c) the x acceleration, a_x, (d) the net force in the y direction, ΣF_y, and (e) the y acceleration, a_y, for the 0.05 ml bubble sliding on the heated surface. Superimposed on (b) and (d) is s_x and on (e) is a_x (not to scale).
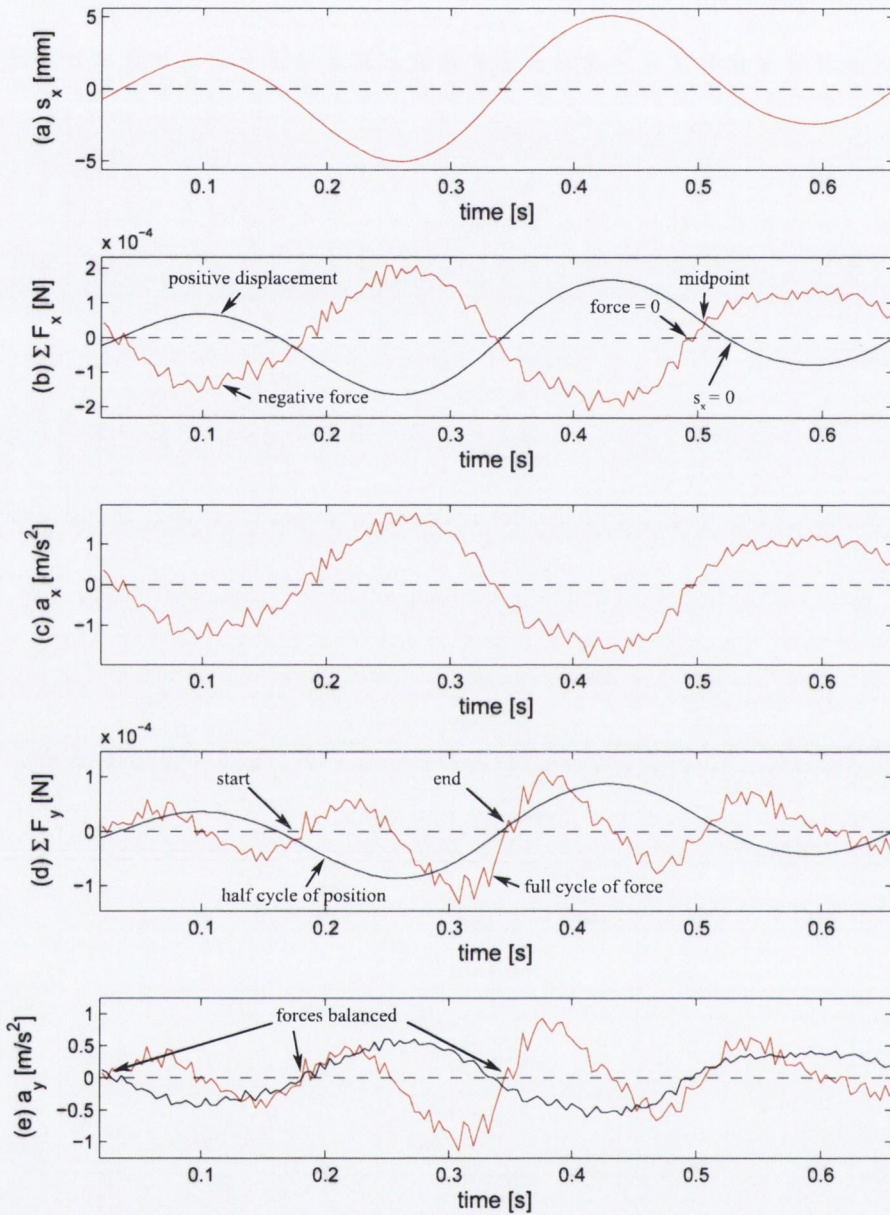
Figure 5.17: From top to bottom; (a) bubble x displacement, s_x, (b) net force in the x direction, ΣF_x, (c) the x acceleration, a_x, (d) the net force in the y direction, ΣF_y, and (e) the y acceleration, a_y, for the 0.10 ml bubble sliding on the heated surface. Superimposed on (b) and (d) is s_x and on (e) is a_x (not to scale).
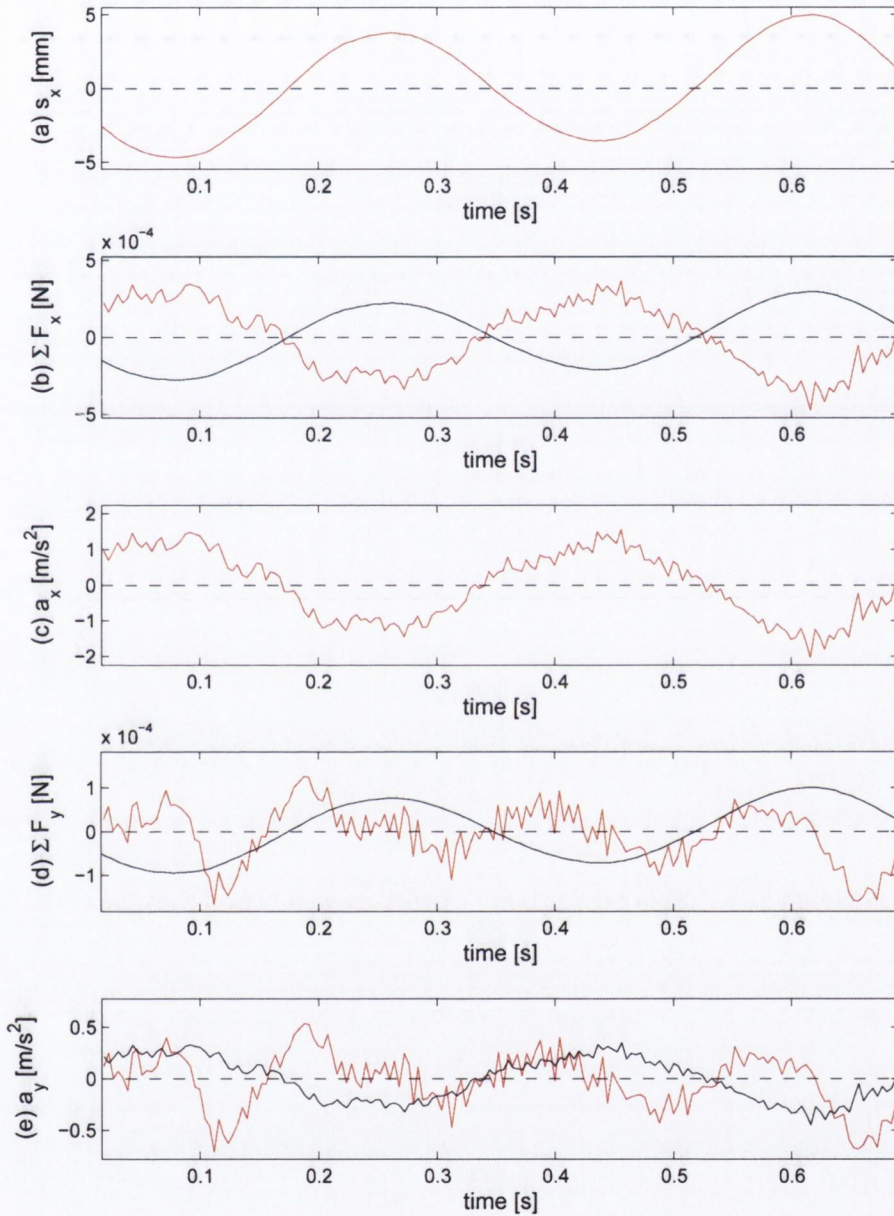
Figure 5.18: From top to bottom; (a) bubble x displacement, s_x, (b) net force in the x direction, ΣF_x, (c) the x acceleration, a_x, (d) the net force in the y direction, ΣF_y, and (e) the y acceleration, a_y, for the 0.2 ml bubble sliding on the heated surface. Superimposed on (b) and (d) is s_x and on (e) is a_x (not to scale).
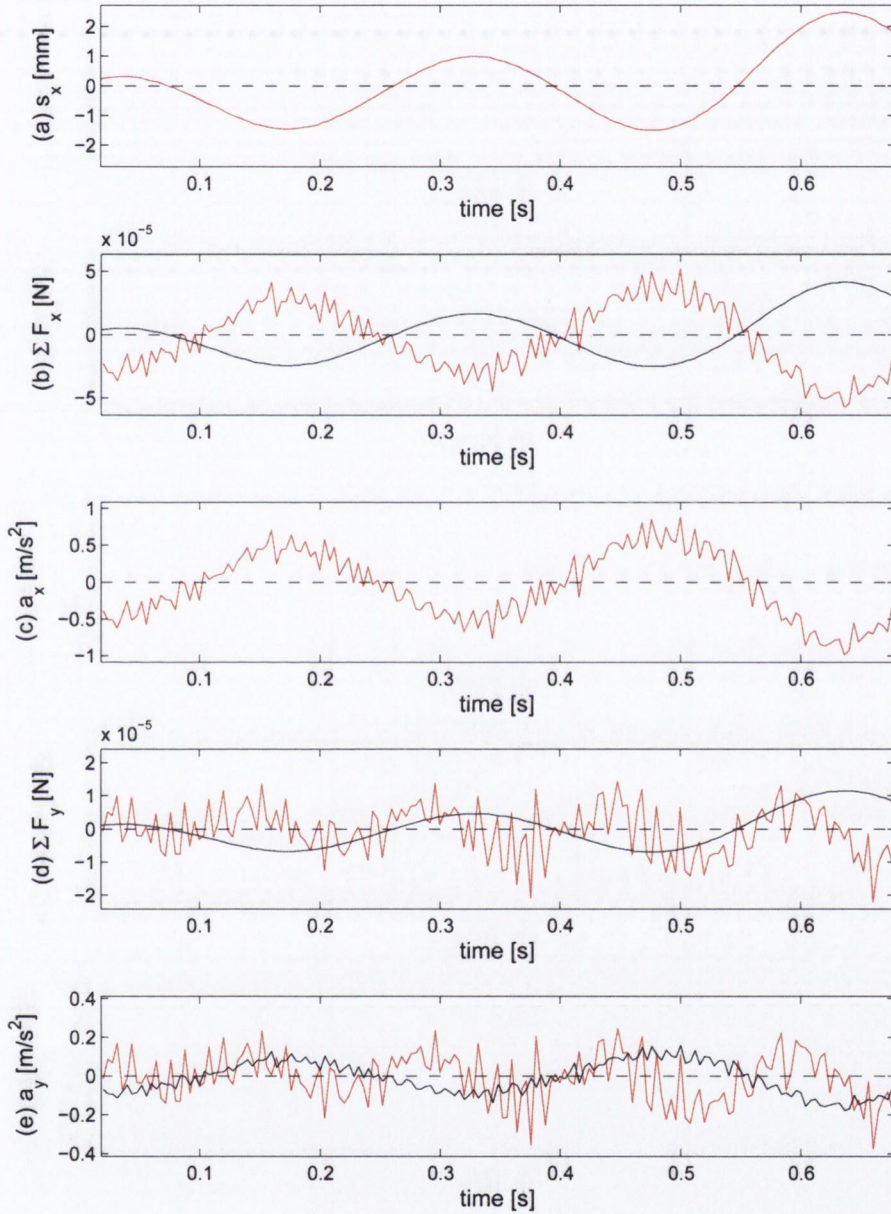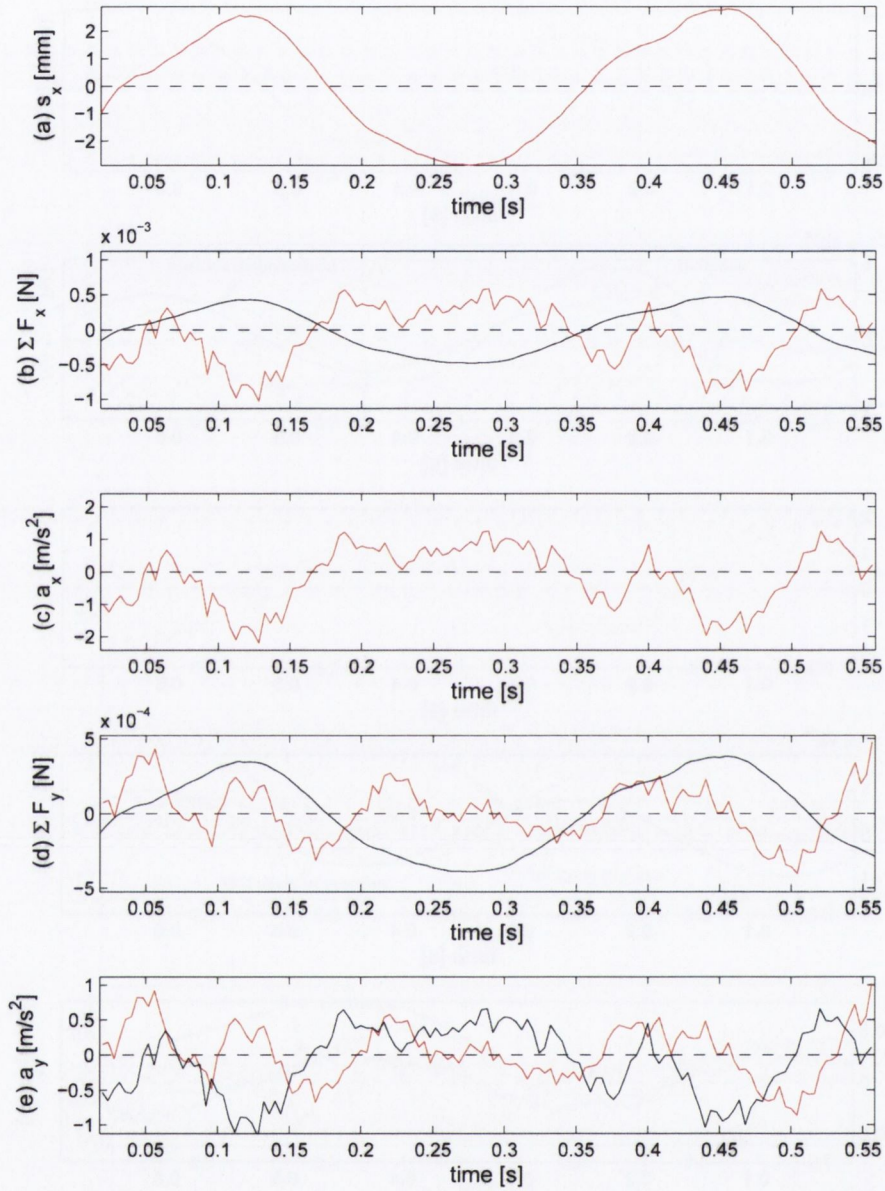
Figure 5.19: From top to bottom; (a) bubble x displacement, s_x, (b) net force in the x direction, ΣF_x, (c) the x acceleration, a_x, (d) the net force in the y direction, ΣF_y, and (e) the y acceleration, a_y, for the 0.4 ml bubble sliding on the heated surface. Superimposed on (b) and (d) is s_x and on (e) is a_x (not to scale).

magnitudes, they are included for completeness. Similarly, tests performed on the non-heated surface illustrate the same trends, although badly affected by noise (discussed at the beginning of the chapter), and are omitted.

Figure 5.17 (a)-(c) show the position, net force and acceleration in the x direction. Superimposed on (b) is the bubble position (black line, not to scale). It can be seen that ΣF_x (the net x force) generally acts to restore the bubble back towards its mean x position (i.e. towards $s_x = 0$). It appears that when the bubble position is positive, ΣF_x, and therefore a_x is negative. This is not strictly true; the points where the x forces and acceleration change direction (i.e. at $\Sigma F_x = 0$ & $a_x = 0$) do not coincide with the mean x position, $s_x = 0$. This is partly due to the fact that the mean is calculated over the full test section, even though the oscillation amplitude varies slightly throughout the test, ideally the mean should be calculated for each cycle but this introduces problems of its own since the amplitude can vary within that cycle. It is true, however, that ΣF_x, and therefore a_x, change their direction somewhere close to the midpoint between each local position maximum (i.e. somewhere close to midway between $|s_x| = \max$). The maximum net x force and acceleration for the 0.1 ml bubble are roughly 2×10^{-4} N and 1.8 m/s^2.

Figure 5.17 (d) and (e) show the net y force as calculated from the y acceleration. Superimposed on (d) is the bubble position, s_x, and on (e) the acceleration in the x direction, a_x (black lines, both not to scale). It can be seen in Figure 5.17 (d) that each time the bubble completes one half cycle of position oscillation, ΣF_y and a_y complete one full oscillation. The bubble accelerates up to maximum $|v|$ at maximum displacement and then decelerates to a minimum close to $s_x = 0$. Figure 5.17 (e) shows the y acceleration (a_y) with the x acceleration (a_x) superimposed. Although a_y fluctuates at twice the rate of a_x, when a_x is zero, a_y is also zero (or very close to it). This implies that when ΣF_x is zero, ΣF_y is also zero, all the forces acting on the bubble are balanced for a short amount of time. The maximum net y force and acceleration observed are 1×10^{-4} N and 0.9 m/s^2.

Figure 5.16, 5.18 and 5.19 show similar trends although not as clearly as 5.17. Tests with the 0.05 ml bubble (Figure 5.16) exhibited only minute oscillations in the net y force and acceleration, resulting in a poor signal to noise ratio. The trends are

still there, although difficult to make out[4]. With the 0.2 ml bubble, boundary shape oscillations are probably beginning to show their effects, becoming amplified in the 0.4 ml tests. As the volume of the bubble begins to become unevenly distributed, the centroid moves with it, creating a high frequency undulation in the centroid position. It was previously noted that the x and y velocity fluctuate in conjunction with sudden shape fluctuations (see Section 5.2.4). The 0.1 ml bubble has the right balance between a pronounced motion and rigid shape to allow good interpretation of its dynamics.

The bubble's acceleration in the x or y direction is dictated by the sum of all the individual forces acting in the x and y directions. If the net force in the y direction is positive, the bubble will accelerate ($a_y > 0$) in the y direction. If it is negative, the bubble will decelerate ($a_y < 0$). The same can be said of the x forces. Only one force acts on the bubble to make it move, buoyancy. The buoyancy force, F_b, acts directly upwards against gravity but if the bubble is sliding on a surface, only the component acting parallel to the surface is considered ($F_{b,y}$). Since F_b is based on the bubble volume, it is considered constant (neglecting any volume change due to change in pressure as the bubble rises through the fluid). Once moving, numerous other forces impede and affect that motion, including drag forces, marangoni forces and forces generated where the bubble contacts the surface.

Figures 5.20 to 5.23 illustrate (a) the net x force, ΣF_x, superimposed with bubble position, s_x (dashed line, not to scale) and (b) the relative values of the buoyancy force, $F_{b,y}$ (black line) and net y retarding force, $F_{d,y}$ corresponding to the tests previously discussed in Figures 5.16 to 5.19. The retarding force is considered to be the sum of all the other forces acting on the bubble apart from buoyancy. The buoyancy force is calculated based on the volume of water displaced by the bubble; only the component acting in the y direction is considered as the z component is balanced by the surface. Since buoyancy only acts in the y direction, some component of the drag force must

---

[4]It is worth noting that De Vries et al. [32] calculated the lateral lift force on a free rising bubble ($d_e = 1.6$ mm) to be 2.4×10^{-5} N. For the 0.05 ml bubbles in the present study ($d_e \approx 5.5$ mm), the maximum x force is calculated to be approximately 2.5×10^{-5} N. Although the bubbles in the present study are larger, the inclined surface results in lower velocity and possibly lower observed forces. The result indicates that the forces are within the correct order of magnitude.

cause the bubble to oscillate in the x direction and accelerate and decelerate in the y direction. The net x and y drag forces are calculated from the x and y acceleration.

Figure 5.20: (a) the net forces acting in the x direction, ΣF_x (red line) and bubble x displacement, s_x (black dashed line, not to scale) and (b) drag forces in the y direction, $\Sigma F_{d,y}$ (red line), and the buoyancy force in y direction, $F_{b,y}$ (black line), for the 0.05 ml bubble on a heated surface.

Once again, only results for the 0.1 ml bubble on the heated surface (Figure 5.21) are discussed in detail here. Figure 5.20, 5.22 and 5.23 all illustrate similar trends but differing magnitudes, they are included for completeness. Similarly, tests performed on the non-heated surface illustrate the same trends, although badly affected by noise (discussed in Section 5.2.4), and are omitted.

Comparing Figure 5.21 (b) with Figure 5.16 (e) shows that when the sum of the drag forces in the y direction, $\Sigma F_{d,y}$ exceeds the buoyancy force, the bubble will begin to decelerate in the y direction (i.e. the y velocity is reducing). Conversely, if $\Sigma F_{d,y}$ is less than the buoyancy force, the bubble will accelerate in the y direction. The figure indicates that there is a periodic change in net drag force in the y direction. There also exists a net drag force in the x direction, $\Sigma F_{d,x}$, that oscillates between the positive and negative x directions. This indicates that there is a periodic nature to the strength of the net forces in the x direction. For every period of oscillation of
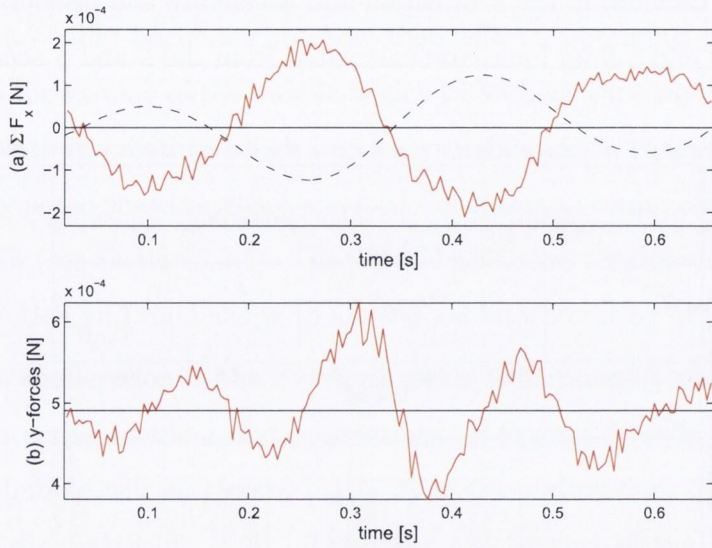
Figure 5.21: (a) the net forces acting in the x direction, ΣF_x (red line) and bubble x displacement, s_x (black dashed line, not to scale) and (b) drag forces in the y direction, $\Sigma F_{d,y}$ (red line), and the buoyancy force in y direction, $F_{b,y}$ (black line), for the 0.1 ml bubble on a heated surface.
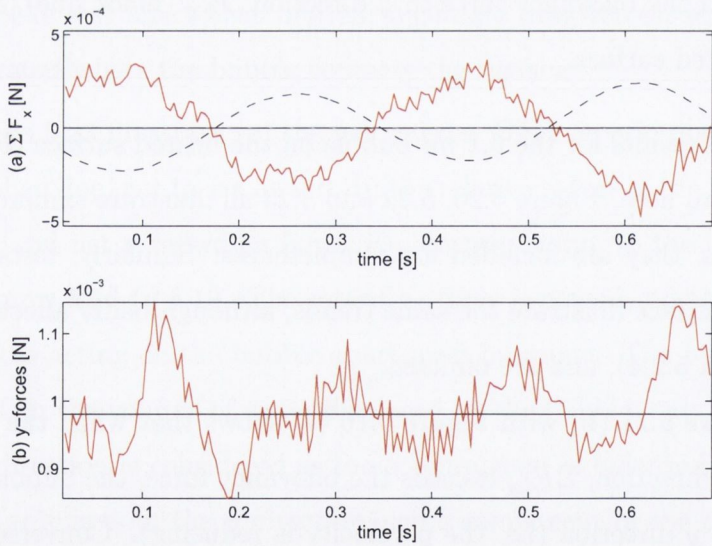
Figure 5.22: (a) the net forces acting in the x direction, ΣF_x (red line) and bubble x displacement, s_x (black dashed line, not to scale) and (b) drag forces in the y direction, $\Sigma F_{d,y}$ (red line), and the buoyancy force in y direction, $F_{b,y}$ (black line), for the 0.2 ml bubble on a heated surface.
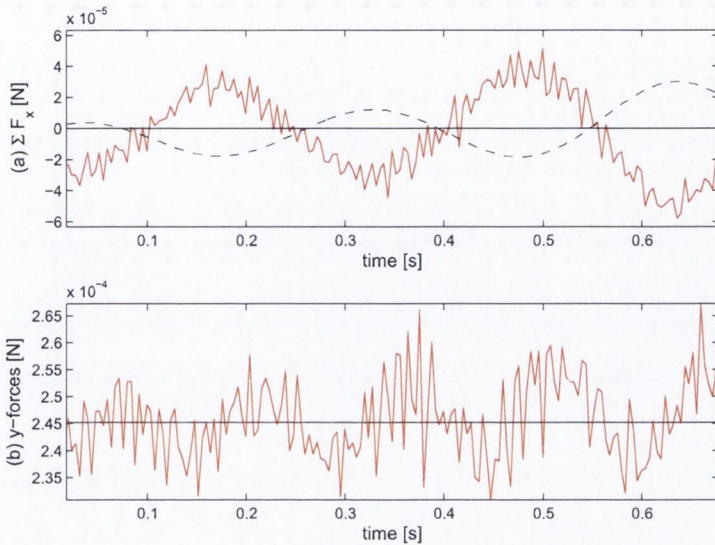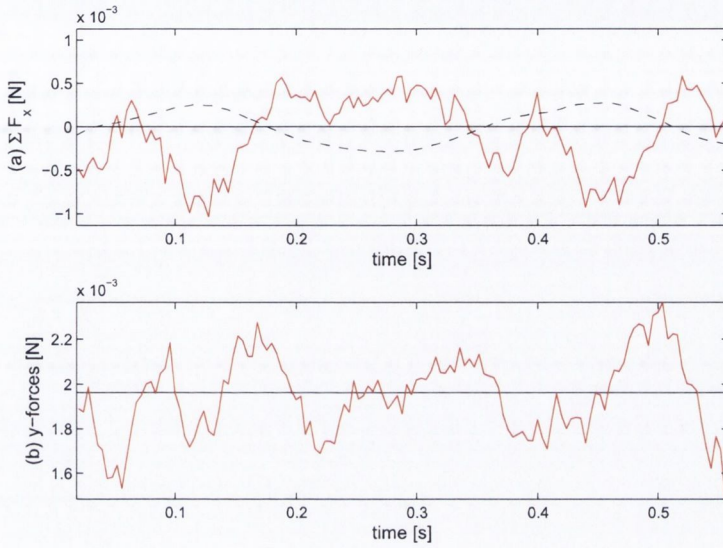
Figure 5.23: (a) the net forces acting in the x direction, ΣF_x (red line) and bubble x displacement, s_x (black dashed line, not to scale) and (b) drag forces in the y direction, $\Sigma F_{d,y}$ (red line), and the buoyancy force in y direction, $F_{b,y}$ (black line), for the 0.4 *ml* bubble on a heated surface.

$\Sigma F_{d,x}$, $\Sigma F_{d,y}$ oscillates twice. The net $\Sigma F_{d,x}$ causes the bubble to oscillate as it moves along the surface as observed in the previous sections. This indicates the existence of a possible continuous periodic development and shedding of the wake behind the bubble. The wake appears to shed alternately resulting in the positive and negative x forces, giving the bubble its oscillatory nature.

Previously discussed bubbles oscillated in a relatively steady state as they slid along the test section, i.e. the path and velocity fluctuations were relatively constant in frequency and amplitude. The next section discusses the characteristics of bubbles that did not conform to this general trend.

5.2.6 Transitional tests: bubble dynamics

Although numerous tests are classified as transitional, almost all still exhibit some steady state motion over the length of the test surface. Only the most extreme tests are considered here. All 0.4 *ml* bubbles sliding on the heated surface exhibited roughly steady state behaviour so results for the non-heated surface are included instead. The

more natural (stable) state for the bubble appears to be one which oscillates. In only one test did the bubble travel rectilinearly for any significant distance but eventually there were signs of periodic motion. The bubble motion is never observed to change from zig-zag to rectilinear. Most transitional tests are broadly characterised by the transition from high to low y velocity and the onset of strong x velocity oscillations. Figures 5.24 to 5.27 illustrate the position, velocity and shape fluctuations for bubbles that exhibited transitional behaviour. They are in the same format as Figures 5.12 to 5.15.

Figure 5.24 illustrates the only example where the bubble exhibited near rectilinear motion. Up until approximately $s_y = 150\ mm$ the bubble travels in a straight line, then begins to veer to the right, then left. Although the path is approximately straight, the y velocity is fluctuating and increasing. This reaches a maximum just before the bubble begins to turn, at $s_y = 150\ mm$. Beyond $s_y = 150\ mm$, v_y begins to decrease as v_x begins to oscillate; the bubble is starting to zig-zag. The motion of this particular bubble (up to $s_y = 150\ mm$) would indicate that the wake still exhibits a periodic behaviour but the net force in the x direction is zero ($v_x = 0$). The net y drag force is oscillating which results in the bubble accelerating and decelerating in the y direction. It would appear that there are two components to the drag force. When the bubble is oscillating these components are out of phase with each other but before this, when the bubble is traveling in a straight line the components are in phase. The drag components consist of areas of low pressure that gradually build in strength to a maximum, they are then shed and the cycle repeats. This figure may illustrate the transition from in phase (simultaneous) shedding to out of phase (alternate) shedding. Perhaps when $|v|$ reaches an upper limit an instability in the wake results in bias in the strength of one of the two wake components. This would result in a net x force in one direction, causing the bubble to move in that direction. Once this happens, the motion of the bubble itself may contribute to the alternate wake shedding mechanism. The alternate mode of shedding and resulting path oscillation appears to be more stable than simultaneous shedding so the bubble is never observed to return to rectilinear motion. These ideas will be discussed further in Sections 5.3, 5.4 and 5.5. The mean $|v|$ for this test are the highest at this volume. It would appear that bubbles traveling

Figure 5.24: Bubble shape, velocity and position for the transitional 0.05 ml bubble sliding on the heated surface. The colour of the boundary represent (a) v_x, (b) v_y and (c) $|v|$ at that instant. The velocity variation in the (d) x and (e) y direction with time are supplied as a reference.
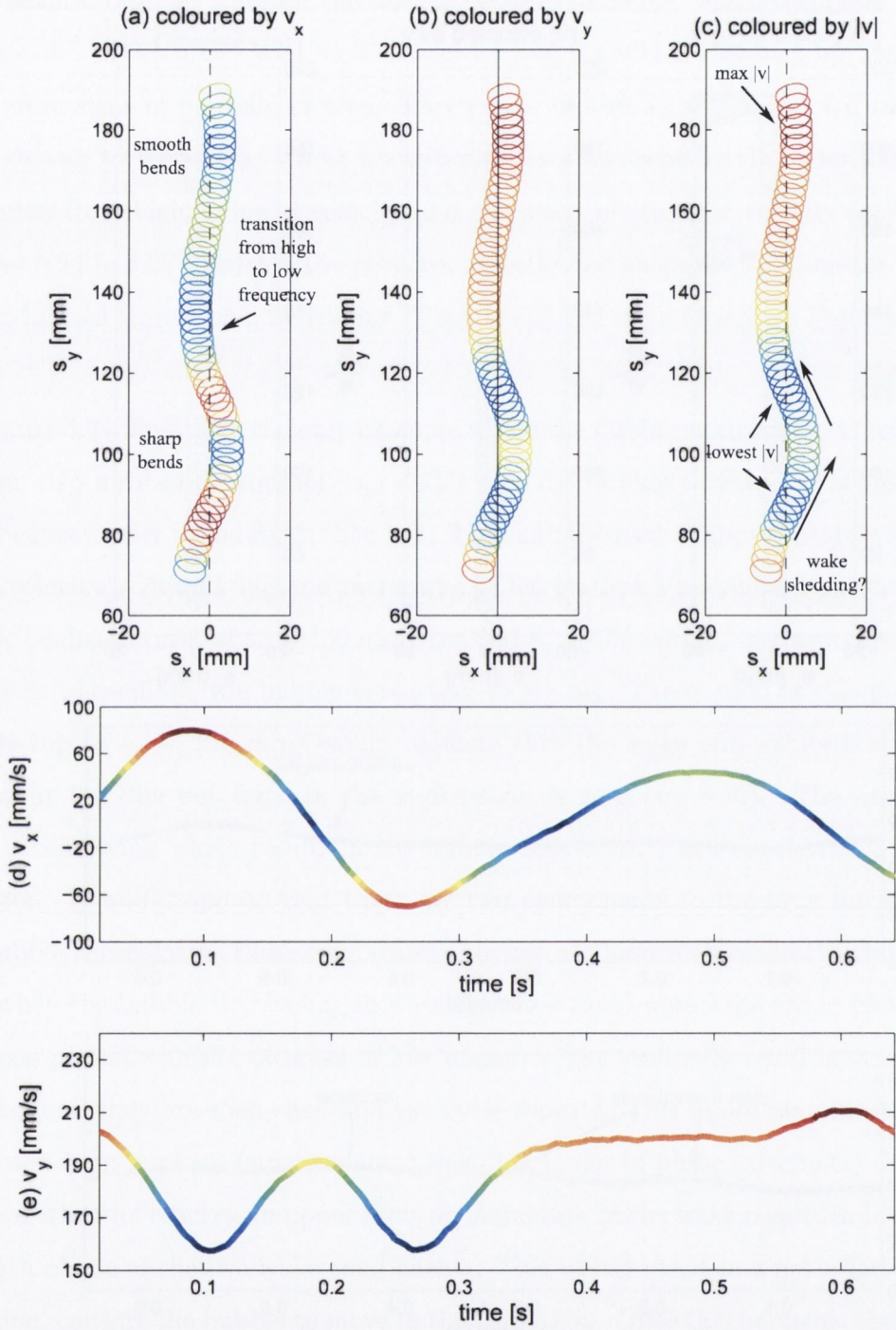
Figure 5.25: Bubble shape, velocity and position for the transitional 0.1 ml bubble sliding on the heated surface. The colour of the boundary represent (a) v_x, (b) v_y and (c) $|v|$ at that instant. The velocity variation in the (d) x and (e) y direction with time are supplied as a reference.
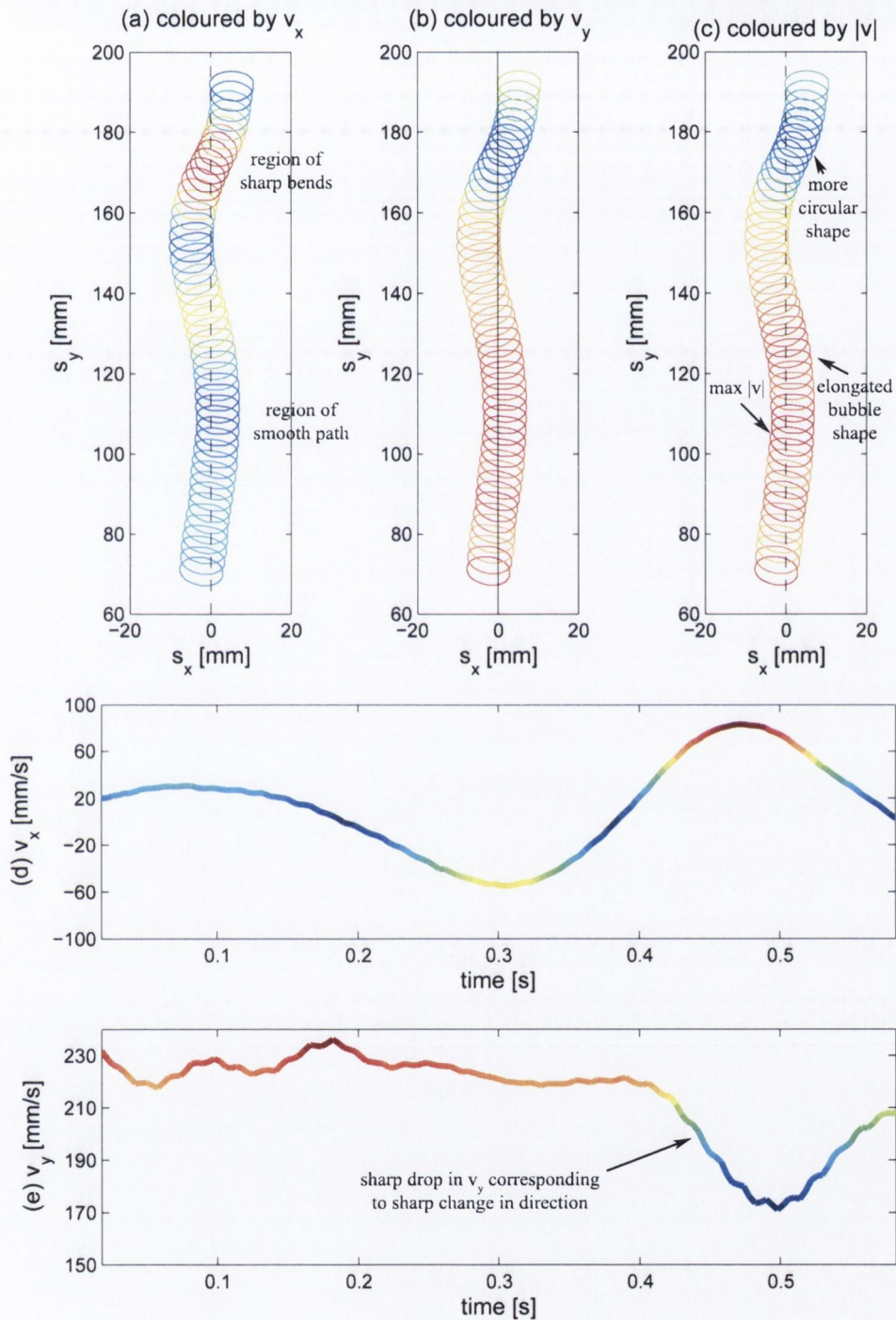
Figure 5.26: Bubble shape, velocity and position for the transitional 0.2 ml bubble sliding on the heated surface. The colour of the boundary represent (a) v_x, (b) v_y and (c) $|v|$ at that instant. The velocity variation in the (d) x and (e) y direction with time are supplied as a reference.
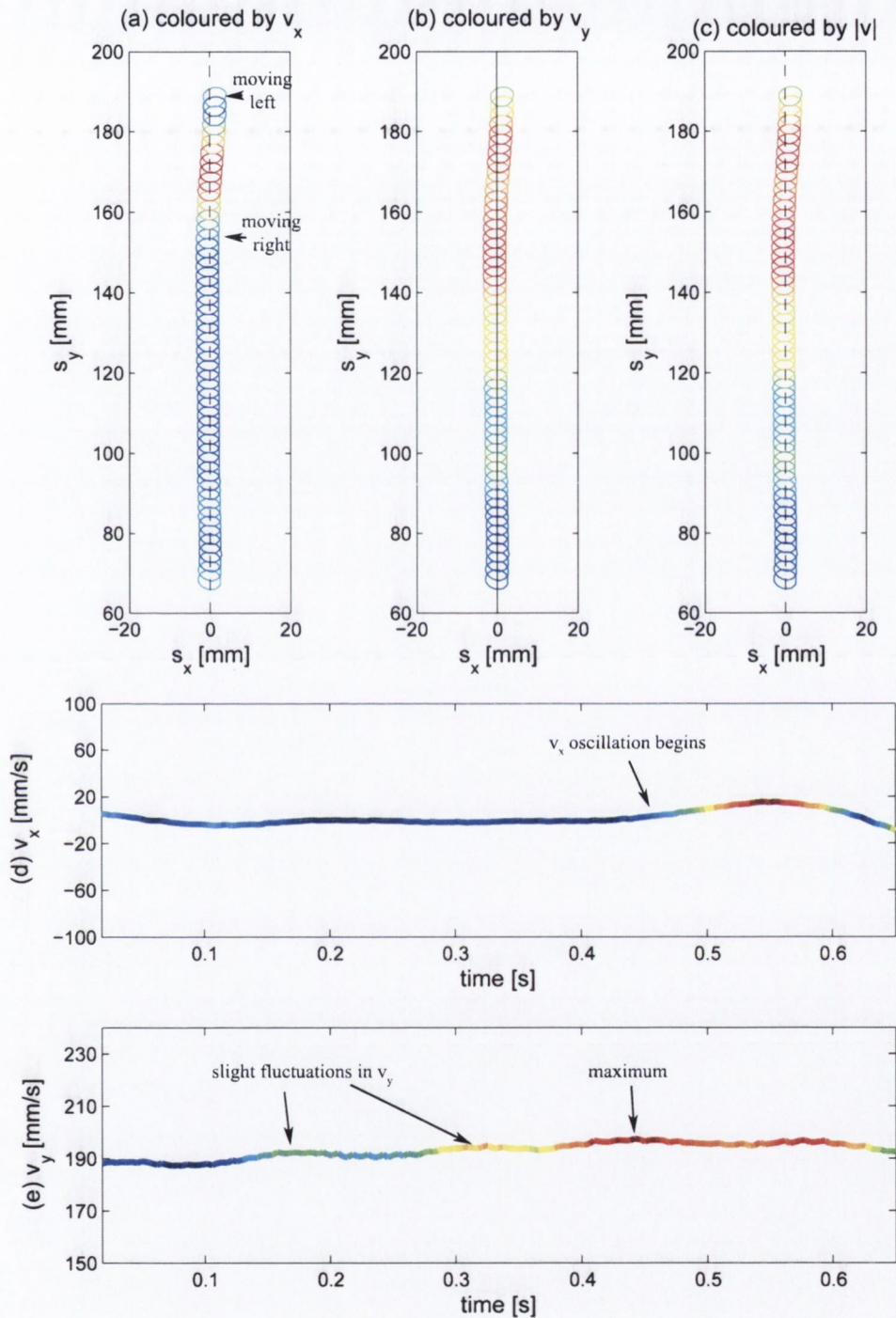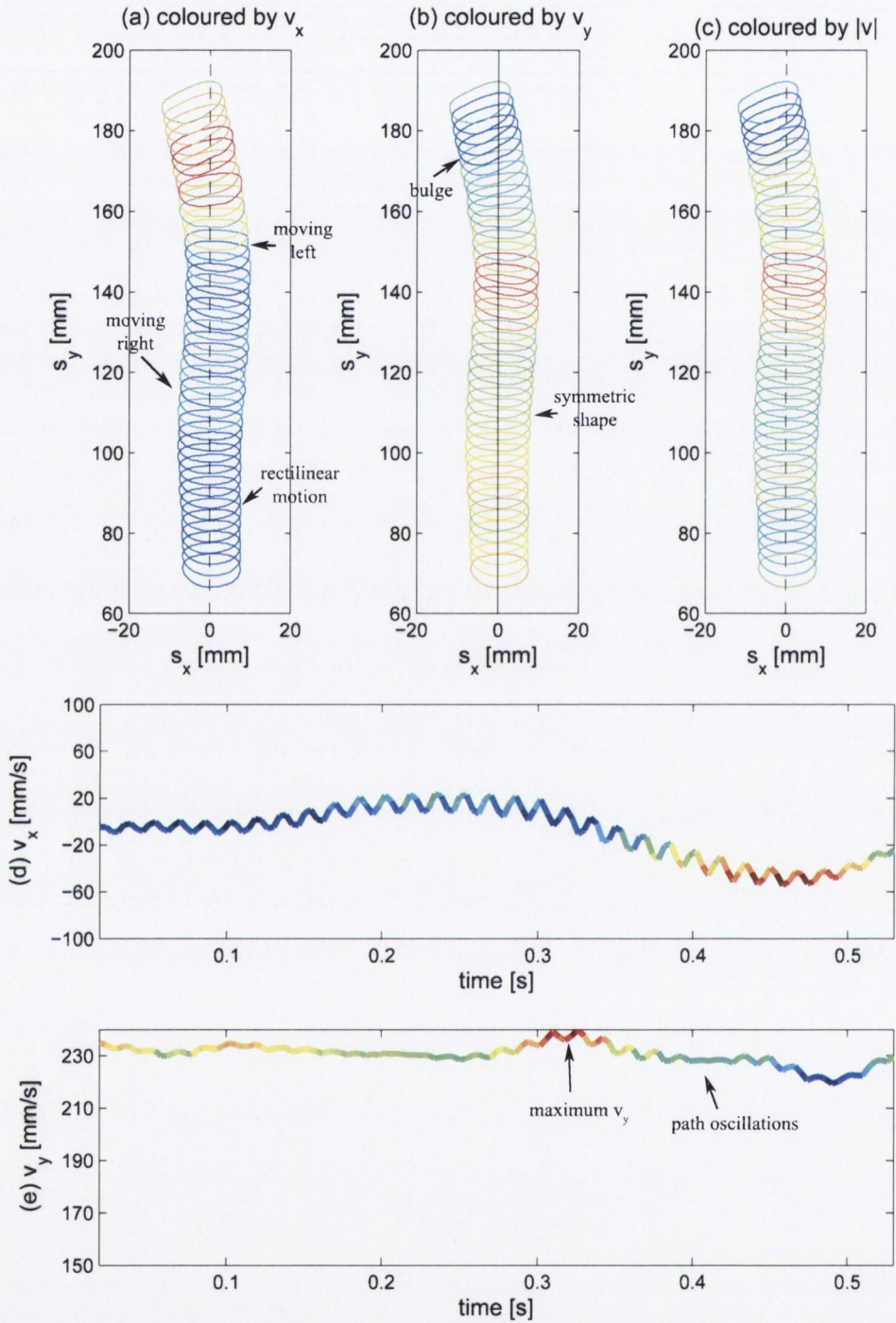
Figure 5.27: Bubble shape, velocity and position for the transitional 0.4 *ml* bubble sliding on the non-heated surface. The colour of the boundary represent (a) v_x, (b) v_y and (c) $|v|$ at that instant. The velocity variation in the (d) x and (e) y direction with time are supplied as a reference.

in a straight line (or close to it) achieve higher velocities. In generally, transitional tests, whether on heated or non-heated surfaces, have the highest mean velocities as indicated by the + symbols in Figure 5.10.

Most transitional tests were observed to go from high velocity, low frequency oscillations to high frequency, low velocity oscillations. Figure 5.25 shows one of only a small number of tests that appeared to do the opposite. The 0.1 ml bubble, in this case, goes from high to low path oscillation frequency at approximately $s_y = 130$ mm. The bubble does not travel straight after this point, like in Figure 5.24, but its path is noticeably smoother. Just before the onset of the smoother path, i.e. between $s_y = 80 - 120$ mm, the bubble performs two sharp changes in direction during which the bubble moves at its lowest $|v|$. It then accelerates constantly in the y direction to a maximum $|v|$ at $y = 180$ mm. The reason for this may once again lie in the behaviour of structures in the wake. The two sharp curves may correspond to a relatively large shedding of wake material, one on each bend. Once these have been shed the bubble has less total drag and begins to accelerate up to a maximum velocity. The wake force components still appear out of phase as the bubble is constantly traveling in the positive x direction. This indicates that the strength of one of those drag components is greater than the other and their combined strength is less than the buoyancy force. Since each of the wake components are shed alternately, whichever is shed first has a head start over the other (on the next phase of wake build up), resulting in a net x force in the positive x direction. This is not general behaviour, the bubble oscillation is usually roughly constant but it demonstrates the variability observed throughout the tests. These observations will be discussed further in Section 5.5.2 in relation to heat transfer.

The 0.2 ml bubble, Figure 5.26, has similar features to both the 0.05 and 0.1 ml transitional bubbles. Like the 0.05 ml bubble its y velocity changes from high to low, but, similar to the 0.1 ml bubble, it has a fluctuating x velocity. In contrast to the 0.1 ml bubble, this test shows a long period of relatively smooth path ($s_y = 65 - 150$ mm) followed by a series of sharp curves ($s_y = 150 - 190$ mm). Bubbles of this volume are now large enough to observe shape fluctuations. It appears elongated and roughly constant until $|v|$ is at its lowest, upon which the shape is more circular (i.e. it has a

lower eccentricity). The effects of the wake in this test appear similar to that of the 0.05 ml bubble but possibly slightly out of phase, since the bubble is initially moving in the positive x direction. In this case, the bubble accelerates up to its maximum $|v|$ at $s_y \approx 105$ mm and then begins to oscillate and decelerate thereafter. As fluid is alternately shed from the wake the bubble exhibits stronger oscillations. It is possible that the path curvature may reflect the strength or size of material being ejected from the wake.

Figure 5.27 shows a near rectilinear path but only up until about $s_y = 90$ mm. After this it begins to curve right slightly, then left. From $s_y = 70$ mm onwards, v_y oscillates up to a maximum at $s_y = 140$ mm, then begins to fall off as the bubble oscillates. The bubble eccentricity gradually increases, but remains symmetric, up until about $s_y = 140$ mm, then, as the bubble curves left, it loses symmetry and becomes slightly bulged on its left hand side. As the strength of the pair of wake structures changes, so does the effect it has on the bubble shape. These features will be discussed in more detail in Section 5.5, in relation to heat transfer and in the next section, in relation to fluid motion. The noise present in this figure is characteristic of non-heated tests as highlighted in Section 5.2.4.

5.3 Fluid motion

When the bubble accelerates due to the buoyancy force, motion is generated in the fluid that surrounds it. The motion of the fluid, in turn, exerts a force on the bubble in the form of pressure differences around the interface of the bubble. The force it exerts can produce shape changes and path fluctuations. If the nature of the wake is periodic, this too will be reflected in its motion and velocity. This section presents the results of an investigation into the motion of the fluid in a plane parallel to, and at a distance of 3 mm, from the surface. By analysis of the raw photographic images taken by the PIV system, some additional bubble dynamics, specific to the PIV setup, will be presented here.

5.3.1   Bubble dynamics: PIV setup

The behaviour of the bubble altered dramatically between the tests discussed in Section 5.2 (recorded with the Bubble dynamics and heat transfer setup) and those discussed here (recorded with the PIV and heat transfer setup). This is attributed to the only difference between the two setups; the addition of seeding particles to the water. These are required by the PIV system as described in Chapter 2 Section 2.1 and Chapter 3. Numerous papers (e.g. Frumkin & Levich [2], Griffith [3], Alves et al. [4], Duineveld [5], Clift et al. [6] and Saito et al. [7]) have been published specifically on or related to the topic of surfactants and their effects on bubble dynamics. Surfactants are impurities in the fluid phase that gather on the boundary between the fluid and gas phase. They are forced towards the rear of the bubble by the fluid where they inhibit the motion of the interface. This alters the boundary condition of some or all of the surface from that of 'slip' to 'no slip', which in turn changes the behaviour of the fluid.

Figure 5.28 shows the mean velocity of each test and the mean for all tests at each specific volume for the PIV setup. Included are the previous results for the Bubble motion setup (dashed lines, see Figure 5.10). The figure conforms to the trend
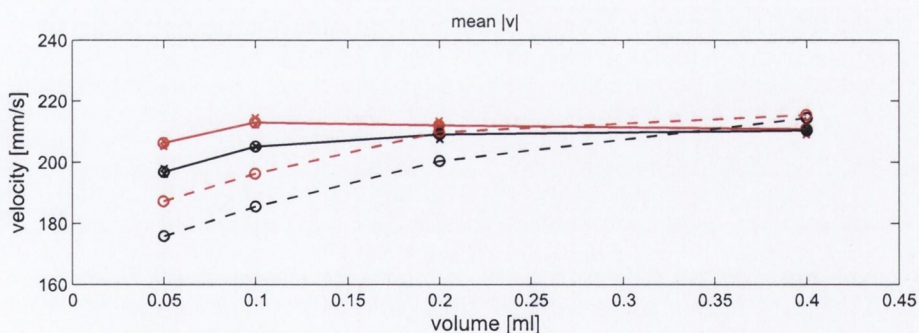
Figure 5.28: Mean bubble velocity magnitude, $|v|$, for each individual test ($\times$) including the mean of all tests at each volume ($\circ$), for both the heated (red) and non-heated (black) surface for the PIV setup. The dashed line represents tests performed for the Bubble motion setup (see Figure 5.10).

that bubbles sliding on the heated surface travel faster than those on the non-heated surface, the difference being of similar value to those in the Bubble motion tests. This observation, once again, can be attributed to the increased fluid velocity (see Section 5.1) generated by the thermal boundary layer, not present in non-heated tests. The effects of which diminish with increased volume, possibly due to the interaction of larger bubbles with slow moving fluid outside the boundary layer.

The figure also shows that, in general, bubbles for the PIV setup travel faster than those in the Bubble motion setup, the exception being the 0.4 ml bubble. It has been previously noted for the Bubble motion setup (see transitional tests, Section 5.2.6) that bubbles exhibiting only slight path oscillations have the highest velocities. Bubbles in the PIV setup, which all exhibit only minor path oscillations, have a corresponding high velocity. The greatest increase in velocity, when compared to the Bubble motion setup, is for the 0.05 and 0.1 ml bubbles which both show an increase of approximately 20%.

The bubble velocity on the heated surface increases with volume up to 0.1 ml and then decreases very slightly thereafter. For the non-heated surface the bubble velocity consistently increases with volume but the effects diminish rapidly. The addition of seeding particles appears to have its strongest effects on bubbles of small volume such as the 0.05 and 0.1 ml bubbles.

Figures 5.29 to 5.32 show the bubble shape variation over a time span of 0.16 s (20 frames of the PIV camera) for bubbles sliding on the heated surface. They also illustrate some limitations experienced with the PIV setup. As the bubble changes shape, some of its surface reflects light from the laser directly into the camera, causing a bright spot on the image (the colourmap for these images have been inverted for clarity so the bright reflection can be seen as a dark region on the left hand side of the bubble in, for example, Figures 5.29: image 6-8 and 14-17). When this occurs, it is impossible to accurately calculate velocity vectors in the region obscured by the reflection. In conjunction with this, the bubble itself prevents light from the laser sheet illuminating particles on the right hand side of the bubble, once again prohibiting vector calculation (this region is just visible in the photographs as a bright band extending from the right hand side of the bubble out of the frame, it is most obvious in Figures 5.31). For these

reasons, the PIV fluid measurement technique is most accurate in regions away from the bubble interface as was intended for this study. In all of the images the camera is observing the $x - y$ plane and the bubble is traveling from bottom to top. The observation window moves with the bubble in order to keep it in the center of the frame. Images of bubbles sliding on the non-heated surface exhibited similar shape fluctuations and are omitted here.
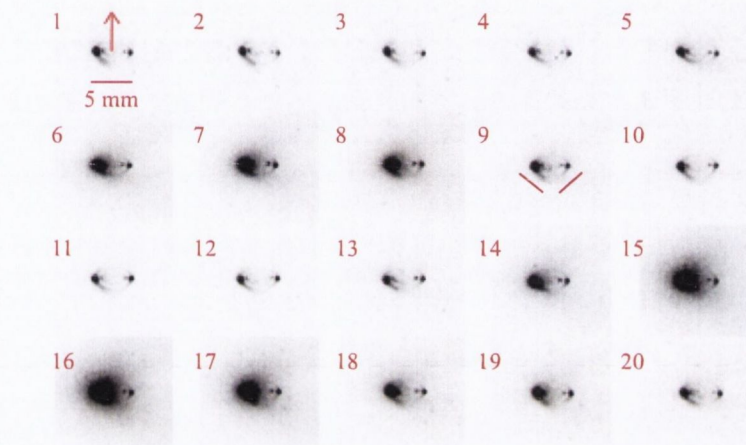
Figure 5.29: Bubble shape fluctuations on a heated surface over a period of 20 frames (0.16 s) for the 0.05 ml bubble using the PIV setup. Images are taken directly from the PIV system camera.

Figure 5.29 shows the 0.05 ml bubble sliding on the heated surface. Although difficult to see, careful inspection of these images reveals that the bubble shape is fluctuating as it slides along the surface (this is easier to observe in a sequence of moving images). The overall shape itself exhibits a higher eccentricity than those observed in the Bubble motion tests (see Figures 5.12 to 5.15), where the shape remained roughly constant and circular. As the bubble moves, the rear of the bubble appears to get drawn backwards and then released periodically. Image 1 shows the bubble with the rear extended, the back of the bubble forms a rough 'u' shape (illustrated in image 9) while the front is curved smoothly[5]. By image 5 it has returned to a more ellipsoidal shape with two different curvatures on the front and back surfaces respectively. Image

---

[5]More accurately, the rear of the bubble appears shaped like three sides of a hexagon but the u-shape description is used here for convenience.
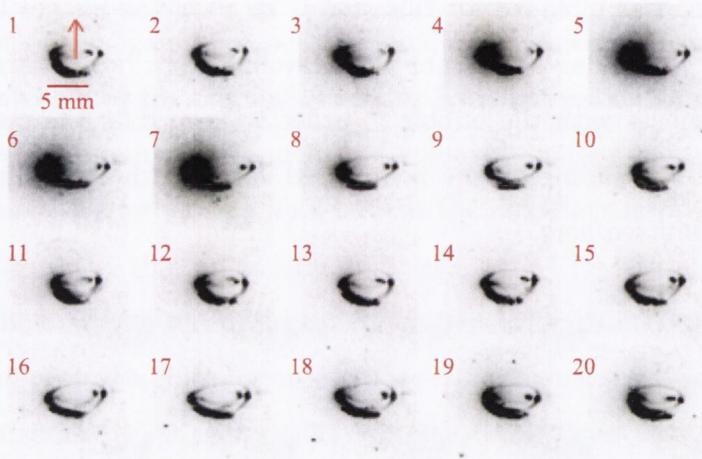
Figure 5.30: Bubble shape fluctuations on a heated surface over a period of 20 frames (0.16 s) for the 0.1 ml bubble using the PIV setup. Images are taken directly from the PIV system camera.
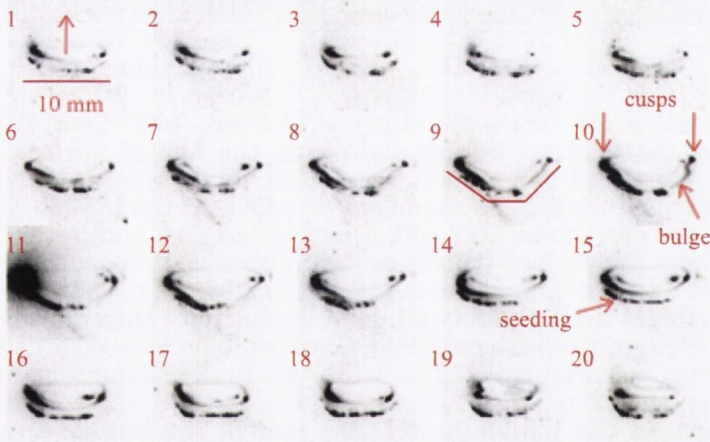
Figure 5.31: Bubble shape fluctuations on a heated surface over a period of 20 frames (0.16 s) for the 0.2 ml bubble using the PIV setup. Images are taken directly from the PIV system camera.
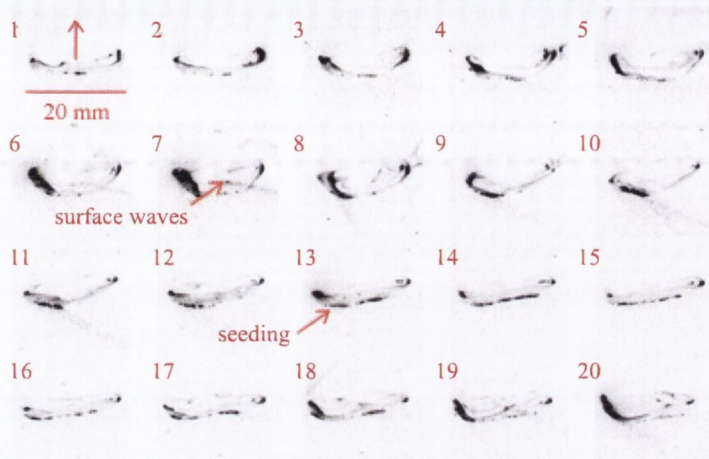
Figure 5.32: Bubble shape fluctuations on a heated surface over a period of 20 frames (0.16 s) for the 0.4 ml bubble using the PIV setup. Images are taken directly from the PIV system camera.

9, once again, shows the 'u' shape, returning to ellipsoid by image 13. The period of the shape oscillation appears to be approximately 9 frames which equates to 14 Hz, this relates to a 'path' oscillation of approximately 7 Hz (bubbles in the PIV setup exhibited only minor path oscillations). The bubble also appears to be changing orientation very slightly. By image 5, the bubble is rotated slightly clockwise and by image 13 this is reversed, i.e. the bubble is rotated anti-clockwise. Although very small in amplitude, the bubble does appear to be traveling with a sinusoidal motion.

When compared to Figure 5.24, the only test in the Bubble motion setup to show approximately straight line motion, these bubbles appear more deformable. The fact that there is only slight variation in the bubble path coupled with the symmetric shape of the bubble possibly indicates simultaneous shedding of wake structures. The build up of the strength of these structures, and their shedding, could lead to the shape fluctuations observed. As they grow in strength the bubble shape becomes elongated along the minor ellipse axis, and the rear gets drawn backwards. When these detach, the bubble returns to its ellipsoidal shape (this is probably coupled with a decrease in velocity as the wake gathers strength along with an increase in velocity as the wake detaches but it is not possible to confirm this with the current results). The slight change in orientation indicates a small, alternating difference in the relative strengths

201

of the wake structures.

Figure 5.30 shows the 0.1 ml bubble sliding on the heated surface. At this volume, the shape oscillations are much more apparent. The bubble width, and therefore eccentricity, is constantly changing as it moves. Image 1 shows the bubble with low eccentricity, this rises consistently to a maximum at image 6, completing the cycle by image 11. Throughout this cycle the curvature of the front of the bubble appears to remain constant while the rear of the bubble undergoes shape change. The period of shape oscillations is approximately 11 Hz and once again the bubble exhibits a slight fluctuation (5.5 Hz) in orientation and path.

Figure 5.31 illustrates the 0.2 ml bubble shape fluctuations. Image 1 shows the bubble with low eccentricity and a roughly ellipsoidal shape, by image 6 the front of the bubble has become more elongated but still has similar curvature. The rear, however has developed two, angled, flat regions either side of a third, horizontal flat region, similar to the 0.05 and 0.1 ml bubbles. This is at its most obvious in image 9 where the rear of the bubble approximates a rough 'u' shape with a slightly curved front. Very shortly after this, in image 10, the two flattened sides bulge outwards forming two sharp cusps on the left and right hand sides of the bubble, the front of the bubble is almost flat. For the next 7 or so images (images 11-17) the bubble eccentricity reduces and the cycle is complete by approximately image 17. This cycle corresponds to a shape oacillation frequency of approximately 7 Hz (3.5 Hz path oscillations). For the whole duration, the bubble remains roughly symmetrical about its minor elliptical axis and does not appear to change orientation. It is possible to see small, densely packed, regions of seeding particles traveling with the bubble very close to the rear face, these are highlighted in image 15. It is not possible to tell whether these are on the bubble surface or in the fluid immediately behind the bubble but it does indicate that they are accumulated by the bubble and may affect the fluid and bubble motion. The effects of the fluid wake structures on the bubble shape are becoming dramatic.

For the 0.4 ml bubble sliding on the heated surface, the behaviour is more chaotic. Figure 5.32 shows numerous surface waves traveling across the bubble interface. The bubble does appear to have a fluctuating eccentricity but it is difficult to quantify given the large deformities in shape. One thing to note is the very high aspect ratio

a bubble of this volume can achieve, by image 15 the width (x direction) to length (y direction) ratio is approximately 6 to 1. Again, in these images, it is possible to see a dense gathering of seeding particles in a region close to the rear of the bubble as indicated in image 13. In general, bubbles in the PIV setup exhibit much larger shape fluctuations than those in the Bubble motion setup as can be observed by comparison back to Figure 5.13, although none deform as much as the 0.4 ml bubble shown here. The following section discusses the fluid measurements made in the bubble wake in order to gain insight to the previously mentioned wake structures.

5.3.2 Fluid dynamics

The wake behind bubbles is generally divided into two regions; the primary and secondary wake (see Fan & Tsuchiya [1] for a good description). The primary wake is considered 'attached', it occupies a region immediately behind the bubble and moves with it. The secondary wake consists of fluid shed from the primary wake, which travels downstream relative to the bubble. There is still much debate as to the detailed structure and nature of both the primary and secondary wakes as described in Chapter 2.

So far, observations of the behaviour of the bubble have been used to infer the nature of the wake. The following section presents the results of PIV measurements of the fluid flow in a plane parallel to the heated surface in order to further understand the nature of the wake and its effects on heat transfer. Similar trends in fluid motion were observed in both the heated and non-heated tests and as such the non-heated tests are omitted. Where differences do occur, reference will be made throughout the text. Figure 5.33 and 5.36 (left) show the fluid velocity magnitude, $|v_f|$ and (right) the fluid vorticity, ω_z. Top and bottom images have a time separation of approximately 2 seconds (1.78, 2.26, 1.94 and 2.42 s for the 0.05, 0.1, 0.2 and 0.4 ml bubbles respectively).

Figure 5.33 shows contours of the fluid velocity magnitude and vorticity in the wake of the 0.05 ml bubble sliding on the heated surface. Superimposed on these figures are the images of the bubble taken directly from the PIV camera. Since the nature

of the wake appears to be periodic, the figures can give the reader an insight into the evolution of the fluid structures as time elapses. Fluid structures observed immediately behind the bubble have just been created. In order to see what these develop into the reader only has to look further downstream of the bubble (i.e. values of s_y lower than the bubble position). Alternatively, the reader can observe structures further downstream of the bubble and work backwards to the bubble position to visualise how these structures evolved. Very close to the bubble the measurement technique is affected by reflections and shadowing and as such precise values in this region should be considered cautiously. Figure 5.33 (a) and (c) show the fluid velocity magnitude, $|v_f|$ at two intervals separated by 1.72 s. Downstream of the bubble (e.g. from $s_y = 60-100$ mm), in Figure 5.33 (a), it is possible to see several areas of elevated velocity positioned each side of the bubble path (in reality the 'area' affected is actually a volume but area is used here due to the two-dimensional measurement technique). Although not always obvious, these develop in sets with one strong and one weak component. The stronger component alternates between the left and right side in each successive set up to the bubble position. Near the bubble, the separate regions of elevated fluid velocity gradually come closer to each other and begin to overlap at the bubble path ($s_y = 150 - 180$ mm). This indicates that two regions of high velocity fluid emanate from close to the rear of the bubble on the left and right hand side apparently simultaneously. One region is reduced in strength compared to the other and both travel away from each other at an angle, north-east and north-west of the bubble path respectively. Small regions show the maximum fluid velocities of approximately 80 mm/s immediately behind the bubble reducing to about 20 mm/s over the 2 second timespan. As time passes the stronger region continues to move and grow in size as the velocity continues to reduce (Figure 5.33 (c)).

Figure 5.33 (b) shows two paired regions of elevated vorticity emanating from the rear of the bubble. Each region itself, located either side of the bubble path, consists of two smaller regions with oppositely signed vorticity, one usually stronger than the other. On the left of the bubble path the region with strongest vorticity is anti-clockwise (coloured red) while on the right hand side the strongest is clockwise (coloured blue). These are shed from each side of the bubble apparently simulta-

Figure 5.33: Fluid velocity (left) and vorticity (right) for the 0.05 *ml* bubble sliding on a heated surface. Clockwise vorticity is coloured blue, anti-clockwise is coloured red. The bubble outline (obtained from the PIV camera) and path are superimposed. The top row is separated from the bottom row by approximately 2 *s*.
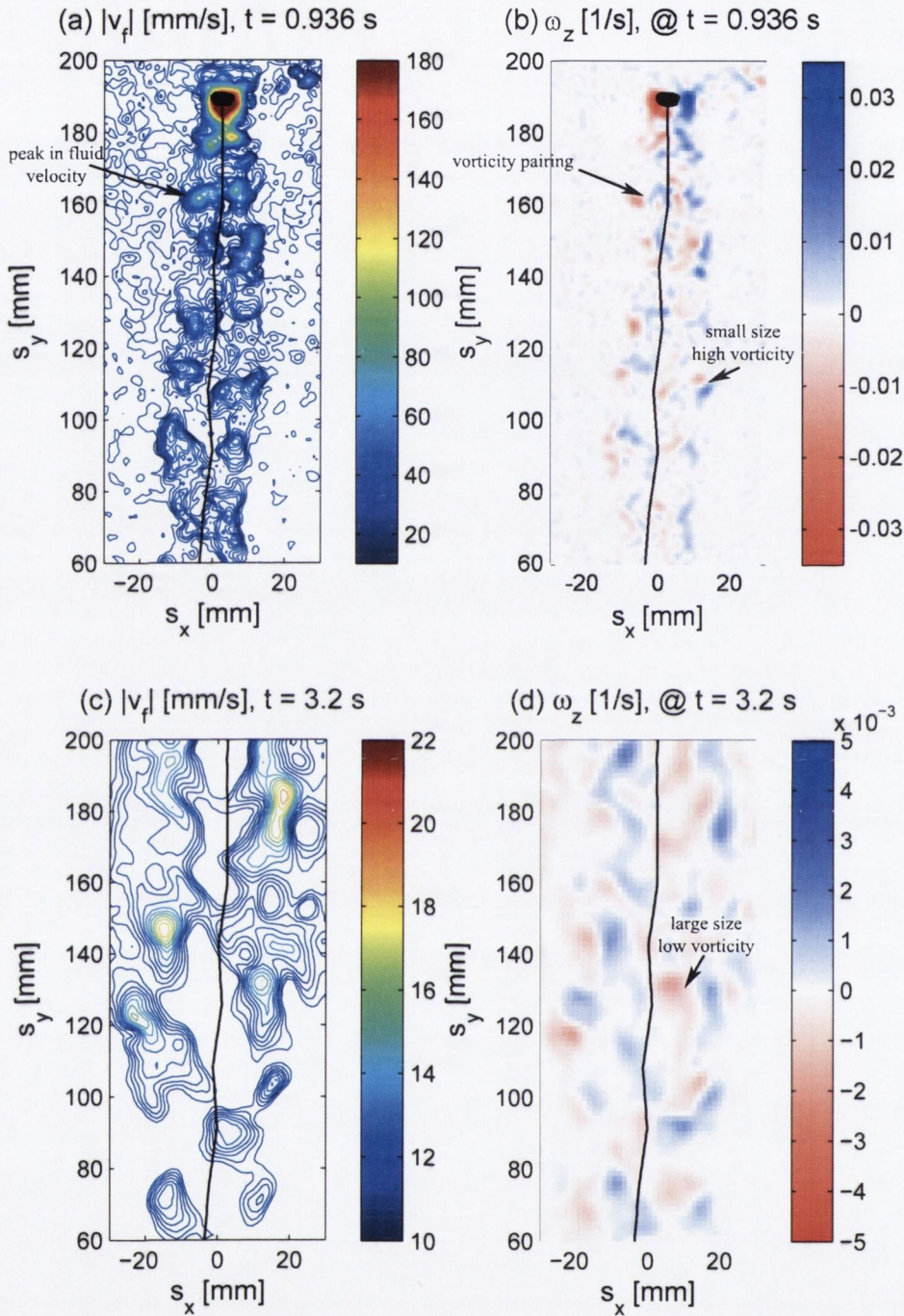
Figure 5.34: Fluid velocity (left) and vorticity (right) for the 0.1 ml bubble sliding on a heated surface. Clockwise vorticity is coloured blue, anti-clockwise is coloured red. The bubble outline (obtained from the PIV camera) and path are superimposed. The top row is separated from the bottom row by approximately 2 s.
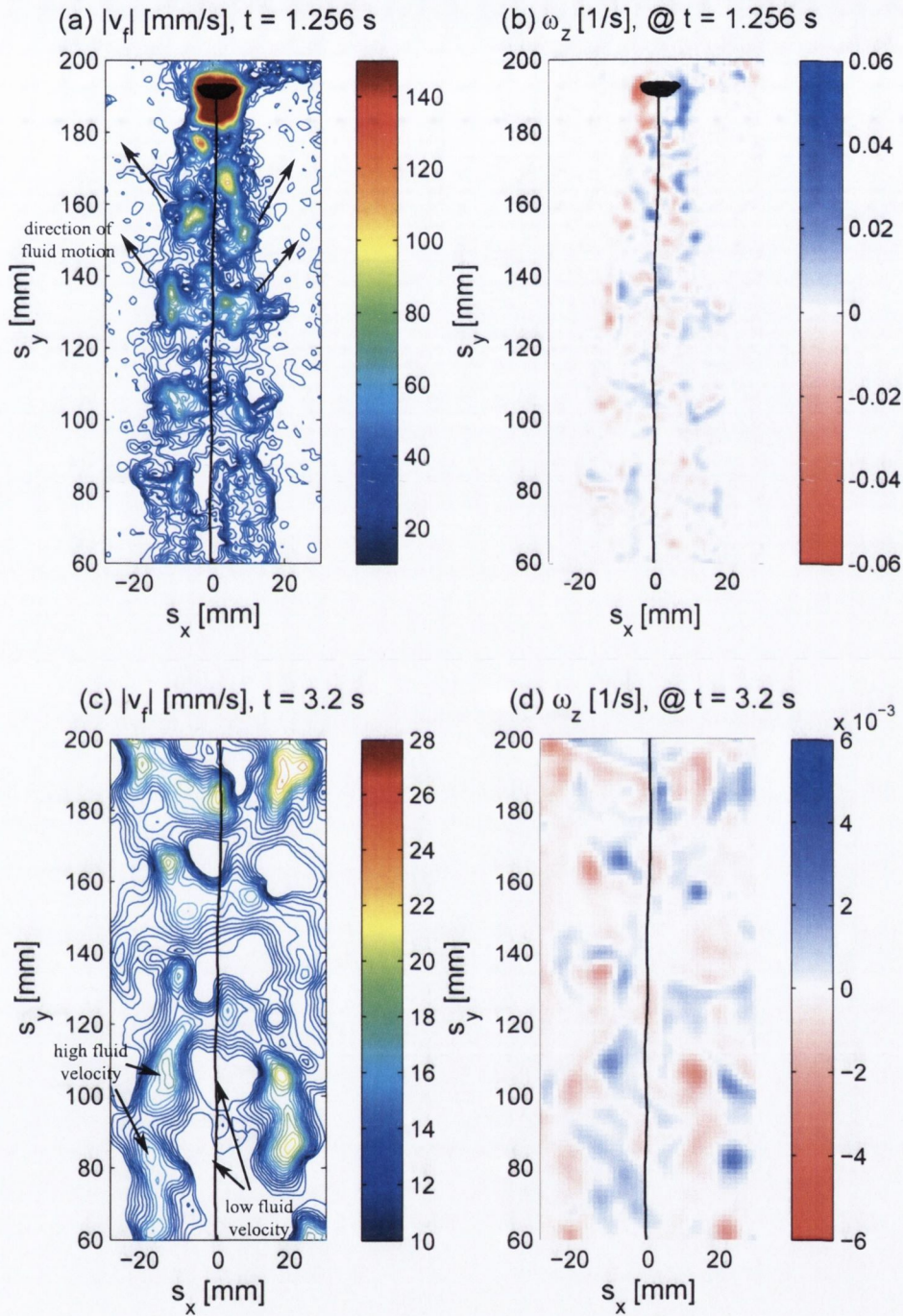
Figure 5.35: Fluid velocity (left) and vorticity (right) for the 0.2 ml bubble sliding on a heated surface. Clockwise vorticity is coloured blue, anti-clockwise is coloured red. The bubble outline (obtained from the PIV camera) and path are superimposed. The top row is separated from the bottom row by approximately 2 s.
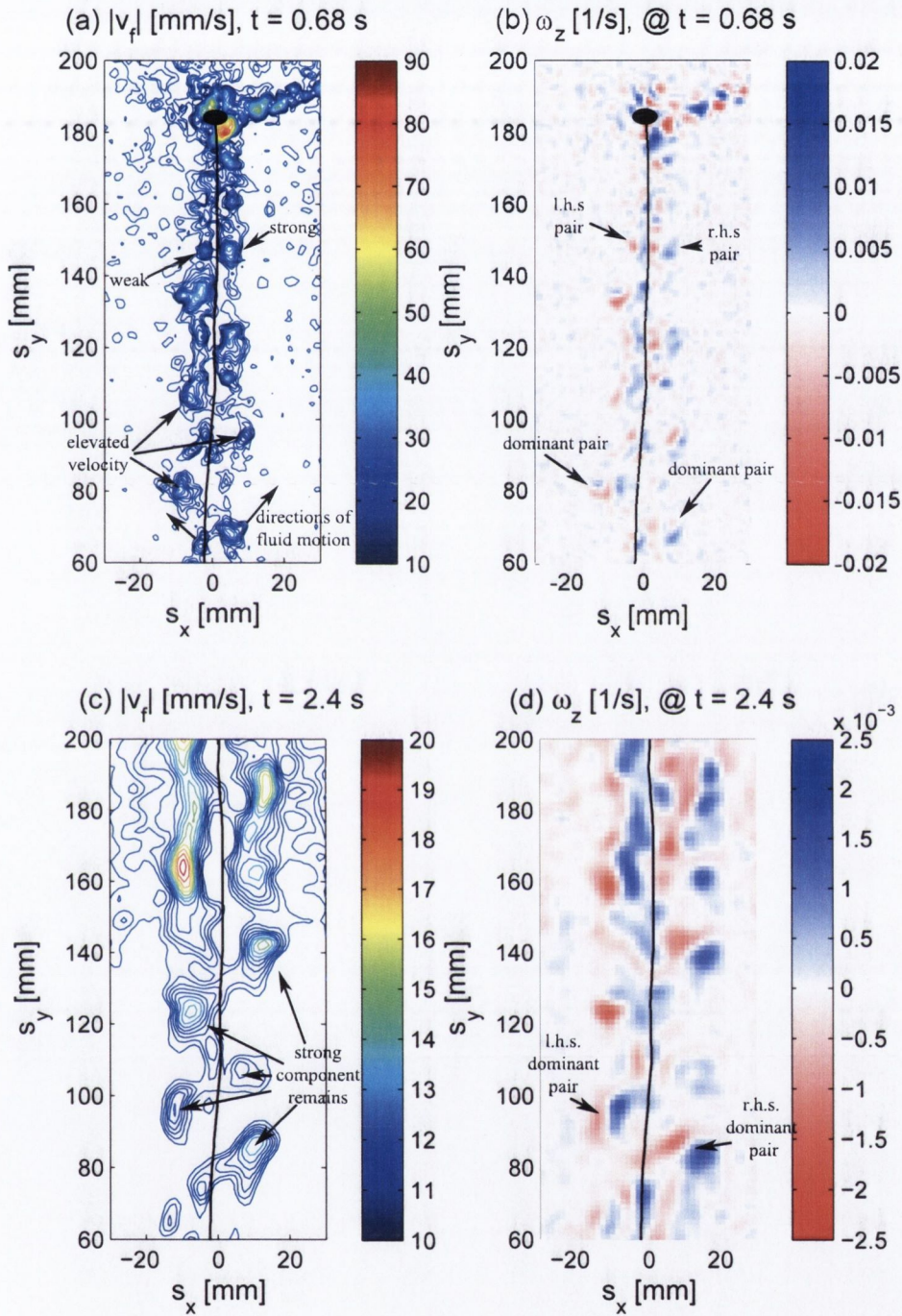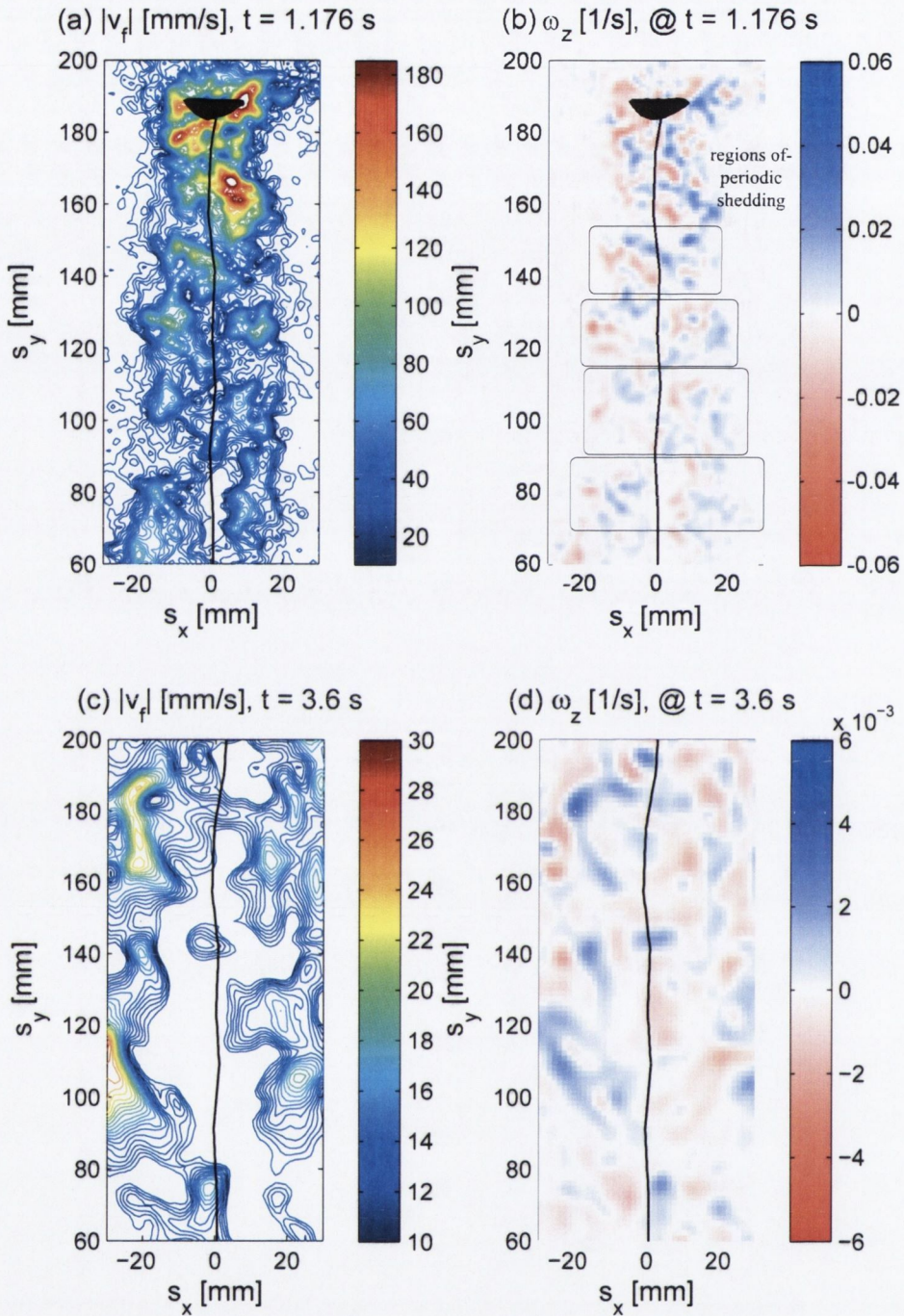
Figure 5.36: Fluid velocity (left) and vorticity (right) for the 0.4 *ml* bubble sliding on a heated surface. Clockwise vorticity is coloured blue, anti-clockwise is coloured red. The bubble outline (obtained from the PIV camera) and path are superimposed. The top row is separated from the bottom row by approximately 2 *s*.

neously, with the high velocity regions corresponding to their centers (i.e. the zone between the two oppositely signed vorticity regions). As they travel downstream, one of the pair diminishes in strength faster than the other, leaving a dominant pair (Figure 5.33 (d)). The dominant pair appear alternately from the wake and persist for a relatively long time after the bubble has passed (effects can still be observed 20 s after the bubble passage). They eventually dissipate and the natural boundary layer velocity resumes. There is a close link between the bubble shape shown in Figure 5.29 and the ejection of regions of high vorticity from the rear of the bubble. Each time the bubble shape oscillates, pairs of high vorticity regions are ejected. Thus, the frequency of shedding is equal to the shape oscillation frequency, 14 Hz. The slight fluctuation in bubble orientation, and resulting sinusoidal path, indicates that the orientation may result in, or reflect, the shedding of the dominant region of elevated vorticity. The areas of vorticity seem relatively stable and are still quite coherent, although diminished in strength, after the 2 second time span.

The fluid velocity magnitude and vorticity for the 0.1 ml bubble sliding on a heated surface is shown in Figure 5.34. The figure shows a general increase in both the velocity and vorticity magnitude and the area of fluid influenced by the bubble's motion. Once again the wake is periodic, high vorticity regions emanating from each side of the rear of the bubble and traveling downstream relative to the bubble. Similar to the 0.05 ml bubble, the peaks in the fluid velocity magnitude all correspond to the central region between the paired regions of counter rotating vorticity. Usually one of the pair is stronger than the other, the dominance typically alternating between left and right although this is less obvious in this particular test. The bubble path representation indicates a change in the direction of the bubble with each ejection from the wake. Once again there is a strong link between bubble shape fluctuations and vorticity ejection frequency, both occurring at approximately 11 Hz. Careful inspection of the bubble images and fluid measurements indicate that the vorticity regions are shed when the bubble is at is highest eccentricity (most elongated). As the vortices move away the bubble shape returns to a lower eccentricity. This will be discussed in detail in Section 5.4. Small regions immediately behind the bubble show fluid velocity as high as 160 mm/s, reducing to approximately 22 mm/s after 2 seconds. As time

elapses, the small regions of vorticity grow in size and reduce in strength and are still clearly visible after 2 seconds.

Figure 5.35 shows similar trends to the 0.05 and 0.1 ml bubble. The figure shows that the wake behind the 0.2 ml bubble is becoming more chaotic, with high fluid velocities ($\approx 140\ mm/s$) and and a greater affected area. It is still possible to identify the regions of high fluid velocity and vorticity being shed periodically and simultaneously from the bubble. As time elapses the vortex pairs grow in area, reduce in strength and move away from the bubble path. The shedding frequency of vortices and shape fluctuations in this case is 7 Hz. After 2 seconds (Figure 5.35 (c) and (d)), the areas of elevated $|v_f|$ are generally confined to regions either side of the bubble path surrounding an area of low fluid velocity.

When the volume is increased to 0.4 ml it becomes difficult to identify any coherent structures in the wake. Figure 5.36 shows the velocity magnitude and vorticity for the 0.4 ml bubble. There are numerous areas of high velocity and vorticity. Close inspection of a sequence of images does reveal that the regions of high velocity have a periodic nature of shedding but it is difficult to see this in a still image (these regions are highlighted in Figure 5.35 (b)). The area of fluid affected by the bubble passage grows in conjunction with the bubble size. Maximum fluid velocities of 180 mm/s are observed close to the bubble, reducing to approximately 30 mm/s after 2 seconds. Once again, the region close to the bubble path has relatively low fluid velocity surrounded by regions of of elevated velocity.

Similar observations were made for both the heated and non-heated tests. In both cases the bubble shed areas of elevated velocity and vorticity. In the heated tests these regions moved outwards and in the positive y direction along with the natural convection flow. In the non-heated tests the areas remained relatively stationary in the y direction after shedding.

As previously mentioned, the bubble behaves differently depending on whether the rig is set up for PIV or Bubble motion tests. As a consequence of this, the effects on heat transfer differ between the two setups. By understanding how the bubble affects fluid motion, and in turn, how this affects heat transfer, it is hoped that a connection can be made between heat transfer aspects observed in both the PIV and Bubble

motion setups. This may give an insight as to how the fluid behaves in the Bubble motion tests (for which there is no fluid measurement). The next sections deal with the effects of sliding bubbles on heat transfer for both the PIV and Bubble motion setups respectively.

5.4 Heat transfer: PIV setup

In this section, the effect of fluid motion on heat transfer from the surface is discussed. Where possible this will be linked back to bubble motion and shape characteristics previously observed. In order to observe the enhancement effects on heat transfer due to the bubble, results are presented of the heat transfer enhancement factor, ϵ,

$$\epsilon = \frac{h}{h_0} \tag{5.3}$$

the surface to bulk water temperature difference,

$$\Delta T = T_s - T_\infty \tag{5.4}$$

and the heat transfer coefficient,

$$h = \frac{\ddot{q}}{\Delta T} \tag{5.5}$$

where T_s and T_∞ are the surface temperature and bulk water temperature respectively, h is the heat transfer coefficient during bubble passage and h_0 is the heat transfer coefficient due to natural convection alone, i.e. before bubble passage. Some figures use the temperature difference to illustrate the cooling effect of the bubble, where

$$T_{diff} = T_0 - T_s \tag{5.6}$$

In this case the difference relates to the drop in surface temperature due to the bubble passage, i.e. the difference between the bubble passage temperature, T, and the surface temperature for natural convection, T_0.

Before the bubble is released onto the surface the heat flux is approximately constant over the test area at 2200 W/m^s (A constant current is supplied to the foil at 70 *amps* for all tests). When the bubble slides over the surface there is plus or minus $10 - 15$ % variation in this in the small regions with high spatial temperature gradient.

This is mainly due to the effects of lateral conduction but also accounts for thermal capacitance, heat transfer through the rear of the foil and radiation effects, although small (see Chapter 4). The surface temperature varies by about $4\,°C$ over the length of the test section due to the effects of the thermal boundary layer and h varies from about 270 to 200 $W/m^2 K$ from bottom to top.

Figures 5.37 to 5.40 show the interaction between fluid velocity, vorticity and the heat transfer enhancement factor, ϵ. Figures (a) and (b) show the velocity and vorticity maps from Figures 5.33 to 5.36 overlapped with the corresponding enhancement factor value at that specific point in time. The colourbar in the figures represent values of ϵ (although the colourbar in Figure 5.33 to 5.36 can be used to look up the specific velocity and vorticity values). Figure 5.37 to 5.40 (c) and (d) show the same tests advanced in time by 1.78, 2.26, 1.94 and 2.42 s for the 0.05, 0.1, 0.2 and 0.4 ml bubbles respectively.

Figure 5.37 shows data for the 0.05 ml bubble. It is possible to see isolated patches of elevated enhancement factor ($\epsilon > 2.2$) at periodic intervals starting from the rear of the bubble and extending away from the bubble path (as indicated in the figure). The peaks are surrounded by a general increase in enhancement. This total area of enhancement starts off at a size approximately the width of the bubble (at $y = 175$ mm) but gradually expands to 4 or 5 times the width over a relatively short period of time (Figure 5.37 (c)). Observation of the velocity and vorticity shows that these high enhancement patches develop just moments after high vorticity regions appear. Once detached from the bubble the elevated vorticity regions quickly move away from the bubble path leaving a region of cooling behind them. Even though the high velocity/vorticity regions have moved away, the cooled area remains. The region containing the dominant pair of elevated vorticity has a greater cooling effect on the surface as illustrated by the alternating direction of the areas of elevated heat transfer (Figure 5.37 (d)). Figure 5.40 (c) and (d) shows the same results after approximately 2 seconds. The most noticeable feature is that the dominant vorticity pair are still present, although diminished in strength. This would indicate that these structures are quite stable in the wake. The region of cooling is still expanding but at an ever decreasing rate. The areas of elevated $|v_f|$ correspond to the advancing edge of increased

Figure 5.37: Enhancement factor, ϵ, overlapped with (left) fluid velocity (gray contours) and (right) vorticity (red, white and blue) for the 0.05 ml bubble sliding on a heated surface. The bottom images are advanced in time by approximately 2 s. Clockwise vorticity is coloured blue, anti-clockwise is coloured red. The bubble outline and approximate path are superimposed.
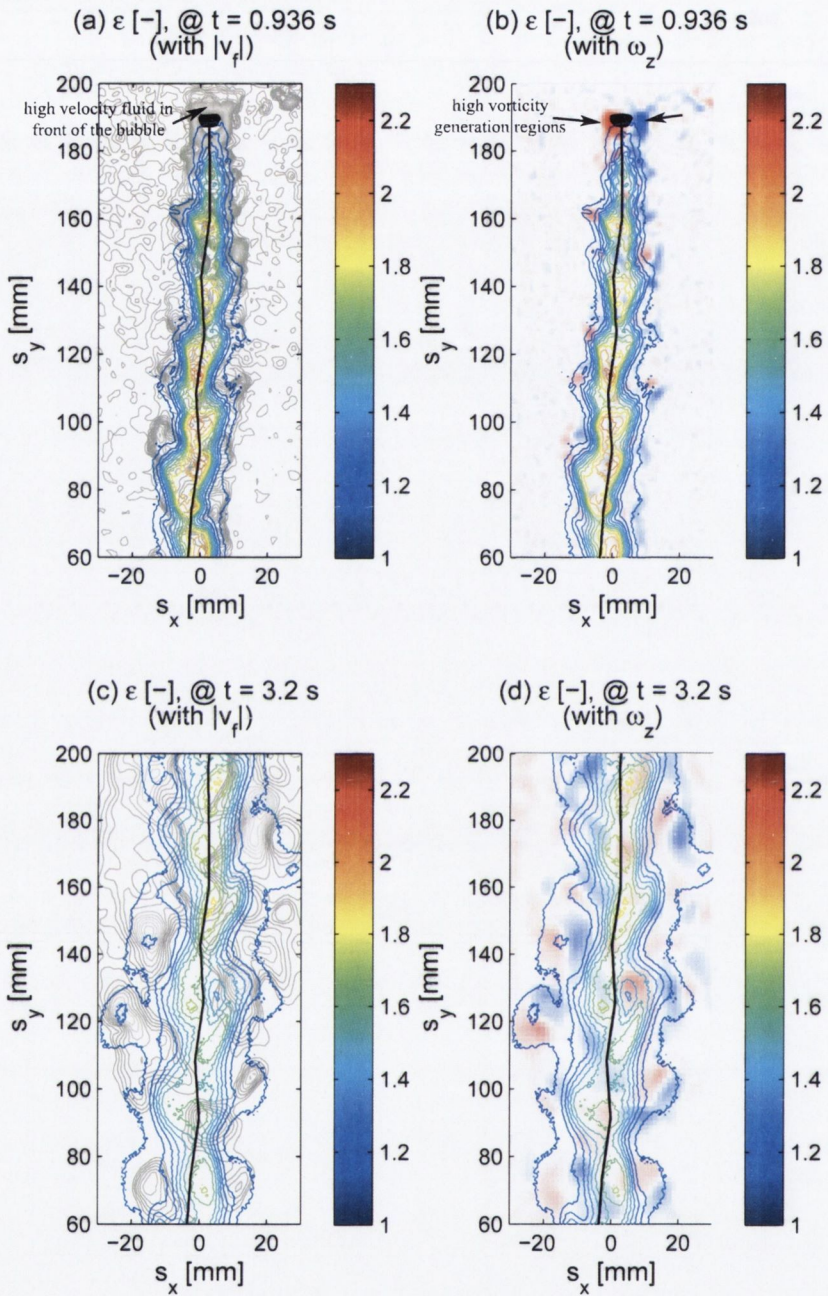
Figure 5.38: Enhancement factor, ϵ, overlapped with (left) fluid velocity (gray contours) and (right) vorticity (red, white and blue) for the 0.1 ml bubble sliding on a heated surface. The bottom images are advanced in time by approximately 2 s. Clockwise vorticity is coloured blue, anti-clockwise is coloured red. The bubble outline and approximate path are superimposed.
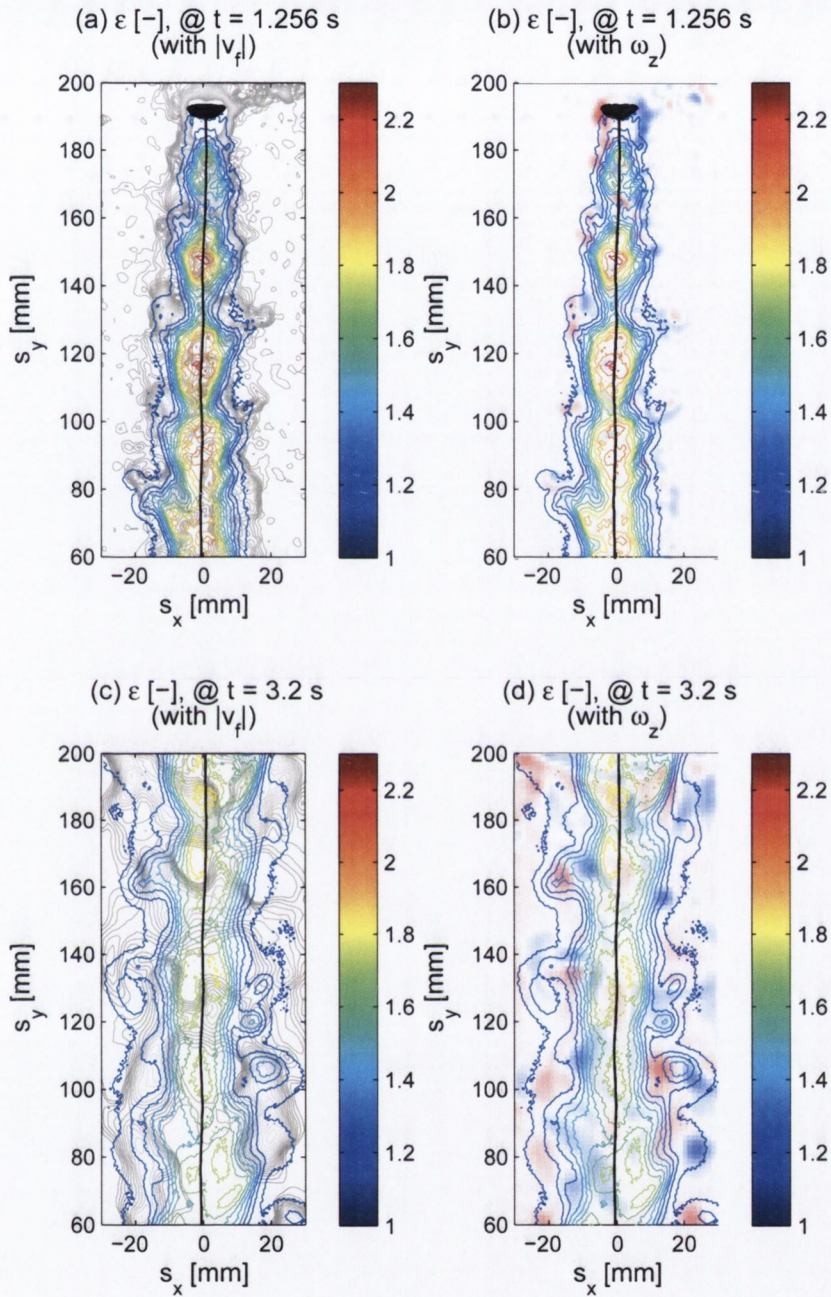
Figure 5.39: Enhancement factor, ϵ, overlapped with (left) fluid velocity (gray contours) and (right) vorticity (red, white and blue) for the 0.2 ml bubble sliding on a heated surface. The bottom images are advanced in time by approximately 2 s. Clockwise vorticity is coloured blue, anti-clockwise is coloured red. The bubble outline and approximate path are superimposed.
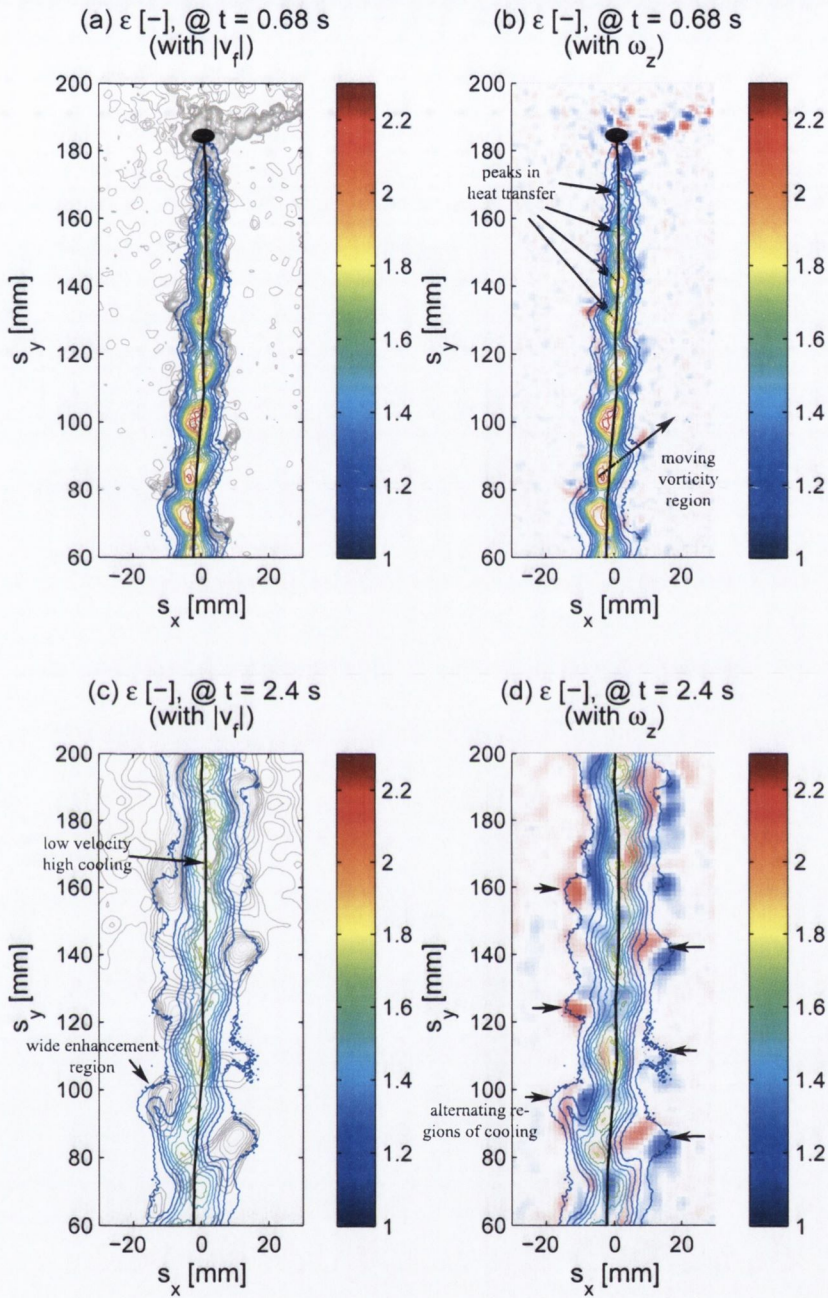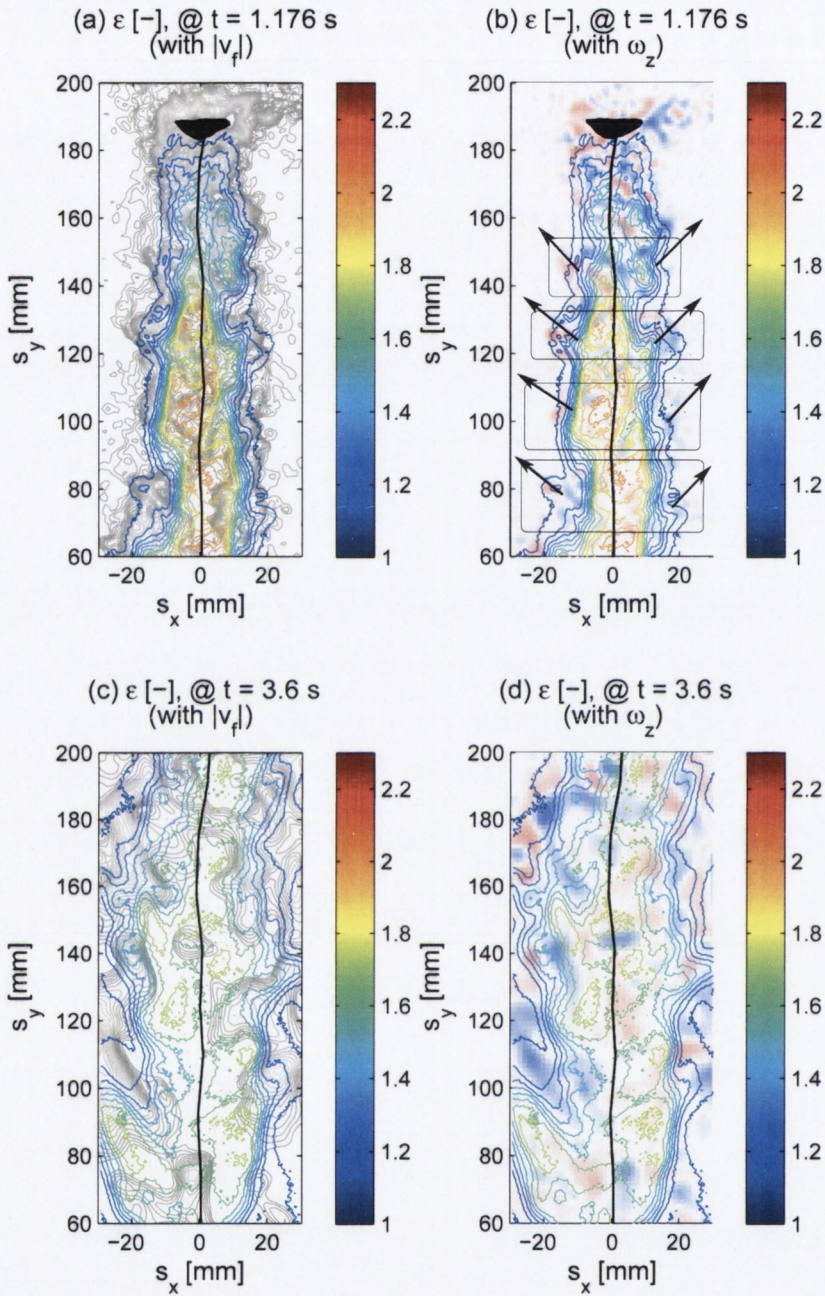
Figure 5.40: Enhancement factor, ϵ, overlapped with (left) fluid velocity (gray contours) and (right) vorticity (red, white and blue) for the 0.4 ml bubble sliding on a heated surface. The bottom images are advanced in time by approximately 2 s. Clockwise vorticity is coloured blue, anti-clockwise is coloured red. The bubble outline and approximate path are superimposed.

enhancement, although the peaks in enhancement now correspond to a region of low fluid velocity. The high velocity fluid does not appear to cool the adjacent surface instantly, i.e. there is a time lag between the position of high velocity and increased ϵ. The regions may contain heated fluid from the thermal boundary layer and as such is ineffective at cooling the adjacent surface. It is also possible that the high velocity fluid has not impacted on the surface yet given that the fluid measurement plane is 3 mm away.

Figure 5.38 shows data for the 0.1 ml bubble. Immediately in front of the bubble, there is an area of increased fluid velocity moving the same direction as the bubble. This is the result of the bubble pushing fluid ahead of it as it moves. Two more regions of high fluid velocity exist each side of the bubble, each relating to regions of high, oppositely signed vorticity. As the bubble moves, fluid accelerates around its curved sides generating vorticity at a high rate. The vorticity is supplied to the wake, which in turn ejects it downstream of the bubble.

Similar trends can be seen in Figures 5.38 and 5.39 for the 0.1 and 0.2 ml bubbles respectively. The maximum enhancement factor observed is close to that of the 0.05 ml bubble, $\epsilon \approx 2.2$, but the area affected by the bubble is increasing constantly with volume. Figures 5.38 and 5.39 (c) and (d) show the 0.1 and 0.2 ml bubble after approximately 2 seconds has elapsed. Although somewhat more chaotic than the 0.05 ml bubble, the same trends can be observed.

Figure 5.40 shows the effects of increasing the volume to 0.4 ml. Although much more chaotic, including the bubble shape fluctuations previously discussed in Section 5.3.1, similar trends to that of the other tests can be seen. As the horizontal lines on Figure 5.40 (b) illustrate, there still appears to be periodic shedding of vorticity just prior to areas of elevated ϵ traveling away from the bubble path at an angle.

Figure 5.41 shows a greatly enlarged view of the wake of the 0.2 ml bubble sliding on the non-heated surface. The image examines an area of 20×30 mm^2. The non-heated test is used to remove the effects of the thermal boundary layer, so the bubble is moving through a stationary liquid. The thermal boundary layer's motion can distort the effects being highlighted here. Once again, the same structures can be seen for all bubble volumes although becoming more chaotic by 0.4 ml, as such, only the 0.2 ml

bubble is shown. The figure shows the path lines for the 0.2 *ml* bubble superimposed with velocity vectors. The length of the vectors represent the velocity magnitude and the colour represents the vorticity (blue clockwise and red anti-clockwise). The bubble passed this area approximately 3 seconds prior to this image.
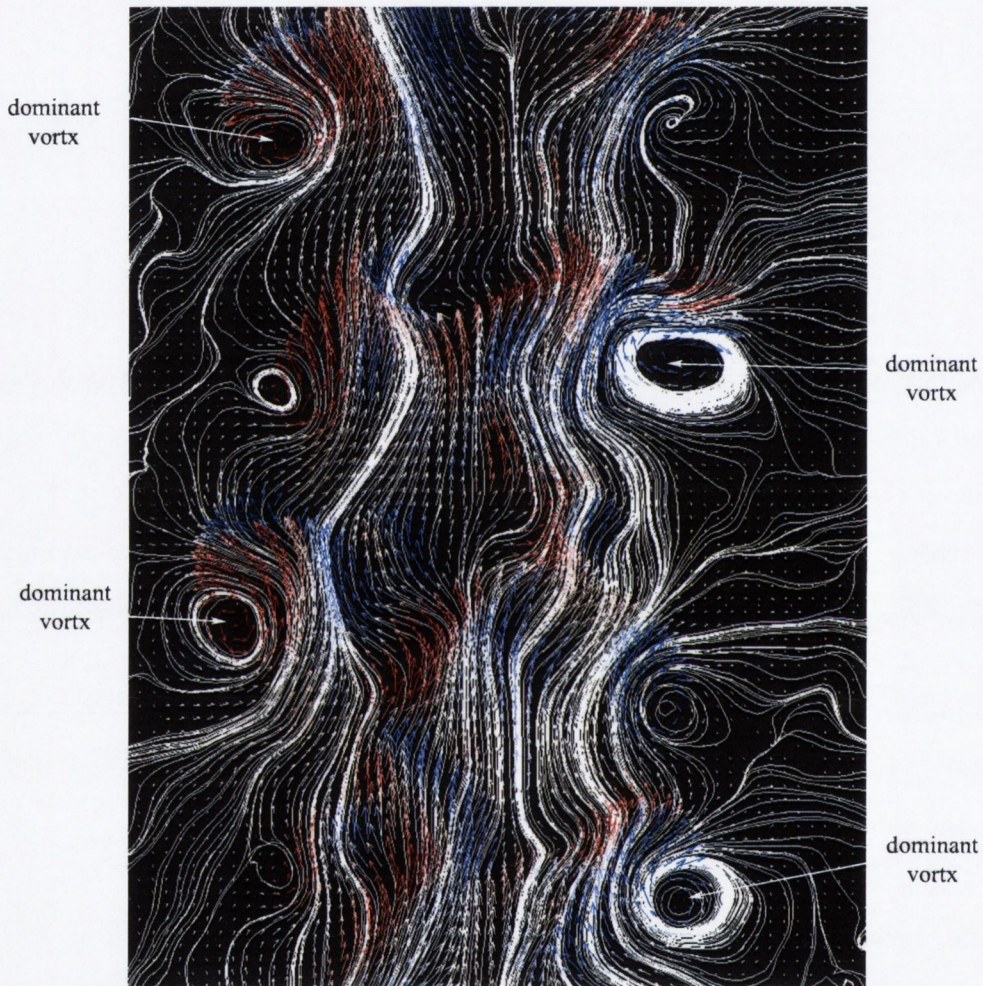
Figure 5.41: Close-up view of the wake of the 0.2 *ml* bubble sliding on the non-heated surface. White lines represent path lines of the flow. Velocity vectors represent the magnitude and direction of the flow while their colour represents vorticity (blue clockwise, red anti-clockwise).

The figure contains four periods of wake ejection. In previous figures (Figure 5.33 to 5.36), these were described as pairs of regions containing both positive and negative

vorticity. It was noted that left of the bubble path the anti-clockwise vorticity dominated, while to the right the clockwise vorticity dominated. It was also noted that the strength of the dominant vorticity changes side with each ejection from the wake. The figure indicates that each region of counter rotating vorticity actually only corresponds to one vortex, indicated by the closed circular regions of path lines. At each ejection, in this measurement plane, two counter rotating vortices detach from the primary wake, one from each side of the bubble. The strength of these vortices alternates between each side resulting in the streamline patterns observed. At the bottom of the figure, the right hand side vortex is much stronger than the left. In the next set above this, the left hand side is dominant and so on. It is these vortices that move outwards from the bubble path, cooling adjacent regions of the surface. Flow moving around the closed path lines follows a snake like path, resulting in the additional regions of oppositly signed, lower strength vorticity close to the vortex itself.

Figures 5.42 to 5.45 show the heat heat transfer coefficient (left) and the temperature difference, ΔT (right). The top and bottom images are separated by approximately 2 s. These correspond to the images shown in Figures 5.37 to 5.40. The fluid velocity plots are omitted for clarity but reference can be made to Figures 5.37 to 5.40 when required. These images, although useful in their own right, can also be used to infer fluid motion at the heated surface, 3 mm away from the fluid measurement plane. Either through increased velocity or lower temperature, moving fluid leaves its impression in the thermal image. Observation of these maps perhaps shows more clearly the periodic nature of the bubble's cooling effect. The change in frequency with volume can be seen for the 0.05, 0.1 and 0.2 ml bubbles but it is difficult to see in the 0.4 ml test without the aid of fluid measurements.

Figure 5.42 shows the 0.05 ml bubble. By comparing the top images in the figure with their counterparts on the bottom it is possible to see how the vortices evolve and interact with the heat transfer from the surface. It can be seen that moments after the vortices have been shed, a distinct triangular shaped region of elevated heat transfer develops (as indicated in Figure 5.42 (a)). This distorts in the direction of the dominant vortex and eventually terminates in in a mushroom shaped cooled region (more obvious in the ΔT images, Figure 5.42 (d)). Analysis of the bubble

Figure 5.42: The heat transfer coefficient, h (left), and the temperature difference, ΔT (right), for the 0.05 *ml* bubble. Superimposed on the upper images is the bubble outline and approximate path. Top and bottom images are separated by approximately 2 *s*.
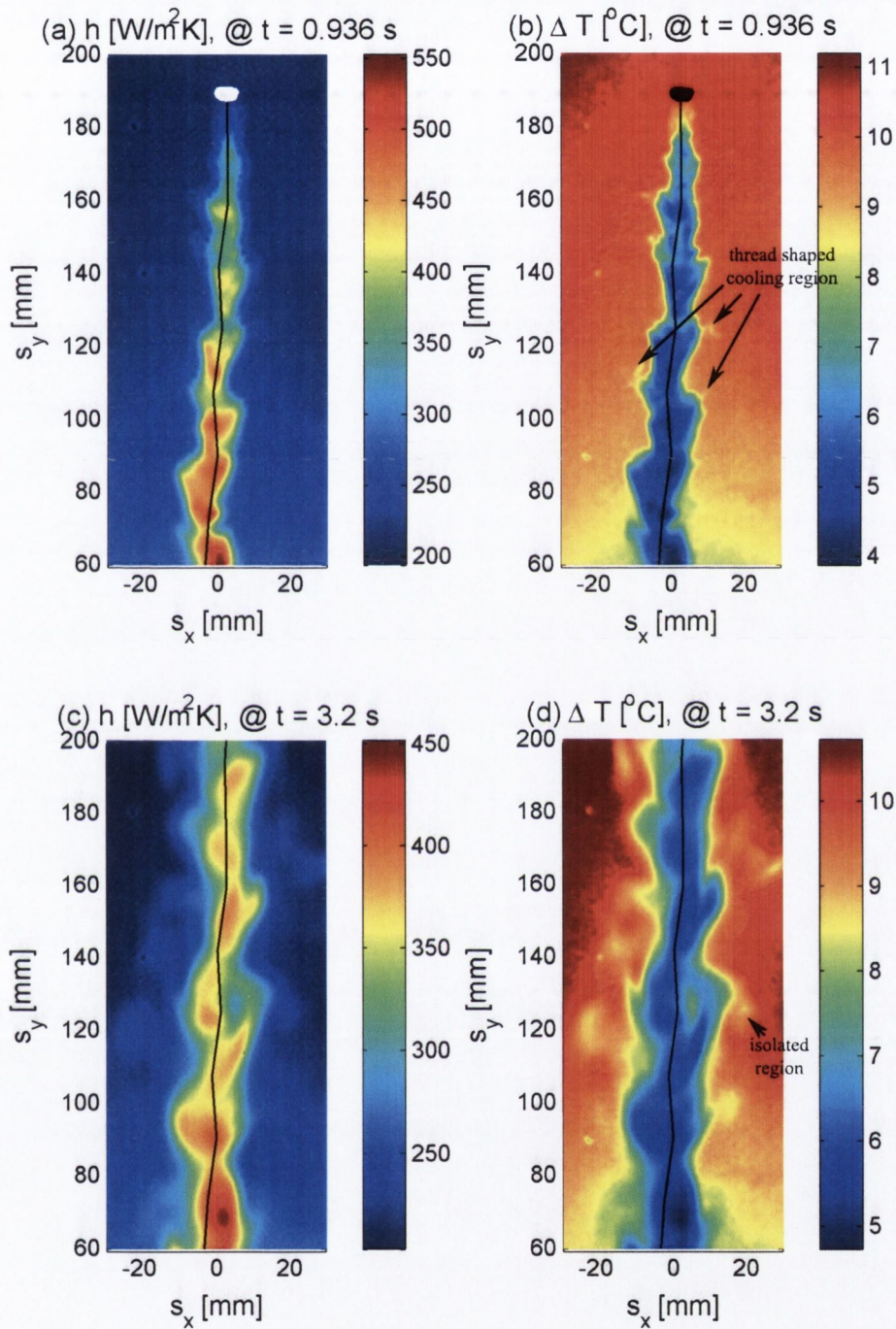
Figure 5.43: The heat transfer coefficient, h (left), and the temperature difference, ΔT (right), for the 0.1 ml bubble. Superimposed on the upper images is the bubble outline and approximate path. Top and bottom images are separated by approximately 2 s.

Figure 5.44: The heat transfer coefficient, h (left), and the temperature difference, ΔT (right), for the 0.2 ml bubble. Superimposed on the upper images is the bubble outline and approximate path. Top and bottom images are separated by approximately 2 s.
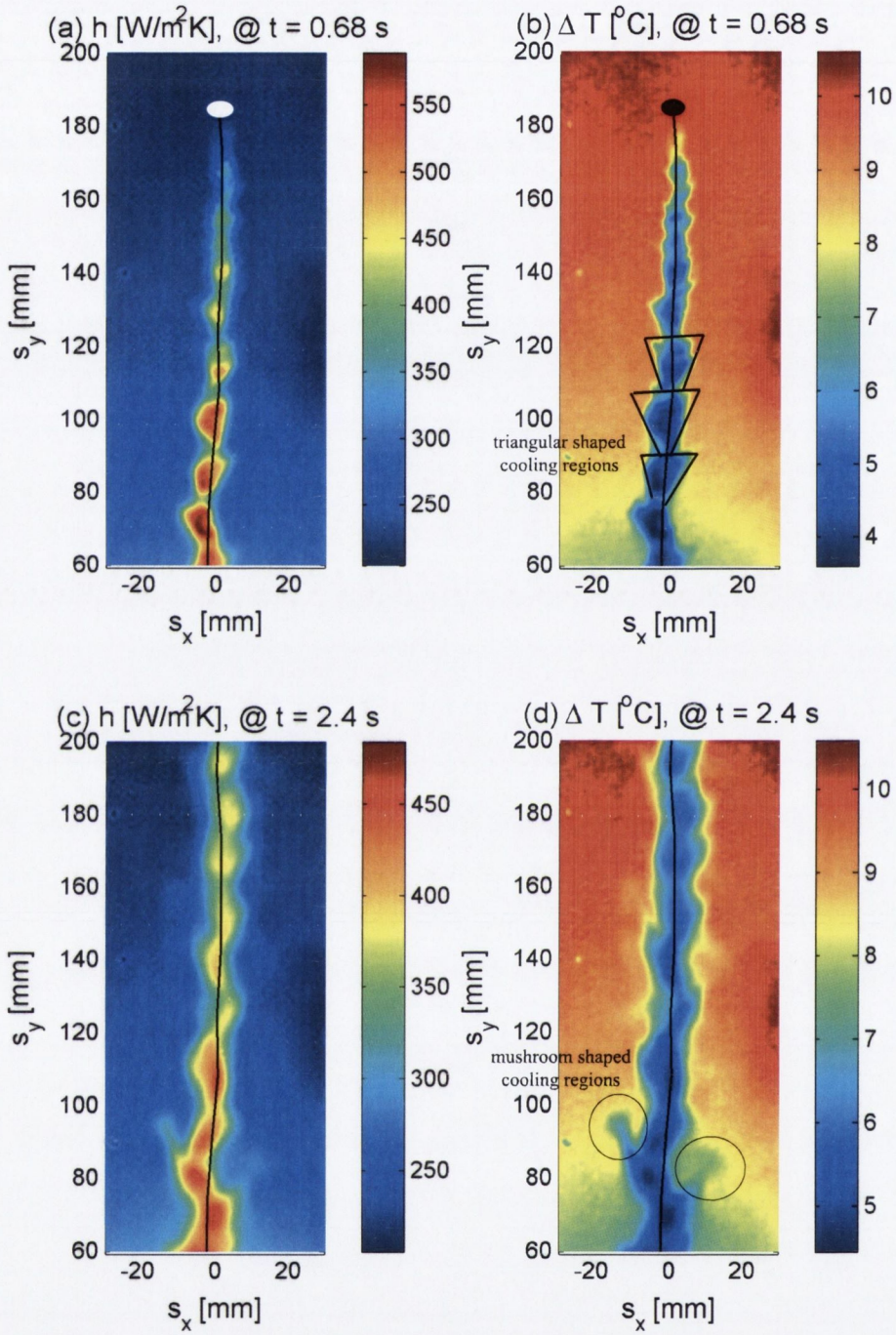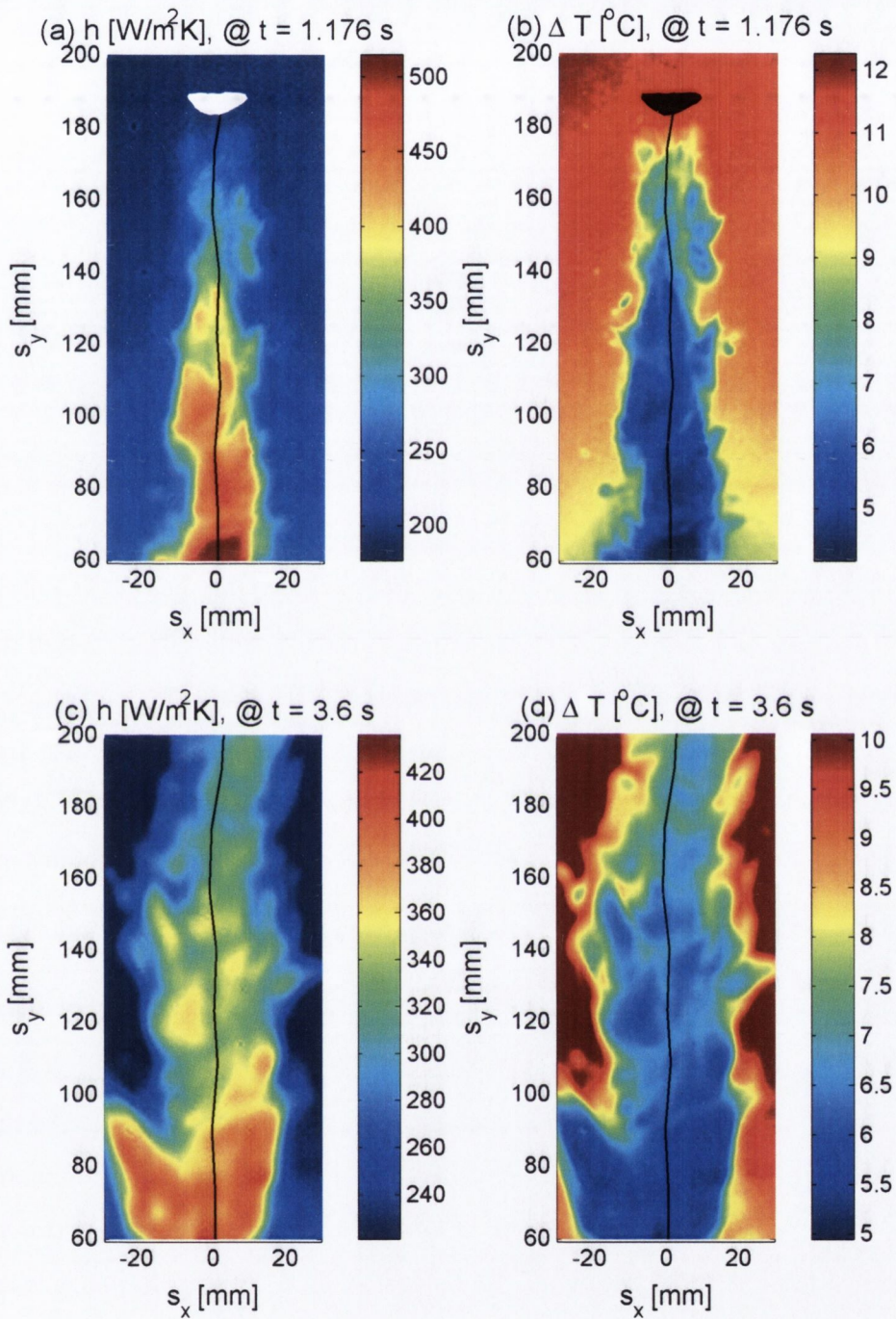
Figure 5.45: The heat transfer coefficient, h (left), and the temperature difference, ΔT (right), for the 0.4 ml bubble. Superimposed on the upper images is the bubble outline and approximate path. Top and bottom images are separated by approximately 2 s.
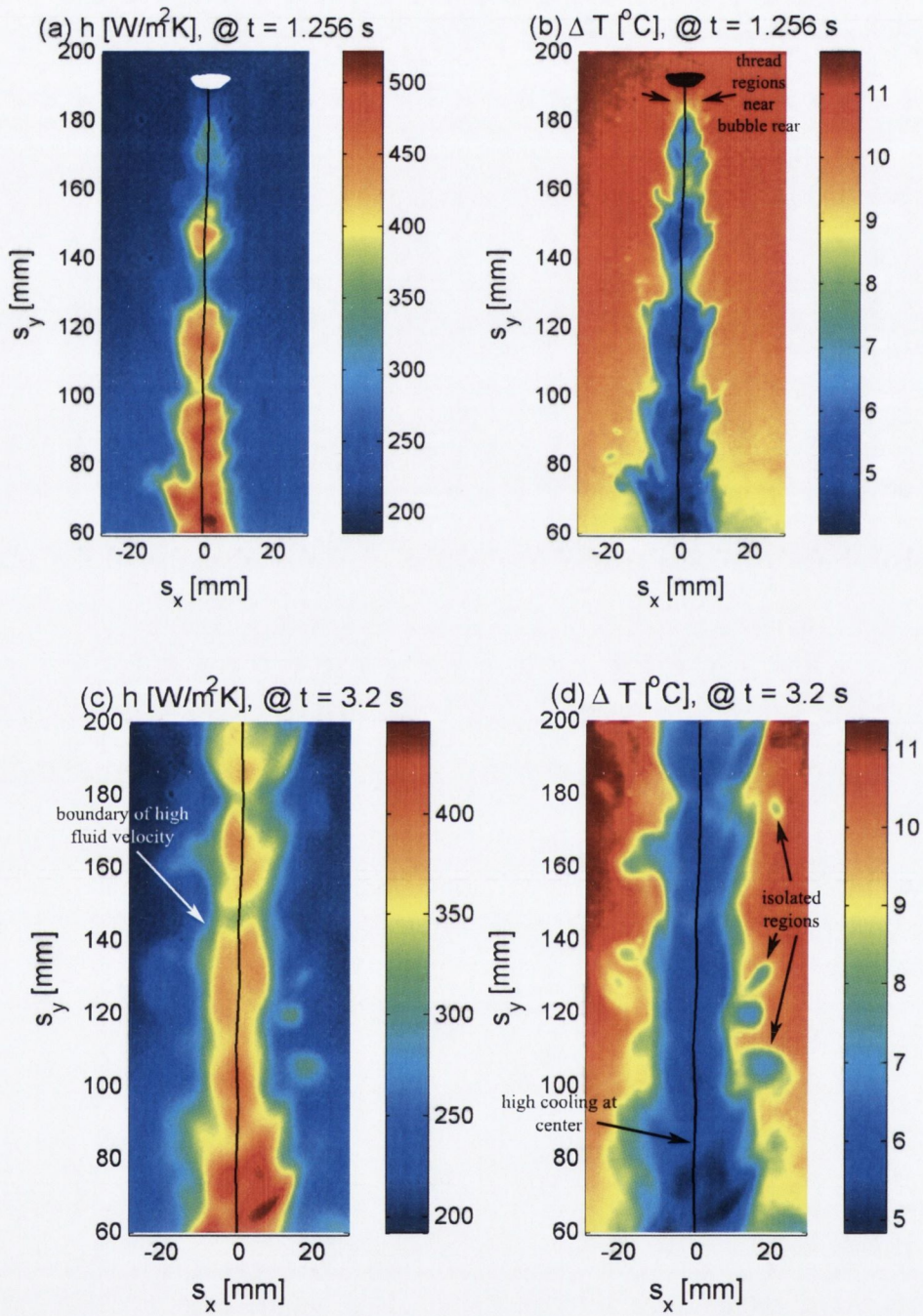
images reveals that this is closely linked to the bubble shape fluctuations, as will be discussed later. The advancing edges of the region are associated with high fluid velocity encircling each vortex.

The 0.1 ml bubble (Figure 5.43) has a similar pattern to its cooling effects. Even in the early stages of vortex separation, small thread like regions of cooling extend ahead of the dominant vortex as highlighted in the ΔT plots. As time advances, these cooled regions continue to expand, often surrounded by small isolated regions of cooling. These isolated regions could be related to the vortices although it is difficult to tell without additional fluid measurement. The increase in volume has a significant effect on the area affected by the bubble.

Figure 5.44 shows the effect of increasing the volume to 0.2 ml. More visible in these images, due to the larger volume, is the region immediately behind the bubble. Two thread like regions of cooling extend back from each side of the rear of the bubble. Simultaneous analysis of a sequence of thermal images with bubble shape reveals that these regions originate from the center (at the bubble path) and move outwards as the bubble widens (this will be examined in more detail later). They detach from the edge of the left and right of the bubble simultaneously when it is at its highest eccentricity (maximum elongation), the bubble then returns to a lower eccentricity and the cycle repeats. This appears to be the point at which the vortices detach from the bubble and begin to travel downstream. Perhaps as they detach, cooled fluid from the bulk has to be drawn in to replace them, resulting in the regions of high enhancement factor observed in Figures 5.37 to 5.40 (the central peaks). The vortices then move out and away from this region, cooling the surface as they move. As time advances (bottom row of Figure 5.44), the images show a cooled region approximately twice the width of the bubble with scattered, isolated patches of elevated heat transfer coefficient each side of a local maximum. The elevated fluid velocity is concentrated near the advancing boundary of cooling. For the 0.4 ml bubble (Figure 5.45) the wake appears more chaotic, illustrating long threads and large blocks of cooling. The larger bubble volume results in a much larger affected area.

Figure 5.46 shows a sequence of close up images for the 0.2 ml bubble sliding on the heated surface. Each image in the sequence is separated by 0.008 s. The sequence

contains one full oscillation of the bubble shape, i.e. one cycle of the periodic wake. The contours represent the temperature difference between the current frame and the natural convection temperature before bubble passage, $T_0 - T_s$. The outermost contour corresponds to $-0.2\,°C$ decreasing by $0.4\,°C$ for each contour thereafter. The area being observed measures $28 \times 40\ mm^2$.

In image 1, the bubble is approaching its maximum elongation. Cooling in the wake is concentrated in two regions behind the edges of the bubble and an additional region is located just to the left of center. The bubble is slightly rotated in the anti-clockwise direction. Image 2 appears to be the moment when vortices detach, the edges of the bubble quickly recoil forward immediately after detachment and by image 3 the shape is quickly becoming ellipsoidal. The two regions of cooling located behind the bubble edges apparently get left behind as the relative distance between them and the bubble increases. It is these same regions that are associated with the shed vortices (observed in the PIV results) and elevated heat transfer enhancement factor. They slowly move north-east and north-west respectively.

Images 3-6 show the bubble returning to an ellipsoidal shape, possibly because the detached vortices, which had been building in strength prior to this, can not influence the bubble shape anymore. The cooled region reflects the reduction in width. The region of cooling just left of rear center continues to move left over this range although is not noticeable after image 9 or so. Image 7 shows the beginning of another dramatic change in bubble shape. Between images 7 and 12, flat regions (indicated in image 11) develop on each side of the rear of the bubble as the bubble flattens in the z-direction (perpendicular to surface), previously highlighted in Figure 5.31. On close inspection of a sequence of moving images, it appears that fluid is moving over the bubble from front to back, flattening it as it moves. Images 11 and 12 show the rear flat regions bulge out slightly and by image 13, the fluid most likely impacts on the surface causing an elevated region of cooling. This is the region of maximum heat transfer enhancement observed in Figures 5.37 to 5.40, one for each shape oscillation.

The bubble outline in images 13-17 are, to varying degrees, partially obscured by light sheet reflection but it is still possible to see the shape becoming elongated in the x direction and shorter in the y direction, the rear flat regions begin to smooth

(1) cooling regions

(2) recoil / recoil

(3) relatively stationary cooling region

(4) shape transition towards ellipsoidal

(5)

(6) reduction in width

(7) motion of cooling region

(8)

(9)

(10)

(11) flattened interface

(12) bulged interface

(13)

(14) elevated cooling region

(15)

(16)

(17) elongation

(18) new cooling regions

(19) bias on r.h.s.

(20)
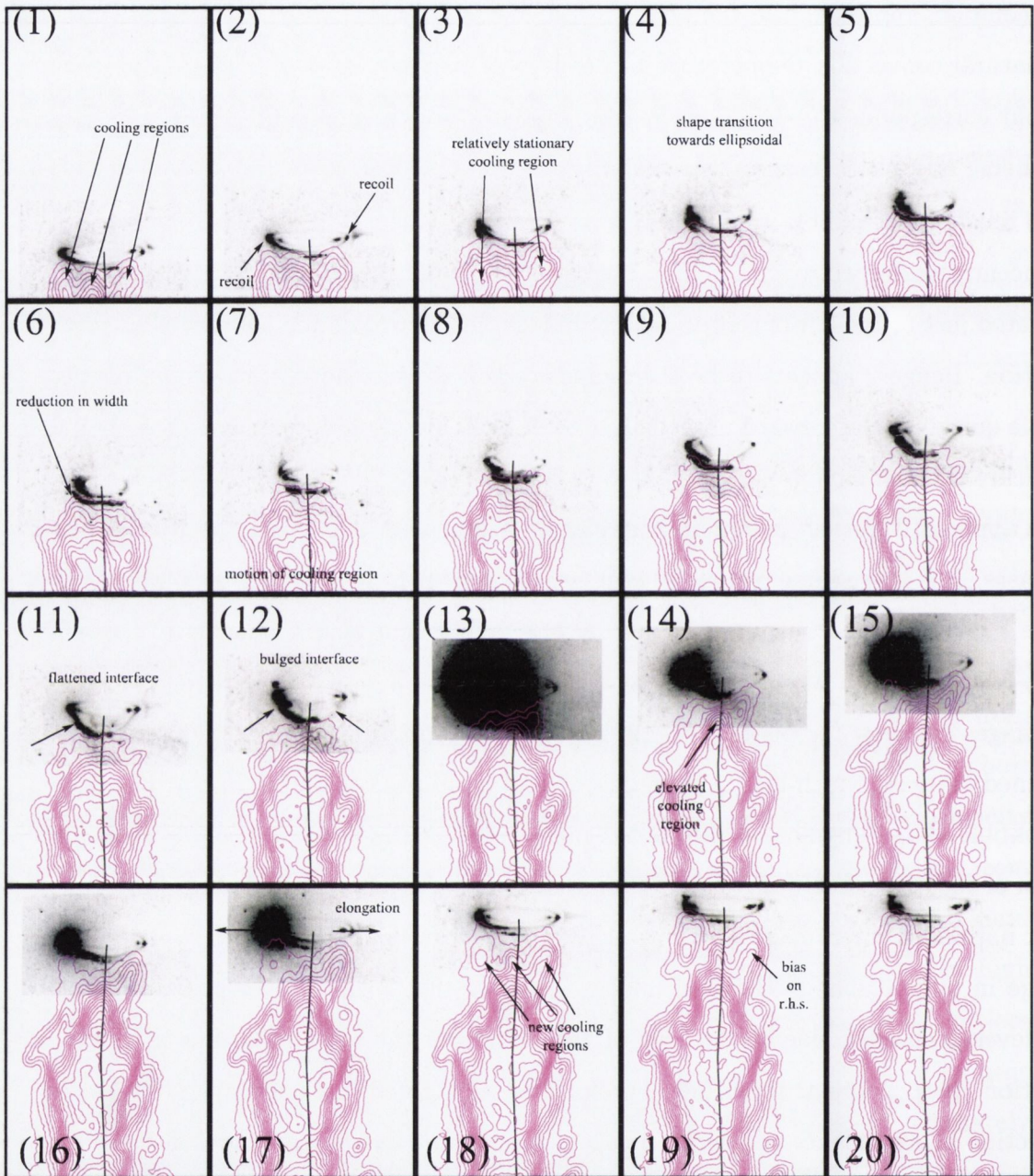
out. As the bubble widens, it is once again reflected in surface cooling. Over this range of images (13-17) it is possible to see the cooling regions located at the bubble edges and center develop (previously mentioned in relation to images 1-3, highlighted in image 17), the edge regions are most likely related to vortex development and subsequent detachment. As the vortices grow in strength they cause the bubble to become elongated while also having a cooling effect on the surface. This time the bias of the central region is to the right hand side. These regions continue to move with the bubble until image 18, where the cycle repeats itself. The edges of the bubble recoil forward and the vortices once again detach. The bubble now has a slightly clockwise rotation.

The bias in the direction of the central cooling region, first left and then right, coupled with the bubble orientation, may reflect the alternating nature of the vortex strength and direction (see Figures 5.37 to 5.40 and Figure 5.46). Strangely, the maximum heat transfer enhancement factor observed, $\epsilon = 2.2$, was roughly the same in all tests, regardless of volume. This was not the case in tests performed with the Bubble motion setup which are discussed next. It is also important to note that no cooling effects immediately beneath the bubble were recorded.

It would appear that there is a symbiotic relationship between bubble motion and fluid motion and the effects on heat transfer enhancement. The periodic nature of the fluid flow around the bubble results in periodic bubble motion and shape characteristics which in turn result in periodic effects on cooling. Although the bubble in PIV tests behaves differently to the Bubble motion tests, they both exhibit a periodic nature and as such may have more in common than is first apparent.

5.5   Heat transfer: Bubble motion setup

Heat transfer results for the Bubble motion setup are divided into two sections corresponding to the steady state and transitional tests previously described in Section 5.2. Results are presented of the surface to bulk fluid temperature difference, ΔT, and heat transfer coefficient enhancement factor, ϵ, to allow easy comparison to results from the PIV setup. Superimposed on these images are the bubble shape and the bubble path.

5.5.1 Heat transfer: steady state

The same tests previously described in Figure 5.12 to 5.15, regarding bubble dynamics, are presented here in relation to heat transfer. Heat transfer aspects observed for transitional tests will be discussed in Section 5.5.2.

Figure 5.47 and 5.48 show the results for the 0.05 ml bubble at $t = 0.552$ and 2.768 seconds respectively. Immediately apparent is the oscillating effect of the bubble's motion on heat transfer. The trail of cooling in the wake follows a snake like path. This quickly moves away from the bubble path in each direction, left or right, depending on the direction the bubble was traveling at the time of separation. Immediately behind the bubble, the cooling effect appears intermittent with small local regions of high enhancement separated by regions of lower enhancement. There is no evidence of the triangular regions of cooling previously observed for the PIV setup. These were deemed to be the result of simultaneous shedding of vortices from each side of the bubble. In this case, as time passes, the cooled regions roughly take the shape of the letter 'i', inclined at an angle to the vertical (one for each zig and zag of the bubble, as indicated in the figure). The dot on the 'i' takes the rough shape of a mushroom, a shape previously observed in the PIV tests (Figure 5.42 to 5.45). The maximum enhancement factor observed for the 0.05 ml bubble is approximately 3.7, compared with 2.2 for the PIV setup. Periodic, isolated patches of local maximum enhancement are highlighted in Figure 5.47 (b), similar to those in Figure 5.37 to 5.40. These appear to occur twice in every path oscillation giving them a generation frequency of twice the path oscillation frequency, i.e. approximately 6 Hz.

The 0.1, 0.2 and 0.4 ml bubbles (Figure 5.49 to 5.54) all exhibit similar trends to the 0.05 ml bubble although by 0.4 ml the cooled regions appear more chaotic. The maximum enhancement factors observed foe these tests are 3.7, 6 and 6.8 for the 0.1, 0.2 and 0.4 ml bubbles. These are all substantially larger than those observed for the PIV tests and increase with bubble volume. Once again, the cooling is confined to regions that roughly form an 'i' shape as time evolves, each region alternating left and right of the bubble path. A slight oscillation in the bubble path results in a much larger oscillation in the path of cooling behind the bubble. This also moves with the

natural convection flow, from bottom to top, as time elapses.

Given that the cooling effects seem broadly similar for all bubble volumes, Figure 5.55 shows a close-up view one half period of bubble oscillation for the 0.2 ml bubble only. This is comparable to Figure 5.46 for the PIV setup. The figure shows a sequence of images of the bubble outline, bubble path and contours of temperature difference between the current image and natural convection $(T - T_0)$. The path is coloured by the bubble velocity magnitude, $|v|$ (red = high, yellow = low). Each image in the figure is separated by 0.008 s and the area measures 28×60 mm^2.

This sequence will illustrate a region of cooling detaching from the primary wake and being shed to the left of the bubble as it negotiates the curved path. Image 1 shows the bubble just after entering the frame. The wake consists of two narrow regions of cooling extending back from the left and right hand side of the bubble base, as indicated by the arrows. They appear to be inside the bubble boundary but in reality they are most likely very close to each side of the contact region between bubble and plate. The cooling effect of the right hand side is stronger than the left. Immediately behind the bubble there is cooling but to a lesser extent. At the very bottom of the image there is a region of high cooling identified by the steep temperature gradient (highlighted in image 2), this is part of the previous ejection from the wake and will travel in a north east direction with time. Image 2-6 show the narrow regions of cooling at the bubble base growing in strength forming two localised regions of maximum cooling, highlighted in image 6.

By image 7 the cooling effect on the right hand side of the bubble is much stronger than the left, the bubble is turning right and accelerating. This trend continues up until image 16 where the bubble is just past the apex. Image 17 reveals a region of elevated cooling appearing towards the rear left hand side of the bubble (this is probably present before this point but is indicated in image 17). It is moving from right to left as the bubble moves. The bubble is now decelerating. This will form the front of a region of cooling that will be ejected from the wake and travel northwest (just like the previous ejection to the right). It is around this point that the 0.4 ml bubble develops its cusp (Figure 5.5). The cusp appears to be related to vortex detachment (see Fan & Tsuchiya [1]) so it is at this point where fluid is shed from the
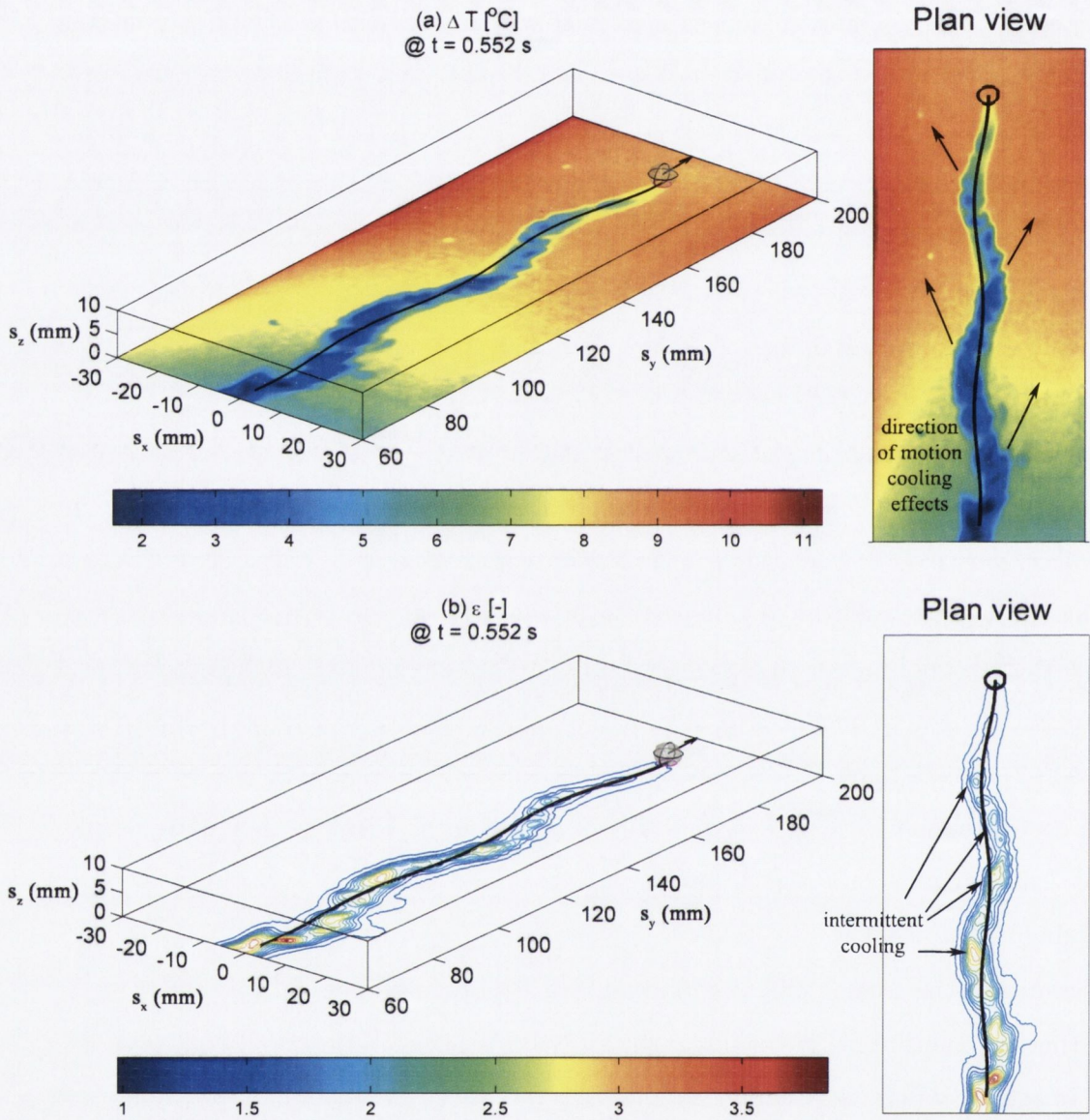
Figure 5.47: (a) Surface to bulk fluid temperature difference, ΔT, and (b) ϵ for the 0.05 ml steady state bubble at $t = 0.552$ s. Superimposed on the images are the bubble position, three dimensional shape and path.
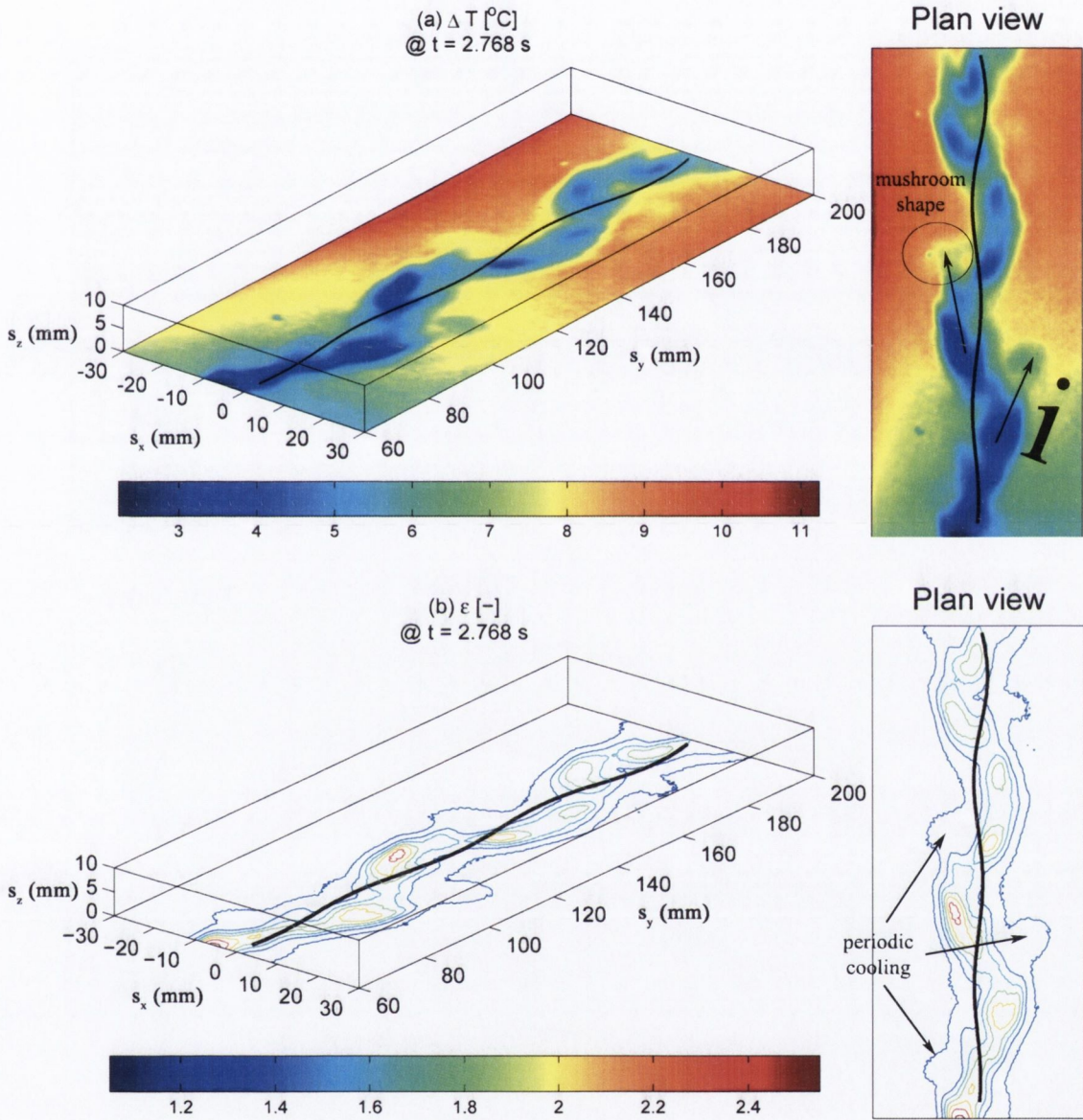
Figure 5.48: (a) Surface to bulk fluid temperature difference, ΔT, and (b) ϵ for the 0.05 ml steady state bubble at $t = 2.768$ s. Superimposed on the images are the bubble position, three dimensional shape and path.
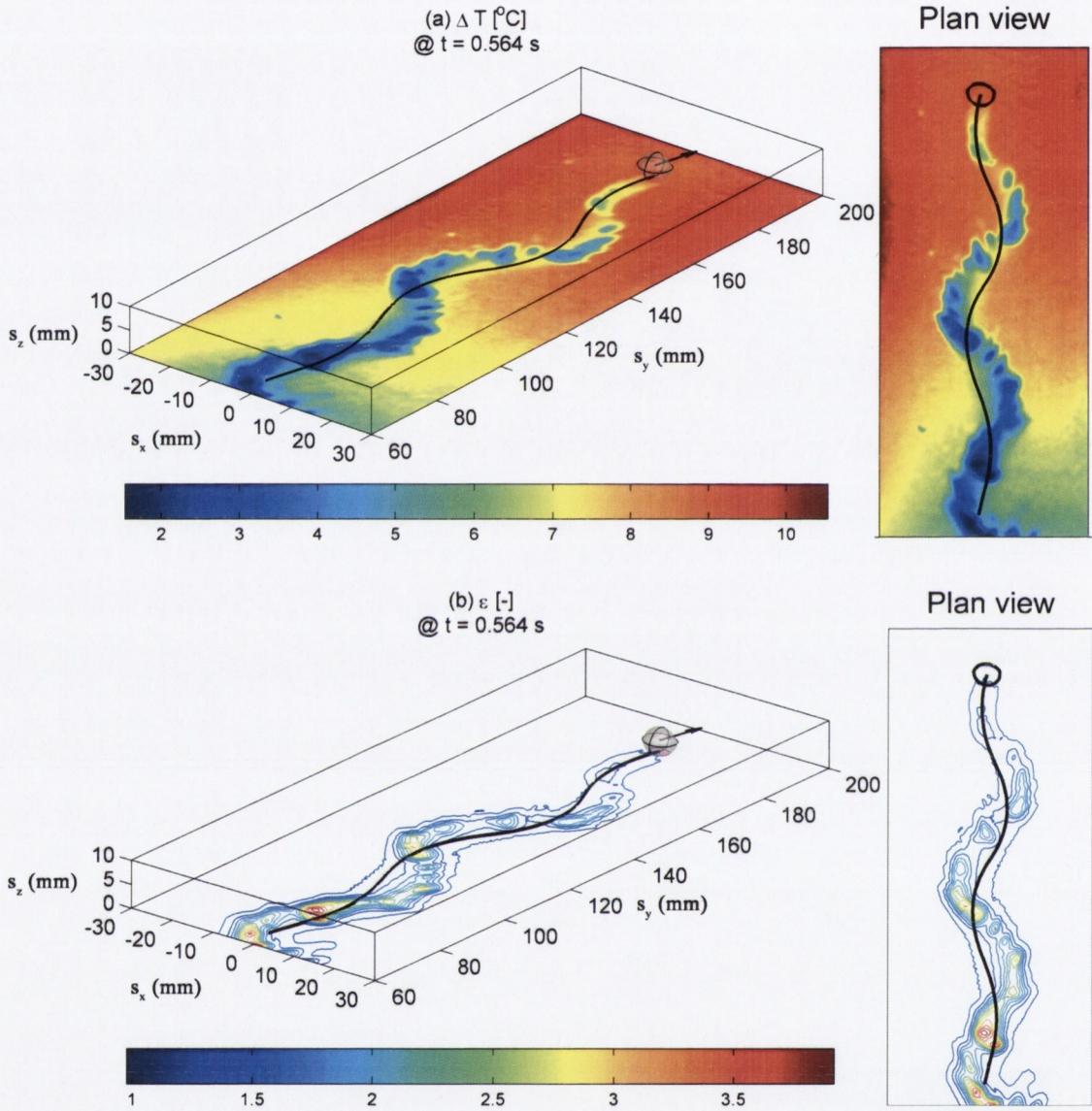
Figure 5.49: (a) Surface to bulk fluid temperature difference, ΔT, and (b) ϵ for the 0.1 ml steady state bubble at $t = 0.564$ s. Superimposed on the images are the bubble position, three dimensional shape and path.
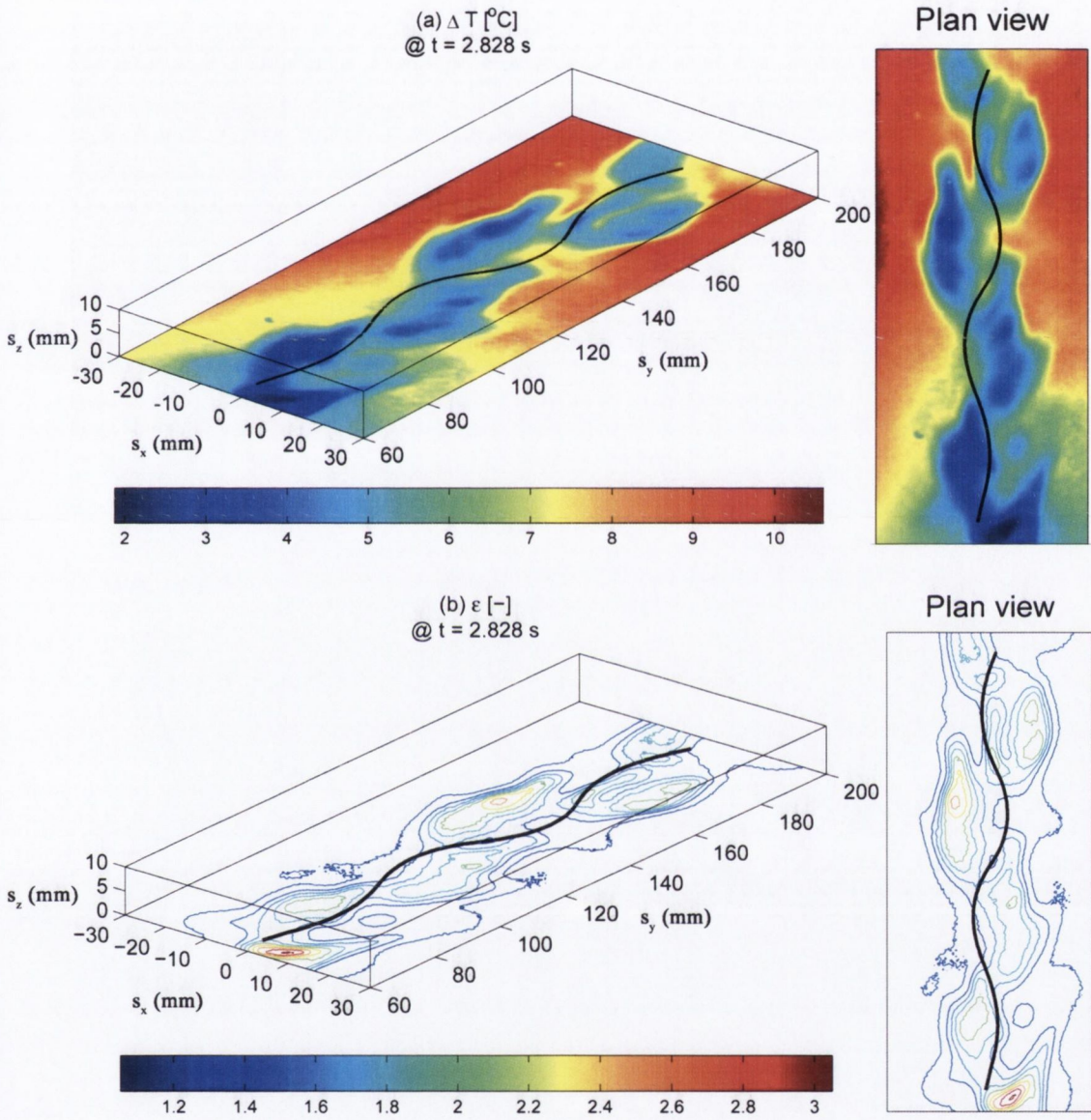
Figure 5.50: (a) Surface to bulk fluid temperature difference, ΔT, and (b) ϵ for the 0.1 ml steady state bubble at $t = 2.828$ s. Superimposed on the images are the bubble position, three dimensional shape and path.
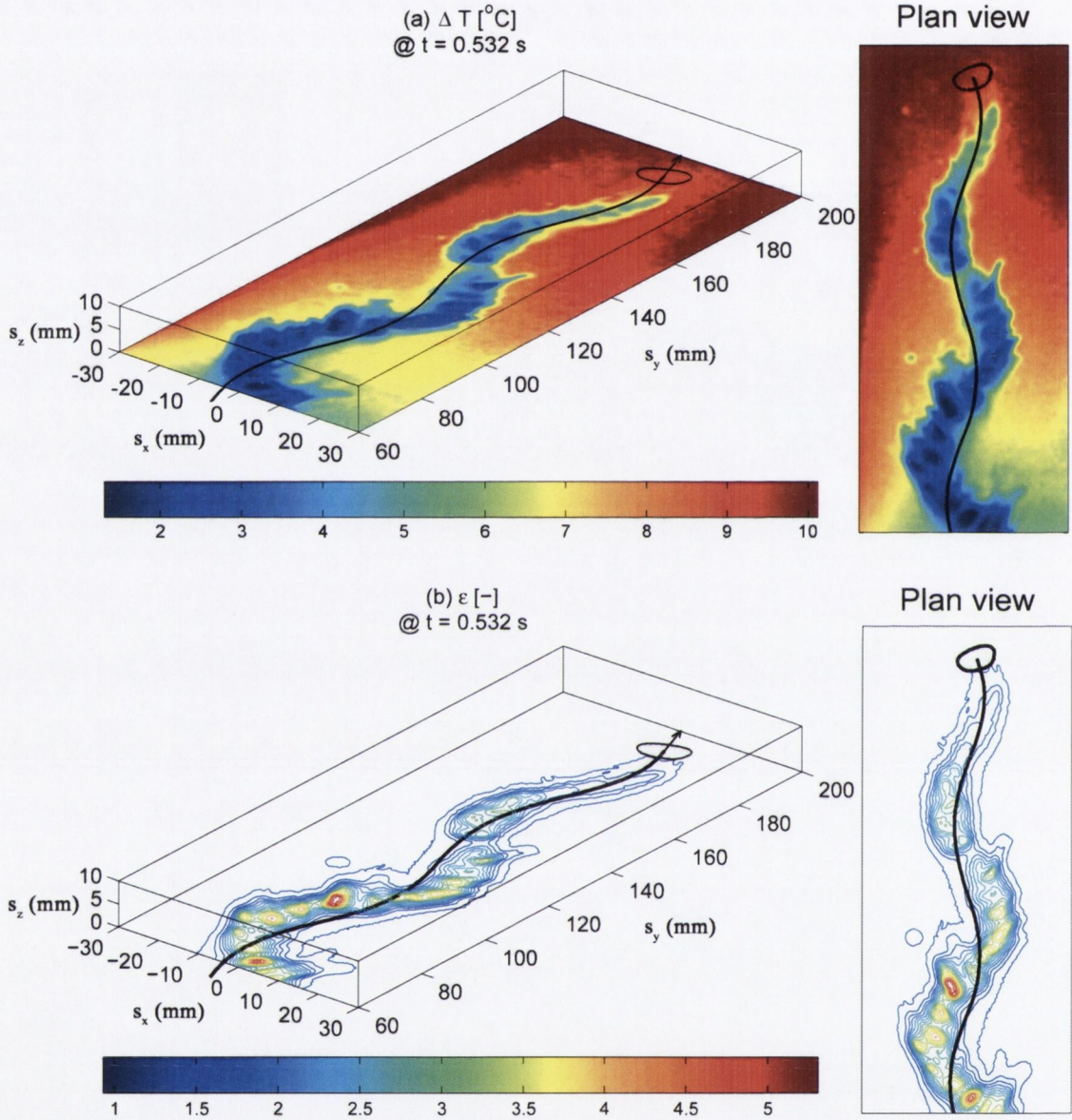
Figure 5.51: (a) Surface to bulk fluid temperature difference, ΔT, and (b) ϵ for the 0.2 ml steady state bubble at $t = 0.532$ s. Superimposed on the images are the bubble position, three dimensional shape and path.
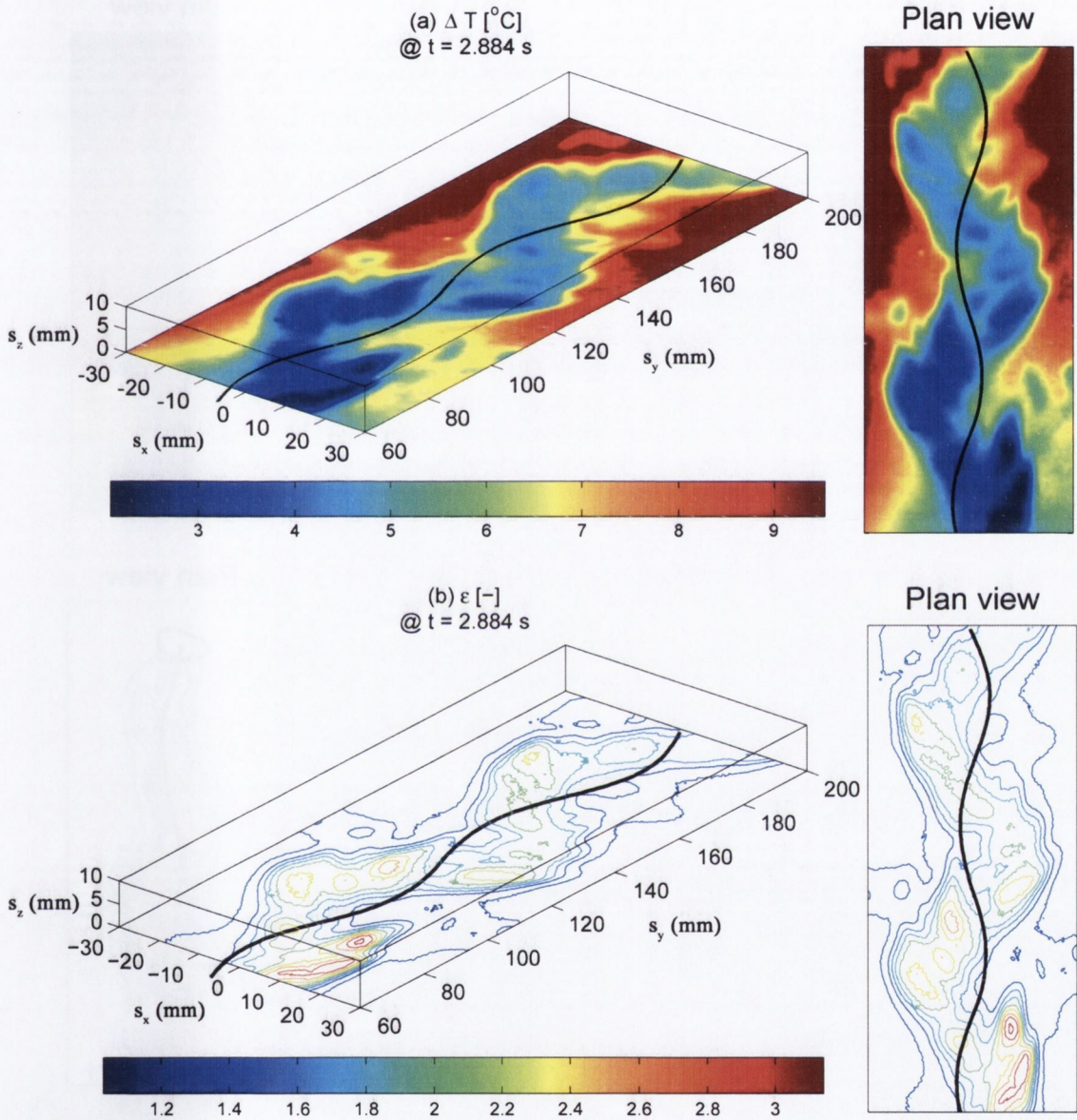
Figure 5.52: (a) Surface to bulk fluid temperature difference, ΔT, and (b) ϵ for the 0.2 ml steady state bubble at $t = 2.884$ s. Superimposed on the images are the bubble position, three dimensional shape and path.
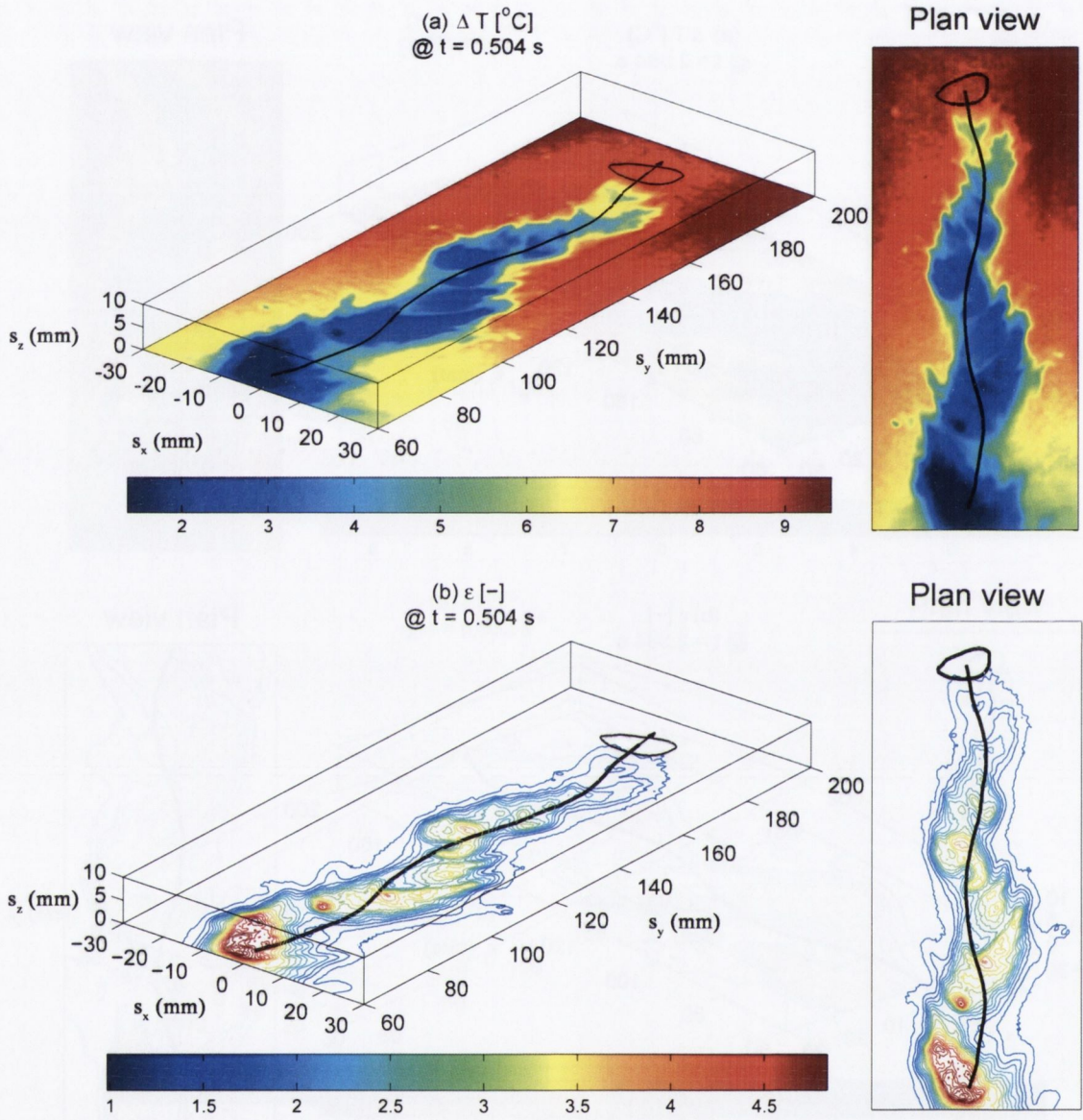
Figure 5.53: (a) Surface to bulk fluid temperature difference, ΔT, and (b) ϵ for the 0.4 ml steady state bubble at $t = 0.504$ s. Superimposed on the images are the bubble position, three dimensional shape and path.
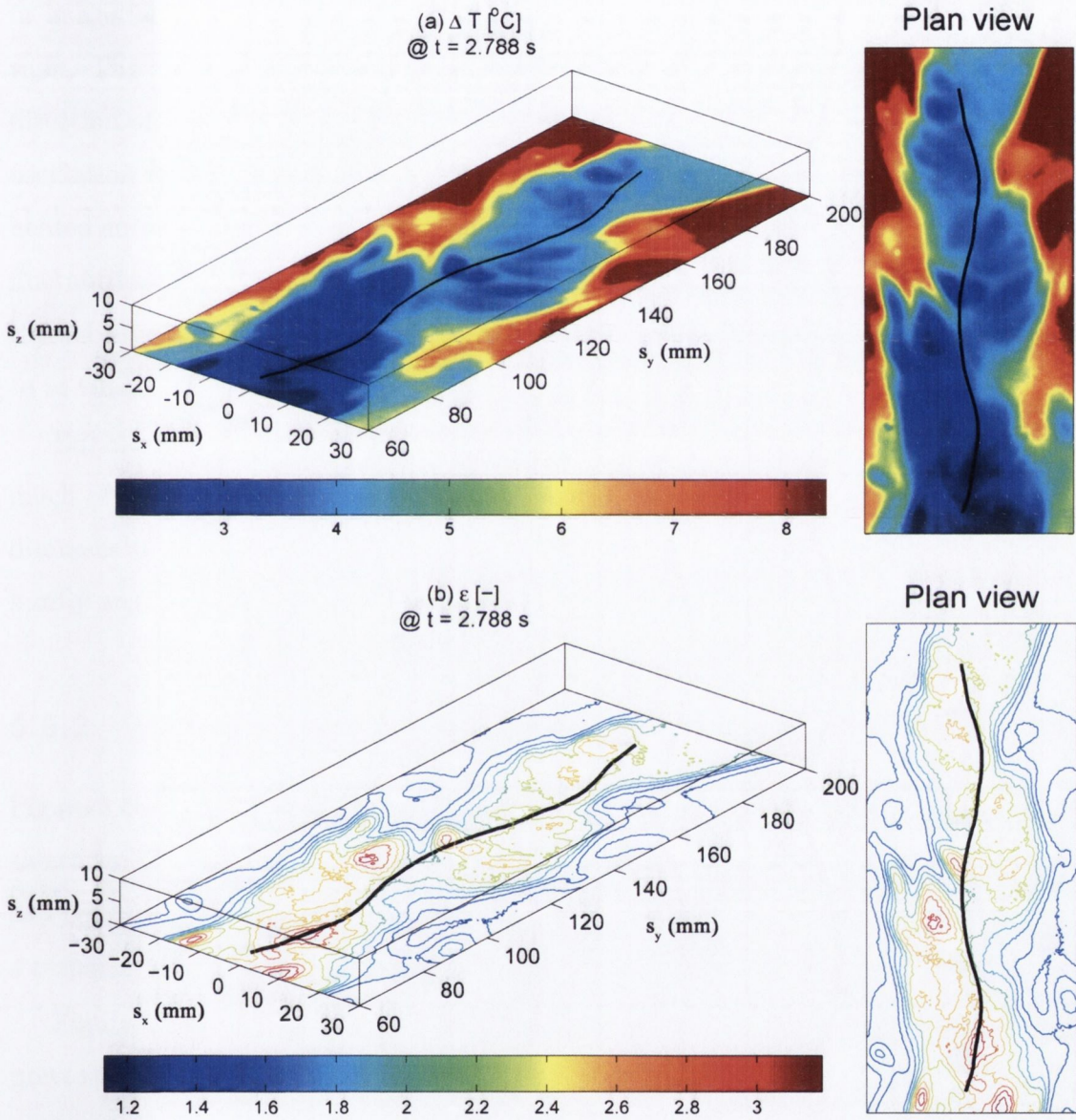
Figure 5.54: (a) Surface to bulk fluid temperature difference, ΔT, and (b) ϵ for the 0.4 ml steady state bubble at $t = 2.788\ s$. Superimposed on the images are the bubble position, three dimensional shape and path.
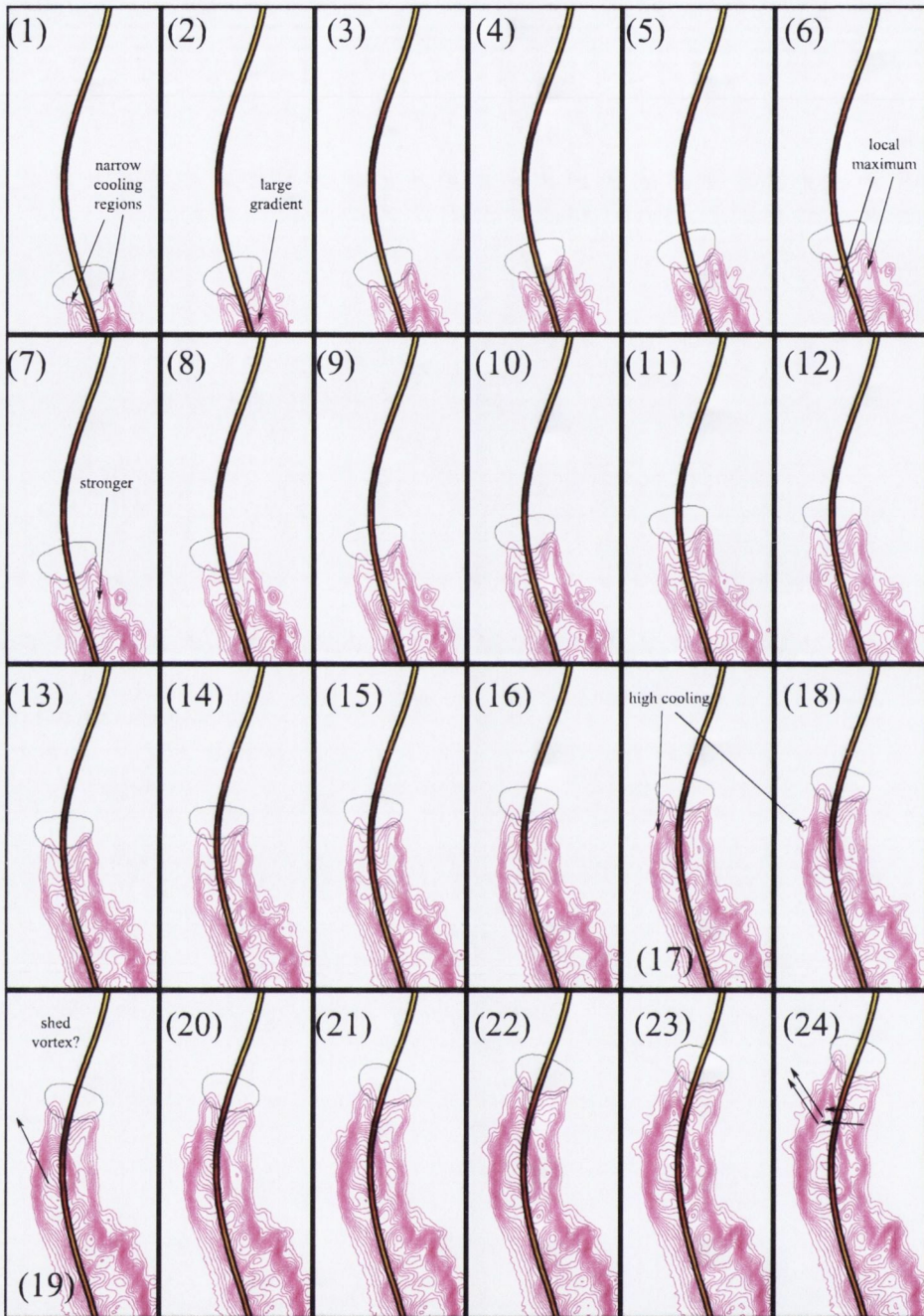
Figure 5.55: Close up sequence of 0.2 ml steady state bubble for the Bubble motion setup. Overlapped are the bubble outline, the temperature difference, $T_0 - T_s$, and the bubble path. The path is coloured by velocity, red = high, yellow = low. The time separation between images is 0.008 s. Outermost contours correspond to $-0.2\,°$C decreasing by 0.4 $°$C for each contour thereafter.

primary wake and travels downstream relative to the bubble.

Images 18 to 24 show that as the central cooling region moves from right to left, it drags regions of cooling with it from the right hand side of the bubble (indicated in image 24). The left hand side of the bubble now exhibits higher cooling than the right. The cycle repeats on each half period of bubble path oscillation, alternating the direction of wake shedding. The frequency of wake shedding is twice the bubble path oscillation frequency, corresponding to approximately 6 *Hz* for bubbles sliding on the heated surface and 5 *Hz* for the non-heated surface (see Figure 5.8). Very little shape fluctuations are observed over the test range compared to those in the PIV setup (only the 0.4 *ml* bubble exhibits any large scale fluctuations). These results will be returned to in Chapter 6 for interpretation.

Bubbles that were deemed to exhibit transitional bubble motion generally show much of the same characteristics with regard to heat transfer. The following section discusses two tests, one which exhibited large path oscillations and one which exhibited hardly any.

5.5.2 Heat transfer: transitional

Figure 5.56 to 5.59 show two examples taken from tests deemed transitional previously shown to Figures 5.25 and 5.24 respectively. The figures employ the same presentation as Figures 5.47 to 5.53 with the bottom images separated from the top by 2.1 and 2.2 *s* respectively.

Figure 5.56 shows the 0.1 *ml* transitional bubble. The bubble in this test was previously noted for its quick succession of sharp turns followed by a smoother, curving path. Observation of its cooling effect in relation to wake shedding reveals a possible reason for this behaviour. As previously mentioned, the wake appears to be shed at approximately the same time as the bubble reaches its maximum x displacement. In this example the bubble appears to have two massive ejections from the wake in quick succession and in different directions. Starting at the bottom of Figure 5.56(a) and (b), the bubble turns sharply right. This results in the large region of cooling to the left of the bubble path, clearly visible in Figure 5.56 (a). The cooled region grows

rapidly and is quite large after approximately 2 seconds. As the bubble rounds the curve, it turns sharply left, resulting in a second large ejection to the right hand side. As the bubble begins to follow the smooth curved path, it changes direction again but at a much slower rate, curving to the right. Even still, fluid detaches from the wake and results in a smaller region of cooling just left of the bubble path (visible in both top and bottom images but more obvious as time advances). There seems to be a close link between the bubble's motion and the cooling effect of the wake ejected. The sharper the turn, the higher the cooling. This may be related to the strength of the proposed vortices being shed from the wake. Sharped turns either lead to, or are the result of, large ejections from the primary wake.

Figure 5.58 shows the 0.05 *ml* bubble. This test was noted to be the only one of the Bubble motion tests to show near rectilinear motion, although periodic motion was evident near the top of the image. This test is important because it could provide a link between tests in the PIV setup (which exhibited very little path oscillation) with tests in the Bubble motion setup (which exhibited large oscillatory motion). The heat transfer patterns appear to show characteristics from both the PIV and Bubble motion setups. Visible in the images are roughly inverted triangular regions of cooling with a maximum located at the bubble path between the two corners of the triangle (There are two of these regions indicated in Figure 5.58 (a), but numerous are present). This may be easier to observe in the enhancement plots which show its effects more clearly. The top left and right of this region are moving away from the bubble path at an angle, originating from very near a region of high enhancement. This is very similar to the patterns of cooling observed for the PIV tests (Figure 5.42). They are associated with vortices being shed from the primary wake which are located at the head of the advancing cooling regions. It was observed that, in an alternating manner, one of the vortices in a pair was always stronger than the other and resulted in greater cooling. This was also indicated as a possible reason for the small path oscillations observed in the PIV tests. As time elapses, the enhancement plot shows patterns that are strikingly similar to those observed in the PIV tests. At each local maximum in enhancement, there appears to be a smaller, less cooled region to either its right or left as indicated in the figure. These could be the effects of the dominant vortex in the shed pair. In

fact, above $s_y = 100 \ mm$, the small region appears on alternating sides of the region of high enhancement. To conclude, up until $s_y = 150 \ mm$, the bubble generates trends in heat transfer that are very similar to the PIV tests. From analysis of fluid motion in relation to heat transfer (Section 5.4), these inverted triangular regions of elevated heat transfer correspond to simultaneous shedding of vortices from the primary wake, one on each side of the bubble path. In the PIV setup these are coupled with shape fluctuations not observed for the Bubble motion setup. It is possible that the similar trends between the two setups suggests similar fluid structures.

Above $s_y = 160 \ mm$ the bubble path begins to curve, periodic path oscillation have set in. The slight turn to the right at $s_y = 160 \ mm$ is coupled with a relatively large discharge from the wake typical of bubbles observed in the Bubble motion tests. There is a corresponding one to the right of the bubble path at $s_y = 190 \ mm$ as the bubble turns left. The shapes of these regions are typical of those observed in all of the other Bubble motion tests. They also fit in with the alternating pattern to the heat transfer as highlighted by arrows 1-5 in Figure 5.58 (b). By counting the rate at which areas of elevated enhancement appear, the vortex shedding frequency is found to be approximately 12 Hz. This corresponds closely with the vortex shedding frequency for 0.05 ml bubbles in the PIV tests.

It would appear that the mechanism of vortex shedding for oscillating bubbles develops from the mechanism observed for non-oscillating bubbles, such as those in the PIV setup. It appears that the dominant vortex grows in strength and eventually causes the bubble to move slightly in the x or y direction. Once this occurs, the mechanism feeds into itself and the bubble oscillates, discharging the wake either side of the bubble path. This idea is developed further in the next chapter in which all the results presented so far will form the basis of a discussion on the nature of the wake behind sliding, oscillating bubbles.
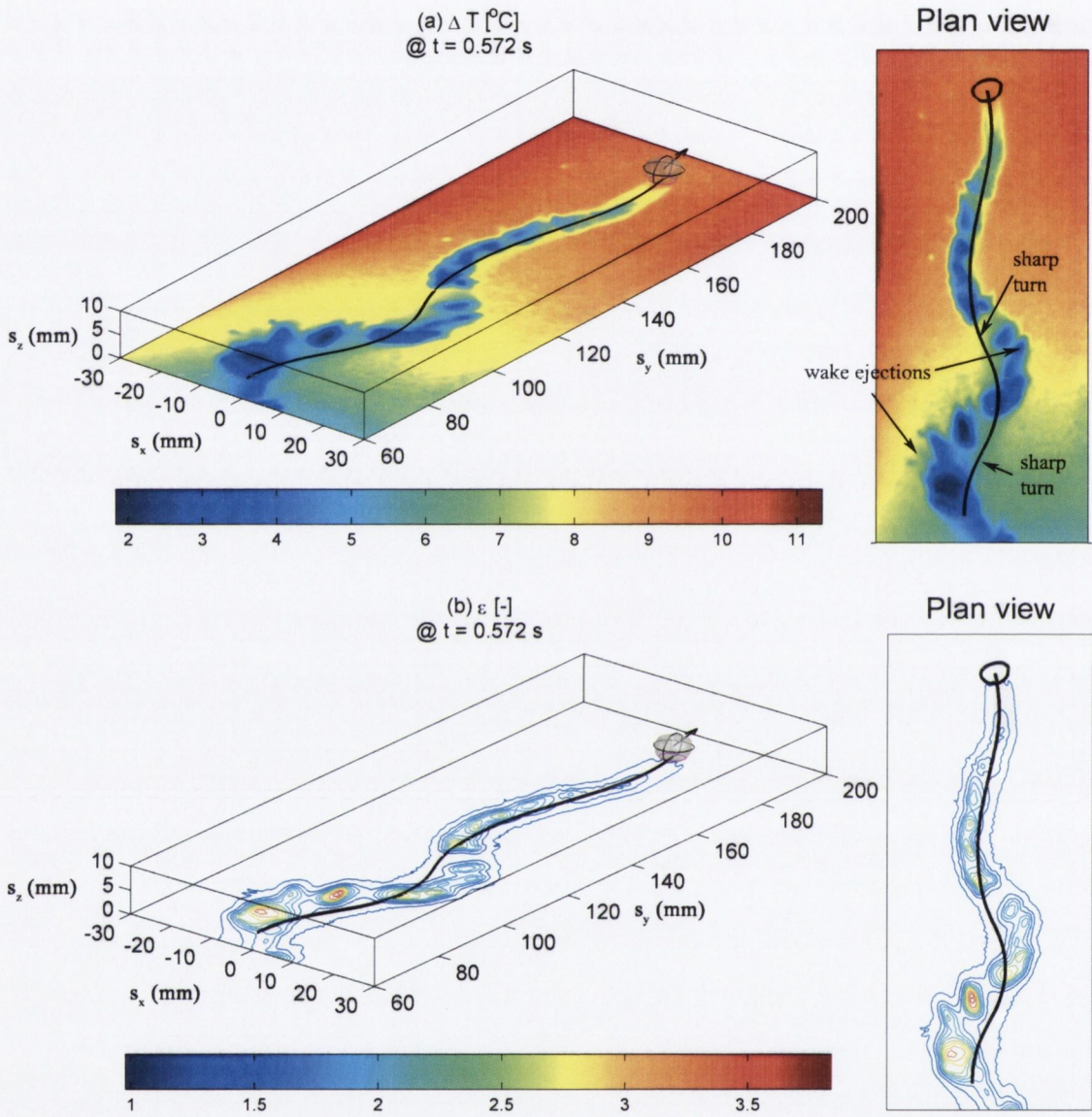
Figure 5.56: (a) Surface to bulk fluid temperature difference, ΔT, and (b) ϵ for the 0.1 ml transitional bubble at $t = 0.572$ s. Superimposed on the images are the bubble position, three dimensional shape and path.
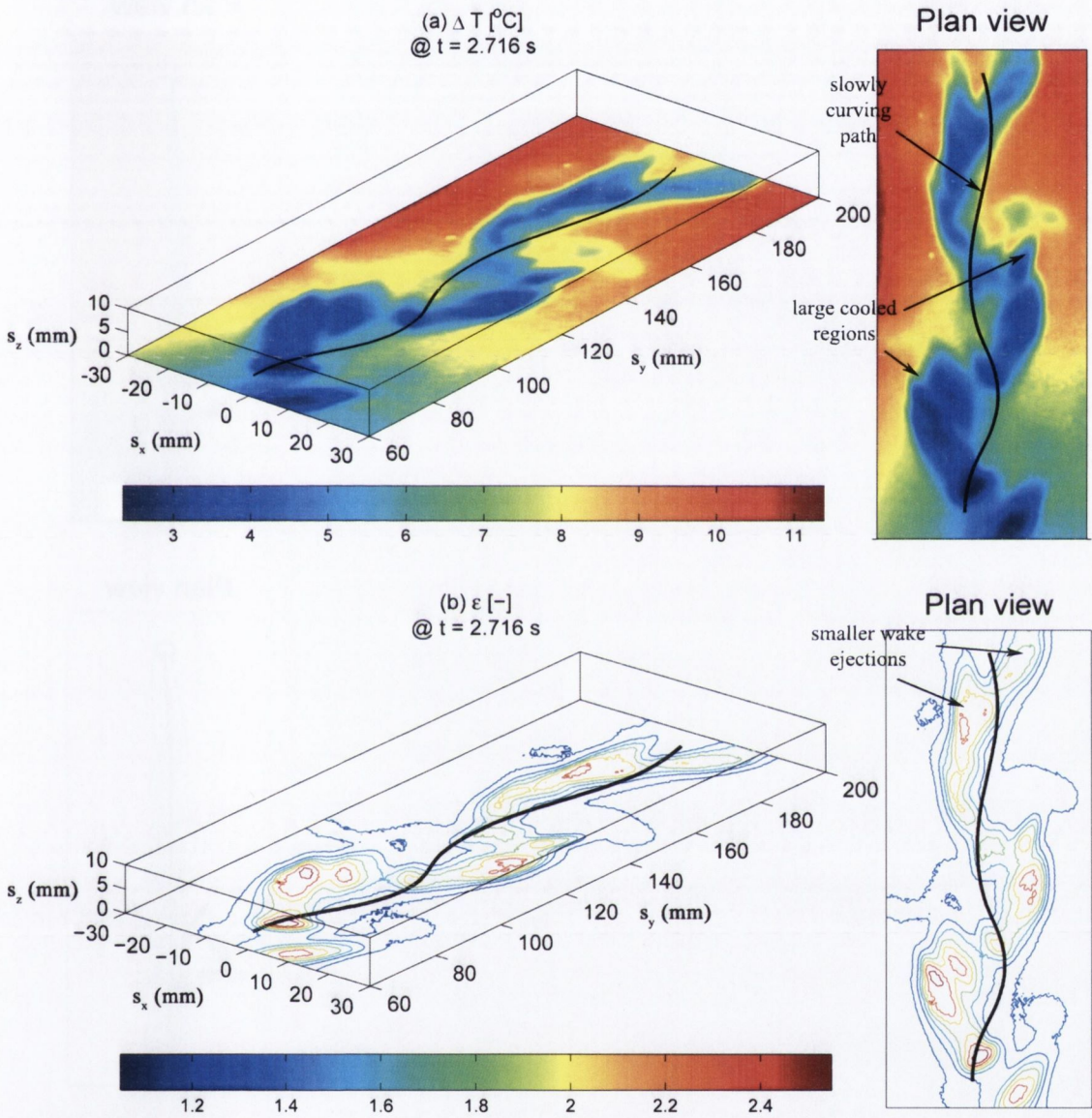
Figure 5.57: (a) Surface to bulk fluid temperature difference, ΔT, and (b) ϵ for the 0.1 ml transitional bubble at $t = 2.716$ s. Superimposed on the images are the bubble position, three dimensional shape and path.
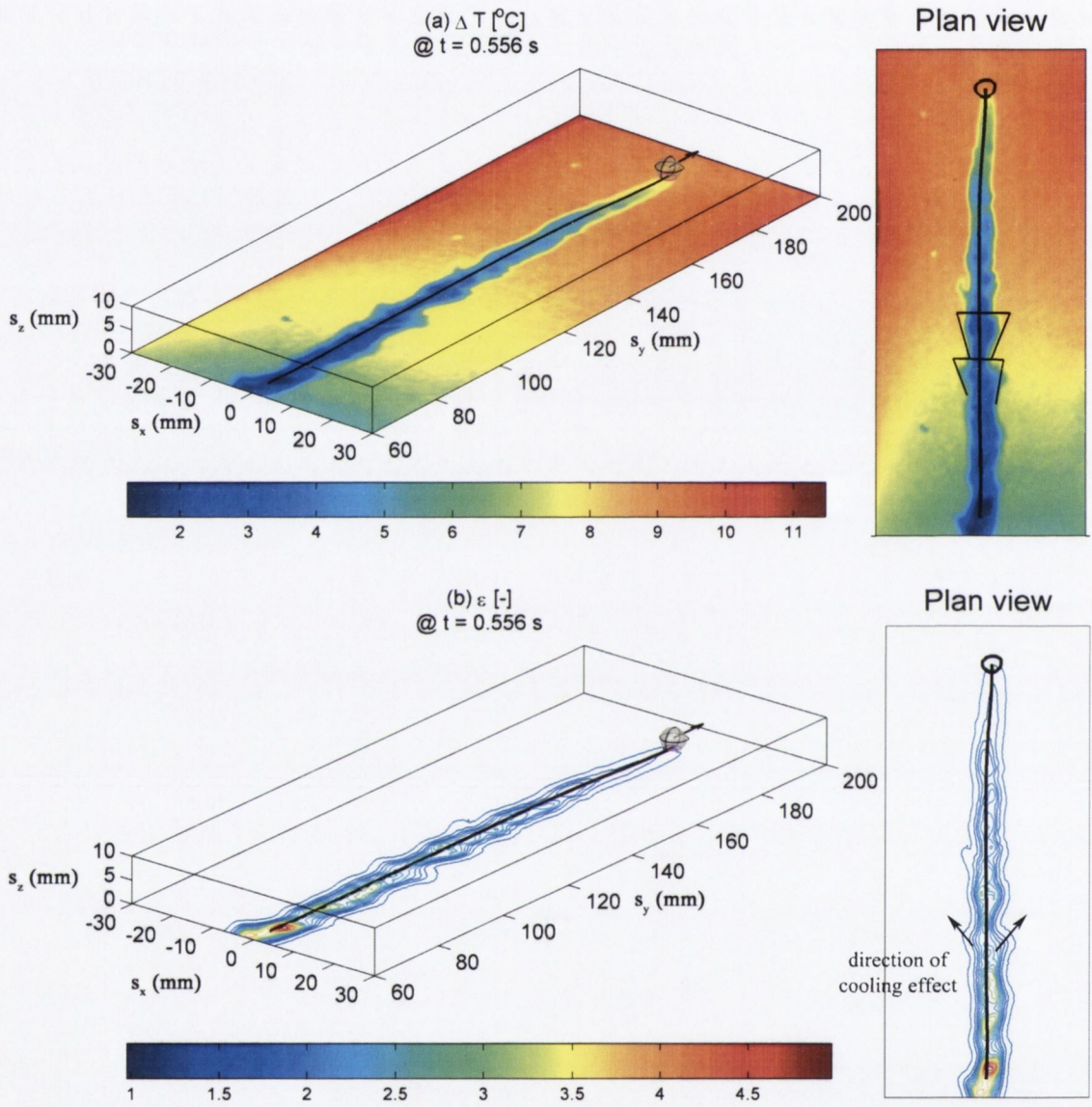
Figure 5.58: (a) Surface to bulk fluid temperature difference, ΔT, and (b) ϵ for the 0.05 ml transitional bubble at $t = 0.556\ s$. Superimposed on the images are the bubble position, three dimensional shape and path.
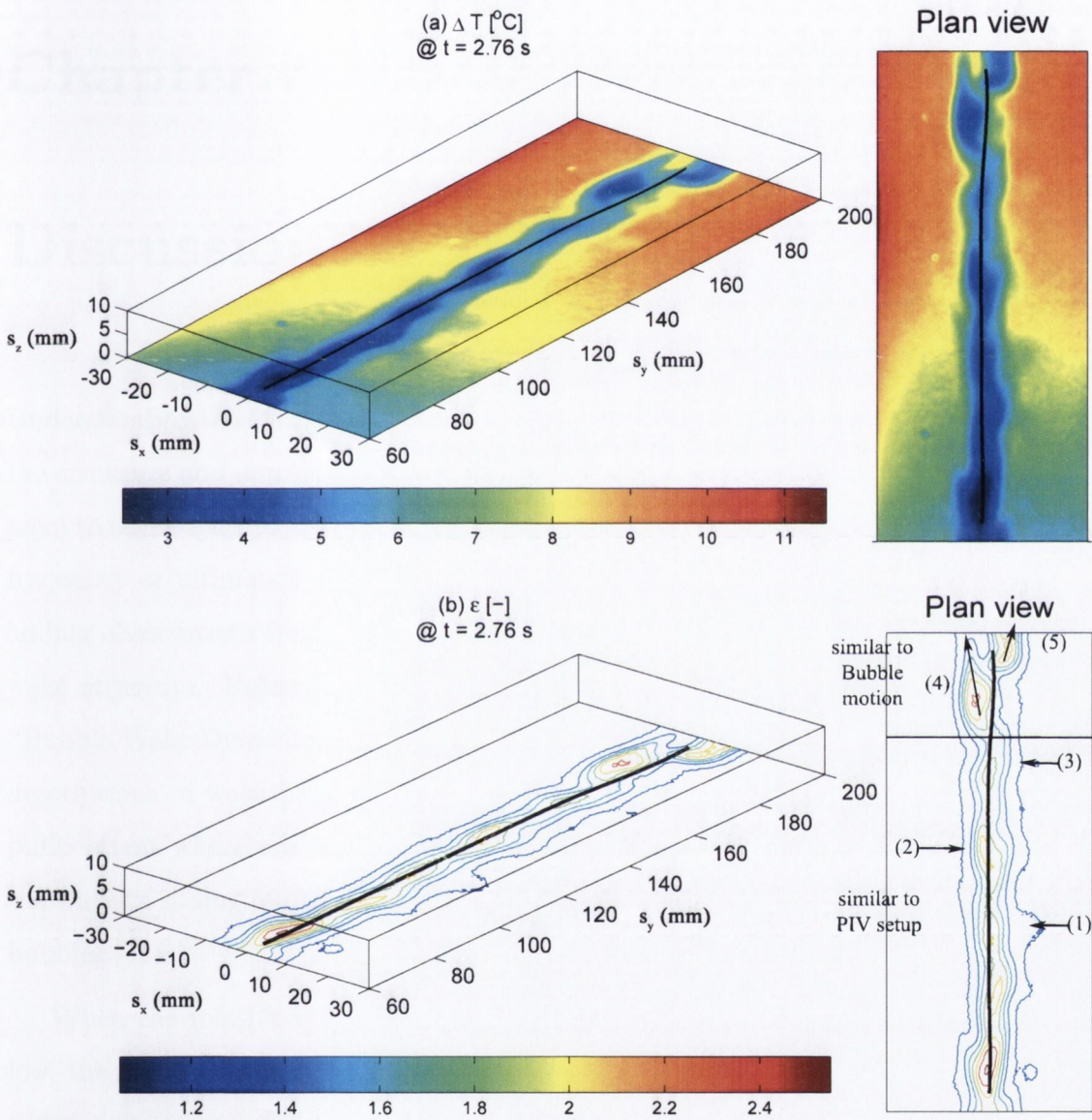
Figure 5.59: (a) Surface to bulk fluid temperature difference, ΔT, and (b) ϵ for the 0.05 ml transitional bubble at $t = 2.76$ s. Superimposed on the images are the bubble position, three dimensional shape and path.

Chapter 6

Discussion

Understanding the effects of a sliding bubble on heat transfer requires understanding of the structure and nature of the bubble wake. All of the results presented in Chapter 5 seem to relate back to the behaviour of the wake, be it shape, path, velocity, oscillation frequency or ultimately heat transfer. This chapter will discuss the results observed, adding observations from the literature in order to obtain a possible description of the wake structure. Reference is made to the work of Fan & Tsuchiya [1], whose book "Bubble Wake Dynamics in Liquids and Liquid-Solid Suspensions" provides excellent descriptions of wake phenomena. Additional reference will be made to more recent publications where relevant. There is limited information in the literature regarding the wake of sliding bubbles, and as such, most comparisons will be made to free rising bubbles.

When the relative velocity between the bubble and the surrounding fluid is very low, the fluid will closely follow the bubble interface. The whole contour of the bubble forms part of a streamline. This only occurs when the Reynolds number is sufficiently low; for bubbles in water the diameter is in the order of $1\ mm$. As the Reynolds number exceeds a critical value, the flow over the surface will start to separate. For bubbles in water, the Reynolds number will increase with volume. This is due to the increased characteristic length and, because of the increased volume, an increase in buoyancy and therefore velocity.

For Reynolds numbers just above the critical value, the separated streamlines will

rejoin some distance behind the bubble, forming a closed region described as the wake. The 'wake' is formally described as the entire region of non-zero vorticity downstream of a bubble in uniform flow. It is generally divided into two regions; the near and far wake. The near wake concerns fluid flow near the rear of the bubble such as vortex formation, growth and shedding. The far wake consists of the remainder of the wake. At low Reynolds numbers, a recirculation region consisting of a toroidal shaped vortex (which appear as two counter rotating vortices in cross section) exists immediately behind the bubble at a constant relative distance. A further increase in Reynolds number leads to unstable free streamlines and complicated flow patterns. For an illustration of the wake description see Chapter 2, Figure 2.10.

The interaction between the fluid and the bubble interface determines its shape and the extent of the fluid disturbances. Therefore, the fluid structures can be described in terms of the bubble shape as is done in Chapter 5 Section 5.3. The shape is found to be dependent on eight parameters: gravity (g), terminal velocity (U_T), equivalent diameter (d_e), fluid density (ρ_f) and viscosity (μ_f), bubble density (ρ_b) and viscosity (μ_b) and surface tension (σ). For small bubbles $(d_e < 1\ mm)$, surface tension forces dominate resulting in a spherical bubble. For bubbles of intermediate sizes, such as those in the present study, surface tension and fluid inertia are dominant (with fluid viscosity and surfactants providing a major contribution, see Chapter 2, Section 2.1). This results in complex shape, motion and wake characteristics. Bubbles of this size are generally referred to as ellipsoidal although this is a generalisation, the instantaneous shape can be quite varied.

The dynamic pressure acting on the bubble determines its shape. High pressure at the front stagnation point results in an inward pressure against the bubble front surface. At the sides the flow must accelerate around the bubble interface resulting in decreased pressure. This causes the bubble sides to protrude outwards (see Chapter 2, Figure 2.10 for pressure distribution). Downstream of the bubble, the presence of the wake ensures the pressure is not recovered. An elongation in the direction perpendicular to the bubble motion is predicted. The results presented in Chapter 5, Section 5.2.1 and 5.3.1 on bubble shape confirms this. Shapes can be predicted when the Reynolds, Morton and Eötvös numbers are known, and by using the shape regime

248

map in Figure 2.6 in Chapter 2. Bubbles in the present study have properties outlined in Tables 6.1 and 6.2 for the Bubble motion and PIV setups respectively. They fall into the category of oblate ellipsoids.

Bubble volume (ml)	0.05	0.1	0.2	0.4
Equivalent diameter, d_e (mm)	5.54	6.98	8.79	11.07
Average width, b (mm)	6	7	10	16
Terminal velocity, U_T (mm/s)	175	185	200	210
Reynolds number (d_e), Re	1211	1614	2197	2975
Reynolds number (b), Re_b	1312	1618	2500	4300
Morton number, Mo	2.55×10^{-11}	2.55×10^{-11}	2.55×10^{-11}	2.55×10^{-11}
Eötvös number, Eo	2.99	4.74	7.53	11.96
Orientation angle, (θ_b)	20	20	20	15
Oscillation frequency, (Hz)	3	3	3	3

Table 6.1: Bubble and fluid parameters for the bubble motion setup: Equivalent diameter is calculated as the diameter of a sphere with the equivalent volume, the Reynolds number is presented twice based on both the equivalent diameter, d_e, and the average bubble width in the direction perpendicular to the flow, b.

As a bubble rises, work is done on the fluid by the bubble at a rate equal to the velocity times the buoyancy force. In very viscous fluids, this work is dissipated due to the effects of viscosity and a purely rectilinear motion results. In a less viscous fluid, not all of the work is dissipated by viscosity, some is converted into wake shedding which induces secondary motion[1]. This is related to periodic wake shedding behind the bubble, the onset of both wake shedding and periodic motion occurring simultaneously. Secondary motion can take the form of spiraling or zigzagging, with the bubble orienting itself to have its major axis perpendicular to the instantaneous velocity vector[2]. These criteria match the observations for the present study presented in Chapter 5, Sections 5.2.1 and 5.3.1. The orientation is also closely related to wake shedding; Table 6.1 presents the maximum orientation angle, θ_b, observed for tests that exhibited oscillation. These angles correspond well with the results presented in Fan

---

[1]Secondary motion refers to path oscillations.

[2]Note: these observations break down for high Morton number systems such as air bubbles in mineral oil; bubble motion in such systems is always rectilinear.

Bubble volume (ml)	0.05	0.1	0.2	0.4
Equivalent diameter, d_e (mm)	5.54	6.98	8.79	11.07
Average width, b (mm)	6	8	11	20
Terminal velocity, U_T (mm/s)	188	195	210	215
Reynolds number (d_e), Re	1301	1701	2307	2975
Reynolds number (b), Re_b	1410	1950	2887	5375
Morton number, Mo	2.55×10^{-11}	2.55×10^{-11}	2.55×10^{-11}	2.55×10^{-11}
Eötvös number, Eo	2.99	4.74	7.53	11.96
Orientation angle, (θ_b)	2	2	2	2
Oscillation frequency, (Hz)	14	11	7	-

Table 6.2: Bubble and fluid parameters for the PIV setup: Equivalent diameter is calculated as the diameter of a sphere with the equivalent volume, the Reynolds number is presented twice based on both the equivalent diameter, d_e, and the average bubble width in the direction perpendicular to the flow, b.

& Tsuchiya [1] which predicts an angle of 25° for rising bubbles over this Reynolds number range. Figure 2.20 in Chapter 2 illustrates that bubbles in this study are characterised as unstable, since the Reynolds number exceeds the critical value for instability of $Re_{os} > 200$ and therefore should exhibit secondary motion. The path oscillation frequency is also presented in Table 6.1; this was found to be lower than values presented in Fan & Tsuchiya [1] (reported as varying from 7-4 Hz over d_e range from $2-8.5$ mm), most likely due to the reduction in velocity attributed to the inclined surface.

Bubble shape fluctuations also need to be quantified. While the bubble shape is generally described as ellipsoid, at any one moment in time it can be far from that. The instantaneous bubble shape is the result of superposition of various modes of interface fluctuations taking place at different amplitudes and frequencies (Fan & Tsuchiya [1]). The dominant mode can be periodic, characterised as an elongation and contraction of the bubble width that occurs at twice the bubble path oscillation. The same trend is observed in the present study and is highlighted in Chapter 5, Section 5.5. For larger bubbles (usually spherical cap bubbles), the base can oscillate in conjunction with vortex shedding, as shown in Figure 6.1. The bubble edge region is periodically

stretched and released in conjunction with changing flow patterns. This figure indicates the moment of vortex release, which is close to the point described in the present study for the 0.4 *ml* bubble. Reference is made to this in Chapter 5, Sections 5.2.1, 5.3.2 and 5.5.1. Tests in the PIV setup demonstrated this simultaneously on each side of the bubble while those in the Bubble motion setup illustrated it alternating from side to side with each wake ejection. The slight differences observed may be due to the differing setups; the figure presents experiments performed with a 50 *mm* wide 'two dimensional' bubble. Two dimensional bubbles are obtained by releasing the bubble between two parallel plates separated by, typically, 10 *mm* or so.
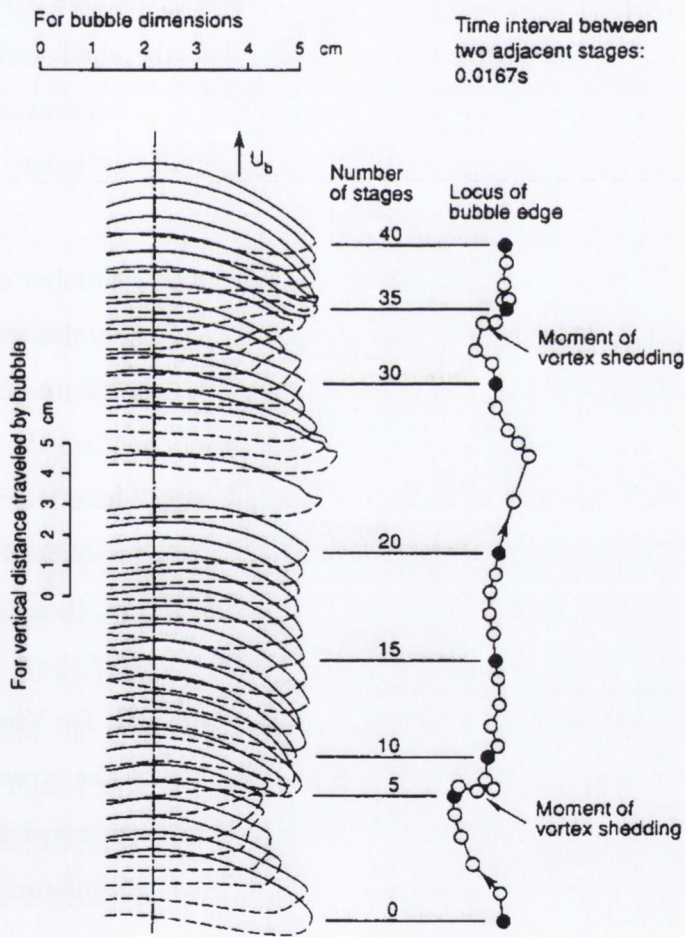

Figure 6.1: Illustration of bubble boundary shape oscillations in conjunction with vortex detachment. Each outline is separated by 0.0167 *s*. The top of the bubble is represented as a solid line, the bottom a dashed line, Fan & Tsuchiya [1].

As mentioned at the onset of this chapter, understanding the wake structure is essential to understanding both bubble dynamics and the effect on heat transfer. The wake is generally divided into two parts; the primary and secondary wakes. The primary wake exists immediately behind the bubble remaining at a fixed distance. Inside the primary wake circulatory flow patterns may exist but the boundary between it and the secondary wake may not be clearly defined. The secondary wake has an open structure. It can contain free shear layers and vortices shed from the primary wake and its boundaries are not clearly identified. Some secondary wakes have been known to contain vortex streets (in two dimensional cross section) such as those illustrated in Chapter 2, Figures 2.11 and 2.12. Structures in the secondary wake have been likened to phenomena observed behind solid cylinders such as the Kármán vortex street[3]. Experiments reproduced in Fan & Tsuchiya [1] show that the shed vortices behind a two dimensional bubble (10-20 mm bubble between 10 mm separation) arranged themselves into a regular configuration just like those behind a cylinder. The bubble took on an elliptical shape and exhibited a zig-zag motion.

The three dimensional wake is quite difficult to define and a number of configurations have been proposed and experimentally observed such as toroidal vortex rings, helical vortices, bispiral vortices and horseshoe vortex loops. Literature for rising bubbles, whose parameters are in the region of the present study, confirm the existence of horseshoe vortices (sometimes referred to as hairpin vortices). These have been found to shed in alternating directions, resulting in the oscillatory nature of the bubble path. They have also been observed to shed repeatedly in one direction, then change direction and shed repeatedly again. Illustrations and photographs of these can be seen in Chapter 2, Figures 2.13 and 2.14, 2.15 and 2.16 (Brücker [31], De Vries et al. [32] and Sanada et al. [35]). Figure 6.2 reproduces a schematic of the structure of this type of wake, in this case, behind a sphere. The horseshoe vortex consists of a series of interconnected distorted rings, a possible three dimensional configuration for the Kármán vortex street previously mentioned.

---

[3]The Kármán vortex street consists of an asymmetric double row of vortices which can be located a considerable distance behind the cylindrical object. Vortices shed symmetrically can eventually align into the characteristic structure of the Kármán street.
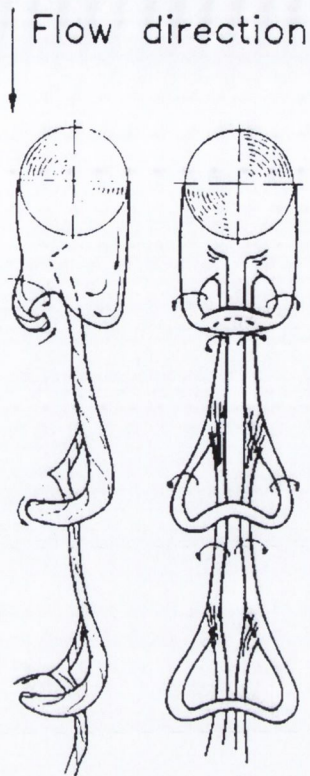
Figure 6.2: Schematic representation of the vortex configuration in the wake of a solid sphere at $Re = 1000$ viewed from two mutually perpendicular directions, Fan & Tsuchiya [1].

Results from the PIV setup indicated a series of counter rotating vortices, simultaneously shed from the wake, that travel downstream of the bubble (e.g. Chapter 5, Figure 5.33 to 5.36 and a close up view in Figure 5.41). The patterns in the heat transfer results (for the PIV setup) illustrated inverted triangular regions of cooling. The cooling was linked to vortex shedding from the bubble synchronised with bubble shape fluctuations; these cooled the surface as they moved outwards from the bubble path at an angle. Highlighted in Figure 5.46 was the appearance of a localised region of cooling between the two vortices, close to the time of shedding; this was the region of highest observed enhancement of heat transfer.

It is proposed that the wake behind the sliding bubbles in the PIV setup is of the form illustrated in Figure 6.2 for solid spheres. This would account for the observed

vortices (see Figures 5.33 to 5.36) which, in reality, are probably connected to each other (we only see a cross-section through each side of the loop but the loop is connected out of plane). The growth and shedding of a vortex sheet of this structure would result in the observed bubble shape fluctuations. It would also account for the observed patterns in the heat transfer results, where the growing vortices leave a region of cooling in the shape of an inverted triangle. Similarly, it is possible that as the top of the ring is shed towards the rear of the bubble center, a large region of cooling would be created, such as the local maximum in enhancement factor observed in Chapter 5, Figures 5.47 to 5.53. Not much literature exists on the nature of the wake behind sliding bubbles, but the behaviour of bubbles in the present study shares all the characteristics observed for rising bubbles, so it is possible that the wake is of similar structure. If the two vortices are actually connected, fluid visualisation in a plane perpendicular to the surface should reveal rows of isolated vortices emanating from the bubble wake. Figures 6.3 and 6.4 give a rare view of such a plane. It is clear to see from these two figures that not only are there multiple vortices traveling downstream but there is also a vortex immediately behind the bubble. It is not possible to know from the current results if this is the wake structure or not, but it is a plausible option.

Figure 6.3: Far field fringe pattern around and behind a sliding bubble in a liquid with small superheat, the temperature difference between two consecutive fringes is $0.0255\,°C$. The bubble is sliding from left to right and the surface is inclined to $15°$ ($\Delta T_{sub} = 0.5\,°C$, $T_w - T_s = 1\,°C$, $Ra = 1.26 \times 10^9$), Qiu & Dhir [64].

It is also proposed that the wake structure for the Bubble motion setup is similar to the one outlined above. The discussion about Figure 5.58 (in Chapter 5) gives an
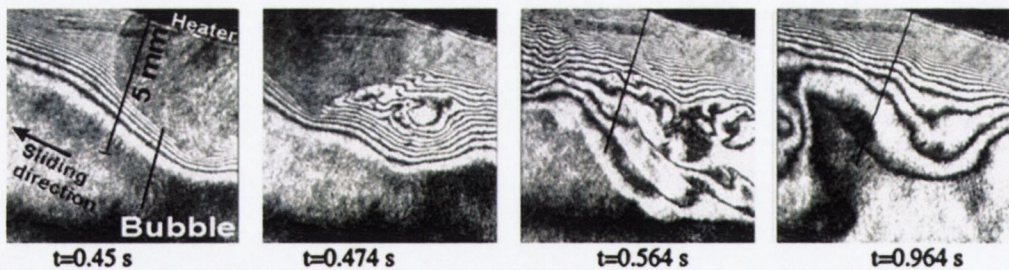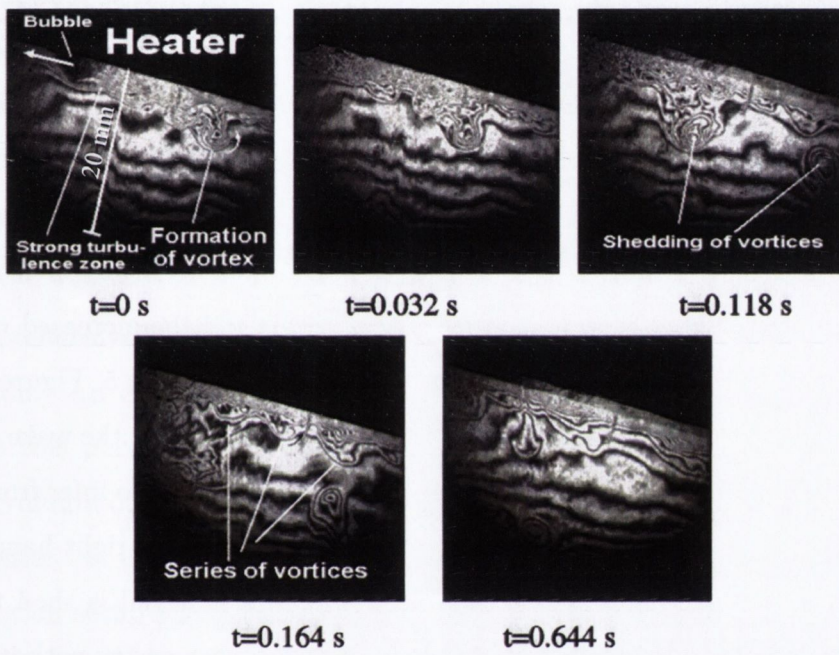
Figure 6.4: Far field fringe pattern around and behind a sliding bubble in subcooled liquid at small superheat, the temperature difference between two consecutive fringes is $0.0255\,°C$. The bubble is sliding from left to right and the surface is inclined to $15°$ $(\Delta T_{sub} = 2.7\,°C,\ T_w - T_s = 0.4\,°C,\ Ra = 2.4 \times 10^9)$, Qiu & Dhir [64].

insight as to how it might develop. As previously noted, the figure shows trends in heat transfer that were common to both the PIV and Bubble motion setup. The bubble first travels straight and appears to be shedding simultaneous vortices that leave a characteristic pattern of cooling (previously only observed in the PIV setup). This would indicate a wake similar to the one just described. As the bubble reaches the upper end of the test section it appears to shed this wake to one side only, resulting in the bubble commencing oscillation. The transition from one mode of wake ejection to the other is relatively smooth with a gradual move to its oscillating motion. We have already observed that bubbles in the PIV tests exhibit very small amplitude path oscillations. This is coupled with the emission of vortex pairs that alternate in dominant strength. It is possible to imagine the effect of this taken to the extreme, where one vortex in the pair becomes grossly larger than the other. This would result in greater path fluctuations, which may themselves contribute to stronger vortices in a self sustaining stability. The oscillatory nature of the bubble and the increased vortex strength could result in the heat transfer patterns observed in Chapter 5, Figure 5.55, while also explaining the bubble shape and motion. These results show the wake being alternately shed left and right as the bubble moves. It is also possible to infer from the observed cooling that, as the wake is shed left, it drags fluid from the right hand side of the wake. Thus, on each oscillation of bubble path, wake material is shed twice; once with the dominant vortex on the left, which drags the weaker vortex with it from the right and once with the dominant vortex on the right, dragging the left vortex with it. This may explain the difference observed between the enhancement levels in Bubble motion and PIV tests, the former being much higher than the latter. Since one of the vortices of the oscillating bubble grows to a much higher strength, it is able to cool the surface more effectively, resulting in elevated heat transfer enhancement.

Chapter 7

Conclusions

The effects of a single sliding air bubble on fluid motion and heat transfer have been investigated. This includes the dynamic behaviour of the bubble surface and motion.

A comprehensive literature review identified sliding bubbles as a poorly understood phenomenon. An experimental apparatus has been designed and built in order to investigate this phenomenon. The apparatus is capable of delivering single bubbles of known volume onto a heated surface that can be inclined between 0 and $45°$ to the horizontal. It can operate in one of two setups; Bubble motion and PIV. The Bubble motion setup allows simultaneous measurement of bubble position and shape characteristics and heat transfer while the PIV setup measures fluid velocity and heat transfer.

Computer code has been specifically developed to combine all the data for analysis, forming a three dimensional virtual representation of the real environment. In addition, properties of the bubble shape and motion are calculated. The code also quantifies losses from the foil heater surface and calculates the corrected surface heat flux.

Results have been presented detailing the bubble motion, heat transfer and fluid motion for bubble volumes of 0.05, 0.1, 0.2 and 0.4 ml sliding on both heated and non-heated surfaces. The surface is inclined at $30°$ from horizontal. Results indicate that most aspects of bubble dynamics and heat transfer can be attributed to the nature of the wake behind the sliding bubble, the structure of which has been proposed.

The experimental apparatus is in place and has been validated. The following section proposes additional work that could be performed to further the current understanding of sliding air bubbles.

7.1 Future work

A parametric study could be performed by varying the bubble volume, surface inclination angle, surface heat flux and possibly different fluids. The corresponding data could be used to build a sliding bubble shape regime map similar to that in Figure 2.6 presented by Bhaga & Weber [16].

It would be interesting to quantify the effects of surfactants on bubble shape and motion. In the present study, it was found that the addition of PIV seeding particles changed the behaviour of the bubble and its wake. The bubble motion setup could be used to get accurate bubble position and shape characteristics as the concentration of seeding particles is increased, highlighting the effect of the seeding particles.

Additional fluid measurements are required to fully understand the nature of the bubble's wake. By moving the camera closer to the surface, higher spatial resolution could be obtained. Higher frame rates would result in better temporal resolution. In addition, orienting the laser sheet perpendicular to the surface (in both the y-z and x-z planes) could confirm the existence of the proposed horseshoe vortex wake structure.

Publications

Previous work by the author has yielded publications in both journal and conference proceedings in the following fields: bubbles rising past a heated surface, bubbles sliding on an inclined heated surface and swirling air jets. The following is a list of these publications.

- B. G. Donnelly, T. S. O'Donovan and D. B. Murray, "Surface Heat Transfer due to Sliding Bubble Motion" in *Applied Thermal Engineering*, vol. 2, 2008.

- B. G. Donnelly, D. B. Murray and T. S. O'Donovan, "Bubble Enhanced Heat Transfer from a Vertical Heated Surface" in the *Journal of Enhanced Heat Transfer*, vol. 15, 2008.

- B. G. Donnelly, D. B. Murray and G. Byrne, "Sliding Bubble Motion and Heat Transfer from a Submerged Heated Plate", in the 7th *ECI International Conference on Boiling Heat Transfer*, Florianopolis, Brazil, 2009.

- B. G. Donnelly, D. B. Murray and T. S. O'Donovan, "Enhancement of Heat Transfer from a Submerged Inclined Surface due to Sliding Bubble Motion", in the *ASME-JSME Thermal Engineering Summer Heat Transfer Conference*, Vancouver, British Columbia, Canada, 2007.

- B. G. Donnelly, T. S. O'Donovan and D. B. Murray, "Surface Heat Transfer due to Sliding Bubble Motion", in the 10th *UK National Heat Transfer Conference*, Edinburgh, Scotland, 2007.

- C. Kinsella, B. G. Donnelly, T. S. O'Donovan and D. B. Murray, "Heat Transfer Enhancement from a Horizontal Surface by Impinging Swirl Jets", in *Eurotherm*

2008, Eindhoven, The Netherlands, 2008.

- B. G. Donnelly, "Bubble Enhanced Heat Transfer" in the 11th *Annual Sir Bernard Crossland Symposium*, Limerick, Ireland, 2008.

Bibliography

[1] L. S. Fan and K. Tsuchiya. *Bubble Wake Dynamics in Liquids and Liquid-Solid Suspensions*. Butterworth-Heinemann Series in Chemical Engineering, 1990.

[2] A. Frumkin and V. G. Levich. On surfactants and interfacial motion (in russian). *Zhurnal Fizicheskoi Khimii*, 21:1183–1204, 1947.

[3] R. M. Griffith. The effect of surfactants on the terminal velocity of drops and bubbles. *Chemical Engineering Science*, 17(12):1057–1070, 1962.

[4] S. S. Alves, S. P. Orvalho, and J. M. T. Vasconcelos. Effect of bubble contamination on rise velocity and mass transfer. *Chemical Engineering Science*, 60(1):1–9, 2005.

[5] P.C. Duineveld. *Bouncing and Coalescence of Two Bubbles in Water*. PhD thesis, The University of Twente, The Netherlands, 1994.

[6] R. Clift, J. R. Grace, and M. E. Weber. *Bubbles, Drops and Particles*. Academic Press, 1978.

[7] T. Saito, K. Sakakibara, Y. Miyamoto, and M. Yamada. A study of surfactant effects on the liquid-phase motion around a zigzagging-ascent bubble using a recursive cross-correlation piv. *Chemical Engineering Journal*, 158(1):39–50, 2010.

[8] R. M. Davies and G. Taylor. The mechanics of large bubbles rising through extended liquids and through liquids in tubes. *Proceedings of the Royal Society of London. Series A, Mathematical and Physical Sciences*, 200(1062):375–390, 1950.

[9] P. G. Saffman. On the rise of small air bubbles in water. *Journal of Fluid Mechanics*, 1(03):249–275, 1956.

[10] J.S. Hadamard. Mouvement permanent lent d'une sphère liquide et visquence dans un liquide visqueux. *C. R. Acad. Sci.*, 152:1735–1738, 1911.

[11] W. Rybczyński. On the translatory motion of a fluid sphere in a viscous medium (in german). *Bull. Int. Acad. Poll. Sci. Lett.*, 2:40, 1911.

[12] W. N. Bond and D. A. Newton. Bubbles, drops, and stokes' law. *Philos. Mag.*, 5:794–800, 1928.

[13] N. M. Aybers and A. Tapucu. The motion of gas bubbles rising through stagnant liquid. *Heat and Mass Transfer*, 2(2):118–128, 1969.

[14] J. R. Grace, T. Wairegi, and T. H. Nguyen. Shapes and velocities of single drops and bubbles moving freely through immiscible liquids. *Transactions of the Institution of Chemical Engineers*, 54(3):167–173, 1976.

[15] A. I. Johnson and L. Braida. The velocity of fall of circulating and oscillating liquid drops through quiescent liquid phases. *Can. J. Chem. Eng.*, 1957.

[16] D. Bhaga and M. E. Weber. Bubbles in viscous liquids: Shapes, wakes and velocities. *Journal of Fluid Mechanics*, 105:61–85, 1981.

[17] F. Durst, B. Schöenung, K. Selanger, and M. Winter. Bubble-driven liquid flows. *Journal of Fluid Mechanics*, 170:53–82, 1986.

[18] G. W. Govier and K. Aziz. *The Flow of Complex Mixtures in Pipes*. Van Nostrand Reinhold Co, 1972.

[19] F. Raymond and J. M. Rosant. A numerical and experimental study of the terminal velocity and shape of bubbles in viscous liquids. *Chemical Engineering Science*, 55(5):943–955, 2000.

[20] M. C. Ruzicka. On bubbles rising in line. *International Journal of Multiphase Flow*, 26(7):1141–1181, 2000.

[21] A. Tomiyama, G. P. Celata, S. Hosokawa, and S. Yoshida. Terminal velocity of single bubbles in surface tension force dominant regime. *International Journal of Multiphase Flow*, 28(9):1497–1519, 2002.

[22] H. M. Choi, T. Kurihara, H. Monji, and G. Matsui. Measurement of particle/bubble motion and turbulence around it by hybrid piv. *Flow Measurement and Instrumentation*, 12(5-6):421–428, 2002.

[23] G. Celata, M. Cumo, F. D'Annibale, and A. Tomiyama. The wake effect on bubble rising velocity in one-component systems. *International Journal of Multiphase Flow*, 30(7-8):939–961, 2004.

[24] G Celata, F D'Annibale, P Di Marco, G Memoli, and A Tomiyama. Measurements of rising velocity of a small bubble in a stagnant fluid in one- and two-component systems. *Experimental Thermal and Fluid Science*, 31(6):609–623, 2007.

[25] J. Hua and J. Lou. Numerical simulation of bubble rising in viscous liquid. *Journal of Computational Physics*, 222(2):769–795, 2007.

[26] J. Hua, J. F. Stene, and P. Lin. Numerical simulation of 3d bubbles rising in viscous liquids using a front tracking method. *Journal of Computational Physics*, 227(6):3358–3382, 2008.

[27] A. Gupta and R. Kumar. Lattice boltzmann simulation to study multiple bubble dynamics. *International Journal of Heat and Mass Transfer*, 51(21-22):5192–5203, 2008.

[28] L. Amaya-Bower and T. Lee. Single bubble rising dynamics for moderate reynolds number using lattice boltzmann method. *Computers & Fluids*, 39(7):1191–1207, 2010.

[29] R. Collins. Structure and behaviour of wakes behind two-dimensional air bubbles in water. *Chemical Engineering Science*, 20:851–853, 1965.

[30] G. K. Batchelor. A proposal concerning laminar wakes behind bluff bodies at large reynolds number. *Journal of Fluid Mechanics*, 1:388–398, 1956.

[31] C. Brücker. Structure and dynamics of the wake of bubbles and its relevance for bubble interaction. *Physics of Fluids*, 11(7):1781, 1999.

[32] A. W. G. de Vries, A. Biesheuvel, and L. van Wijngaarden. Notes on the path and wake of a gas bubble rising in pure water. *International Journal of Multiphase Flow*, 28(11):1823–1835, 2002.

[33] A. W. G. de Vries. *Path and wake of a rising bubble*. PhD thesis, University of Twente, 2001.

[34] K. Lunde and R. J. Perkins. Shape oscillations of rising bubbles. *Applied Scientific Research*, 58(1):387–408, 1997.

[35] T. Sanada, M. Shirota, and M. Watanabe. Bubble wake visualization by using photochromic dye. *Chemical Engineering Science*, 62(24):7264–7273, 2007.

[36] G. Mougin and J. Magnaudet. The generalized kirchhoff equations and their application to the interaction between a rigid body and an arbitrary time-dependent viscous flow. *International Journal of Multiphase Flow*, 28(11):1837–1851, 2002.

[37] T. Sanada, A. Sato, M. Shirota, and M. Watanabe. Motion and coalescence of a pair of bubbles rising side by side. *Chemical Engineering Science*, 64(11):2659–2671, 2009.

[38] K. Tsuchiya. *Wake Dynamics Behind a Single Gas Bubble in a Liquid and Liquid-Solid Fluidised Media*. Ph. d, Ohio State University, 1987.

[39] A. Ongoren and D. Rockwell. Flow structure from an oscillating cylinder part 1. mechanisms of phase shift and recovery in the near wake. *Journal of Fluid Mechanics*, 191(-1):197–223, 1988.

[40] I. Žun and J. Grošelj. The structure of bubble non-equilibrium movement in free-rise and agitated-rise conditions. *Nuclear Engineering and Design*, 163(1-2):99–115, 1996.

[41] G. Brenn, V. Kolobaric, and F. Durst. Shape oscillations and path transition of bubbles rising in a model bubble column. *Chemical Engineering Science*, 61(12):3795–3805, 2006.

[42] T. R. Kalra and P. H. T Uhlerr. Properties of bluff-body wakes. In *4th Australian Conference, Hydraulics and Fluid Mechanics*, Melbourne, Australia, 1971.

[43] K. Tsuchiya and L. S. Fan. Near-wake structure of a single gas bubble in a two dimensional liquid-solid fluidised bed: Vortex shedding and wake size variation. In *American Institute of Chemical Engineers Annual Meeting*, volume 43, pages 1167–1181, Miami Beach, Florida, 1986.

[44] G. M. Lazarek and H. Littman. Pressure field due to a large circular capped air bubble rising in water. *Journal of Fluid Mechanics*, 66(Part 4):673–687, 1974.

[45] T. Maxworthy. Bubble rise under an inclined plate. *Journal of Fluid Mechanics*, 229:659–673, 1991.

[46] H. Tsao and D. L. Koch. Observations of high reynolds number bubbles interacting with a rigid wall. *Physics of Fluids*, 9(1):44–56, 1997.

[47] G. Sateesh, Sarit K. Das, and A. R. Balakrishnan. Analysis of pool boiling heat transfer: effect of bubbles sliding on the heating surface. *International Journal of Heat and Mass Transfer*, 48(8):1543–1553, 2005.

[48] C. W. M. van der Geld. On the motion of a spherical bubble deforming near a plane wall. *Journal of Engineering Mathematics*, 42(2):91–118, 2002.

[49] A. Perron, L. I. Kiss, and S. Poncsák. An experimental investigation of the motion of single bubbles under a slightly inclined surface. *International Journal of Multiphase Flow*, 32(5):606–622, 2006.

[50] A. L. Perron, L. I. Kiss, and S. Poncsák. Motion of single bubbles moving under a slightly inclined surface through stationary liquids. *International Journal of Multiphase Flow*, 32(12):1311–1325, 2006.

[51] X. Li, D. K. Hollingsworth, and L. C. Witte. Vapor bubble rise under a heated inclined plate. *Experimental Thermal and Fluid Science*, 32(2):529–544, 2007.

[52] A. Zaruba, D. Lucas, H. Prasser, and T. Höhne. Bubble-wall interactions in a vertical gas-liquid flow: Bouncing, sliding and bubble deformations. *Chemical Engineering Science*, 62(6):1591–1605, 2007.

[53] B. Podvin, S. Khoja, F. Moraga, and D. Attinger. Model and experimental visualizations of the interaction of a bubble with an inclined wall. *Chemical Engineering Science*, 63(7):1914–1928, 2008.

[54] K. Cornwell. The influence of bubbly flow on boiling from a tube in a bundle. *International Journal of Heat and Mass Transfer*, 33(12):2579–2584, 1990.

[55] S. D. Houston and K. Cornwell. Heat transfer to sliding bubbles on a tube under evaporating and non-evaporating conditions. *International Journal of Heat and Mass Transfer*, 39(1):211–214, 1996.

[56] D. B. R. Kenning and Y. Y. Yan. Pool boiling heat transfer on a thin plate: features revealed by liquid crystal thermography. *International Journal of Heat and Mass Transfer*, 39(15):3117–3137, 1996.

[57] N. Kaneyasu, F. Yasunobu, U. Satoru, and O. Haruhiko. Effect of surface configuration on nucleate boiling heat transfer. *International Journal of Heat and Mass Transfer*, 27(9):1559–1571, 1984.

[58] K. Cornwell and I. A. Grant. Heat transfer to bubbles under a horizontal tube. *International Journal of Heat and Mass Transfer*, 41(10):1189–1197, 1998.

[59] Y. Y. Yan, D. B. R. Kenning, and K. Cornwell. Sliding and sticking vapour bubbles under inclined plane and curved surfaces. *International Journal of Refrigeration*, 20(8):583–591, 1997.

[60] D. B. R. Kenning and Y. S. Kao. Convective heat transfer to water containing bubbles: Enhancement not dependent on thermocapillarity. *International Journal of Heat and Mass Transfer*, 15(9):1709–1717, 1972.

[61] G. E. Thorncroft and J. F. Klausner. The influence of vapor bubble sliding on forced convection boiling heat transfer. *Journal of Heat Transfer*, 121(1):73–79, 1999.

[62] G. E. Thorncroft, J. F. Klausner, and R. Mei. An experimental investigation of bubble growth and detachment in vertical upflow and downflow boiling. *International Journal of Heat and Mass Transfer*, 41(23):3857–3871, 1998.

[63] M. A. Atmane and D. B. Murray. The effect of the liquid motion induced by air and vapor bubbles on heat transfer around a cylinder. *International Journal of Heat and Mass Transfer*, 48(6):1084–1095, 2005.

[64] D. Qiu and V. K. Dhir. Experimental study of flow pattern and heat transfer associated with a bubble sliding on downward facing inclined surfaces. *Experimental Thermal and Fluid Science*, 26(6-7):605–616, 2002.

[65] D. B. R. Kenning, O. E. Bustnes, and Y. Y. Yan. Heat transfer to a sliding vapour bubble. In *Boiling 2000: Phenomena and Emerging Applications*, Girdwood, Alaska, 2000.

[66] B. B. Bayazit, K. Hollingsworth, and L. C. Witte. Heat transfer enhancement caused by sliding bubbles. *Journal of Heat Transfer*, 125(3):503–509, 2003.

[67] Y. M. C. Delauré, V. S. S. Chan, and D. B. Murray. A simultaneous piv and heat transfer study of bubble interaction with free convection flow. *Experimental Thermal and Fluid Science*, 27(8):911–926, 2003.

[68] S. Manickam and V. K. Dhir. Holographic interferometric study of heat transfer associated with a single vapor bubble sliding along a downward-facing heater surface. volume 2003 of *Proceedings of the ASME Summer Heat Transfer Conference*, pages 317–327, Las Vegas, Nevada, United States, 2003. American Society of Mechanical Engineers, New York, NY 10016-5990, United States.

[69] D. Li, S. Manickam, and V. K. Dhir. A numerical study of a single bubble sliding on a downward facing heating surface. San Francisco, California, United States, 2005.

[70] A. J. Addlesee and K. Cornwell. Liquid film thickness above a bubble rising under an inclined plate. *Chemical Engineering Research and Design*, 75(7):663–667, 1997.

[71] S. C. M. Yu and C. P. Tso. Simulation of fiber optic sensors in determination of thin liquid film thicknesses. *Advances in Engineering Software*, 22(1):55–62, 1995.

[72] X. Li, D. K. Hollingsworth, and L. C. Witte. The thickness of the liquid microlayer between a cap-shaped sliding bubble and a heated wall: Experimental measurements. *Journal of Heat Transfer*, 128(9):934–944, 2006.

[73] H. W. Coleman and W.G. Steele. *Experimentation, validation, and uncertainty analysis for engineers*. John Wiley and Sons, 2009.

[74] T. Fujii and H. Imura. Natural-convection heat transfer from a plate with arbitrary inclination. *International Journal of Heat and Mass Transfer*, 15(4):755–764, IN5–IN6, 765–767, 1972.

[75] D. E. Fussey and I. P. Warneford. Free convection from a downward facing inclined flat plate. *International Journal of Heat and Mass Transfer*, 21(2):119–126, 1978.

Appendix A

Certificate of Calibration

| Certificate Number: | M04481 | | Issue Date: | 14-04-2003 |

Customer.:	University of Dublin		
Description.:	RTD Probe	S. O. No.:	09971
Type No.:	PR-11-2-100-M30-200-1/10DIN	Serial No.:	4

The above instrument has been calibrated. All measurements made were referenced to standards of the laboratory whose values are traceable to UK National Standards. Copies of tests performed are on file at Omega Engineering Limited, Irlam, Manchester and are available upon request.

STD Temperature °C	Recorded Probe Temperature °C	Uncertainty of Measurement °C
0.00	0.05	0.15
49.95	50.10	0.18
99.90	100.05	0.20
200.20	200.20	0.27
300.20	300.1	0.37

Test Conditions	Humidity	35 %
	Temperature	22 °C

Instruments Used:	OE01, OE204, OE52

Calibrated By:	S. C. Roach

Signed:

Quality Manager

Ref: RTD.doc

The expanded uncertainties are based on the standard combined uncertainty multiplied by a coverage factor of K=2 providing a confidence probability of 95%

269